Dielectric polymer nanocomposites for energy storage

Junjin Che

THÈSE PRÉSENTÉE

POUR OBTENIR LE GRADE DE

DOCTEUR DE

L'UNIVERSITÉ DE BORDEAUX

ÉCOLE DOCTORALE DES SCIENCES CHIMIQUES

SPÉCIALITÉ Polymères

Par

Junjin CHE

Nanocomposites de Polymère Diélectrique Pour Le Stockage d'énergie

Sous la direction de : Cécile ZAKRI
Co-directeur : Jinkai YUAN

Soutenue le 6 Juillet 2022

Membres du jury :

M. Alain Sylvestre	Professeur, CNRS, G2ELAB	Rapporteur
Mme Jannick Duchet-Rumeau	Professeur, INP, INSA Lyon	Rapportrice
M. Philippe Poulin	Directeur de recherche, CNRS, Bordeaux	Examinateur
Mme Annie Colin	Professeur, CNRS, ESPCI, Paris	Examinatrice
M. Jinkai YUAN	Chargé de recherche, CNRS, Bordeaux	Co-directeur de thèse
Mme Cécile ZAKRI	Professeur, CNRS, Université de Bordeaux	Directeur de thèse

Résumé

Les condensateurs diélectriques possèdent une densité de puissance intrinsèque élevée, mais ils souffrent d'une faible densité énergétique. Aujourd'hui, les systèmes électroniques et électriques avancés, qui nécessitent une intégration et une miniaturisation poussent au développement rapide de nouveaux matériaux diélectriques à haute densité énergétique et à haute efficacité. Les matériaux diélectriques aqueux à forte polarisation couplés à une forte résistance au claquage sont très prometteurs pour fabriquer des condensateurs diélectriques de manière durable. Les colloïdes constituent une classe prometteuse de matériaux pouvant être traités par l'eau. Ils constituent des blocs de construction attrayants pour l'assemblage à base d'eau de solides aux propriétés diélectriques émergentes. Dans cette thèse, nous proposons une nouvelle voie vers des matériaux diélectriques à haute énergie en construisant des nanocomposites polymères basés sur des colloïdes, en particulier sur du latex de fluorure de polyvinylidène (PVDF). Nous avons d'abord utilisé une technique à base d'eau pour préparer des diélectriques entièrement polymères constitués de nanoparticules de latex PVDF à 3% en poids dispersées dans la matrice d'alcool polyvinylique (PVA). Cette approche combine idéalement la haute permittivité du PVDF et la haute résistance au claquage du PVA, conduisant ainsi à une densité d'énergie élevée de 8,1 J/cm^3 à ~515 MV/m, qui est 300% supérieure à celle de chaque composant polymère. Les résultats indiquent que les contre-ions autour des particules de latex PVDF peuvent être confinés lorsque les nanoparticules sont naturellement dispersées et isolées dans une matrice isolante. Pour augmenter davantage la teneur en latex de PVDF et profiter pleinement de sa polarisation tout en maintenant les pertes de conduction à un niveau limité, nous utilisons du chitosan protoné, un polymère hydrosoluble bioressource, pour interagir électrostatiquement avec les nanoparticules de PVDF chargées négativement et contrôler le niveau de neutralisation de la charge des particules hybrides de PVDF. De plus, la présence du chitosan empêche la coalescence des particules de latex et favorise l'auto-assemblage des nanoparticules de PVDF pour former des films minces très compacts. Une telle structure est très favorable pour profiter de la polarisation élevée du PVDF tout en éliminant les courants de fuite avec des barrières entre les particules. Il est intéressant de

constater qu'au point dit isoélectrique (rapport massique chitosan/PVDF optimisé=0,8/99,2), la solution du mélange présente un potentiel zêta proche de 0, et les nanocomposites résultants présentent la résistance au claquage et la densité d'énergie les plus élevées (10,14 J/cm^3), soit près de 400 % de plus que le film de latex de PVDF pur. Le principe validé a été étendu avec succès à d'autres systèmes colloïdaux, tels que le latex de polystyrène et les dispersions d'argile, indiquant la polyvalence de l'approche proposée pour développer des matériaux composites diélectriques à haute énergie. Enfin, sur la base des encres diélectriques colloïdales développées, nous avons appliqué la technique d'impression par jet d'encre pour imprimer des condensateurs diélectriques compatibles avec l'électronique imprimée. Les particules de latex PVDF enrobées de chitosan au-delà du point isoélectrique sont bien dispersées dans l'eau. Le chitosan sert de liant pour améliorer largement la qualité du film, mais il attire les contre-ions négatifs dans le système. Pour confiner ces ions, des films composites à structure sandwich sont imprimés en intercalant des couches de nanofeuillets de nitrure de bore (BNNS) entre des couches de PVDF. Les nanocouches de BNNS qui sont perpendiculaires au champ électrique servent de barrière efficace pour bloquer le transport et l'avalanche de charges et conduisent finalement à une amélioration de la résistance au claquage (~610 MV/m) et de la densité de stockage d'énergie (15.04 J/cm^3). Cette thèse devrait donner des indications pour la conception et le développement de matériaux diélectriques à haute énergie pouvant être traités par l'eau.

Mots clés : Nanocomposites polymères diélectriques, Latex polymère, Stockage d'énergie, Solution aqueuse, Colloïdale, Propriétés diélectriques.

Abstract

Dielectric capacitors possess an intrinsic high power density but they suffer from the low energy density. Today, advanced electronic and electrical systems that require high integration and miniaturization drive the rapid development of new dielectric materials of high energy density and efficiency. Waterborne dielectric materials with high polarization coupled with high breakdown strength are highly promising to manufacture dielectric capacitors in a sustainable manner. Colloidal is a promising class of water-processable materials. They are attractive building blocks for the water-based assembly of solids with emergent dielectric properties. In this thesis, we proposed a new route towards high-energy dielectric materials by constructing polymer nanocomposites based on colloidal, particular on polyvinylidene fluoride (PVDF) latex. We first employed a water-based technique to prepare all-polymeric dielectrics consisting of 3 wt% PVDF latex nanoparticles dispersed within the polyvinyl alcohol (PVA) matrix. This approach ideally combines the high permittivity of PVDF and high breakdown strength of PVA, therefore leading to a high energy density of 8.1 J/cm^3 at ~515 MV/m, which is 300% greater than that of each polymer component. The results indicated that the counter ions around PVDF latex particles can be well confined when the latex nanoparticles are naturally dispersed and isolated in an insulating matrix. To further increase PVDF latex content and fully profit from its polarization while maintaining the conduction losses on a limited level, we proposed to use protonated chitosan, a bioresource water-soluble polymer, to electrostatically interact with negatively charged PVDF nanoparticles and control the level of charge neutralization of PVDF hybrid particles. Moreover, the existence of chitosan prevents the coalescences of latex particles and drives the self-assembly of PVDF nanoparticles to form closely packed but segregated thin films. Such structure is highly favorable for profiting from the high polarization of PVDF while eliminating leakage currents with barriers between particles. It is interesting to find that, at the so-called isoelectric point (optimized chitosan/PVDF mass ratio=0.8/99.2), the mixture solution shows a zeta potential near 0, and the resulting nanocomposites demonstrate the highest breakdown strength and energy density (10.14 J/cm^3), which is almost 400% higher than pure PVDF latex film. The validated principle

has been successfully extended to other colloidal systems, such as polystyrene latex, and clay dispersions, indicating the versatility of the proposed approach to developing high-energy dielectric composite materials. Finally, based on the developed colloidal dielectric inks, we have applied inkjet printing technique to print dielectric capacitors that are compatible with printed electronics. PVDF latex particles coated by chitosan beyond the isoelectric point are dispersed well in water. Chitosan serves as a binder to largely improve the film quality, but it attracts negative counter ions into the system. To confine these ions, sandwich-structured composite films are printed by intercalating layers of boron nitride nanosheet (BNNS) between PVDF layers. The BNNS nanolayers that are perpendicular to the electric field serve as efficient barrier to block the transportation and the avalanche of charges and finally lead to improved breakdown strength (610 MV/m) and energy storage density (15.04 J/cm^3). This thesis is expected to give guidance for the design and development of water-processable high-energy dielectric materials using colloidal as starting material.

Keywords: Dielectric polymer nanocomposites, Polymer latex, Energy storage, Aqueous solution, Colloidal, Dielectric properties

Acknowledgment

On September 18, 2018, I left my beloved country for the first time and started my new academic journey in France. I feel very privileged to have spent four fantastic years of my life at CRPP and to have pursued my PhD here. The four-year life and research has been an amazing, wonderful, and difficult experience. Fortunately, I have met caring and supportive supervisors who have helped me a lot in my life and research. In addition, I have made many good friends with whom I could share my happiness or sadness. Otherwise, these four years might have been doubly difficult and painful for me. I know deep in my heart that without their help, I would not have been able to achieve the success I have today. Therefore, I appreciate sincerely their help and supports, and I am especially grateful to the following people.

First of all, I would like to thank the jury members, M. Alain Sylvestre, Mme Jannick Duchet-Rumeau, Mme Annie Colin and M. Philippe Poulin, to have accepted to evaluate my thesis, particularly the two reporter, M. Sylvestre and Mme Duchet-Rumeau.

I would like to thank my supervisor Jinkai Yuan. Our story started in the summer of 2017, and I am very grateful for all the assistances since we met in Xi'an, not only for the opportunity to pursue my PhD in France, but also for taking care of my life after I arrived in Bordeaux, and for his valuable guidance in research studies during the last four years, especially in the careful revision of each presentation and paper. I am very appreciative of all the time and efforts that he gave to me and all that he has inspired me for science. I could not imagine how I would have been able to obtain this PhD without his guidance and help. The knowledge and experience I have gained with him will be very beneficial for me to continue my academic research in the future. I wish him not only great success in the field of dielectric materials and soft matter but also the cultivation of a large number of talented young scientists.

In addition, I would like to thank my supervisor and lab director, Cécile Zakri. As a director, she keeps all kinds of complicated paperwork in order, which is helpful for all PhD students to focus on their research. As a supervisor, she takes care of all aspects of the doctoral school and lab. She had given a lot of suggestion, guidance during the progress discussion of my thesis, which helps me a lot on my research, especially helping me to further improve the

quality of my dissertation. Her rigor in research has deeply influenced me, and I really appreciate her dedication.

During my research in the lab, I received a lot of assistance from our NTG team. I would like to thank the team leader Philippe Poulin for the advice and guidance during each discussion, which helped me better understand and carry out my thesis project. Thanks to Uncle Wilfrid Neri for his technical supports for my experiments and for helping me to learn French, which has taught me a lot about France that I couldn't learn from books, and of course, I will never forget the eggs he brings to me every week, they are really delicious. I would like to thank Mbolotiana for actively ordering and providing me with chemicals to ensure the smooth running of my experiments. I would like to thank Alain, Christèle, and Brigitte for helping me in each group meeting and in my daily work. I would also like to thank my colleagues who worked with me - Marco for guiding my experiments when I just arrived and Julien for teaching me how to use electrospinning. In addition, I enjoyed every interaction with Emmanuel both in research and in life. I am deeply touched by his commitment to research and wish him all the best in his trip to Japan. I am grateful to Sarah for her unfailing support. I would like to thank Sarah for sharing her knowledge of French wine, cheese and other cultures with me. I would like to thank David for his sharing and help in research, helping me to achieve many 3D printed staff. Of course, the kebab he betted for the football match was also very tasty. I enjoyed spending time with Minh Than on the soccer field, tennis and ping-pong, and of course, I appreciate his inspiration on my research. Thanks to Massinissa for sharing his knowledge in research and French (although many of them are bad words for David and me), and it was great to play with him in badminton. I would like to thank Quanping Zhang, working together has grown my insight and driving me all over Western Europe was also a very memorable trip. I would also like to thank Sara for her help with my project and the delicious jams she shared, particularly in the French writing and correction of my thesis. Of course, I cannot forget the collaboration and interaction with Ming, Xiaoyang, Joao, Sheila, Daisy, Maylis, Saban, Romain and Luna in the lab, as well as my interns Marina and Kika for helping me in my research.

I would also like to thank Isabelle, Ahmed, Eric, Joanna and Frédéric, Jean-Luc, Julien, and Emmanuelle, who provided me with technical assistance during my PhD research. Special thanks to Isabelle and Ahmed, who helped me a lot in solving problems with the experimental apparatus (especially TEM and XRD). And of course, thanks to Eric for training my experiment. Besides, the ping pong time with him was very relaxing.

Thanks to all my CRPP friends, Marco, Armand, Lachlan, Romain, Clemente, Victoria and Lucas in my office A123, who are always willing to talk and help me and share the interesting things in life, even though I am not always in the office. I would like to thank Valentine, Hanaé, Valentin, Claire, Rawan, Liu Bin, Arantza, Flavia, Alejandra, and David, I am happy to have spent a significant part of my PhD career here with them. I would also like to thank the other CRPP colleagues Hanna, Simone, Rajam, Maëva, Wael, Romain, Li Hongwei, Nouha, Ludmilla, Fréd, Florian, Lou Dandan, Lin Zi, Wang Longfei, Tatjana, Henri, In Seong, Antoine, Ludovic, Marie-Charlotte Nathalie, Mayte and so on.

Thanks to all our Chinese friends in Bordeaux. Zhang Tingting, Zhu Hongmei, etc. who came to Bordeaux together. I cannot forget the wonderful moments with Song Qilei on the weekends, drinking and talking, running and traveling, his rational thinking and straightforward character benefit me a lot. I cannot forget the time when I played soccer with Hou Lei, Zhao Luming and Song Dongming. Of course, happy times include jogging and hanging out on the market with Liu Peizhao, Liu Shaolin, Yuan Xiaojiao, Kang Naixin, Ma Fujing and Zhao Fenghuan. Thanks to Zhou Xueshi for helping me to mend my ski pants in the Alps, enjoy the walking on the streets at Paris with Liu Xinyi, and thanks Wu Liang for the simulations of my experiments. Moreover, I am grateful to Xia Chenghui and Pi Haohong for not only exercising happily together but also always helping me in life such as fixing my bike. Of course, I will never forget the countless other times we had drinks, barbecues, and celebrated Chinese New Year together. Thanks to their company, I was not alone during these four years of laboratory life. I hope we can meet again in the future and share new joy and happiness with each other.

I would also like to thank my friends from all over Europe who accompanied me during these four years. Even though we could only see each other during our holidays. Many thanks to

Han Mingyu in Paris, Han Yangyang in Zurich, Huang Juan in Barcelona, Ling Hongbin in Leuven, Fan Jimin, Wang Danni and others in Germany for your care and hospitality. Special thanks to my university classmate and my dear friend, Huang Xin, who now lives in Helsinki. Thanks to his help, I was able to get a preliminary understanding of my PhD project before I even started, so that I could adapt to it more easily and could go further. I would also like to thank Zhang Maolin for the support and help, understanding and tolerance she gave me at the critical moment of my PhD. Although thousands of miles away, and there was the interference of time difference, each other felt like a stone's throw away, and really read and understood me, and made me smile forever in the boring dissertation writing, thanks to her, dear Maolin.

Importantly, I would like to thank the China Scholarship Council (CSC) for its financial support.

Last but not the least, I am very grateful to my family, especially my parents, for raising me and supporting me all the time. As the only child in my family, they have been unconditionally encouraging and helpful over the past 30 years, from the time I croaked to today. It has allowed me to focus on my research and not worry about anything else. I love them forever!

CHE Junjin (车俊瑾)

Acronyms

AC	alternative current
AEAPS	N-(2-aminoethyl)-3-aminopropyltrimethoxysilane
ArPTU	aromatic polythiourea
BCPs	block copolymers
BN	boron nitride
BNNS	boron nitride nanosheet
BOPP	biaxially-oriented polypropylene
BST	barium strontium titanate
c-BCB	crosslinked divinyltetramethyldisiloxane-bis(benzocyclobutene)
CED	cohesion energy density
CF	carbon fiber
CH_3COONa	sodium acetate
CNT	carbon nanotubes
DC	direct current
DMF	dimethylformamide
DNA-CTMA	deoxyribonucleic acid- cetyltrimethylammonium
DSC	differential scanning calorimetry
ESR	equivalent series resistance
HCl	hydrochloric acid
IPA	isopropyl alcohol
LDPE	low density polyethylene
LTNO	Li and Ti co-doped NiO
MBS	methyl methacrylate-butadiene-styrene
MMT	montmorillonite
MWNT	multiwall carbon nanotubes

NaOH	sodium hydroxide
Oh	Ohnesorge number
P-E loop	electric hysteresis return line
PA11	poly(ω-aminodecanoyl)
PBNPF	p{bis[(norbornene pyrrolidinium hexafluorophosphate)phenyl]perylene 2,3,6,7-tetra[bis-(trifluoromethyl)phenyl]bisimide}
PBHPF	p{bis(4-methoxyl-1,6-heptadiyne) perylene 2,3,6,7-tetra[bis(trifluoromethyl)phenyl]-bisimide}
PTNP	p[N-3,5-bis(trifluoromethyl)biphenyl-norbornene pyrrolidine]
PC	polycarbonate
PDADMAC/PANa	p(diallyldimethylammonium chloride)/poly (acrylic acid sodium salt)
PE	polyethylene
PEI	polyetherimide
PET	polyethylene terephthalate
PEEU	poly(arylene ether urea)
P(DMTDMG)	poly(dimethyltin 3,3-dimethylglutarate)
PI	polyimide
PMGS	glycidyl ether grafted poly(methylhydrosiloxane)
PMMA	poly(methyl methacrylate)
PMP	poly(4-methyl-1-pentene)
PMSEMA	poly(2-(methylsulfonyl)ethyl methacrylate)
PS	polystyrene
PVA	poly(vinyl alcohol)
PVDF	polyvinylidene fluoride
PVDF-HFP	poly(vinylidene fluoride)-co-hexafluoropropylene
PVDF-TrFE-CTFE	poly(vinylidene fluoride-co-trifluoroethylene)
Re	Reynolds number
rGO	reduced graphene oxide

SEM	Scanning electron microscope
SMA	styrene-maleic anhydride
TEM	transmission electron microscope
TPU	thermoplastic polyurethane
THF	tetrahydrofuran
XRD	X-ray diffraction

Symbols

E_b	breakdown strength
U_b	breakdown voltage
C	capacitance
C_0	capacitance in a vacuum
ε^*	complex dielectric constant
ε_c	composites dielectric constant
$P(E)$	cumulative breakdown probability
ε	dielectric constant
D	dielectric displacement
P_d	dipolar polarization
E	electric field
P_e	electronic polarization
W_{loss}	energy loss
U_e	energy released from the capacitor
U_{max}	energy stored in the capacitor
U_l	energy loss
η	energy storage efficiency
ΔH_c	enthalpy of fusion at the melting point
ε_f	fillers dielectric constant
f	frequency

T_g	glass transition temperature
ε''	imaginary part of the relative permittivity
P_{int}	interface polarization
P_i	ionic polarization
B	line broadening at half the maximum intensity
R_L	load resistor
$tan\ \delta$	loss tangent
χ	magnetization per unit volume
ε_m	matrix dielectric constant
D	mean size of the crystalline domains
P_{max}	maximum polarization
l	nozzle of diameter
φ_p	percolation threshold
P	polarization intensity
P_{power}	power density
ε_r	relative dielectric constant
ε'	real part of the relative permittivity
P_r	remnant polarization
K	shape factor
β	shape parameter
α	sum of the various polarization
γ	surface tension
τ	time constant
ε_0	vacuum dielectric constant
ψ	viscosity
Φ_f	volume fractions of the filler
Φ_m	volume fractions of the matrix
V	volume of dielectric materials

X_c	weight fraction of crystallinity
λ	X-ray wavelength

Table of Contents

Chapter 1

Fundamentals of High-Energy Dielectric Materials and Colloidal

1.1 General Introduction

In recent years, with the rapid development of the global economy and the advance in technology, the demand for energy in human society has been rising. However, due to the excessive consumption of traditional fossil energy sources such as coal, oil and natural gas, these non-renewable resources have gradually started to be depleted, which not only causes the energy shortage more and more seriously but also leads to a large amount of environmental pollution, threatening the survival and safety of human beings[1]. The exploration and utilization of new energy sources, such as solar, wind, biomass, geothermal and tidal energy, has become an inevitable choice for sustainable development. Since these energy sources are scattered, unstable and intermittent, their storage and conversion have been a standing challenge for researchers. Among these, storage and conversion of electrical energy is the focus of current research, especially the low-cost and environmentally friendly energy conversion and storage systems, such as batteries, fuel cells, dielectric capacitors and electrochemical capacitors, which are attracting enormous attention[1].

Due to the high power density, excellent charging and discharging capability, wide operating temperature range, long service life, environmental friendliness, dielectric capacitors as a passive electronic component storing energy in the form of the electrostatic field have been widely applied in many fields such as new energy, smart grid, hybrid vehicles, medical electronics, electronic weapons systems[2], as shown in **Figure 1-1**. The core of dielectric energy storage technology relies on dielectric energy storage materials. The development of high-performance and low-cost dielectric energy storage materials is the top priority of dielectric energy storage technology research. Nowadays, driven by the rapid evolution of microelectronic devices as well as nanoelectronic devices, the requirements for integration, miniaturization, intelligence, flexibility and reliability are putting forward the rapid development of new dielectric materials that offer advantages of lightweight, low-cost, multi-function, high power and facile processing[3].

In this chapter, fundamental issues of capacitors and dielectric materials are first addressed, including the basic concept and definition of capacitance and dielectric constant. Particularly,

some characteristics of dielectric materials that determine the energy storage density are discussed, including polarization, dielectric losses, as well as breakdown strength (the maximum electric field that a dielectric material can sustain without a shortcut). The recent progress toward high-energy polymeric composite materials in the field will be reviewed and some long-standing challenges for solving the paradox between polarization and breakdown strength are discussed. This chapter also highlights the recently emerged new materials (i.e., colloidal particles) and new processes (i.e., inkjet printing) that are used to make high-energy dielectric capacitors.

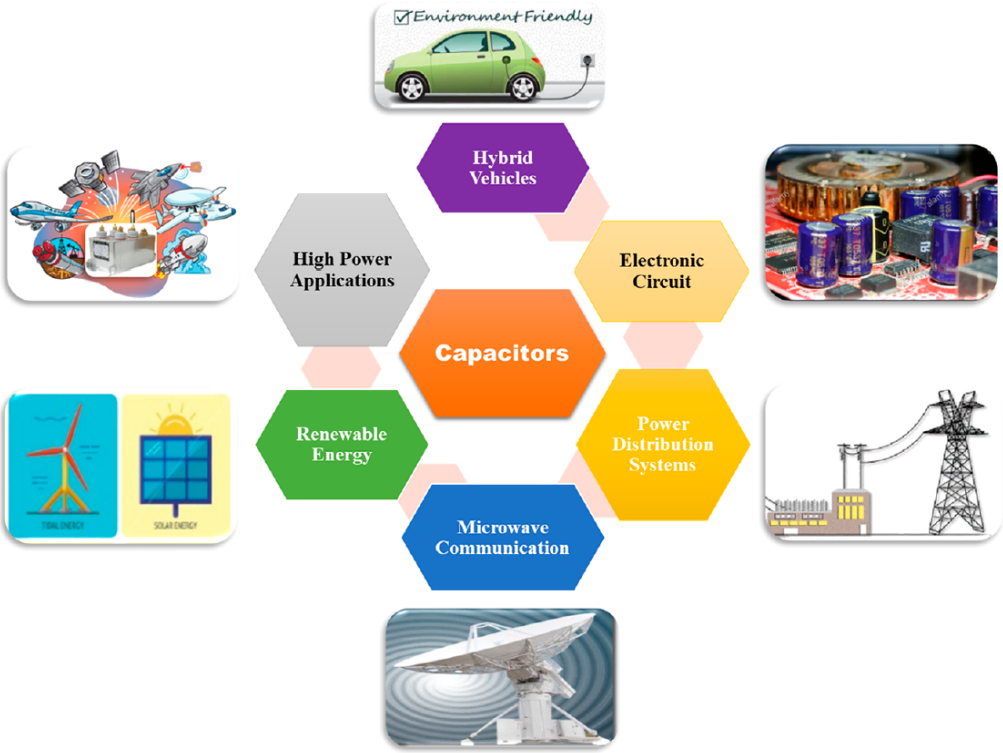

Figure 1-1. Essential applications of dielectric capacitors in various fields[2].

1.2 Capacitor Fundamentals

1.2.1 Capacitance

A capacitor is a passive component that stores energy in the form of an electrostatic field via electric displacement (or polarization), which results from the separation of electric charges or alignment of dipolar in an insulating material upon application of an electric field (**Figure 1-2**). The first recorded capacitor was the Leiden bottle invented by Ewald Georg von Kleist

and Pieter van Musschenbroek in the 1840s[4]. To date, the common construction of capacitors is still evolving from the Leiden bottle[5]. Normally, a capacitor consists of two parallel conducting plates with an area *A*, namely positive and negative electrodes, separated by an insulating material with a thickness *d*. The dielectric material, located between two electrodes, has a wide band gap that prevents the transport of free electrons inside, as shown in **Figure 1-2** (a). The dielectric materials undergo polarization, dielectric losses, breakdown and conduction under an external electric field. The polarization is the relative displacement of the center of positive and negative charges in a molecule induced by the external electric field, generating an electric dipole moment. Such charge separation-induced polarization is the basic working principle of energy storage in dielectric materials[5].

While applying a voltage *U* on the capacitor, the amount of charge generated on each plate is *Q*. To define the character of capacitors to store charges, the physical quantity of capacitance is used to quantify, which is defined as:

$$C = \frac{Q}{U} \tag{1.1}$$

The capacitance C_0 in a vacuum is determined by the overlapping area of the positive and negative plates and the distance between the two polar plates, which is expressed as:

$$C_0 = \frac{A\varepsilon_0}{d} \tag{1.2}$$

where ε_0 is the vacuum dielectric constant, 8.85×10^{-12} F/m. Yet, as the inter-electrode space is filled with dielectric materials as depicted in **Figure 1-2** (b-c) and applied with an external electric field, the net charges inside the dielectric will accumulate at the dielectric/electrode interfaces. This in turn induces an electric field in the opposite direction to the external electric field. The created opposite internal electric field reduces the overall field so that the materials can withstand an applied electrostatic field of several hundred MV/m and store more charges relative to the air-filled capacitors at the same electric field. The capacitance can be calculated by

$$C = \frac{A\varepsilon}{d} \tag{1.3}$$

where ε is the permittivity of the introduced dielectric materials.

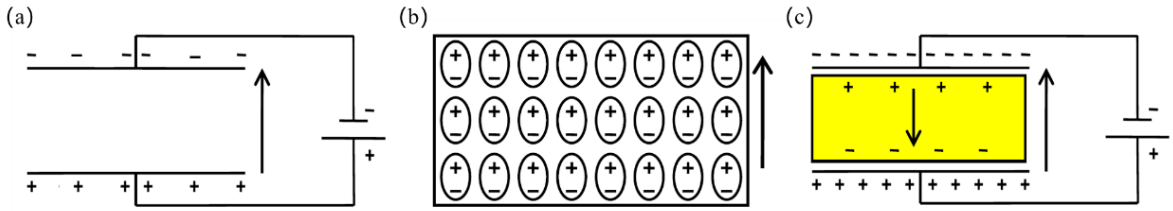

Figure 1-2. (a) Empty capacitor, (b) polarization of dielectric materials and (c) a capacitor filled with dielectric materials.

1.2.2 Dielectric Constant

The relative permittivity is a macroscopic parameter that characterizes the polarization properties of a dielectric material and is determined by the intrinsic properties of the dielectric material, independent on the applied electric field. In general, the relative permittivity can be defined by the ratio of the capacitance, the charge of the dielectric capacitor and the corresponding parameters of the vacuum capacitor, as follows[5]:

$$\varepsilon_r = \frac{\varepsilon}{\varepsilon_0} = \frac{C}{C_0} = \frac{Q}{Q_0} \tag{1.4}$$

Given the constant overlapping area *A* and spacing *d* of the two electrode plates, it can be noted that the higher the degree of polarization of the dielectric, the greater the number of induced charges on the plates, the greater the relative permittivity, the greater the capacitance value of the electrostatic capacitor, as illustrated by

$$C = \frac{A\varepsilon_0\varepsilon_r}{d} \tag{1.5}$$

However, under an alternating electric field, the dielectric constant of dielectric material is not a constant anymore, which is dependent on the applied frequency, the electric field and the temperature as well. To characterize this electrical behavior, a new physical quantity is introduced, namely the complex dielectric constant, with the following equation[6]:

$$\varepsilon^* = \varepsilon' - i\varepsilon'' = \varepsilon_0\varepsilon_r - i\varepsilon'' \tag{1.6}$$

$$\varepsilon' = \varepsilon'_{induced\ dipole} + \varepsilon'_{alignment\ of\ dipole} \tag{1.7}$$

$$\varepsilon'' = \varepsilon''_{dipole\ loss\ factor} + \varepsilon''_{ionic\ conductance} \tag{1.8}$$

where ε' is the real part of the relative permittivity representing the amount of dipole alignment both induced and permanent, which is related to the energy storage in the dielectric, and ε'' is

the imaginary part of the relative permittivity representing the dipole loss factor plus ionic conduction, which is related to the energy loss in the dielectric.

1.2.3 Polarization

The capability of a dielectric material to store charges under an external electric field depends on the polarization of the material. In general, polarization occurs when the center of positive and negative charges does not coincide or deviate under an applied electric field. As shown in **Figure 1-3**, dielectric materials exhibit different polarization mechanisms at different frequencies, corresponding to different relaxation characteristics[2].

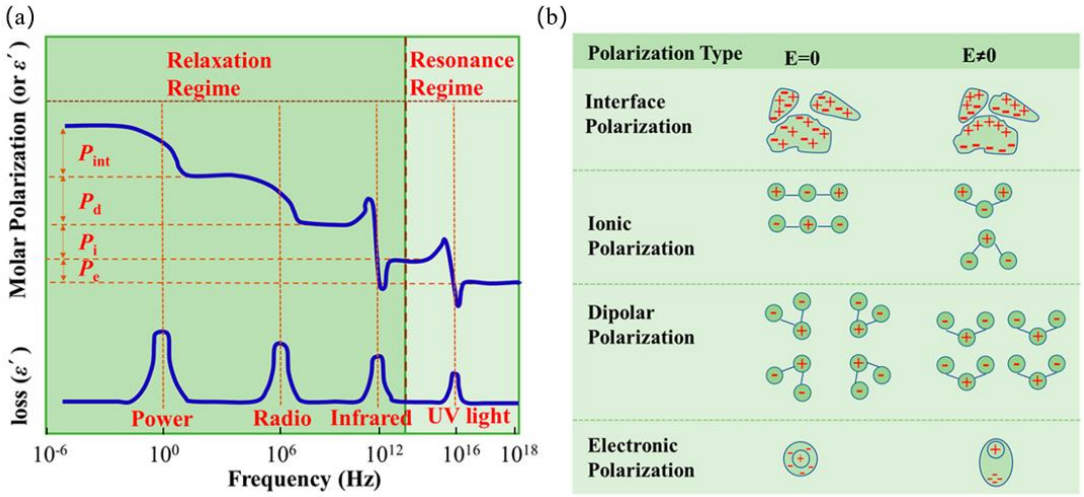

Figure 1-3. (a) Dielectric constant and dielectric loss responses of various polarizations at a wide-range of frequencies. (b) Schematic representation of different types of polarizations before and after the application of electric fields.

As the frequency increases, the dielectric constant of the dielectric material gradually decreases because the polarization response gradually fails to keep up with the variation of frequency in dielectric materials, resulting in a weaker contribution to the overall dielectric constant. The dielectric constant of materials is therefore mainly contributed at different frequency ranges by different polarization mechanisms, such as electronic polarization (P_e), ionic polarization (P_i), dipolar polarization (P_d) and interface polarization (P_{int}) [2, 7-8].

Electronic polarization P_e is the result of an applied electric field, which causes the electron cloud around an atom to deviate from its original center. The center of positive and negative charge no longer coincide, resulting in polarization with a certain direction, as shown

in **Figure 1-3** (b). This type of deviation is not permanent and the polarization disappears once the applied electric field has been removed. This polarization mechanism is common to all-dielectric materials. Due to the fast electron motion, the response time for electron polarization is very short, around 10^{-14}~10^{-16} s, which results in this polarization relaxation being generated at a high frequency of around 10^{15}~10^{16} Hz.

Ionic polarization P_i, known as vibrational polarization or displacement polarization, is caused by the displacement of cations and anions under an electric field, as shown in **Figure 1-3** (b). When an electric field is applied to an ionic substance, the cations and anions are displaced in opposite directions until ionic bonding forces prevent this process from occurring, inducing a dipole moment. This polarization is mainly found in inorganic crystalline, glass and ceramic materials and is the main polarization mechanism affecting the dielectric constant of these kinds of materials. The response time of ion polarization is also very short, around 10^{-12} ~10^{-13} s, corresponding to a polarization relaxation frequency of around 10^{12} Hz.

Dipolar polarization P_d also referred to as orientation polarization usually occurs in polar dielectrics, which have permanent dipoles in such materials as polar polymers and ceramics. Normally, the dipole in a polar medium is randomly oriented and its net dipole moment is zero. As shown in **Figure 1-3** (b), when an external electric field is applied, the dipole tends to reorient in the direction of the applied electric field, resulting in a non-zero net dipole moment and polarization. Orientation polarization is the main polarization mechanism for most polymers and some ceramic dielectrics. Since the dipole motion process is usually temperature dependent, the response time of oriented polarization is strongly temperature-dependent, roughly in the range of 10^{0} ~ 10^{-9} s. The corresponding polarization relaxation frequency is also widely distributed, approximately 10^{4}~10^{10} Hz.

Interface polarization P_{int} is also known as space charge polarization, which is usually associated with the macroscopic migration of charge within a medium when an electric field is applied. These charges consist mainly of free electrons, holes, ions or various other charged impurities. They are often trapped and grouped by physical barriers such as defects, voids, impurities, grains or phase interfaces. These accumulated charges distort the local electric field

and cause polarization, thereby increasing the dielectric constant of the material. Interfacial polarization is particularly important in heterogeneous or multiphase systems, such as polymer-ceramic nanocomposites. Interfacial polarization involves the long-range movement of ions and therefore has a long response time of about 10^{-4} s and is usually only observed at low frequencies (about 10^{-3}~10^{3} Hz). This polarization is also known as Maxwell-Wagner polarization.

The total polarization rate of dielectric material is obtained as the sum of the various polarization mechanisms possessed by the type of material. It can be described by the following equation[9]:

$$\alpha = \alpha_e + \alpha_i + \alpha_d + \alpha_{int} \tag{1.9}$$

where α_e, α_i, α_d and α_{int} represent electronic polarization, ionic polarization, orientation polarization and interfacial polarization, respectively. The relationship between the dielectric constant of materials and its polarization can be described by the Clausius-Mosotti model[10]:

$$\varepsilon = \frac{3}{1-\frac{N\alpha}{3\varepsilon_0}} - 2 \left(0 < \alpha < \frac{3\varepsilon_0}{N}\right) \tag{1.10}$$

in which N is the number of molecules per unit volume and α is the polarization rate per molecule. According to this equation, an increase in the dielectric constant of dielectric material is closely related to an increase in polarization.

1.2.4 Dielectric Loss

The dielectric loss of dielectric material is normally denoted as the angular tangent of the dielectric loss ($tan\ \delta$), which is the ratio of the imaginary part of the dielectric constant to the real part of the dielectric constant and can be expressed by the following formula:

$$tan\ \delta = \frac{\varepsilon''}{\varepsilon'} \tag{1.11}$$

It can be demonstrated that the dielectric loss is also an intrinsic property of the material and is not dependent on the geometry or size of the capacitor. The energy loss (W_{loss}) of an energy storage capacitor device as a result of losses in the dielectric material can be determined by the following equation[11]:

$$W_{loss} \approx \pi \varepsilon' f E^2 tan\, \delta \quad (1.12)$$

Where E is the electric field and f is the frequency. Therefore, the energy loss is dependent on the amount of dielectric loss and permittivity. When the material has a low dielectric loss and low permittivity, the energy loss is low.

In general, dielectric losses in dielectric materials are mainly determined by electron cloud distortion, dipole relaxation, interface polarization and leakage currents. The distortion losses are related to the electron and ion polarization. The dipole relaxation is mainly due to the dipole polarization caused by the movement or rotation of atoms or molecules under alternating electric fields. Interfacial losses are mainly induced by the interfacial polarization between filler and matrix and dielectric relaxation caused by space charges. The conduction losses are mainly due to the direct leakage current of the material.

1.2.5 Breakdown Strength

The dielectric material will lose its dielectric properties and become a conductor under a high enough electric field. This phenomenon is called dielectric breakdown[12]. The maximum voltage corresponding to the breakdown of the dielectric material is the breakdown voltage and the corresponding electric field strength is the breakdown strength. The breakdown strength of the dielectric film can be obtained from the definition:

$$E_b = \frac{U_b}{d} \quad (1.13)$$

where U_b is the breakdown voltage and d is the thickness of the dielectric film. The breakdown mechanism of polymers has been extensively and carefully studied and the breakdown strength is closely related to the thermal, mechanical and electrical properties and microstructure of polymers[13-14]. Depending on the breakdown mechanism, the breakdown process of the dielectric can be classified into the intrinsic electric breakdown, thermal breakdown, electrochemical breakdown and discharge breakdown[15-18]. **Figure 1-4** shows the schematic illustrations of the thermal breakdown and electric breakdown.

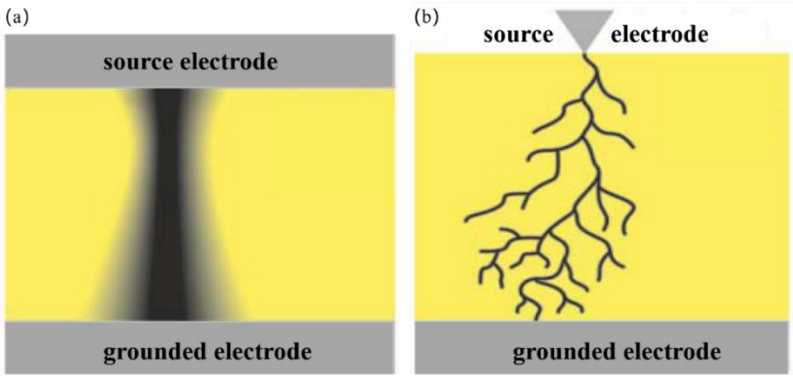

Figure 1-4. Basic illustration of (a) primarily thermal breakdown and (b) electrical treeing in epoxy[19].

A thermal breakdown is a form of solid dielectric breakdown. Due to leakage current, electric loss or pore local gas ionization discharge generated by exothermic, the thermal equilibrium state of heat dissipation and generation would turn into an unbalanced state and the temperature of solid dielectric material would gradually increase under electric field. With the continuation time, the accumulated heat increased. When a certain temperature is reached, the material that undergoes line cracking, vitrification or melting would destroy insulation properties, resulting in a breakdown phenomenon. The thermal breakdown is related to many factors such as internal defects of the medium, thermal conductivity, dopants, strength, shape, porosity and heat dissipation conditions[20-22].

The electrochemical breakdown is a mechanism by which a polymer suffers a dielectric breakdown in the presence of a high electric field. Electric currents generated by strong electric fields in dielectrics can cause electrochemical reactions under certain conditions such as high temperatures. As a result, the dielectric structure has changed, or the separated substances form a conductive pathway between the two electrodes. Dielectric surface and internal discharge in the bubble may also form harmful substances such as ozone, and carbon monoxide, so that the bubble wall corrosion caused by local conductivity increase and local breakdown, and gradually expand into a complete breakdown. The higher the temperature, the longer the voltage applied, and the more likely the chemically formed breakdown will occur. In addition, it is usually found in solid insulation at the operating voltage of electrical equipment, especially in organic insulation materials with poor free resistance[23-25].

Electric breakdown theory is based on the collisional ionization theory of gas discharge[26-27], avalanche theory[28] and tunnel theory[29]. Under a strong electric field, some free electrons may exist in the solid medium due to cold emission or thermal emission. These electrons are accelerated under the external electric field and gain kinetic energy on the one hand. On the other hand, they interact with the lattice vibration and transfer the electric field energy to the lattice. When these two processes are balanced at a certain temperature and field strength, the solid medium has a stable conductivity. While the energy obtained from the electric field is greater than the energy transferred to the lattice vibration, the kinetic energy of the electrons becomes larger and larger. To a certain value of electron energy, the interaction between electrons and lattice vibration leads to the ionization of new electrons, so that the number of free electrons increases rapidly. The conductivity enters into an unstable phase, and a rapid breakdown occurs. It is featured by short time and high breakdown voltage, which is closely related to the uniformity of the electric field, but almost independent on the ambient temperature and the time of applied voltage[30-33].

The breakdown strength of dielectric films fluctuates in a wide range, and published papers usually use two methods to determine the breakdown voltage of dielectric films: one is directly averaging different measurements[34], the other is calculating the intrinsic breakdown strength of the material according to the Weibull distribution[35-37]. From the number of published papers, the second method is more commonly used and in this thesis, the breakdown strength of our dielectric films is also deduced using this method[38-39]:

$$P(E) = 1 - e^{-\left(\frac{E}{E_b}\right)^{\beta}} \tag{1.14}$$

Where $P(E)$ is the cumulative breakdown probability, E is the test breakdown field strength, E_b is the breakdown strength of the composite film at a cumulative probability of 63.2 % and β is the shape parameter, representing the dispersion in the data. In general, the larger the value of β, the more concentrated the breakdown field distribution is and the more reliable the calculated material property is. In general, samples are submerged in insulating silicon oil and 15 spots were tested at different locations for each sample[40], as shown in **Figure 1-5.**

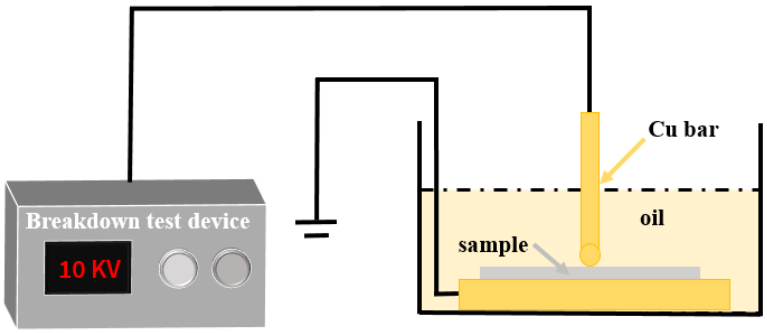

Figure 1-5. Schematic diagram of the breakdown strength measurement.

To ensure the stable and safe operation and suitable service life of capacitors, capacitors are usually used at reduced voltage, namely their operating voltage is usually lower than their breakdown voltage, so the breakdown voltage of capacitors is a critical parameter that has to be considered when designing capacitors.

1.2.6 Energy Storage Density

For all dielectric materials in an electrostatic field, where the conductivity is zero, the relationship between the applied electric field E and the resulting polarization P can be expressed by the following equation[41]:

$$D = \varepsilon_0 E + P = \varepsilon_0 \varepsilon_r E \tag{1.15}$$

where D represents the dielectric displacement. By recombination, the above equation can be evolved as:

$$P = \varepsilon_0(\varepsilon_r - 1)E = \varepsilon_0 \chi E \tag{1.16}$$

where χ is the magnetization per unit volume of the dielectric material. When the dielectric constant of dielectric material is large enough, this means that the value of the dielectric displacement at this point is similar to the value of the polarization. Under a strong alternating electric field, the polarization intensity P (or D) of the dielectric exhibits nonlinear behavior depending on the applied electric field[42]. P (or D) displays a certain hysteresis as a bivariate function of the electric field E over a certain temperature range, calling this P-E (or D-E) electric hysteresis return line, simplified as P-E loop. According to the relationship between E

and *P*, dielectric materials can be classified as linear dielectric, dipolar glass, paraelectric, ferroelectric, and anti-ferroelectric, as shown in **Figure 1-6**[43].

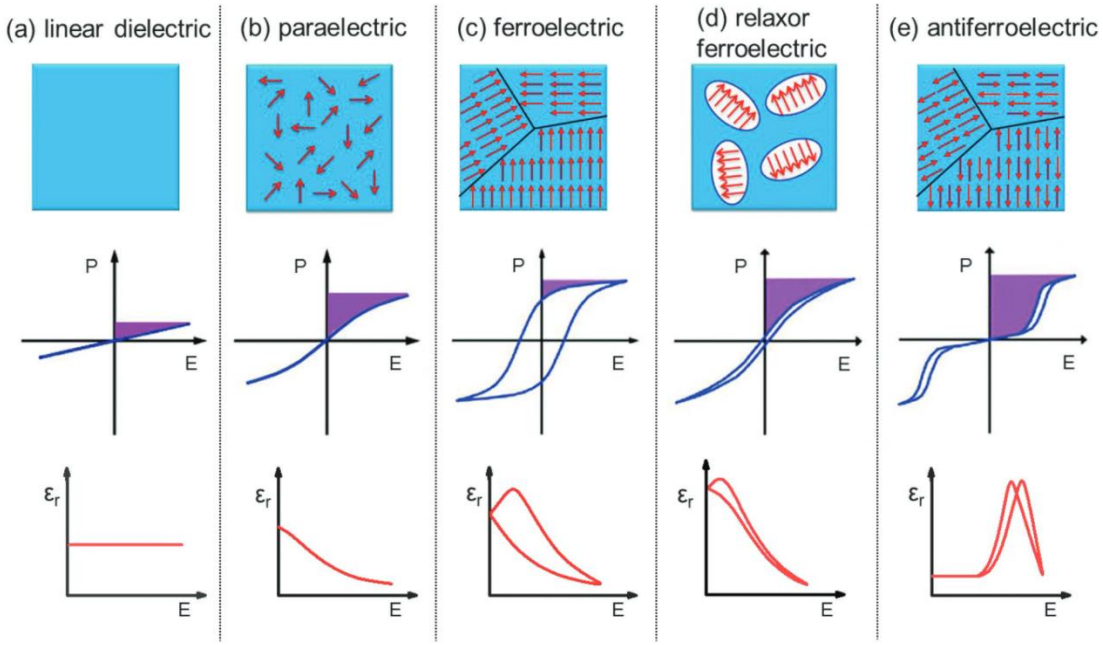

Figure 1-6. Dipole and ferroelectric domain structures (top panel) and typical dependence of polarization (middle panel), and permittivity (bottom panel) on the electric field for (a) linear dielectric, (b) paraelectric, (c) normal ferroelectric, (d) relaxor ferroelectric, and (e) anti-ferroelectric materials. The shaded area above the *P*-*E* loop represents energy density and the area inside the loop represents energy loss[43]. The shaded area in the middle panel is the discharged energy.

The linear dielectric has a narrow *P*-*E* loop, showing a low energy loss and thus high charge/discharge efficiency. However, its polarization is generally weak due to the absence of net dipole moment in the polymer. They are essentially unpolarized. A typical example of this type of material is the biaxially-oriented polypropylene (BOPP) commercial films. It should be noted that BOPP films, even though they are linear dielectric, have relatively large hysteresis at high fields due to the leakage. For ferroelectric materials, such as polyvinylidene fluoride (PVDF), the *P*-*E* loop is broadened. The polar crystalline polymers contain a large number of ferroelectric domains and therefore exhibit ferroelectricity. The ferroelectric domains in ferroelectric polymers are shunted by the electric field. When the electric field is removed, some ferroelectric domains cannot return to their original positions, and residual polarization occurs, resulting in a large energy loss in ferroelectric materials. In addition, it is possible to

obtain quasi-electric polymers, and anti-ferroelectric polymers by adjusting the interaction between iron dipoles.

The energy storage density of dielectric materials is an extremely important parameter determining the performance of electrostatic capacitors. High energy storage density is the key to achieving the miniaturization, integration, compactness, and intelligence of capacitors, which is essential for promoting the development of advanced electrical and electronic industries. As illustrated in **Figure 1-7** (a), the variation of charge in the dielectric material is reflected in the *P-E* loop with a varying electric field. As the electric field is applied, the polarization of the material is induced and the dielectric material begins to charge so that the electrostatic energy is stored by the dipoles aligning. When the electric field is withdrawn, the dielectric material that completes the charging process can be used as a power source to discharge to another load since the oriented dipoles tend to be randomly distributed again and the stored electrostatic energy can be released, as shown in **Figure 1-7** (b). The integral of the charge curve on the vertical coordinate, namely the area enclosed by the charge curve and the vertical axis is the energy stored in the capacitor, which is represented by U_{max}. Similarly, the integral of the discharge curve over the vertical coordinate, namely the area enclosed by the discharge curve and the vertical axis, is the energy released from the capacitor and is represented by U_e. During the charging process of a dielectric material, the charges can be generated by polarization (e.g. electron polarization and ion polarization) and by the injection from electrodes. And the maximum energy that can be stored is calculated as:

$$U_{max} = \int_{P_m}^{0} EdP \tag{1.17}$$

where P_m is the maximum polarization, and E is the electric field. While, for the discharging, the leakage current or the remnant polarization (P_r, as in the case of ferroelectric materials) results in the stored charge not being completely released, therefore decreasing the energy storage efficiency. In this case, the hysteresis line is not straight even for linear dielectrics at a high electric field due to the presence of leakage currents. The discharged energy density can be therefore calculated by the following integral equation[1, 44-45]:

$$U_e = \int_{P_r}^{P_m} EdP \tag{1.18}$$

where P_r is the remnant polarization.

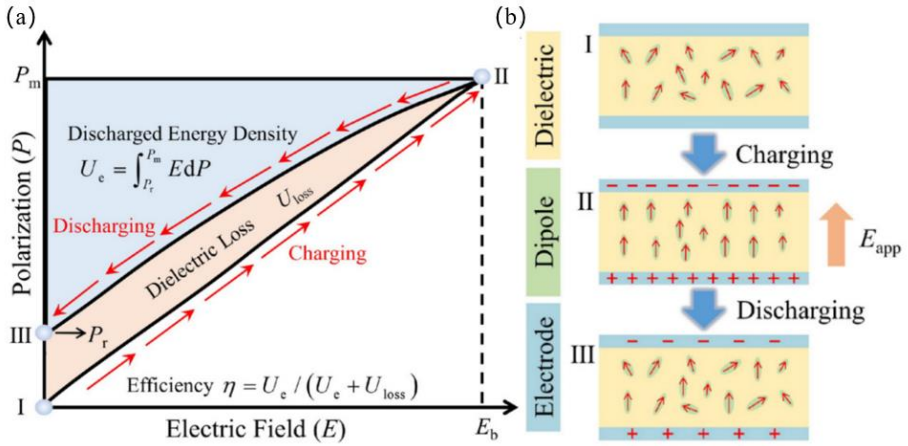

Figure 1-7. (a) Schematic illustration of dielectric energy storage during a charge/discharge process. Points I to II represent the charging process, while points II to III represents the discharge process. (b) Corresponding local dipole states in the dielectrics of points I, II and III[46].

For linear dielectrics, the dielectric constant is independent on the applied electric field and the energy storage density can be simplified as:

$$U_{max} = \frac{1}{2}\varepsilon_0\varepsilon_r E^2 \tag{1.19}$$

As can be seen from this equation, the maximum energy storage density of dielectric materials depends mainly on two factors: the dielectric constant and breakdown strength. The energy storage density is proportional to the dielectric constant and proportional to the square of the breakdown strength, indicating that the breakdown strength has a more significant effect on the energy storage performance of the dielectric. And any small increase in breakdown strength can lead to a significant enhancement in energy storage density if the permittivity of the materials can be well controlled.[47-48]

In addition, the energy storage efficiency (η) is another important parameter to evaluate the energy storage performance of the dielectric material during the charging and discharging process. An ideal capacitor is a perfect insulator without energy loss and a charge/discharge efficiency of 100%. However, this is not the case in practice, as discussed above, both dipole

steering and the prevalent leakage current bring about energy loss, and the dielectric material of the capacitor consumes some of the energy when storing charges, resulting in a charge/discharge efficiency of less than 100%. The energy storage efficiency is defined as [43]:

$$\eta = \frac{U_e}{U_e+U_l} \times 100\% \quad (1.20)$$

where U_l is the energy loss, which mainly comes from the conduction loss and ferroelectric hysteresis during the charge/discharge cycle. The conduction loss usually occurs at low frequencies. A small number of charge carriers in the dielectric can migrate under the applied external electric field and generate a conduction current, which leads to partial energy dissipation through Joule heat. Ferroelectric losses are caused by the orientation polarization hysteresis of the dipole. During the charging and discharging process, due to the phase hysteresis, the ferroelectric phase cannot keep up with the change in the external electric field during the orientation and de-orientation process, resulting in energy loss. This hysteresis also occurs during the crystal phase transition between the polar and nonpolar phases of ferroelectric materials.

1.2.7 Power Density

High power density is a big advantage of dielectric capacitors over other energy storage devices, such as batteries or fuel cells. This feature allows them to be used in diverse pulsed power systems. As shown in **Figure 1-8** (a), the discharged energy storage density can be obtained kinetically by the charge/discharge process using a specifically designed circuit[1, 49-50]. The power density can therefore be deduced by considering the discharged time involved. In detail, the capacitor is first charged by an external source, and then, through a high-speed and high-voltage switch, the stored energy is discharged to a load resistor (R_L) in series with the capacitor. As shown in **Figure 1-8** (b), the voltage across the resistor U(t) is recorded. The fitting to the curves by the equation $U(t) = U_0 e^{-(\frac{t}{\tau})}$ yields the time constant (τ). The change of τ obtained from the fitting to different time ranges can be associated with the increased effect of equivalent series resistor (*ESR*) of samples at the later discharge process. R_L should be much larger than the ESR of the sample capacitor, so most of the stored energy will be delivered to the

load resistor and the measured energy density will be nearly the same as the stored energy density[51]. Based on the discharging curves, the power density (P_{power}) can be calculated by[1]:

$$P_{power} = \frac{U(t)^2}{R_L} \tag{1.21}$$

The discharged energy density U_e of the dielectric material is further calculated by:

$$U_e = \frac{\int_0^\infty P_{power} dt}{V} = \frac{\int_0^\infty \frac{U(t)^2}{R_L} dt}{V} \tag{1.22}$$

where V is the volume of dielectric materials. The calculated energy density is plotted in **Figure 1-8** (b) as a function of time. The discharge time is defined here as the time that is needed to reach 95% of the final discharge energy over a load resistor[52].

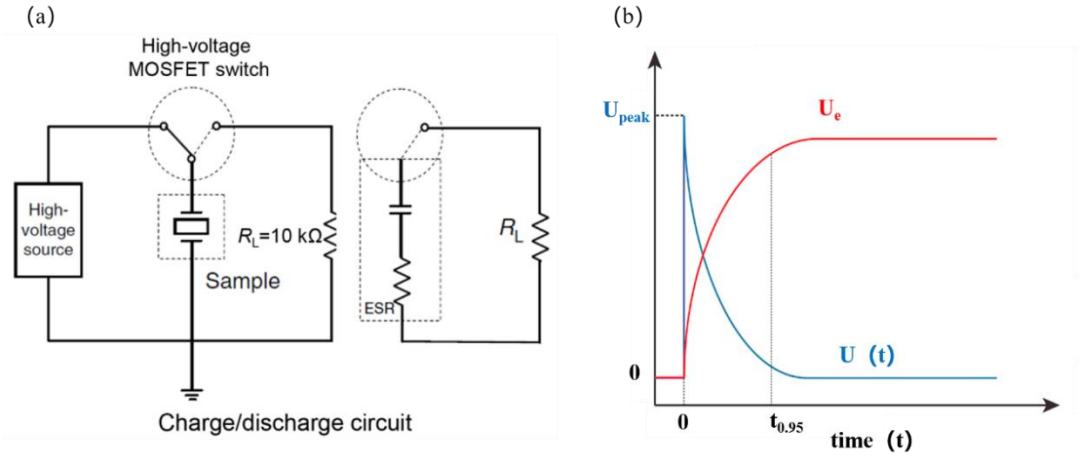

Figure 1-8. (a) Schematic diagram of the fast charge/discharge circuit[52]. (b) The current passed through the load resistor R_L and the calculated discharged energy density as a function of time. The discharged peak voltage U_{peak} denotes the maximum voltage during the discharge process. The discharge time $t_{0.95}$ denotes the time required for the discharged energy density to reach 95% of the final value from the discharge profile.

1.3 Dielectric Polymer Composite Materials

In this section, the progress of high-energy dielectric materials will be reviewed, including ceramics, polymers, and particularly ceramic/polymer and polymer/polymer composite materials. Some strategies for improving the energy storage performances of dielectric polymer composites will be addressed and the long-standing challenges will be highlighted.

As traditional dielectric material, ceramics have been widely used in diverse dielectric capacitors due to their high permittivity and excellent thermal stability. The dielectric constant values of common dielectric ceramic materials are listed in **Table 1-1**. It can be seen that ceramic materials have permittivity ranging from several hundred to thousands, yet accompanying high dielectric loss and relatively low breakdown strength. These features will limit their energy density and storage efficiency. Their technical implementation for high-energy storage capacitors remains challenging. In addition, ceramic materials are heavy in mass and have challenging processing and poor mechanical flexibility, which further limits their application in miniaturized and lightweight electronic devices such as embedded capacitors.

Table 1-1. Dielectric properties of commonly used ceramics for capacitors[2, 53].

Ceramics	ε (1 kHz)	$tan\ \delta$ (1 kHz)	E_b (kV/cm)	U_e (J/cm^3)
$BaTiO_3$	1235	0.012	150	0.829
Al_2O_3	10.1			
$BaTiO_3$-$BiScO_3$	750	0.1	730	6.1
0.88$BaTiO_3$-0.12-$Bi(Mg_{0.5}Ti_{0.5})O_3$	1500	0.01	224	1.81
0.9$(La_{0.02}Li_{0.02}Bi_{0.48}Na_{0.48}Ti_{0.98}Zr_{0.02}O_3)-0.1(Na_{0.73}Bi_{0.09})NbO_3$	935	0.02	178	2.04
0.8(0.92 $Bi_{0.5}Na_{0.5}TiO_3$-0.08$BaTiO_3$)-0.2$(Na_{0.73}Bi_{0.09})NbO_3$	1400	0.028	136	1.36
0.8$(K_{0.5}Na_{0.5})NbO_3$-0.2$SrTiO_3$	6700		400	3.67
0.9$BaTiO_3$-0.1$Bi(Mg_{0.67}Nb_{0.33})O_3$	1500		270	1.13
0.9$K_{0.5}Na_{0.5}NbO_3$-0.1$Bi(Mg_{0.67}Nb_{0.33})O_3$	1100		300	4.08
0.8$(K_{0.5}Na_{0.5})NbO_3$-0.2$Sr(Sc_{1/2}Nb_{1/2})O_3$	1500		295	2.02

Polymers, as alternatives, have been widely used in electrical and electronic applications such as power cables, film capacitors, organic field-effect transistors and artificial muscle brakes due to their high breakdown strength, low dielectric loss, high power density, facile processability, and low weight[54-55]. Polymer dielectric materials, such as semi-crystalline thermoplastic polymers polyester and polypropylene, have not only higher breakdown strength

than ceramic counterparts, but also a graceful failure feature, namely a self-healing ability to repair the breakdown damage point[1, 56]. However, the dielectric constants of polymers are usually low, limiting their further application as energy storage materials in advanced integrated and miniaturized devices[57]. The dielectric properties of various polymer films are summarized in **Table 1-2**.

Table 1-2. Dielectric properties of commonly used polymers for capacitors[57]

Polymer	ε	Maximum operation temperature (°C)	E_b (MV/m)	*tan* δ @ 1kHz	U_e (J/cm^3)
Polypropylene	2.2	105	640	<0.02	1-1.2
Polyester	3.3	125	570	<0.5	1-1.5
Polycarbonate	2.8	125	528	<0.15	0.5-1
Polyethylenenaphlate	3.2	125	590	<0.15	1-1.5
Polyphenylenesulfide	3.0	200	550	<0.03	1-1.5
Polyvinylidenefluoride	12	125	550	<1.8	2.4

1.3.1 Polymer Based Composites

Traditional dielectric ceramics and polymers have respective advantages and disadvantages as dielectric materials. Ceramics possess high permittivity but suffer from low breakdown strength, while polymers possess high breakdown strength but low permittivity. Due to the inverse correlation between the polarization and breakdown strength, the achieved discharged energy density to date is still limited (<5 J/cm^3) for capacitors based on ceramics or polymers alone. Preparing nanocomposites to take advantage of both types of dielectrics is a promising strategy to improve the energy storage capability. **Figure 1-9** shows the advantages and disadvantages of ceramics, polymers and polymer composites to serve as dielectrics, respectively. This approach, which is rationally motivated by the ‘‘mixing rules”, relies on combining high dielectric constant fillers in a high breakdown strength polymer[58, 67].

Kim et al..[59] investigated the dielectric properties and breakdown performance of the polymer-based composites consisting of high-E_b PVDF-HFP matrix and high permittivity $BaTiO_3$ spherical particles. **Figure 1-9** (b) showed an enhanced dielectric constant with

increasing $BaTiO_3$ content compared with pure polymer. The permittivity reached the highest value at 60% $BaTiO_3$ loading. Further adding the fillers into the polymer matrix, the dielectric constant started to be deceased even though it is still high than pure polymer. Yet, the dielectric constant (<40) of the composite is still very low compared to the extremely high value of the ceramic filler.

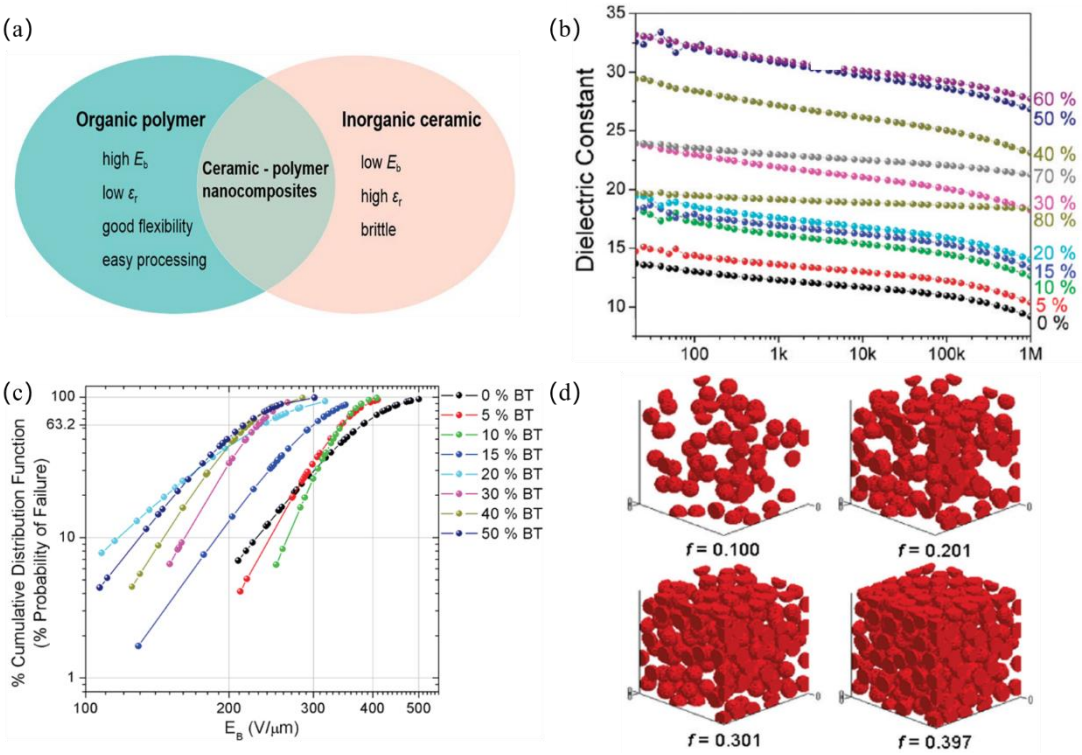

Figure 1-9. (a) The advantages and disadvantages of ceramics, polymers, and polymer composites, respectively. (b) The dependences of dielectric constants on frequency for PVDF-HFP nanocomposites filled with $BaTiO_3$ nanospheres. (c) Percent cumulative distribution function (% probability of device failure) of each nanocomposite as a function of the applied electric field. (d) Examples of particle packing in finite-difference simulations at different volume fractions[38].

As for the dielectric breakdown strength (**Figure 1-9** (c)), it is obvious to see that the introduction of $BaTiO_3$ particles deteriorates the high-field insulating performance and a sudden reduction starts with particles content increasing from 10%. The more fillers added into the matrix, the lower the breakdown strength of composites. Simulations in **Figure 1-9** (d) depicted the particle packing in the nanosphere-based polymer composites. It was found that at

f=0.397, a maximal number of spherical particles has been placed in given model space and no additional particle can be added to this model space. The intended increase of particle volume fraction over *f*=0.397 can only be made by decreasing the volume of the host polymer, which inevitably creates air voids. Therefore, for polymer/ceramic filler composites, achieving high dielectric constants in composites usually requires the addition of large amounts of filler, which not only adversely affects the physical and mechanical properties and processability of the material but also leads to increased losses and reduced breakdown strength of the composite ultimately affecting the energy storage properties of the material. Therefore, it is still challenging to achieve a high dielectric constant while preserving the feature of high breakdown strength of the polymer matrix in the composite.

Compared with ceramic/polymer composites with high loading of fillers to achieve high dielectric constant, polymer composites filled with a small amount of conductive fillers have been investigated. High dielectric constants can be obtained by adding small amounts of filler, and the losses of the system can be kept low as long as the amount of filler is below the percolation threshold of the system. Zhang et al.[60] prepared PVDF/rGO composites by adding in situ rGO at 160°C to a PVDF matrix. **Figure 1-10** (a) showed that the composite had a dielectric constant of 380 and a loss of 0.09 when the rGO content was 1.5%, compared to the values of 10 and 0.02 for pure PVDF, respectively. According to Equation (1.12), the high dielectric loss yields a high energy loss and weakens the energy storage capability. In **Figure 1-10** (b-c), it is noted that the high dielectric loss induced by conductive fillers not only leads to a low energy storage efficiency but also significantly deteriorates the breakdown strength of the composites. Therefore, the discharged energy storage density is low.

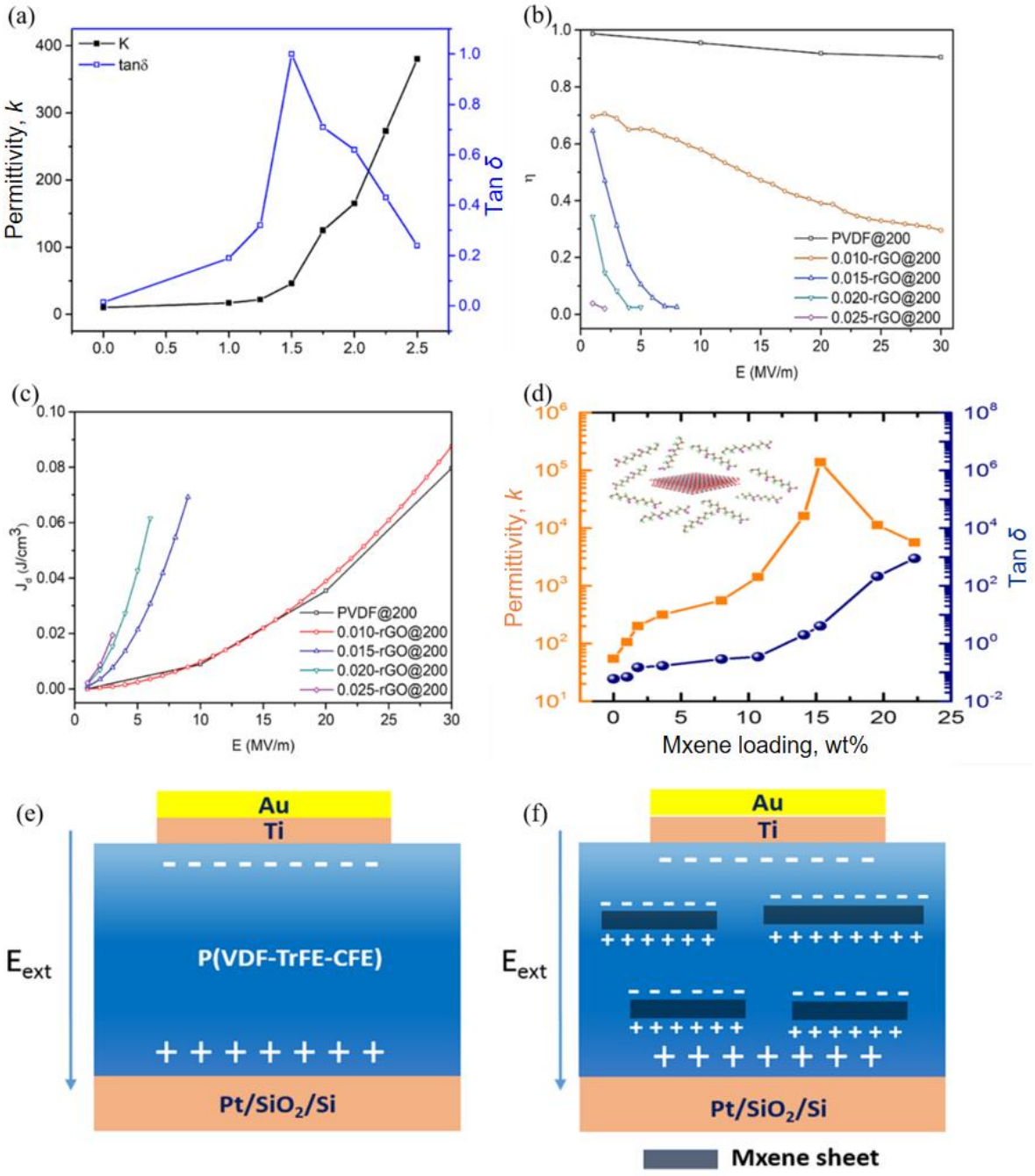

Figure 1-10. (a) Relative dielectric permittivity *k* and dissipation factor as a function of rGO, were measured at 1 kHz, and the (b) energy storage efficiency and (c) discharged energy density were measured at 10 Hz. (d) Dependence of the permittivity and dielectric losses of the MXene/PVDF-TrFE-CFE on MXene loadings measured at room temperature and 1 kHz. (e, f) Schematic illustration of the polarization charges that exist in pristine PVDF-TrFE-CFE and MXene/PVDF-TrFE-CFE composite-based capacitors under an external electric field[61].

Tu et al.[61] added two-dimensional conductive filler MXene ($Ti_3C_2T_x$) nanosheets into the PVDF-TrFE-CTFE matrix to prepare 0-3 composites with a percolation threshold of 15 wt%. When MXene content is 10 wt%, the dielectric constant of MXene/PVDF-TrFE-CTFE composite was 25 times higher than that of the pure matrix, but the loss also increased from 0.06 to 0.35, as shown in **Figure 1-10** (d). The significant increase in the dielectric constant of this system was mainly due to the fact of charge accumulation, leading to the formation of microscopic dipoles at the interface between nanosheets and PVDF-TrFE-CTFE as shown in **Figure 1-10** (e-f). As the conductive filler is added directly to the polymer matrix, the dielectric constant of the system is dramatically improved yet at the expense of a large reduction of the breakdown strength. The final discharged energy density of most of the percolated composites is lower than the virgin polymer matrices.

In addition to creating percolative composites, organic fillers have been also explored in polymer composites to preserve the flexibility of polymer matrices. The organic fillers can ensure good compatibility with the polymer matrix, which improves the filler dispersion, reduces the losses and improves the breakdown strength without deteriorating the flexibility of the polymer even at a high filling degree. Unfortunately, most organic fillers have low dielectric constants. The addition of organic fillers does not lead to a significant increase in the dielectric constant of the composites in many cases. For example, Zheng et al.[62] prepared TPU/PVDF composite films using the solution lay-up method. As shown in **Figure 1-11** (a), the dielectric constant of the composites decreases as TPU content increases. It reaches 8.2 at 5% content of TPU, which is lower than that of pure PVDF (~9.5). However, the breakdown strength enhances and reaches the highest value at 3% (**Figure 1-11**b). The soft chain of TPU serves as a defect modifier for PVDF because it can change the conformation easily to diminish the defect in the matrix and the appropriate content of TPU helps hinder the breakdown damage in the PVDF matrix as well as promotes the breakdown strength of composites. These results showed that the slight decrease of permittivity can be compensated by the increase of breakdown strength, allowing for a superior energy density relative to the virgin polymer matrix. Since the existence of distinct phase separations between TPU and PVDF, the defects

and avoids occur with further increasing TPU loading to decrease the breakdown strength and energy storage performance in **Figure 1-11** (c). In addition, Li et al.[63] mixed aromatic polythiourea (ArPTU) with PVDF using solution lay-up to obtain a high dielectric constant. When the ratio of ArPTU/PVDF =10/90, the dielectric constant of the composite was slightly increased from 8.4 to 9.2, while the breakdown strength increased from 350 MV/m to 700 MV/m. Both the increased dielectric constant and breakdown strength contributed to the largely improved energy density (10.8 J/cm^3) as compared with the pure matrix (1.9 J/cm^3).

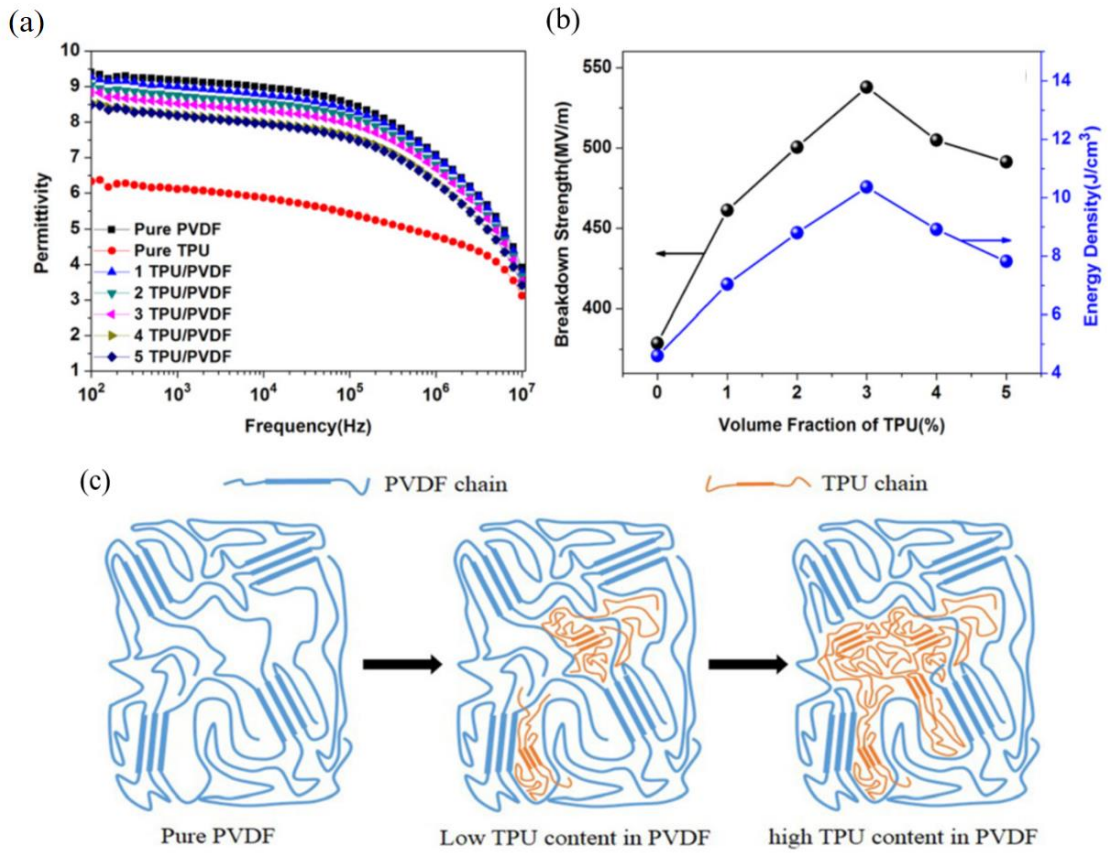

Figure 1-11. The evolution of (a) permittivity, and (b) breakdown strength and energy density of TPU/PVDF composite films following the incremental content of TPU. (c) The schematic diagram of the microstructure of the TPU/PVDF composite system[62].

As demonstrated in the previous discussions, it is not straightforward to have an increased energy density in composites consisting of a high-k nanofiller and high-E_b polymer matrix. Particular attention should be paid to tailoring the multiscale structures of composites to achieve concurrently enhanced permittivity and breakdown strength. In the following section,

we will focus on some models to have an in-depth understanding of the enhancement of permittivity as well as the breakdown strength in composite materials.

1.3.2 Theoretical Model of Composite Permittivity

The effective dielectric constants of polymer matrix composites are obtained based on the respective dielectric constants of the filler and the polymer matrix and are influenced by the amount of added filler and its interrelationship. Several different models have been proposed to determine the effective dielectric constant of composite systems. These models have been developed based on several assumptions and give the theoretical basis for an in-depth understanding of the dielectric properties of polymer-based composite systems.

1.3.2.1 Wiener Rule

Several theoretical models have been established to predict the dielectric constants of polymer composites. The volume-fraction average, which is simply calculated based on a rule of the mixture or the Wiener rule, is a simple but not very accurate method to estimate the effective dielectric constant of a polymer composite material[64]. The general weighting of permittivity varies following the mixing law[65],

$$\varepsilon^{-n} = \sum_{i=1}^{N} \Phi_i \varepsilon_i^n \tag{1.22}$$

where ε_i is the relative permittivity, Φ_i is the volume fraction of the i_{th} phase, $\sum_i \Phi_i = 1$, n is an exponent ranging between $-1 \le n \le +1$, and N is the constituent number of phases in the composite. The exponent, n, is influenced by the spatial connectivity of each phase, as at the extremes, $n = +1$ is parallel connectivity, $n = -1$ is serial connectivity, and $n = 0$ is an equal-weighted mixture of parallel and serial connectivities. For the two-phase composite system, the two simplest forms of connected structures are the parallel-connected structure and the series-connected structure, as shown in **Figure 1-12**. In this case, the effective dielectric constant of the two-phase composite can be calculated by the following equation[64]:

$$\varepsilon_{c,min} = \frac{\varepsilon_m \varepsilon_f}{\varepsilon_m \Phi_f + \varepsilon_f \Phi_m} \tag{1.23}$$

$$\varepsilon_{c,max} = \varepsilon_m \Phi_m + \varepsilon_f \Phi_f \tag{1.24}$$

where Φ_f and Φ_m are the volume fractions of the filler and matrix, ε_f and ε_m are the dielectric constant of the filler and matrix, $\varepsilon_{c,min}$ and $\varepsilon_{c,max}$ are the dielectric constant of the lower and upper dielectric constant of composites, respectively. In most cases, the connected structural morphology of polymer-ceramic two-phase composites is a mixture of statistical distributions of its components instead of a complete parallel or tandem structure, so the effective permittivity of the composite should be between the values determined by Equations (1.23) and (1.24), which means that the permittivity of a two-phase composite is between the $\varepsilon_{c,min}$ and $\varepsilon_{c,max}$, as shown in **Figure 1-12**.

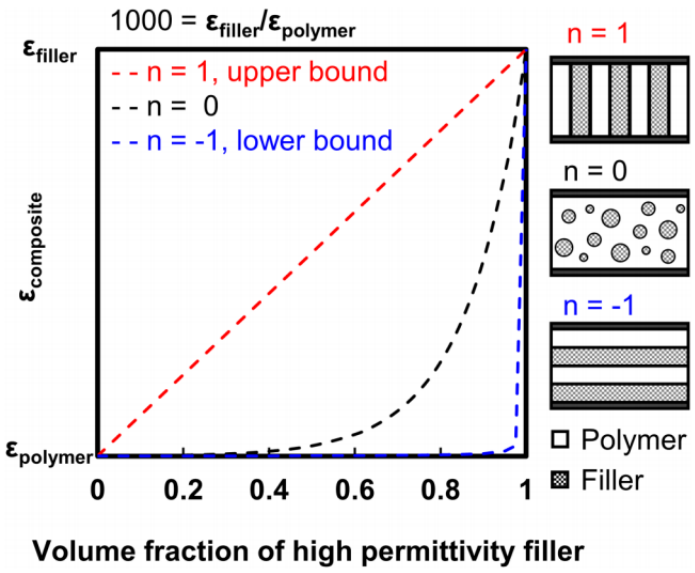

Figure 1-12. Ideal connection ways of two-phase composites, series model (*n*=-1), a mixing model (*n*=0), and parallel model (*n*=1). The black lines stand for electrodes[65].

1.3.2.2 Lichtenecher's Model

Compared to the Wiener models, this model takes the shape of the filled particles into account, which is built on the assumption of the random spatial distribution of filler shapes and orientations in the composite. The model conforms to the equation shown below[66].

$$\log \varepsilon_c = \Phi_m \log \varepsilon_m + \Phi_f \log \varepsilon_f \tag{1.25}$$

where ε_c is the dielectric constant of the whole composite, ε_m the permittivity of matrix and ε_f the permittivity of filler. This model allows for the analysis of filler particle shape dependence and is independent of the processing methods in composites.

1.3.2.3 Maxwell–Garnett Equation

Beyond such rough limit estimation, further steps in modeling the dielectric properties of binary mixtures have been accomplished in the framework of the so-called Wagner theoretical schemes[67]. By equating (1.23) and (1.24), the so-called Sillars[68] or Landzu–Lifshitz[69] rules are written as follows:

$$\varepsilon_c = \varepsilon_m \left[1 + \frac{3\Phi_f(\varepsilon_f - \varepsilon_m)}{2\varepsilon_m + \varepsilon_f}\right] \tag{1.26}$$

However, these rules are only validated for low-volume fractions of fillers and are limited by the electrical conductivity of fillers and matrix. To precisely predict dielectric properties, Maxwell–Garnett equation[70-71] was proposed as follows:

$$\varepsilon_c = \varepsilon_m \left[1 + \frac{3\Phi_f(\varepsilon_f - \varepsilon_m)}{(1-\Phi_f)(\varepsilon_f - \varepsilon_m) + 3\varepsilon_m}\right] \tag{1.27}$$

This equation takes into account the dielectric constant generated by a spherical filler dispersed in the matrix. It should be noted that the Maxwell-Garnett rule ignores the resistivity of the matrix or the filler particles and thus has an advantage over the Landu-Lifshitz mixing rule, which is confined to composites where the resistivity of the filler is higher than that of the matrix. To date, there are several expressions of the Maxwell–Garnett equation, such as Maxwell–Wagner[72] or Rayleigh[73] or Lorentz–Lorenz[74]equation. One of such Maxwell–Garnett equations designed for spherical particles is given as:

$$\frac{\varepsilon_c - \varepsilon_m}{\varepsilon_c + 2\varepsilon_m} = \Phi_f \frac{\varepsilon_f - \varepsilon_m}{\varepsilon_f + 2\varepsilon_m} \tag{1.28}$$

Yu et al. reported[75] the dielectric permittivity and dielectric loss of $BaTiO_3$/PVDF nanocomposites. The experimental dielectric results were well consistent with the predicted values based on this model. As the dispersed particles are not spherical, the equation requires to be modified to accommodate the geometry of the filler particles. Thus, a depolarization factor (*A*), which is related to their deviation from sphericity, was included in Maxwell–Garnett to make it more general[76]:

$$\varepsilon_c = \varepsilon_m \left[1 + \frac{\Phi_f(\varepsilon_f - \varepsilon_m)}{A(1-\Phi_f)(\varepsilon_f - \varepsilon_m)+\varepsilon_m}\right], \quad for\ \Phi_f<0.1 \tag{1.29}$$

The value of *A* can be calculated or can be found in the literature[77]. As *A* = 1/3, this equation turns back to equation (1.28).

1.3.2.4 Bruggeman Self-Consistent Effective Medium Approximation

This model is suitable for systems with high filler content compared to Maxwell-Garnett (Φ_f<0.1), while the samples are lamellas or disks and the fillers are spherical. The model also predicts well when a large amount of filler is added to the matrix and the fillers are close to each other or even agglomerated[78]. Bruggeman's model is as follows.

$$\frac{\varepsilon_f - \varepsilon_c}{\varepsilon_c^{\frac{1}{3}}} = \frac{(1-\Phi_f)(\varepsilon_f - \varepsilon_m)}{\varepsilon_m^{\frac{1}{3}}} \tag{1.30}$$

This equation is applicable for Φ_f up to 0.5, with the constraint that the dispersed spherical fillers do not form a percolative path throughout the matrix. Song et al.[79] reported that the variation of dielectric permittivity was experimentally obtained with the introduction of $BaTiO_3$ nanowires. The experimental results are well consistent with the values predicted by the effective medium theory. The Bruggeman self-consistent effective medium approximation is also considered an extension of the Lichtenker model, where the more complex conditions of composites with anisotropic inclusions will be taken into account.

1.3.2.5 Jaysundere–Smith Equation

The Maxwell-Garnett equation is validated only for low filler content, as illustrated in **Figure 1-13**. Due to the large distance between neighboring particles, the relatively weak interaction of particle-particle is normally neglected in the theoretical prediction of the dielectric constant. While at higher filler content, the interactions between the fillers become very significant due to the proximity of the fillers, especially for nanoparticles. In addition, the electric field generated by the neatly induced distribution of the dipole moment is no longer negligible when calculating the overall field experienced locally in the matrix. Based on this case, Jaysundere and Smith proposed a new model which is relatively more complicated but closer to the real state of the composites. They calculated the electric field of dielectric

spherical particles embedded in a continuous matrix by taking into account the polarization of neighboring particles and derived the following equation[78].

$$\varepsilon_c = \frac{\varepsilon_m \Phi_m + \varepsilon_f \Phi_f \frac{\varepsilon_m}{(2\varepsilon_m + \varepsilon_f)} \left[1 + 3\Phi_f \frac{(\varepsilon_f - \varepsilon_m)}{\varepsilon_m + \varepsilon_f}\right]}{\Phi_m + \Phi_f \frac{3\varepsilon_m}{(2\varepsilon_m + \varepsilon_f)} \left[1 + 3\Phi_f \frac{(\varepsilon_f - \varepsilon_m)}{\varepsilon_m + \varepsilon_f}\right]} \tag{1.31}$$

Compared with experimental results[80], this model correlated well with experimental results below a certain amount of filler loading, while a distinct discrepancy was revealed at a high filler content. To achieve the perfect fitting of permittivity across the entire range of filler content, other models such as the Lichtenecker model were also attempted although no model is valid at high loadings.

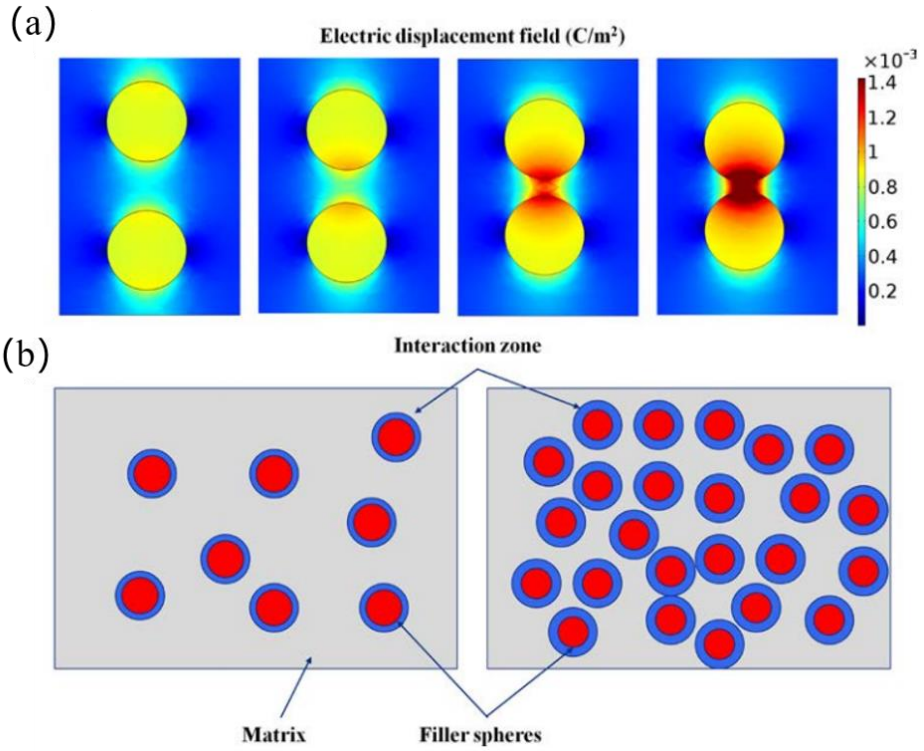

Figure 1-13. (a) Effects of inter-particle distance in electric displacement field in between BT nanoparticles (60, 40, 20, and 10 nm from the left) and (b) schematic of interaction zone concerning inter-particle distance[78].

1.3.2.6 Percolation Theory

For conductive additive filled composites, the formation of a conductive network structure in the composites transforms the material from an insulator to a conductor[81] when the loading of filler reaches the percolation threshold. The use of conductive fillers is motivated by the fact that they not only increase the electrical conductivity but also induce Maxwell-Wagner

polarization, leading to high dielectric constants of conductive filler-polymer composites. Normally, the conductivity of the conductive filler-filled polymer composites shows a nonlinear improvement when the filler concentration is approaching the percolation threshold. This phenomenon should be explained by percolation theory instead of classical mixing rules. At low filler concentrations, the conductive particles are separated from each other, as shown in **Figure 1-14**. The electrical properties of the composite are dominated by the matrix. While increasing filler content, local clusters of particles are formed.

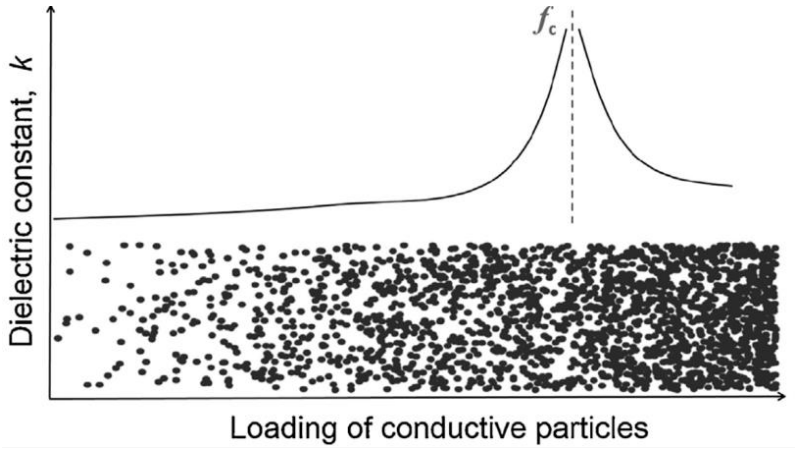

Figure 1-14. Microstructure evolution with increasing particle loading in a polymer matrix. Clusters of the particles in a composite near percolation can form micro capacitors that contribute to a significant increase in the dielectric constant[85].

At the percolation threshold, these clusters form a connected three-dimensional network resulting in a jump in electrical conductivity. The dielectric constant and the conductivity are by the following equation[78, 82-84].

For the dielectric constant:

$$\varepsilon_r \propto \varepsilon_m(\Phi_p - \Phi_f)^{-q}, \quad for\ \Phi_f < \Phi_p \tag{1.32}$$

For the electrical conductivity:

$$\sigma_c \propto \sigma_m(\Phi_f - \Phi_p)^{t}, \quad for\ \Phi_f > \Phi_p \tag{1.33}$$

$$\sigma_c \propto \sigma_m(\Phi_f - \Phi_p)^{-q}, \quad for\ \Phi_f < \Phi_c \tag{1.34}$$

$$\sigma_c \propto \sigma_f^u \sigma_m^{1-u}, \quad for \left|\Phi_f - \Phi_p\right| \to 0 \tag{1.35}$$

Where, φ is the volume fraction of metal particles, φ_p is the percolation threshold of the system, σ_m and σ_f are the conductivity of the polymer and filler, respectively, t and q are the critical exponents in the conductor and insulator regions, which are in the 1.6-2 and 0.8-1 range, and $u = t/(t + q)$. The model gives predictions in the absence of a physical basis but is only applicable to conductive fillers.

The dielectric permittivity of polymer nanocomposites is largely improved as the conductive filler content increases to the vicinity of the percolation threshold through insulator-conductor transition[86]. Tu et al.[61] obtained an ultrahigh permittivity in PVDF-TrFE-CTFE/MXene composites, showing a good agreement with the percolation theory. The dramatically enhanced dielectric permittivity obtained at the vicinity of the percolation threshold is due to the extension of the formed mini capacitors with the adjacent conductive nanofillers as electrodes and the polymer in between as dielectrics. [87]

1.3.3 Mechanisms of Improving Dielectric Strength

Previous research has indicated that the breakdown strength of polymers can be promoted by mixing with nanofillers to form composite materials[88-90]. The breakdown strength of composites is not only determined by the intrinsic properties of fillers and polymer matrix, but also by the dispersion, distribution, and orientation of fillers as well as the interfacial interaction between fillers and polymer matrix. The mechanism of dielectric breakdown in composite materials will be discussed in this section.

1.3.3.1 Effect of Polymer Matrix

The breakdown strength of polymers is determined by many factors, which are divided into ambient conditions and intrinsic properties. The ambient conditions, especially temperature and pressure are quite sensitive to the breakdown strength of polymers. Traditionally, the breakdown strength first remains constant or may slightly increase with boosting the temperature. It reduces monotonically beyond a certain critical temperature[91], which is closely related to the glass transition temperature T_g.

Additionally, mechanical stresses can also influence the breakdown due to the molecular chain motion, crystallinity and free volume[92]. For example, Li et al.[93] used different pressures of 50, 100 and 200 MPa for 1 h of hydrostatic treatment and immediately tested the breakdown strength of each sample. The breakdown strength of the neat LDPE showed an improvement with increasing pressure treatment, which is attributed to the decrease in free volume with applied pressure.

As for the intrinsic properties of polymers, it is accepted that high cohesion energy density (CED) leads to high breakdown strength in pure polymers[94]. As another key parameter of polymers, T_g reveals the chain dynamics and indicates that polymers with low T_g are characterized by highly flexible chains and have the potential to twine around fillers and form strongly interacting interfaces since the strongly interacting soft interfaces are favorable for breakdown performance[91]. Besides, the effect of temperature on the breakdown strength of nanocomposites is similar to that of pure polymers.

1.3.3.2 Filler Effects on Breakdown Strength

Plenty of work has reported the breakdown strength of polymers can be enhanced by incorporating fillers, including ceramic, organic even conductive materials. The type of filler is important for the breakdown of the composites. As reported in both ceramic fillers filled polymer-based composites, LDPE/Al_2O_3 and LDPE/TiO_2, performed good breakdown properties while fillers content is below 2 wt%[88]. However, further increasing filler content, the breakdown strength of the LDPE/Al_2O_3 composites is still high due to the weak polarity and low dielectric constant of Al_2O_3, while a significant reduction is observed in the LDPE/TiO_2 composites, which caused by the strong polarity and high dielectric constant of TiO_2 fillers.

Organic fillers are also considered to improve the breakdown of polymers. As shown in **Figure 1-11**, incorporating a small amount of TPU improved the breakdown strength of the PVDF matrix. This is owed to the fact that the flexible TPU chains can fill well the defects and voids in the PVDF matrix. The conductive fillers can not only largely enhance the dielectric constant, but also contribute to the improvement of breakdown strength. Huang et

al.[90] demonstrated that 0.05 vol% of Ag synthesized in situ in PVDF-HFP substrates induced 50% of the dielectric constant of improvement and 15% of breakdown strength improvement. Such non-intuitive enhancement could be attributed to charge-transfer complexes formed between the nanodots and the polymer chains and enhanced chain mobility in an electric field.

Besides, the dispersion of fillers in the polymer matrix has a great impact on the breakdown performance of composites. It is well known that nanoparticles are difficult to disperse uniformly in the polymer matrix, especially for nanoparticles with large specific surface area and high surface free energy. Since the dispersibility is strongly influenced by its preparation method, Tuncer et al.[95] has prepared EP/TiO_2 composites with different dispersibility by in-situ and ex-situ methods, respectively. There was a significant improvement in the breakdown strength of in-situ nanocomposites compared to the ex-situ nanocomposites. This improvement is attributed to the enhanced dispersion of fillers in the epoxy resin.

In addition to the processing, the surface modification of fillers can change not only the dispersion of fillers but also the interactions with the matrix, which ultimately affects the breakdown behavior[96]. After the modification of TiO_2 with N-(2-aminoethyl)-3-aminopropyltrimethoxysilane (AEAPS), the breakdown strength of LDPE/TiO_2 composites was significantly improved compared to the equivalent system prepared using the unmodified fillers. It is believed that the surface modification enhances the electron scattering, which is majorly driven by the polar groups of AEAPS in the interfacial region. Hence, surface modification is useful to increase the breakdown strength of the nanocomposites by changing the structure of the interfacial region.

Moreover, it is notable that mostly a small content of fillers is beneficial for the breakdown property of composites[40, 88, 97], while excessive addition of fillers resulted in a reduction in breakdown strength. Consequently, there is an optimal loading of fillers, which will result in the best breakdown performance.

1.3.3.3 Mechanisms of Dielectric Breakdown in Nanocomposites

As discussed previously, the breakdown strength of composites is determined by several

factors, including intrinsic properties of fillers and polymer matrices, the dispersion of fillers and the interfaces between fillers and polymer matrix. To have an in-depth understanding of the mechanism of the dielectric failure in the composites, some proposed models are summarized in this section to illustrate the breakdown evolution in the polymer nanocomposites.

1.3.3.3.1 Potential Barrier Model

The potential barrier model has been proposed in the field to explain the breakdown mechanism of nanocomposites based on interfacial region ineraction[40]. As mentioned above, the interface plays a significant role in determining the dielectric properties of nanocomposites[98]. A multi-regional structure of the interface around spherical filler has been proposed, namely the interface between polymer matrix and fillers is divided into three regions from the inside to the outside[97], as schematically represented in **Figure 1-15**.

The bonded region is connected to the surface of fillers and the transition region, which is formed via a portion of counter ions adsorbed by electrostatic Coulomb force around fillers and other forces with a thickness $d_1$as well as a barrier Δf_1. It is believed that a large potential distortion occurs in the bonded region and the deep trap with the highest density was introduced. Moving outward from the surface of the fillers, the density of traps decreases and the shallow traps gradually dominate. The space charge accumulates under the electric field, causing a sharp increase in the electric field, which induced the breakdown evolution to start from the bonded region. The bonded region has a critical effect in the short-term breakdown of the nanocomposite.

The transition region is located between the bonded region and the normal region, where the molecular chains of the polymer matrix are tightly connected to the bonded region and the surface of the filler. The transition region is considered to be crystalline with a greater thickness than that of the bonded region. Since the characteristics of this region are strongly influenced by the cohesive energy density (CED) of the matrix. Besides, the incorporated nanoparticles are able to induce the variation of the mobility of the molecular chains closely related to the T_g and raise the overall crystallinity, both of which influence the breakdown of

nanocomposites. As for the normal region, the characteristic is similar to the polymer matrix where the polymer chains randomly entangle around the fillers.

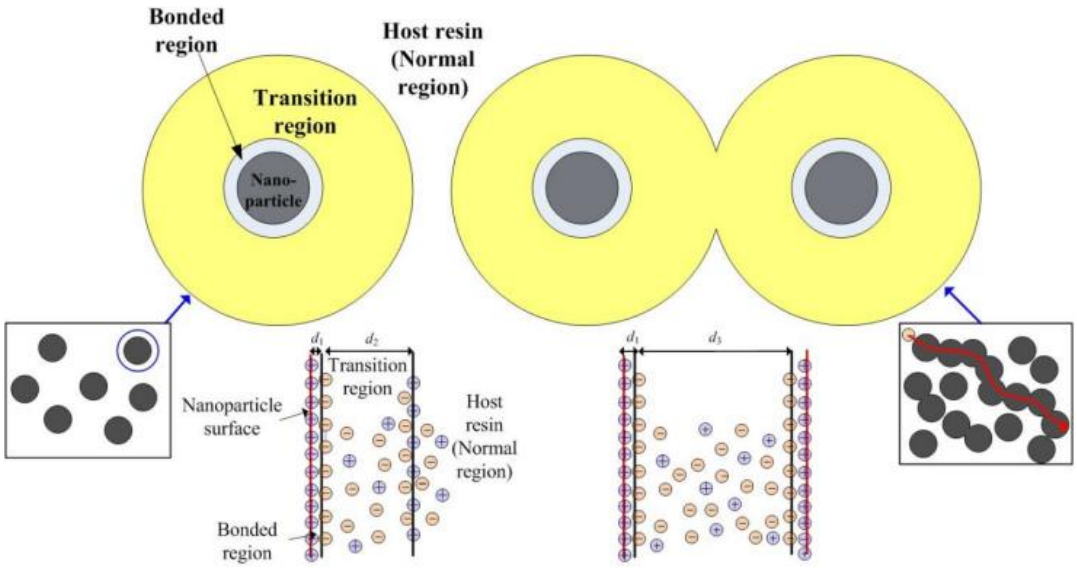

Figure 1-15. Potential barrier model around nanoparticles in nanodielectrics. (a) A schematic of charge distribution around an isolated particle. (b) A schematic of charge distribution when the interaction zone overlaps[40].

In addition, the effects of the interfacial region on the charge transport and breakdown properties are different at various fillers loadings. As shown in **Figure 1-15**, at low filler content, the nanoparticles are isolated and far from each other. In this case, the charge carriers in the polymer could enter the transition region under an electric field via hopping the barrier Δf_3 which is generated in the polymer matrix near the interfacial region[40]. However, it is difficult for the carriers to escape from the transition region because of the reduced carrier mobility, which is caused by the collision process with the defects in the transition region. Moreover, the local traps trap the charge carriers due to the shorter thickness d_2 compared with the mean free path and also reduce the carrier mobility. Thus, the density of mobile carriers is reduced, leading to a high dielectric breakdown. While increasing the filler content in the polymer matrix, the distance between adjacent particles decreases, forming an overlap of the transition region, as shown in **Figure 1-15**. The thickness turns from d_2 to d_3 so that it is longer than the mean free path. In consequence, the carriers are able to obtain enough

energy from the electric field to jump the barrier Δf_1. As the filler content is beyond the percolation threshold, many percolation paths are formed through the overlap of the transition regions of the composite. The carriers mobilize easily along these paths. The mobility and density of the mobile carriers are greatly increased, resulting in enhanced conductivity and reduced breakdown strength.

1.3.3.3.2 Charge Transport Model

The charge transport model elaborates based on the reduced electric field at the cathode, which weakens the electron injection and leads to an increase in breakdown strength. The depression of the electric field at the cathode is associated with the accumulation of negative space charges near the cathode referred to as “homocharge”. Space charge plays an important role in the breakdown behaviors of composites[99-101]. As presented in **Figure 1-16**, the accumulation of negative space charge near the anode is referred to as “heterocharge”, which in turn leads to an increase in the field strength at the anode and an increase in the charge injection at that electrode, declining the breakdown strength.

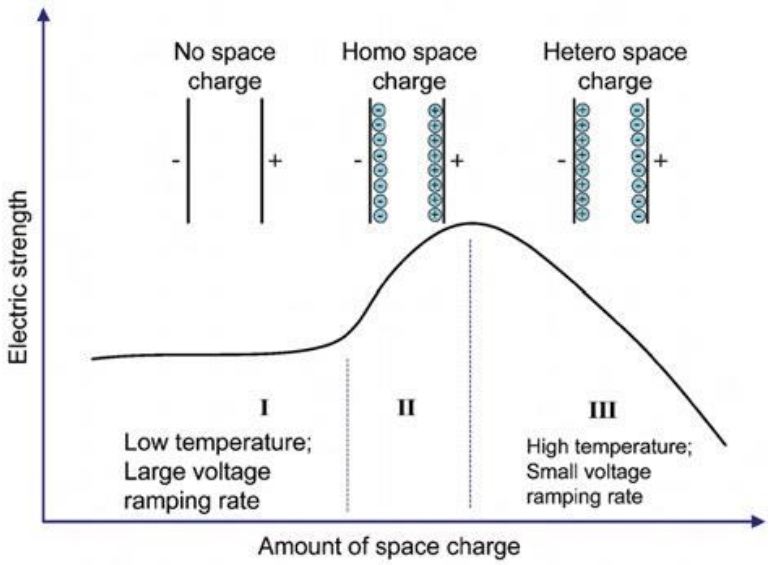

Figure 1-16. Relationship between space charge accumulation and electric strength[104].

The temperature and the rate of voltage rise may significantly influence the nature of the accumulated homocharge or heterocharge. Especially in polymers, charge transport and subsequent accumulation effects are considered in the electron energy band and localized

state models[102]. Nelson et al.[103] reported that the traps in the amorphous region play a crucial role in the electrical conductivity and breakdown strength of the material. In addition, the introduction of fillers can bring more deep traps, resulting in a low carrier mobility and free electrons density and enhancing the breakdown performance.

The bipolar charge model presented here can well describe the breakdown evolution of the polymer matrix. As illustrated in **Figure 1-17**, the breakdown is triggered when the internal electric field exceeds a boundary value[99]. The internal electric field is largely affected by the hole charge packet. The hole charge packet is largely influenced by the charge trapping and untrapping processes. Chen and coworkers[101] confirmed that the breakdown strength enhanced with the increase of the voltage ramp via calculating the inverse power index of LDPE. It was concluded that the dynamics of the space charge determine the maximum local electric field of the dielectrics[100]. Therefore, breakdown always starts from the bulk under DC voltage, since the maximum electric field will keep increasing with the time of applied voltage and move from the anode towards the cathode.

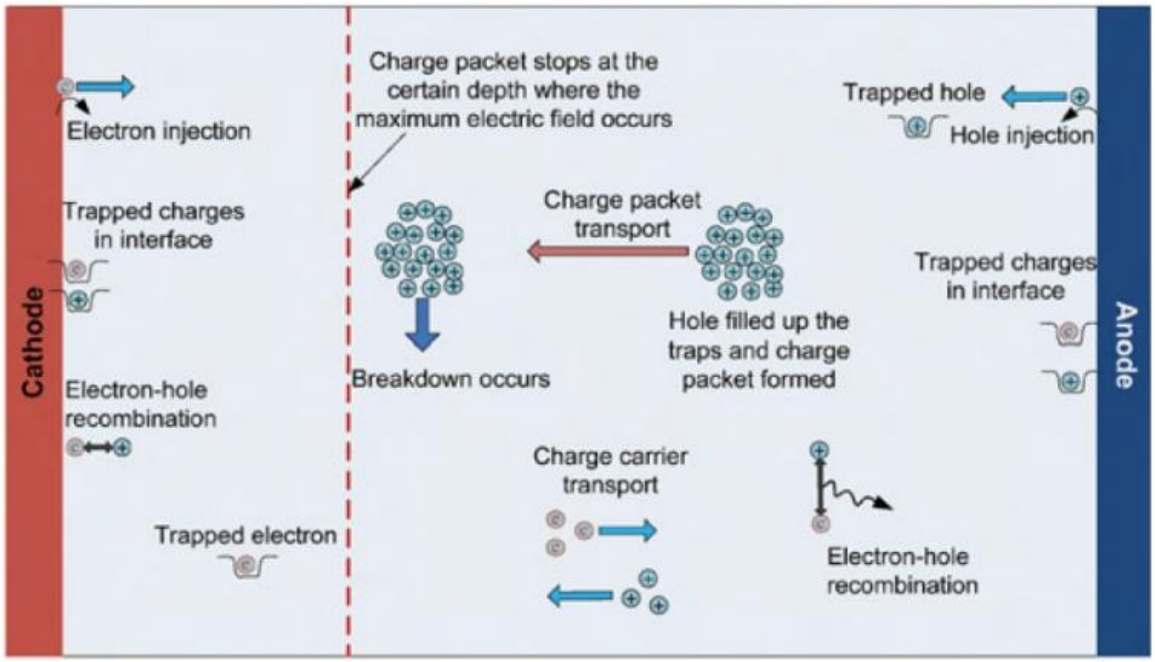

Figure 1-17. Schematic graph of the relationship between space charge accumulation and breakdown in insulating material.

In contrast, the transport direction of the charge carrier remains alternating under AC conditions so that massive charges accumulate near the electrode due to local trapping. In such conditions, the electric field near the electrode is higher than the electric field inside the bulk sample. Therefore, the breakdown starts from the interface between the electrode and the sample and then rapidly passes through the entire bulk. From a macroscopic point of view, the intensity of DC breakdown strength is higher than that of AC breakdown strength.

1.3.3.3.3 Breakdown Path Evolution

Breakdown evolution is defined as the growth of the breakdown path[105-106]. During this evolution, regions with low intrinsic breakdown strength or with high electric field concentration will start breakdown first and turn into a conductor instead of an insulator. Subsequently, the breakdown regions begin to grow into paths and converge with rising the electric field. The overall breakdown occurs as a breakdown path traverses the whole material. Delaying the breakdown of the initiation region and preventing its further growth will contribute to improving the breakdown strength. For polymer-based nanocomposites, the interface between the nanofiller and the polymer matrix is usually the most susceptible to breakdown due to the differences in physicochemical properties (i.e., conductivity, permittivity). The electric field near the polymer/filler interface is largely distorted and highly concentrated on the polymer side[107]. When the size of fillers is reduced to the nanoscale, the inhomogeneous distribution as a result of the aggregation of nanofillers leads to even worse interfacial strength and a higher degree of electric field distortion[108-109]. Therefore, as discussed above, optimizing the dispersion of fillers to avoid aggregation of nanofillers allows for achieving a higher breakdown strength of nanocomposites.

In polymer-based composites, the introduction of fillers brings about a redistribution of the local electric field. The local breakdown and the growth of breakdown paths should be reconsidered. Therefore, modulating the shape, distribution and orientation of the nanofiller can tailor the breakdown strength either via increasing the tortuosity of the pathway or by raising the critical electric field to trigger the overall breakdown. Shen et al. demonstrated the effect of nanofillers with different aspect ratios on the breakdown strength by

two-dimensional phase-field simulations[106]. The breakdown starts at the filler/polymer interface and then the breakdown path starts to grow. For nanoparticle-based composites, the breakdown path growth tends to bypass one of the other nanoparticles encountered to form a twisted breakdown path, as shown in **Figure 1-18** (a-b). However, for composites filled with nanofillers with higher aspect ratios, i.e. nanofibers and nanosheets, the breakdown path tends to penetrate the nanofillers, as presented in **Figure 1-18** (c-d). Therefore, the breakdown paths are approximately linear. The difference in breakdown path growth can also be explained by the electric field distribution in **Figure 1-18** (e). For composites with nanoparticles, the electric field is concentrated in the direction of the two shoulders along the electric field direction. When the front end of the breakdown phase encounters a nanoparticle, it will easily bypass that nanoparticle. For composites with nanofibers, the electric field is concentrated only at the apex of the nanofibers. When the breakdown phase touches the side of the nanofiber, there will be no weak point to direct the growth of the breakdown path. Therefore, the nanofiber-based composites exhibit higher breakdown strength as compared to the nanoparticle-based composites.

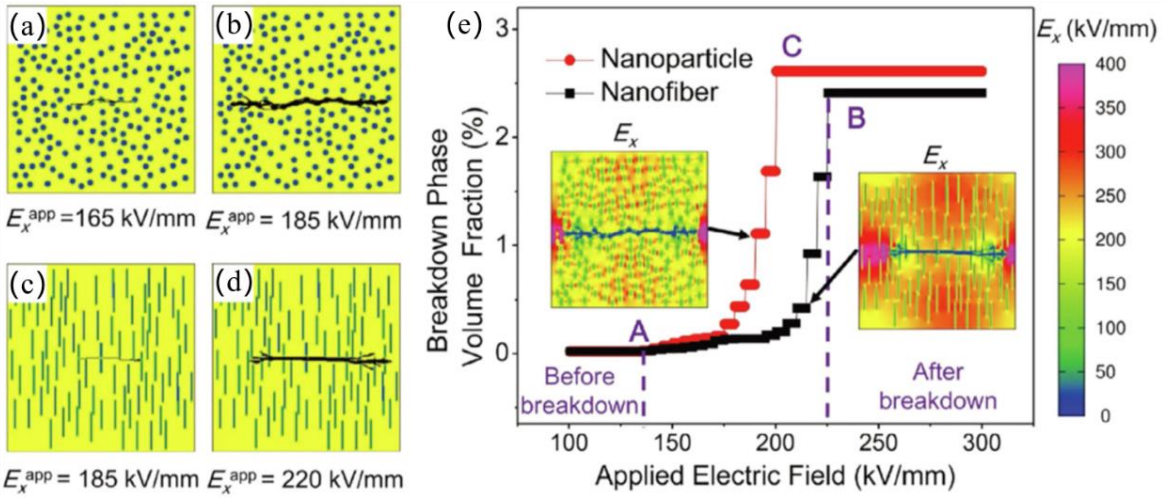

Figure 1-18. 2D phase-field simulations of composites with nanoparticles and nanofibers. (a-b) Breakdown phase evolution of composite with nanoparticles. (c-d) Breakdown phase evolution of composite with nanofibers. (e) The change of the volume fraction of the breakdown phase as a function of the applied horizontal electric field. The insets show the electric field distributions in the composites.

In addition, 3D phase-field simulations were performed to investigate the evolution of the actual breakdown phase. In addition to the pure polymer matrix (S0), five types of 3D nanofillers with a volume fraction of 10% were used for five 3D nanocomposites: vertical nanofibers (S1), vertical nanosheets (S2), random nanoparticles (S3), parallel nanofibers (S4) and parallel nanosheets (S5). As demonstrated in **Figure 1-19** (b), the nanocomposite with vertical nanofibers (S1) is the easiest to disintegrate, while the nanocomposite with parallel nanosheets (S6) is the most difficult to fragment. When the volume fraction of the nanofillers was fixed at 10%, only the nanocomposite filled with parallel nanosheets (S5) has a higher breakdown strength than the pure polymer matrix (S0). Similar to the 2D simulations, the effect of microstructure on the breakdown strength can be understood in terms of the shape of the filler and the local electric field distribution. The vertical distribution of nanofibers makes the electric field more cohesive and allows for easier growth of the breakdown path, while the vertical interface also induces a straight and fast growth of the breakdown. However, parallel nanosheets make the electric field more dispersed and hinder the growth of the breakdown phase. At the same time, the large parallel interfaces also hinder the growth of the breakdown phase. For microstructures S3, S4 and S5, simulations with different volume fractions show that the breakdown intensity will first increase and then decrease for all microstructures, which is verified by experimental data in the literature. In addition, parallel nanofibers (S4) and parallel nanosheets (S5) will yield higher breakdown intensities at optimal volume fractions compared to random nanoparticles (S3). Since the addition of nanofillers affects the electric field distribution and thus the breakdown intensity, it will be effective to regulate the breakdown path by designing nanofibers and nanosheets and controlling their orientation perpendicular to the applied electric field.

Inspired by the simulation, Wang et al.[110] developed a multi-layered structure of PVDF/$BaTiO_3$ composite with various $BaTiO_3$ content in different layers. A layer with 1 vol% of $BaTiO_3$ showed improved breakdown strength as a result of the effective electron traps at the interface. Two layers with 20 vol% of $BaTiO_3$ with improved dielectric constant and polarization were added to the two surfaces of the 1 vol% $BaTiO_3$ layer. As a result, the

dielectric constant and dielectric strength are simultaneously enhanced with the breakdown strength intensity increasing from 300 MV/m to 470 MV/m. The energy density is increased up to 18.8 J/cm^3. The authors' simulations of the electric field distribution and the growth of the breakdown path show that the "intermediate layer" is subjected to a higher local electric field in the film of the sandwich structure due to its low dielectric constant. As a result, the electric field drop on the "soft layers" is reduced and preventing them from early breakdown and promoting the overall breakdown strength. Moreover, it was observed that the electric field in the "soft layer" coalesces above and below the $BaTiO_3$ nanoparticles, while diluting on the left and right sides, similar to the results of phase-field simulations[106]. This redistribution of the electric field at the optimal volume fraction hinders the growth of the tree-like breakdown path.

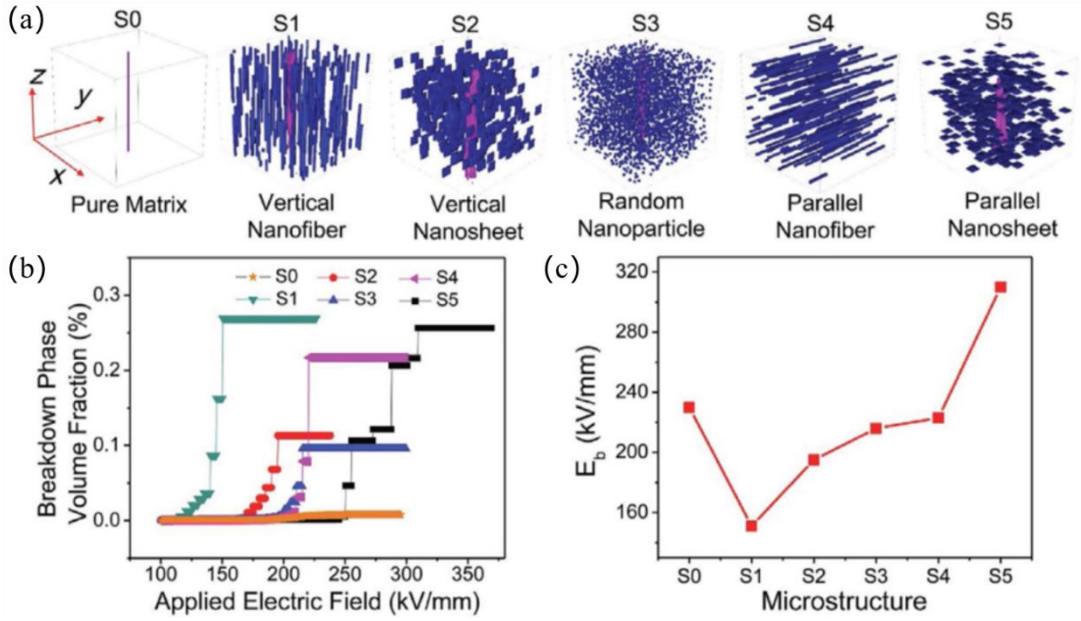

Figure 1-19. 3D phase-field simulations of microstructure effects on breakdown strength. (a) Breakdown path morphology in composites with different microstructures. (b) The breakdown phase volume fraction as a function of the applied electric field. (c) Extracted breakdown strength of composites with different microstructures at nano-fillers content of 10%.

To conclude, the introduction of fillers does affect the breakdown strength of nanocomposites. This variation can be understood in terms of the emerging of a large amount

of interfacial regions and/or the concept of additional "traps". The filler can increase the density and depth of the traps, which impede the transport of charge carriers and subsequently change the space charge dynamics and the distribution of the internal electric field. Besides, the dispersion and distribution of fillers also strongly influence the breakdown performance of composites, which is related to the local electric field distribution and the consequent growth of the breakdown path. It has been demonstrated that the dielectric properties of polymer-based composites are largely influenced by many factors, such as the size, shape, distribution, orientation and intrinsic properties of the filler as well as their interaction with the polymer matrices. Peculiar attention should be paid to interfacial engineering, which plays the most important role in determining the breakdown performance of nanocomposites. Therefore, the processing of high-quality nanocomposites with designed interfacial features highly demands taking into account the following issues. One is the advanced fabrication techniques to achieve desired dispersion and distribution of nanoparticles in the polymer matrix. The other is establishing a desirable interfacial region between fillers and polymer matrices that would afford superior dielectric properties to the one observed in the simply mixed systems.

1.3.4 Processing of Polymer-Based Composites

After clarifying the rules of enhancing permittivity and breakdown strength, in this section, we focus on the state-of-the-art techniques for the processing of dielectric polymer composites with high-energy storage density. Today, there are two main types of strategies commonly used: solid-phase processes and liquid phase processes. The former are generally mechanical methods, which are usually straightforward, relying directly on the effect of external mechanical forces, and are widely used in practical production due to their convenience, low cost and large-scale operation. Mechanical mixing procedures involve direct mixing and melt mixing. In addition, the filler particles can be also added to the polymer matrix by the solution method. Generally, the liquid phase processes guarantee a better dispersion state of the filler and stronger interfacial interactions as compared to the

solid phase processes.

1.3.4.1 Direct Mixing

It is how the filler and matrix are mixed directly with no pre-treatment. By direct mixing method, Dang et al. prepared PVDF-based composite systems with diverse fillers, such as MWNT[111], CF[112], Ni[113], $BaTiO_3$[114], Ni-$BaTiO_3$[115] and LTNO[116]. The dielectric properties of these composites depend on the type of fillers. The disadvantage of the direct mixing method relies on the fact that it is difficult to improve the dispersion of fillers, especially for nanoparticles with large surface area and high surface energy. It is challenging to achieve the desired dielectric constant and breakdown strength using this straightforward procedure because of the formation of microscale agglomeration of nanoparticles, as shown in **Figure 1-20**.

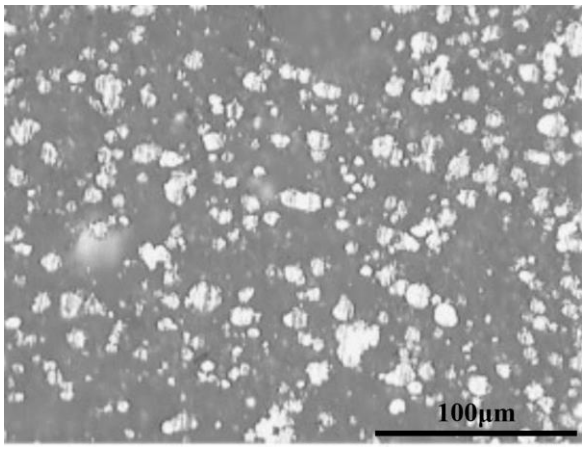

Figure 1-20. Optical micrographs of a polished surface of the Ni/PVDF composites (f_{Ni}=0.16)[113].

1.3.4.2 Melt Mixing

For better mixing of the nanofillers within highly viscoelastic fluids, such as thermoplastic melts of PE and PS, high shear forces can be applied to break down the fillers agglomerates to improve their dispersion. The melt mixing is the most commonly used method to disperse and process polymer-based composites due to the tailored shear stress and the melt-mixing capabilities. Yuan et al.[117] prepared the CNTs/PVDF nanocomposites via melt-mixing, showing a largely improved dielectric constant with no microscale agglomeration of CNTs. In addition to mixing nanoparticles within polymers, it is also efficient for mixing polymer blends. An example can be cited here. The poly(vinylidene

fluoride-hexafluoropropylene) (PVDF-HFP) was extruded with poly(ω-aminodecanoyl) (PA11), then calendered with the mixture in an elastic state to control the crystallization[119]. The styrene-maleic anhydride (SMA) was then introduced as a compatibilizer to enhance the interaction[118], as shown in **Figure 1-21**. Due to the high crystallinity and breakdown strength of PVDF-HFP/PA11-*g*-SMA, the energy density was recorded as high as 15.4 J/cm^3 at 500 MV/m. However, the inhomogeneous dispersion and incompatibility of these polymers are still observed, which limits the further increase of breakdown strength and energy storage density. Moreover, melt processing is performed above the melting point of the polymer, which requires a significant amount of energy and increases a lot the costs. Besides, the viscosity of the melted polymer increases after the addition of filler, especially after a large amount of filler is added. In this case, the processing of the polymer melt becomes difficult.

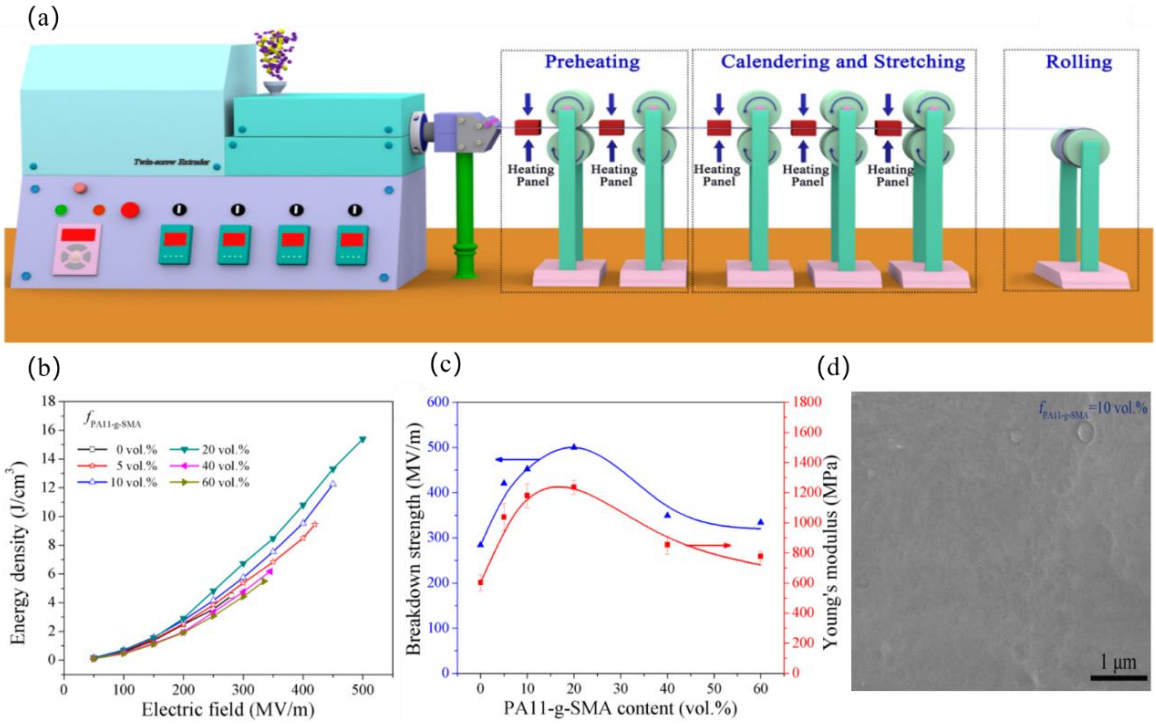

Figure 1-21. (a) Schematic illustration of the fabrication of films by a twin-screw extruder in a continuous process. (b) Dependence of the energy density of PVDF-HFP and PVDF-HFP/PA11-*g*-SMA flexible films with different compositions on the applied electric field, (c) breakdown strength according to the Weibull distribution and Young's modulus of pure PVDF-HFP and PVDF-HFP/PA11-g-SMA flexible films with different compositions. (d) FESEM images of sections of PVDF-HFP/PA11 with 10 vol.% PA11-*g*-SMA[118].

1.3.4.3 Liquid Phase Processes

For the highly filled polymer systems, solid-phase processes become difficult due to the high viscosity of the mixture. However, a large amount of filler particles can be still added to the polymer matrix in solutions. Such liquid-phase processes include solution casting[109], spin coating, tip coating, wet spinning, electrospinning[109] and inkjet printing[119-120]. Among all these processes, solution casting is the most commonly used technique due to the facile yet efficient manipulations. It is desirable to achieve a homogeneous dispersion of nanoparticles in a polymer solution based on water or solvent. As shown in **Figure 1-22** (a), $BaTiO_3$ was first dispersed in PVDF-HFP solution in an organic solvent by ultrasonic treatment. The polymeric nanocomposite film is then cast from the mixture solution onto the glass substrate followed by a thermal treatment to allow evaporation of the solvent and condensation of the polymer.

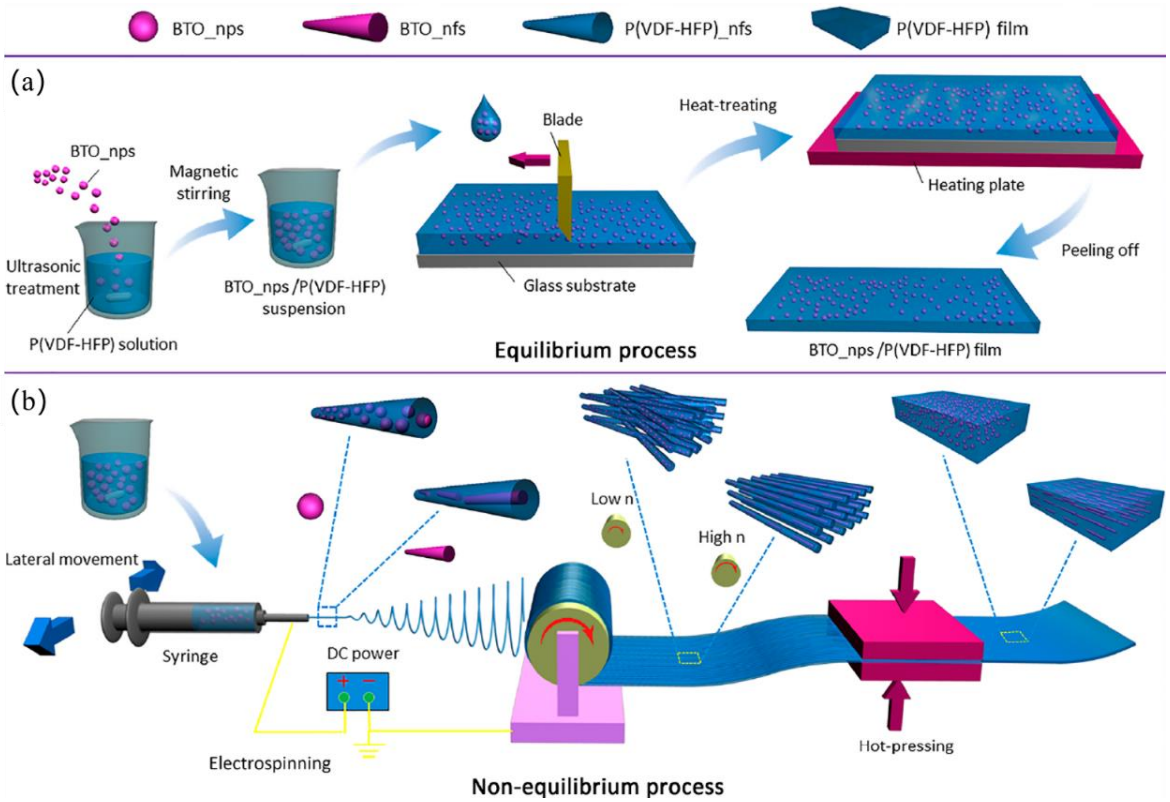

Figure 1-22. (a) Solution casting for preparing the polymer nanocomposite[121]. (b)The combination of electrospinning and hot-pressing methods produces 3D composite structures[122].

During solvent evaporation, nanoparticles with high surface energy are easy to migrate and coalesce into aggregation causing inhomogeneity in the composite film. To improve the compatibility between nanoparticles and polymer matrix and thus inhibit nanoparticle coalescence, surface modification of nanoparticles is required. Moreover, more complicated structures of composites can be designed by combing different processing techniques. For instance, 3D structures of PVDF-HFP/$BaTiO_3$ composites are prepared via electrospinning the composite precursor and followed by hot pressing to obtain the thin and compact film with varying permittivity and breakdown, as shown in **Figure 1-22** (b).

Recently, the inkjet printing technique is largely applied to print dielectric thin films for printed electronics due to its precise position control and the high resolution of printed patterns. This method can produce a continuous line by drying continuous droplets of the electrode or dielectric material inks as shown in **Figure 1-23** (a). A thin film can then be formulated by line-by-line printing. **Figure 1-23** (b-c) shows a tiny inkjet-printed capacitor with a dielectric layer of 700 nm in thickness. The capacitor possessed a high capacitance[120].

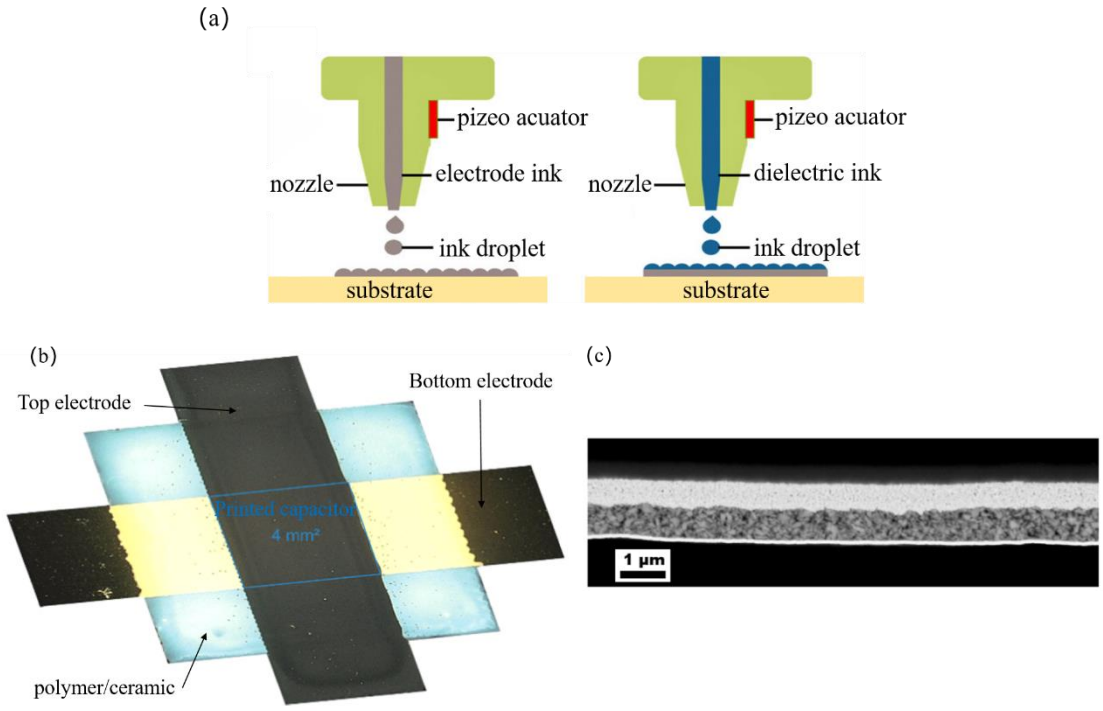

Figure 1-23. (a) Schematic graph of the inkjet printing process. (b) Microscope image and (c) cross-sectional SEM image of a printed capacitor with a polymeric composite dielectric layer with 50 vol% barium strontium titanate (BST) (k~ 40@100Hz)[120].

The Liquid phase processes provide also the possibility of the exploration of the surfactants[123-124], polymer functionalization with diverse chemical components[125]. However, most composite systems require a large number of solvents to completely dissolve the polymer and reduce the viscosity of the composite mixtures. Commonly used solvents include but are not limited to toluene, chloroform, THF or DMF. Most of them are highly toxic and hard to be volatile. This not only makes them difficult to remove from the solid film but also causes environmental pollution issues. Since water-soluble polymers are limited, it has been still a long-standing challenge to achieve high-energy dielectric materials in an eco-friendly and inexpensive manner.

In general, the processes of the composite system are very essential and strongly influence the dielectric properties of composites. The liquid phase process is very promising in terms of controlling the multiscale structures of the composites. However, new materials that are capable of being processed in an aqueous solution, meanwhile have high polarization or high breakdown strength, are still highly needed today for producing well-structured high-energy dielectric materials.

1.3.5 Colloids: Building Blocks of New Dielectric Materials

1.3.5.1 Colloidal Fundamentals

Colloidal dispersions are quite common in our daily life, such as paints, glues and pharmaceuticals. To date, colloidal materials have already been produced that can be manufactured on a large scale and at a low cost. In physicochemical science, a colloid is defined as a mixture of microscopically dispersed insoluble particles of one substance suspended in another substance[126]. Different from a solution, where the solute and solvent constitute only one phase, a colloid is a stable two-phase heterogeneous system, one of which called the dispersed phase, remains dispersed in a finely divided state throughout the other phase. In a colloid, the mixture must be non-settling or take a long time to settle significantly. Due to their good stability and dispersion, colloidal suspensions can be considered a homogeneous mixture. Typically, the size of dispersed particles has a wide range[126], whose

lower limit is the macromolecule size and the upper limit is one of the suspended particles. **Figure 1-24** shows several types of colloidal particles with distinct size, shape, and compositions[127], which allows for the flexible assembling and the formation of complex superstructures.

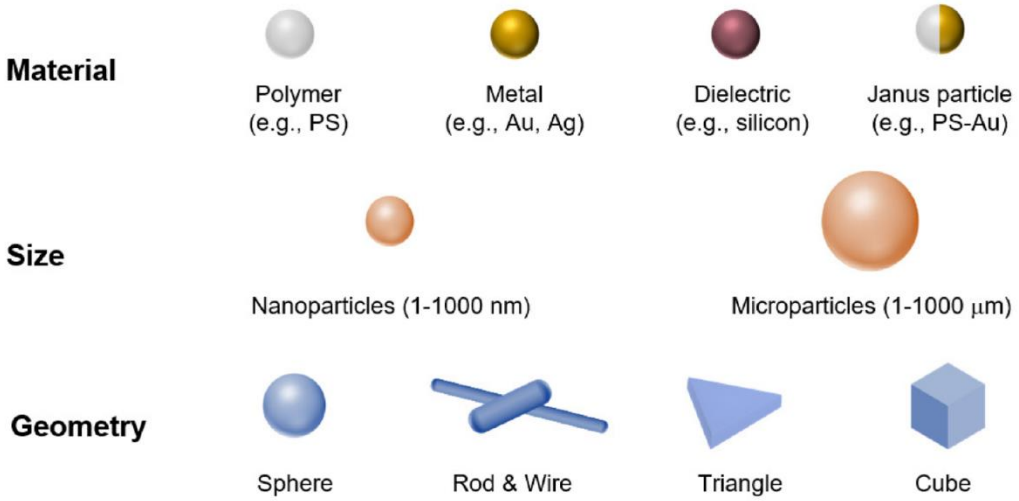

Figure 1-24. Schematics of representative colloidal particles as building blocks in the assembly of superstructures[127].

Depending on the nature of the interaction between the dispersed phase and the dispersion medium, colloids can be classified as hydrophilic and hydrophobic colloids. Hydrophilic colloids are attracted to water, which is able to disperse in water and appear in different states such as gels, suspensions, etc. Hydrophobic colloids have properties opposite to hydrophilic ones. The colloidal particles are repelled by water, and they are also known as reversible colloids.

Regarding the preparation of colloids, the following two methods are currently used[128-129]. A colloidal system can be prepared by synthesizing colloidal particles and distributing these particles throughout the dispersion medium to formulate a stable system. Large particles or droplets can be downsized to colloids by grinding, spraying, or applying shear forces such as shaking, mixing, or high shear stress. For example, paint pigments can be produced by grinding large particles in a special mill. On the other hand, small dissolved molecules can be condensed into colloidal particles by precipitation, coagulation or redox reactions. For example, clouds are formed when water molecules condense and form very

small droplets. The coagulation method forms colloidal particles through the aggregation of molecules or ions. If the particles grow beyond the size range of the colloid, droplets or precipitates are formed yet without creating a colloidal system.

An emulsion is one typical colloidal system prepared via mixing two immiscible liquids, which breaks one liquid into colloidal-sized droplets and then disperses them in the other continuous liquid medium. Oil spills in the ocean can be difficult to clean up, in part because wave action causes oil and water to form emulsions. However, in most emulsions, the dispersed phase tends to coalesce, forms large droplets, and then separates the two phases. Therefore, emulsions often require the addition of emulsifiers for colloidal stabilization, which are designed to inhibit the coalescence of dispersed liquids. The soap can be a good example, which can efficiently stabilize a kerosene emulsion in water.

The excellent stability and dispersion of colloidal solutions are strongly associated with the interaction of colloidal particles. In colloids, the following interactions are mainly present[130-131]: exclusive volume repulsion, electrostatic interactions, van der Waals forces, entropic forces, and steric repulsions. The stability of colloidal solutions is only achieved as the interactions between particles keep them in equilibrium. The sum of the interaction forces between the colloidal particles will determine the dispersion pattern of the colloidal solution[132]. As presented in **Figure 1-25**, if the attractive forces do not exceed the repulsive forces, the particles will not aggregate and remain independently dispersed. Often, the colloidal system can be stabilized by reducing the interfacial tension.

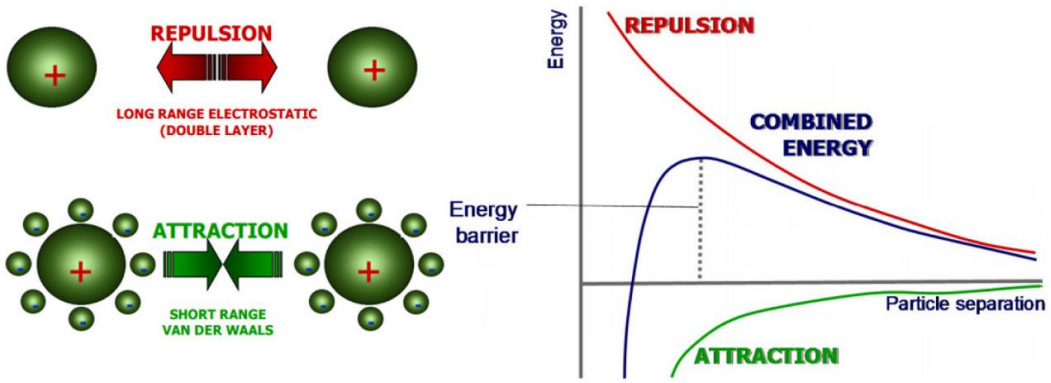

Figure 1-25. Long-range electrostatic repulsion forces and short-range van der Waals attraction forces[133] between neighboring colloids in dispersion media.

Electrostatic stabilization and steric stabilization are the most common methods to prevent aggregation[134], as shown in **Figure 1-26**. The electrostatic stabilization method utilizes the mutual repulsion of opposite charges. Since different phases have different charge affinities, an electric double layer will exist at the interfaces. Colloidal particles have a huge surface area due to their small size, and this effect is greatly amplified in colloids. In stabilized colloids, the dispersed phase has a very low mass and its buoyancy or kinetic energy is too weak to overcome the electrostatic repulsion between the charged layers of the dispersed phase. On the other hand, steric stabilization is achieved by encapsulating the particles with polymers that prevent the particles from coming closer together in the attractive range.

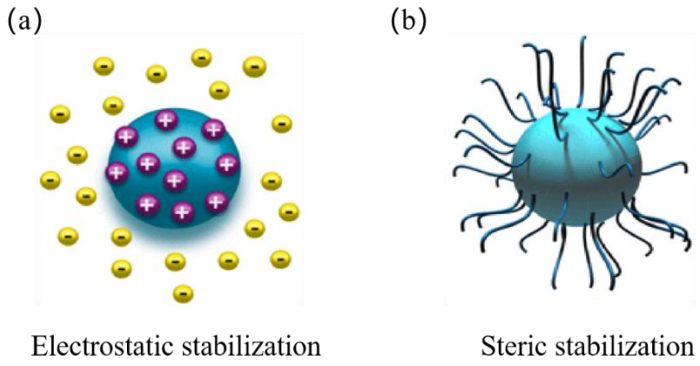

Figure 1-26. Schematic diagram of common methods to prevent aggregation of colloids: (a) electrostatic stabilization and (b) steric stabilization[134].

When the force of attraction between particles is greater than the force of repulsion, the colloids aggregate and the colloidal dispersions will form flocs. Adding salt to the suspension (changing ionic strength) or changing the pH of the suspension can effectively neutralize or screen the surface charge of the particles in the suspension. This decreases the repulsive forces that keep the colloidal particles apart and coagulation occurs under the van der Waals forces. The addition of polymeric flocculants can also link individual colloidal particles together by attractive electrostatic interactions. For example, negatively charged colloidal silica or clay particles can be flocculated by the addition of a positively charged polymer. Alternatively, the addition of non-adsorbent polymers, called inhibitors, leads to aggregation due to entropic effects. Physical deformation of particles, such as stretching, may also cause

van der Waals forces to exceed electrostatic forces, leading to aggregation of colloids in certain directions.

Nowadays, colloids have a wide range of applications in human life and production based on the virtue of their stable properties and cheapness, such as agricultural production, soil fertilization, medical and health care, and daily life production. Particularly, in industrial production and the preparation of new materials, the addition of solid colloidal particles to materials such as metals, ceramics and polymers can not only improve the mechanical properties of the materials, such as impact strength, fracture strength and tensile strength but also improve the optical properties of the materials. Colored glass is made from certain colloidal metal oxides dispersed in the glass. Some gunpowder and explosives in the defense industry must be made into colloids. Colloids are also widely used for the preparation of nanomaterials in different industries, such as mineral processing, the metallurgical industry, the dehydration of petroleum crude oil, and the manufacture of plastics, rubber and synthetic fibers. Colloids are a highly promising material, and their development and application in other fields (e.g. high-energy dielectric applications) is still worthy of anticipation and in-depth investigation.

1.3.5.2 Polymer Latex

Among the colloids, polymer latex is particularly interesting for developing new functional materials, because their colloidal dispersions in aqueous solutions can be processed into solid films with most of the common features of typical polymers.[135]. The use of water as a solvent makes the manufacture and applications of the materials environmentally friendly without the undesirable issues of harsh and volatile solvents. Polymer latex is usually synthesized by emulsion polymerization, which is fast and yields polymers of high molecular weights[136].

Although most polymer latex is water-based, they often also contain additives such as electrolytes, biocides, pigment particles, pH modifiers, and flocculation aids, etc.[136]. These additives are often volatile organic compounds that can lead to pollution and health problems. Therefore, it becomes particularly important how aqueous emulsions can form complete films

without the use of additives. Thus, charge-stabilized emulsion systems without additives have greater potential for environmentally friendly processing and applications.

New developments in emulsion polymerization have driven the production of composite latex particles. Composite latex particles are typically composed of two or more immiscible polymers that undergo phase separation within the particle to produce a variety of possible nanostructures. Core-shell latexes are the most common, which are shown in **Figure 1-27**. These structures are formed when one monomer is significantly more hydrophilic than the other, resulting in a polymer "shell" surrounding a more hydrophobic core. By using two or more polymers in a single latex, it is often possible to achieve unique properties that are not possible with homopolymers. With the advent of complex emulsion coatings, it is possible to modulate film formation by controlling the particle structure without the use of unfriendly additives.

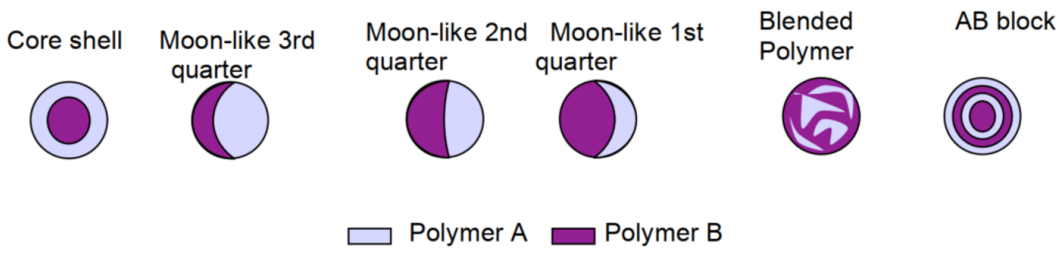

Figure 1-27. Morphologies of composite latex particles made by two immiscible polymers[137].

The block copolymers (BCPs) can be also used to prepare complex latex particles. BCPs are formed via covalent bonding of two or more chemically different polymer blocks that may not be compatible with each other. A large number of BCPs have been demonstrated to separate into a wide variety of structures depending on the portion of the polymer phase present. BCPs can be synthesized into various structures, including diblock and triblock (**Figure 1-28**), and are used in a wide variety of applications such as adhesives and drug delivery[138]. Being different from polymer blends or core-shell structures, immiscible polymers are chemically linked together in BCP latexes. The phase separation occurs at the molecular scale (5-100 nm), yielding a range of possible structures. The properties of BCP latex particles can be tuned by varying the ratio of each block in the polymer.

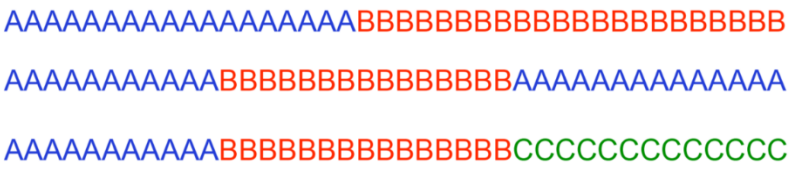

Figure 1-28. Examples of AB diblock, ABA triblock, and ABC triblock copolymers. Each letter represents a different monomer, and each block represents a polymer.

Polymer latex produced by emulsion polymerization is currently used in large quantities, such as acrylic polymers, which are used in textiles due to their excellent adhesion, flexibility and solvent resistance. Styrene-butadiene copolymers have long dominated the market in paper coatings due to their low cost. Latex paints are also popular in the market because of their low odor, low toxicity, ease of processing (ideal for brush or roller application), ease of cleaning with soap and water, faster drying than oil-based paints, and better exterior durability than oil-based paints. Today, more and more thermosetting emulsions with excellent properties have been developed, including cement additives, rheology modifiers, flocculants and water treatment agents. Based on the previous investigation and research on polymer latex, it is easy to associate whether polymers or ceramics with excellent dielectric properties can be prepared into colloidal particles and then processed into energy storage materials. If possible, one can develop dielectric capacitors with high-energy storage performance at a lower cost and more environmentally friendly manner.

1.3.5.3 Polymer Latex Films

The preparation of polymer latex films has long been the topic of extensive theoretical and experimental research. Once the latex dispersion is cast on a substrate, water evaporates from the surface and a dynamic process begins, which is known as latex film formation. The latex undergoes a series of transformations that culminate in the formation of a dry polymer film. The film formation process has been described in **Figure 1-29**[139].

At first, the polymer particles are dispersed in water and move around in Brownian motion. Drying starts with water evaporating from the surface at a similar rate as pure water[140-142]. With continued evaporation of water from the surface, the particles gradually contact each other. As in contact with its adjacent particles, Van der Waals forces keep the particles together. The first stage of drying, called particle consolidation, normally keeps an

almost constant evaporation rate and the concentration of solids reaches 60-70%.

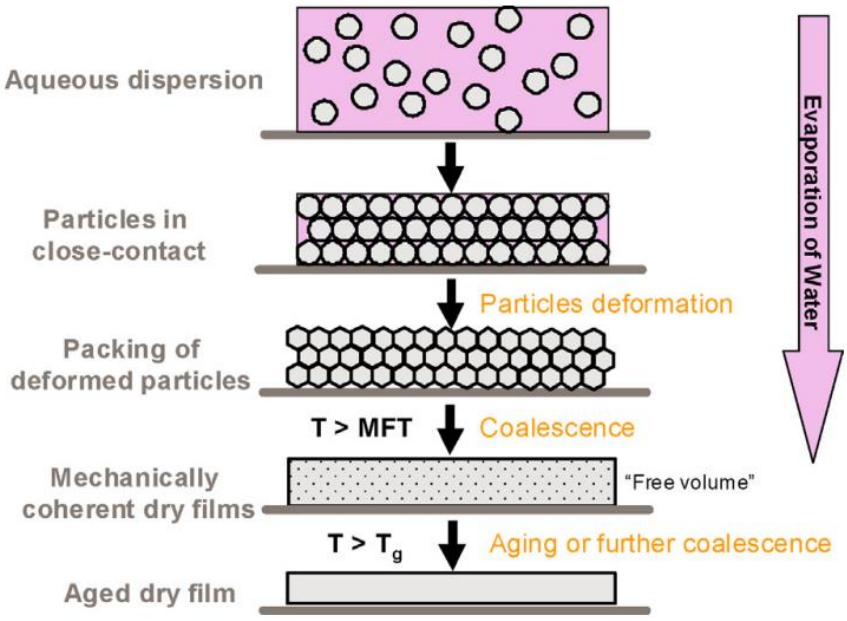

Figure 1-29. Film formation mechanism from aqueous dispersions of latex particles[139].

Then, particles have reached maximum packing and the water level now falls below the top layer of the particles, which is called the second stage. The glass transition temperature (T_g) of latex acts an important role in compacting stage. In this stage, it is necessary to distinguish between hard and soft latex. A hard latex with a higher T_g gives a glassy, hard polymer while a soft latex with a lower T_g deforms and polymer chains are easy to diffuse[143]. During the compacting process, a curved water-gas meniscus is generated between the closely packed particles, resulting in compressive stress to pull the particles together. Typically, a small radius of curvature can generate a low liquid pressure under a meniscus. Therefore, the lower the water level at the surface, the smaller the meniscus radius, leading to a pressure drop within the coating.

Pressure gradients form due to a drop in pressure at the top of the coating, contributing to the flow of water from the interior of the coating to the surface. Despite the resistance caused by pore shrinkage, the liquid is pulled toward the air interface to aid drying. For low viscosity coatings, the shape of the meniscus is kept by resupplying the liquid from the rest of the coating. For high viscous resistance, the meniscus will drop into the pores and reduce the

radius, thereby increasing the driving force of capillary pressure[143].

For a hard latex such as ceramic particles, air may invade the inter-particle spaces and the rate of evaporation decreases. As for a soft latex, when particles concentrate and induce irreversible contact, particles start deformation against each other due to capillary forces, causing the spherical particles to deform to fill into the pore space. Van der Waals forces contribute to the deformation of the particles and suppress the rate of evaporation[143].

The coalescence stage begins with the initial formation of a continuous film (**Figure 1-29**). With the diffusion of the polymer chains from one particle to another and filling the voids, the particle interfaces become not clear and the film obtains mechanical strength. The residual water in the film evaporates through the channels between the particles and the polymer skin diffuses. From a macroscopic point of view, the film becomes transparent since there is no large enough pore to scatter light rays. With time the stresses caused by compaction are dispersed or released by cracking or delamination[144].

1.3.5.3 Challenges to Formulate Dielectric Films

Though the different stages of the formation of a latex film are clear, technologically formulating a uniform and defect-free film is not straightforward. There are several challenges to bypass. The first is the cracking after the coalescence stage, as shown in **Figure 1-30**. Many mechanisms have been proposed to explain the crack formation[145-146]. It is believed that the frequency of cracks and the average crack spacing is closely related to the balance between the elastic energy released during fracture and the energy required to create a new surface. Therefore, the thicker the film thickness, the larger the crack spacing tends to be. These cracks will become defects in the material and would serve as the initial triggering point of the mechanical or dielectric failures. Therefore, it is of importance to reduce the defects in the film formation process to achieve a solid freestanding film with high quality.

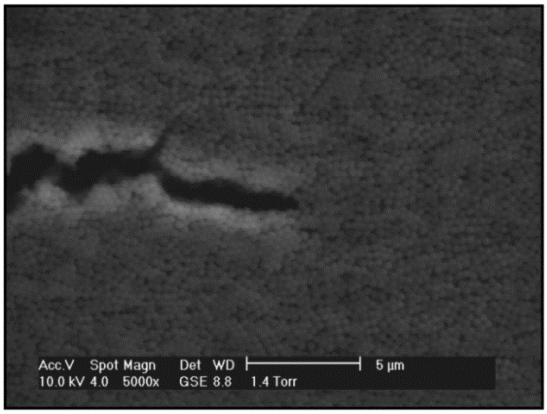

Figure 1-30. SEM image of a propagating crack during an in-situ drying experiment.

In addition to the cracking, the coffee ring effect will also lead to the non-uniformity of the final film, as shown in **Figure 1-31**. The drying of liquid droplets is a complex, non-equilibrium and not easily controlled process[147]. The evaporation of the solvent brings not only the concentration of the solute but also the spatial redistribution of the dispersed phase[147-149]. This phenomenon occurs when the water droplet contact line remains pinned during drying. In detail, during the evaporation of volatile solvents, the capillary flow drives non-volatile solutes to the boundary of the droplet to replenish the rapid local solvent loss through the capillary outflow. As a result, solutes are deposited at the edges of the original droplet and form a coffee ring. Further studies of this non-uniform distribution process suggest that internal flow, including capillary flow[149], Marangoni flow[150-151], dynamics of three-phase contact lines[152-153] and particle-particle/particle-interface interactions[154-155] will affect the redistribution of the particles.

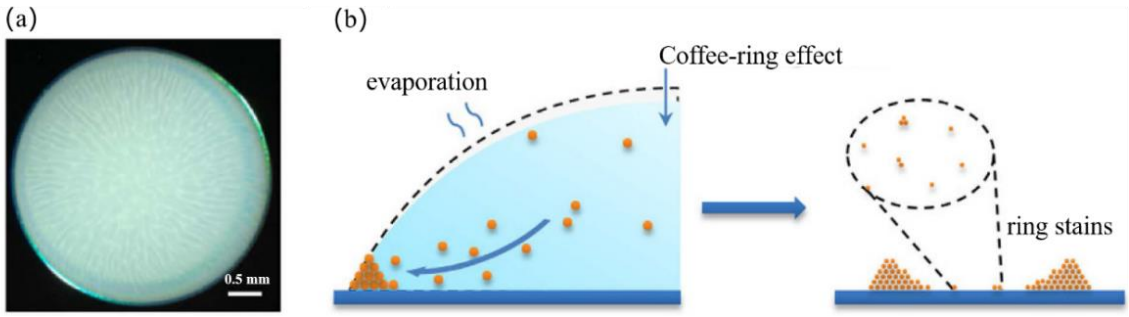

Figure 1-31. (a) Obvious capillary outflow (streamlines in the snapshot) transports the suspended particles to the drop edge, forming ring stains (b).

Several strategies have been proposed to suppress the coffee ring effect to achieve an optimal distribution of solutes. In general, there are three ways to suppress the coffee ring effect. The first is to inhibit the pinning of the contact line. The second is to interfere with the capillary flow to the contact line and the third is to prevent the solute from being transported to the contact line by the capillary flow. Using hydrophobic substrates[156-157] that suppress the nail of the contact line is the most common approach due to its simplicity and the absence of any other external involvement. However, super hydrophobic surfaces are difficult to produce. The alternative methods are to interfere with the capillary flow by electrophoresis[158], acoustics[159] and Marangoni flow[157]. Some methods rely on controlling the particle-interface interactions and transformation of liquid properties[154-155]. These methods have limitations in their application because the necessary properties of the droplet system, such as particle shape, liquid viscosity, and the additive-free requirement, must be satisfied. These processing conditions also influence the final dielectric properties of solidified latex films. Therefore, to overcome the mentioned limitations of existing methods, it is urgent to develop a controllable strategy that should be efficiently applied to most latex solutions yet without the need for substrate modification, the transformation of droplet properties, and the addition of chemical additives.

The final challenge is related to the adverse effect of residue counter ions on the dielectric properties of formulated films. As indicated in the previous section, one of the stabilization mechanisms of colloidal particles is electrostatic repulsion. The charged particles are surrounded by a large amount of counter ions, which will be residue in the film after solidification. As illustrated in **Figure 1-32**, the surface of each colloidal particle forms a bilayer structure. The zeta potential can be considered as the electrokinetic potential tested on the slip plane[133]. The more the slip plane of the bilayer is shifted toward the bulk solution, the smaller the zeta potential. The colloidal solution is considered to be completely stable while the value of the zeta potential is higher than ±30 mV[160]. Higher zeta potential means more charges on the particles and counter ions in the aqueous solution. If the energy of the long-range electrostatic repulsive force is sufficiently high, Brownian motion will occur

without aggregation of solid particles due to a large amount of charge possessed by colloidal particles. This would be of great influence on the low-field and high-field dielectric properties of the films.

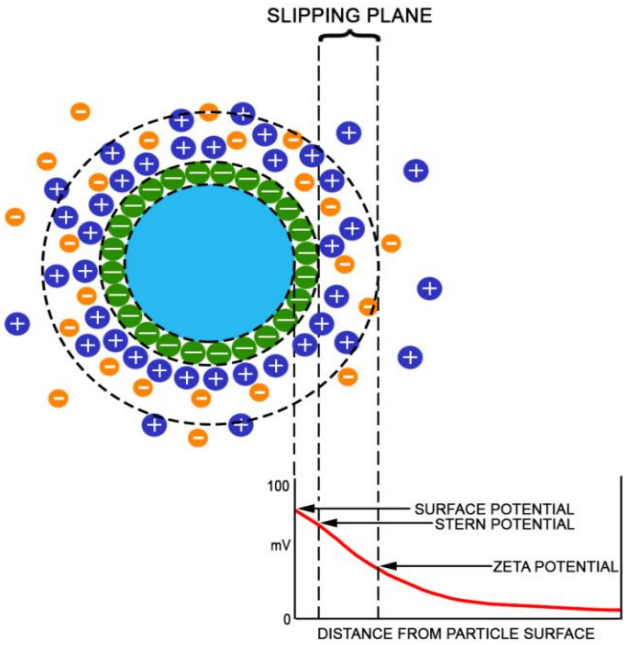

Figure 1-32. The schematic view of the electrical double layer.

1.4 Concluding Remarks

Today, one of the most promising strategies to develop flexible high-energy dielectric materials is to dope polymers with diverse functional fillers, such as ceramic dielectric fillers, conductive nanoparticles, or organic fillers. However, the agglomeration of nanoparticles and the degradation of mechanical properties of polymer composites brought by the addition of rigid inorganic fillers have severely limited their technological implementation. Although composites filled with conductive fillers exhibit improved dielectric constant at very low contents, largely preserving the mechanical properties of the materials. Yet the big challenge still exists, namely the increase in losses and the reduction in breakdown strength of the composites. This decreases the energy storage efficiency and leads to an inferior energy density to the virgin polymers. Being different from the inorganic fillers, organic fillers offer big advantages to develop flexible high-E_b and low-loss composite materials. Because of the ease of processing and the excellent compatibility with the roll-to-roll scale fabrication, they are now attracting more and more attention in the field.

In addition to the selection of raw materials, the employed processes also significantly influence the dielectric properties of polymer composites via modulating the nano, meso and macroscale structures of the composites. Typical fabrication strategies include solid-phase process and liquid-phase process. As compared to the solid-phase process, the liquid ones provide the possibility of incorporating higher content of nanofillers, achieving more uniform dispersions, as well as controlling the multiscale structure of composite materials. However, most composite systems require a large amount of organic solvents to completely dissolve the polymer to reduce the viscosity of the composite mixtures. Today, it is still challenging to develop high-energy polymeric materials in a fully eco-friendly manner, processing in aqueous solutions for example. New waterborne dielectric materials with both high-k and high-E_b are highly needed.

This thesis will definitely focus on developing water-processable dielectric polymer composites for high-energy storage by using new materials and new processes. Colloids are highly promising materials as building blocks to construct functional materials, such as photonic materials, proton conductive membranes, and organic photovoltaic devices. Nevertheless, to date, there are few successful examples to demonstrate their dielectric applications, particularly for high-energy storage. The direct reasons behind this are associated with the difficulties of controlling the defects related to the cracking and/or coffee rings during the solidification of the films. A deeper reason relies on the existence of the counter ions in most of the colloidal systems, of which the stability is maintained via the repulsive interaction between charges on the particles. It is believed that ion-containing materials are not suitable for achieving a high U_e and a high E_b due to the significant conduction loss at a high electric field. In this thesis, we are going to bypass these challenges and demonstrate new colloidal routes toward high-energy dielectric materials. Furthermore, aqueous colloidal solutions can be employed as dielectric inks for various printing technologies. We will also try to implement in this thesis a microfiction technique, inkjet printing, to print the dielectric inks into high-energy dielectric materials.

References

1. Chu, B.; Zhou, X.; Ren, K.; Neese, B.; Lin, M.; Wang, Q.; Bauer, F.; Zhang, Q., A dielectric polymer with high electric energy density and fast discharge speed. *Science* **2006,** *313* (5785), 334-336.
2. Zhang, H.; Marwat, M. A.; Xie, B.; Ashtar, M.; Liu, K.; Zhu, Y.; Zhang, L.; Fan, P.; Samart, C.; Ye, Z.-g., Polymer matrix nanocomposites with 1D ceramic nanofillers for energy storage capacitor applications. *ACS Applied Materials & Interfaces* **2019,** *12* (1), 1-37.
3. Yuan, J. K.; Dang, Z. M.; Bai, J., Unique dielectric properties in polyaniline/poly (vinylidene fluoride) composites induced by temperature variation. *physica status solidi (RRL)–Rapid Research Letters* **2008,** *2* (5), 233-235.
4. Keithley, J. F., *The story of electrical and magnetic measurements: from 500 BC to the 1940s*. John Wiley & Sons: 1999.
5. Khanchaitit, P., *Ferroelectric polymer thin films with high energy density and low loss*. The Pennsylvania State University: 2012.
6. Hilker, B.; Fields, K. B.; Stern, A.; Space, B.; Zhang, X. P.; Harmon, J. P., Dielectric analysis of poly (methyl methacrylate) zinc (II) mono-pinacolborane diphenylporphyrin composites. *Polymer* **2010,** *51* (21), 4790-4805.
7. Qiao, Y.; Yin, X.; Zhu, T.; Li, H.; Tang, C., Dielectric polymers with novel chemistry, compositions and architectures. *Progress in Polymer Science* **2018,** *80*, 153-162.
8. Zhu, L.; Wang, Q., Novel ferroelectric polymers for high energy density and low loss dielectrics. *Macromolecules* **2012,** *45* (7), 2937-2954.
9. Kingery, W. D.; Bowen, H. K.; Uhlmann, D. R., *Introduction to ceramics*. John wiley & sons: 1976; Vol. 17.
10. Omar, M. A., *Elementary solid state physics: principles and applications*. Pearson Education India: 1975.
11. Schaffer, J. P., *The science and design of engineering materials*. Irwin Professional Publishing: 1999.
12. Hill, R.; Dissado, L., Theoretical basis for the statistics of dielectric breakdown. *Journal of Physics C: Solid State Physics* **1983,** *16* (11), 2145.
13. Yao, L.; Pan, Z.; Zhai, J.; Zhang, G.; Liu, Z.; Liu, Y., High-energy-density with polymer nanocomposites containing of SrTiO3 nanofibers for capacitor application. *Composites Part A: Applied Science and Manufacturing* **2018,** *109*, 48-54.
14. Han, K.; Li, Q.; Chanthad, C.; Gadinski, M. R.; Zhang, G.; Wang, Q., A hybrid material approach toward solution-processable dielectrics exhibiting enhanced breakdown strength and high energy density. *Advanced Functional Materials* **2015,** *25* (23), 3505-3513.
15. Zhang, Y.; Li, Y.; Tao, N.; Lu, K., High strength and high electrical conductivity in bulk nanograined Cu embedded with nanoscale twins. *Applied Physics Letters* **2007,** *91* (21), 211901.
16. Zebouchi, N.; Bendaoud, M.; Essolbi, R.; Malec, D.; Ai, B.; Giam, H. T., Electrical breakdown theories applied to polyethylene terephthalate films under the combined effects of pressure and temperature. *Journal of applied physics* **1996,** *79* (5), 2497-2501.

17. Chen, J.; Yu, X.; Fan, Y.; Duan, Z.; Jiang, Y.; Yang, F., Enhanced the breakdown strength and energy density in flexible composite films via optimizing electric field distribution. *Journal of Materials Science: Materials in Electronics* **2017,** *28* (23), 18200-18206.
18. Shen, Y.; Du, J.; Zhang, X.; Huang, X.; Song, Y.; Wu, H.; Lin, Y.; Li, M.; Nan, C.-W., Enhanced breakdown strength and suppressed leakage current of polyvinylidene fluoride nanocomposites by two-dimensional ZrO2 nanosheets. *Materials Express* **2016,** *6* (3), 277-282.
19. Pihera, J.; Kadlec, P.; Prosr, P.; Polanský, R.; Kroupa, T. In *Dielectric breakdown analysis of composites consisting of epoxy resin and polyimide film*, 2020 International Conference on Diagnostics in Electrical Engineering (Diagnostika), IEEE: 2020; pp 1-4.
20. Panov, V.; Vasilyak, L.; Vetchinin, S.; Pecherkin, V. Y.; Son, E., Slow 'thermal'and fast 'streamer-leader'breakdown modes in conductive water. *Journal of Physics D: Applied Physics* **2018,** *51* (35), 354003.
21. Huang, M.; Zhou, Y.; Zhou, Z.; Qi, B., A combined electro-thermal breakdown model for oil-impregnated paper. *Energies* **2017,** *10* (12), 2160.
22. Ran, H.; Li, J.; Zhang, J.; Li, X.; Chen, J. In *Influence of temperature and thermal aging on breakdown voltage of oil-paper insulation*, 2016 IEEE International Conference on High Voltage Engineering and Application (ICHVE), IEEE: 2016; pp 1-4.
23. Hussain, S.; Roberts, E.; Asghar, H.; Campen, A.; Brown, N., Oxidation of phenol and the adsorption of breakdown products using a graphite adsorbent with electrochemical regeneration. *Electrochimica acta* **2013,** *92*, 20-30.
24. Margolin, A., Electrochemical surface breakdown of dielectric. *Chemical Physics Reports* **1997,** *16* (7), 1311-1317.
25. Kuzmenko, N.; Srago, I.; Penkina, N., Electrochemical breakdown of organic pollutants. *Russian Journal of Applied Chemistry* **1993,** *66* (5).
26. O'Dwyer, J. J., Theory of dielectric breakdown in solids. *Journal of the Electrochemical Society* **1969,** *116* (2), 239.
27. O'dwyer, J. In *Breakdown in solid dielectrics*, Conference on Electrical Insulation & Dielectric Phenomena-Annual Report 1982, IEEE: 1982; pp 319-327.
28. O'dwyer, J., The theory of avalanche breakdown in solid dielectrics. *Journal of Physics and Chemistry of Solids* **1967,** *28* (7), 1137-1144.
29. Schroter, M.; Yan, Z.; Lee, T.; Shi, W. In *A compact tunneling current and collector breakdown model*, Proceedings of the 1998 Bipolar/BiCMOS Circuits and Technology Meeting (Cat. No. 98CH36198), IEEE: 1998; pp 203-206.
30. Zhao, P.; Guo, L., Numerical Simulations of Air Breakdown by Microwave With Two Orthogonal Electric Fields. *IEEE Transactions on Plasma Science* **2018,** *46* (3), 489-493.
31. Tarasenko, V.; Naidis, G.; Beloplotov, D.; Lomaev, M.; Sorokin, D.; Babaeva, N. Y., Streamer Breakdown of Atmospheric-Pressure Air in a Non-Uniform Electric Field at High Overvoltages. *Russian Physics Journal* **2018,** *61* (6).
32. Yamaguchi, K.; Kobayashi, D.; Yamamoto, T.; Hirose, K., Theoretical investigation of the breakdown electric field of SiC polymorphs. *Physica B: Condensed Matter* **2018,** *532*, 99-102.

33. Loktionov, E. Y.; Pasechnikov, N.; Protasov, Y. S.; Protasov, Y.; Telekh, V., Laser-Induced Electric Breakdown of Krypton in the UV–Near IR Spectral Region. *Journal of Applied Spectroscopy* **2015,** *82* (4), 607-613.
34. Xia, W.; Xu, Z.; Wen, F.; Li, W.; Zhang, Z., Crystalline properties dependence of dielectric and energy storage properties of poly (vinylidene fluoride-chlorotrifluoroethylene). *Applied Physics Letters* **2010,** *97* (22), 222905.
35. Zhou, X.; Chu, B.; Neese, B.; Lin, M.; Zhang, Q., Electrical energy density and discharge characteristics of a poly (vinylidene fluoride-chlorotrifluoroethylene) copolymer. *IEEE transactions on dielectrics and electrical insulation* **2007,** *14* (5), 1133-1138.
36. Job, A. E.; Alves, N.; Zanin, M.; Ueki, M. M.; Mattoso, L. H.; Teruya, M. Y.; Giacometti, J. A., Increasing the dielectric breakdown strength of poly (ethylene terephthalate) films using a coated polyaniline layer. *Journal of Physics D: Applied Physics* **2003,** *36* (12), 1414.
37. Claude, J.; Lu, Y.; Wang, Q., Effect of molecular weight on the dielectric breakdown strength of ferroelectric poly (vinylidene fluoride-chlorotrifluoroethylene) s. *Applied Physics Letters* **2007,** *91* (21), 212904.
38. Kim, P.; Doss, N. M.; Tillotson, J. P.; Hotchkiss, P. J.; Pan, M.-J.; Marder, S. R.; Li, J.; Calame, J. P.; Perry, J. W., High energy density nanocomposites based on surface-modified BaTiO3 and a ferroelectric polymer. *ACS nano* **2009,** *3* (9), 2581-2592.
39. Preetha, P.; Thomas, M. J., AC breakdown characteristics of epoxy nanocomposites. *IEEE Transactions on Dielectrics and Electrical Insulation* **2011,** *18* (5), 1526-1534.
40. Li, S.; Yin, G.; Bai, S.; Li, J., A new potential barrier model in epoxy resin nanodielectrics. *IEEE Transactions on Dielectrics and Electrical Insulation* **2011,** *18* (5), 1535-1543.
41. Lines, M. E.; Glass, A. M., *Principles and applications of ferroelectrics and related materials*. Oxford university press: 2001.
42. Yang, L.; Allahyarov, E.; Guan, F.; Zhu, L., Crystal orientation and temperature effects on double hysteresis loop behavior in a poly (vinylidene fluoride-co-trifluoroethylene-co-chlorotrifluoroethylene)-graft-polystyrene graft copolymer. *Macromolecules* **2013,** *46* (24), 9698-9711.
43. Zhu, L., Exploring strategies for high dielectric constant and low loss polymer dielectrics. *The journal of physical chemistry letters* **2014,** *5* (21), 3677-3687.
44. Tang, H.; Lin, Y.; Sodano, H. A., Synthesis of high aspect ratio BaTiO3 nanowires for high energy density nanocomposite capacitors. *Advanced Energy Materials* **2013,** *3* (4), 451-456.
45. Tang, H.; Sodano, H. A., Ultra high energy density nanocomposite capacitors with fast discharge using Ba0. 2Sr0. 8TiO3 nanowires. *Nano letters* **2013,** *13* (4), 1373-1379.
46. Wang, J.; Shen, Z.-H., Modeling-guided understanding microstructure effects in energy storage dielectrics. *Microstructures* **2021,** *1* (1), 2021006.
47. Zhou, Z.; Tang, H.; Sodano, H. A., Scalable synthesis of morphotropic phase boundary lead zirconium titanate nanowires for energy harvesting. *Advanced Materials* **2014,** *26* (45), 7547-7554.
48. Tang, H.; Lin, Y.; Sodano, H. A., Enhanced energy storage in nanocomposite capacitors

through aligned PZT nanowires by uniaxial strain assembly. *Advanced Energy Materials* **2012,** *2* (4), 469-476.

49. Hao, X., A review on the dielectric materials for high energy-storage application. *Journal of Advanced Dielectrics* **2013,** *3* (01), 1330001.
50. Ahn, C. W.; Amarsanaa, G.; Won, S. S.; Chae, S. A.; Lee, D. S.; Kim, I. W., Antiferroelectric thin-film capacitors with high energy-storage densities, low energy losses, and fast discharge times. *ACS applied materials & interfaces* **2015,** *7* (48), 26381-26386.
51. Chu, B.; Zhou, X.; Neese, B.; Zhang, Q.; Bauer, F., Relaxor ferroelectric poly (vinylidene fluoride-trifluoroethylene-chlorofluoroethylene) terpolymer for high energy density storage capacitors. *IEEE transactions on dielectrics and electrical insulation* **2006,** *13* (5), 1162-1169.
52. Khanchaitit, P.; Han, K.; Gadinski, M. R.; Li, Q.; Wang, Q., Ferroelectric polymer networks with high energy density and improved discharged efficiency for dielectric energy storage. *Nature communications* **2013,** *4* (1), 1-7.
53. Yang, L.; Kong, X.; Li, F.; Hao, H.; Cheng, Z.; Liu, H.; Li, J.-F.; Zhang, S., Perovskite lead-free dielectrics for energy storage applications. *Progress in Materials Science* **2019,** *102*, 72-108.
54. Wang, Y.; Zhou, X.; Chen, Q.; Chu, B.; Zhang, Q., Recent development of high energy density polymers for dielectric capacitors. *IEEE Transactions on Dielectrics and Electrical Insulation* **2010,** *17* (4), 1036-1042.
55. Lehmann, P., Overview of the electric launch activities at the French-German Research Institute of Saint-Louis (ISL). *IEEE Transactions on Magnetics* **2003,** *39* (1), 24-28.
56. Ford, T. A.; Edward, H. W., Polyvinylidene fluoride and process for obtaining the same. Google Patents: 1948.
57. Rabuffi, M.; Picci, G., Status quo and future prospects for metallized polypropylene energy storage capacitors. *IEEE transactions on plasma science* **2002,** *30* (5), 1939-1942.
58. Shrout, T. R.; Zhang, S. J., Lead-free piezoelectric ceramics: Alternatives for PZT? *Journal of Electroceramics* **2007,** *19* (1), 113-126.
59. Zhang, X.; Jiang, J.; Shen, Z.; Dan, Z.; Li, M.; Lin, Y.; Nan, C. W.; Chen, L.; Shen, Y., Polymer nanocomposites with ultrahigh energy density and high discharge efficiency by modulating their nanostructures in three dimensions. *Advanced Materials* **2018,** *30* (16), 1707269.
60. Zhang, Y.; Wang, Y.; Qi, S.; Dunn, S.; Dong, H.; Button, T., Enhanced discharge energy density of rGO/PVDF nanocomposites: The role of the heterointerface. *Applied Physics Letters* **2018,** *112* (20), 202904.
61. Tu, S.; Jiang, Q.; Zhang, X.; Alshareef, H. N., Large dielectric constant enhancement in MXene percolative polymer composites. *ACS nano* **2018,** *12* (4), 3369-3377.
62. Zheng, M.-S.; Zha, J.-W.; Yang, Y.; Han, P.; Hu, C.-H.; Wen, Y.-Q.; Dang, Z.-M., Polyurethane induced high breakdown strength and high energy storage density in polyurethane/poly (vinylidene fluoride) composite films. *Applied Physics Letters* **2017,** *110* (25), 252902.
63. Li, W.; Jiang, L.; Zhang, X.; Shen, Y.; Nan, C., High-energy-density dielectric films

based on polyvinylidene fluoride and aromatic polythiourea for capacitors. *Journal of Materials Chemistry A* **2014,** *2* (38), 15803-15807.

64. Barber, P.; Balasubramanian, S.; Anguchamy, Y.; Gong, S.; Wibowo, A.; Gao, H.; Ploehn, H. J.; Zur Loye, H.-C., Polymer composite and nanocomposite dielectric materials for pulse power energy storage. *Materials* **2009,** *2* (4), 1697-1733.
65. Sada, T.; Tsuji, K.; Ndayishimiye, A.; Fan, Z.; Fujioka, Y.; Randall, C. A., Enhanced high permittivity BaTiO3–polymer nanocomposites from the cold sintering process. *Journal of Applied Physics* **2020,** *128* (8), 084103.
66. Luo, B.; Wang, X.; Wang, Y.; Li, L., Fabrication, characterization, properties and theoretical analysis of ceramic/PVDF composite flexible films with high dielectric constant and low dielectric loss. *Journal of Materials Chemistry A* **2014,** *2* (2), 510-519.
67. Böttcher, C. J. F.; van Belle, O. C.; Bordewijk, P.; Rip, A.; Yue, D. D., Theory of electric polarization. *Journal of The Electrochemical Society* **1974,** *121* (6), 211Ca.
68. Sillars, R., The properties of a dielectric containing semiconducting particles of various shapes. *Institution of Electrical Engineers-Proceedings of the Wireless Section of the Institution* **1937,** *12* (35), 139-155.
69. Landauer, R., The electrical resistance of binary metallic mixtures. *Journal of applied physics* **1952,** *23* (7), 779-784.
70. MAXWELL-GARNETT, J. C., Colours in metal glasses and in metallic films. *Phil. Trans. R. Soc. Lond, A* **1904,** *203*, 385-420.
71. Tuncer, E.; Gubański, S. M.; Nettelblad, B., Dielectric relaxation in dielectric mixtures: Application of the finite element method and its comparison with dielectric mixture formulas. *Journal of Applied Physics* **2001,** *89* (12), 8092-8100.
72. Wagner, K., The after effect in dielectrics. *Arch. Electrotech* **1914,** *2* (378), e394.
73. Nelson, S.; You, T.-S., Relationships between microwave permittivities of solid and pulverised plastics. *Journal of physics D: applied physics* **1990,** *23* (3), 346.
74. Shen, L.; Savre, W.; Price, J.; Athavale, K., Dielectric properties of reservoir rocks at ultra-high frequencies. *geophysics* **1985,** *50* (4), 692-704.
75. Yu, K.; Wang, H.; Zhou, Y.; Bai, Y.; Niu, Y., Enhanced dielectric properties of BaTiO3/poly (vinylidene fluoride) nanocomposites for energy storage applications. *Journal of applied physics* **2013,** *113* (3), 034105.
76. Van Beek, L., Dielectric behaviour of heterogeneous systems. *Progress in dielectrics* **1967,** *7* (71), 113.
77. Nan, C.-W., Physics of inhomogeneous inorganic materials. *Progress in materials science* **1993,** *37* (1), 1-116.
78. Dang, Z.-M.; Yuan, J.-K.; Zha, J.-W.; Zhou, T.; Li, S.-T.; Hu, G.-H., Fundamentals, processes and applications of high-permittivity polymer–matrix composites. *Progress in materials science* **2012,** *57* (4), 660-723.
79. Song, Y.; Shen, Y.; Liu, H.; Lin, Y.; Li, M.; Nan, C.-W., Enhanced dielectric and ferroelectric properties induced by dopamine-modified BaTiO 3 nanofibers in flexible poly (vinylidene fluoride-trifluoroethylene) nanocomposites. *Journal of Materials Chemistry* **2012,** *22* (16), 8063-8068.
80. Hu, H.; Zhang, F.; Luo, S.; Chang, W.; Yue, J.; Wang, C.-H., Recent advances in rational

design of polymer nanocomposite dielectrics for energy storage. *Nano Energy* **2020,** *74*, 104844.

81. Wilkinson, D.; Langer, J.; Sen, P. N., Enhancement of the dielectric constant near a percolation threshold. *Physical Review B* **1983,** *28* (2), 1081.
82. Rahaman, M.; Chaki, T.; Khastgir, D., Modeling of DC conductivity for ethylene vinyl acetate (EVA)/polyaniline conductive composites prepared through insitu polymerization of aniline in EVA matrix. *Composites science and technology* **2012,** *72* (13), 1575-1580.
83. Dang, Z.-M.; Nan, C.-W.; Xie, D.; Zhang, Y.-H.; Tjong, S., Dielectric behavior and dependence of percolation threshold on the conductivity of fillers in polymer-semiconductor composites. *Applied Physics Letters* **2004,** *85* (1), 97-99.
84. Nan, C.-W.; Shen, Y.; Ma, J., Physical properties of composites near percolation. *Annual Review of Materials Research* **2010,** *40*, 131-151.
85. Yuan, J., Percolation of carbon nanomaterials for high-k polymer nanocomposites. *Chinese Chemical Letters* **2017,** *28* (11), 2036-2044.
86. Grannan, D.; Garland, J.; Tanner, D., Critical behavior of the dielectric constant of a random composite near the percolation threshold. *Physical review letters* **1981,** *46* (5), 375.
87. Guan, S.; Li, H.; Zhao, S.; Guo, L., Novel three-component nanocomposites with high dielectric permittivity and low dielectric loss co-filled by carboxyl-functionalized multi-walled nanotube and BaTiO3. *Composites Science and Technology* **2018,** *158*, 79-85.
88. Li, S.; Yin, G.; Li, J. In *Breakdown performance of low density polyethylene nanocomposites*, 2012 IEEE 10th International Conference on the Properties and Applications of Dielectric Materials, IEEE: 2012; pp 1-4.
89. Takala, M.; Karttunen, M.; Salovaara, P.; Kortet, S.; Kannus, K.; Kalliohaka, T., Dielectric properties of nanostructured polypropylene-polyhedral oligomeric silsesquioxane compounds. *IEEE Transactions on Dielectrics and Electrical Insulation* **2008,** *15* (1), 40-51.
90. Huang, X.; Zhang, X.; Ren, G.-K.; Jiang, J.; Dan, Z.; Zhang, Q.; Zhang, X.; Nan, C.-W.; Shen, Y., Non-intuitive concomitant enhancement of dielectric permittivity, breakdown strength and energy density in percolative polymer nanocomposites by trace Ag nanodots. *Journal of Materials Chemistry A* **2019,** *7* (25), 15198-15206.
91. Ieda, M., Dielectric breakdown process of polymers. *IEEE Transactions on Electrical Insulation* **1980,** (3), 206-224.
92. Park, C.; Okajima, K.; Hara, M.; Akazaki, M., Effect of heat treatment on dielectric strength of polyethylene terephthalate under compressive stress. *IEEE Transactions on Electrical Insulation* **1983,** (4), 380-389.
93. Li, S.; Wang, W.; Yu, S.; Sun, H., Influence of hydrostatic pressure on dielectric properties of polyethylene/aluminum oxide nanocomposites. *IEEE Transactions on Dielectrics and Electrical Insulation* **2014,** *21* (2), 519-528.
94. Sabuni, H.; Nelson, J., Factors determining the electric strength of polymeric dielectrics. *Journal of Materials Science* **1976,** *11*, 1574-1576.
95. Tuncer, E.; Polizos, G.; Sauers, I.; James, D. R.; Ellis, A. R.; More, K. L., Epoxy

nanodielectrics fabricated with in situ and ex situ techniques. *Journal of Experimental Nanoscience* **2012,** *7* (3), 274-281.

96. Ma, D.; Siegel, R. W.; Hong, J.-I.; Schadler, L. S.; Mårtensson, E.; Önneby, C., Influence of nanoparticle surfaces on the electrical breakdown strength of nanoparticle-filled low-density polyethylene. *Journal of Materials Research* **2004,** *19* (3), 857-863.
97. Li, S.; Yin, G.; Chen, G.; Li, J.; Bai, S.; Zhong, L.; Zhang, Y.; Lei, Q., Short-term breakdown and long-term failure in nanodielectrics: A review. *IEEE Transactions on Dielectrics and Electrical Insulation* **2010,** *17* (5), 1523-1535.
98. Lewis, T., Interfaces are the dominant feature of dielectrics at the nanometric level. *IEEE transactions on dielectrics and electrical insulation* **2004,** *11* (5), 739-753.
99. Matsui, K.; Tanaka, Y.; Takada, T.; Fukao, T.; Fukunaga, K.; Maeno, T.; Alison, J. M., Space charge behavior in low density polyethylene at pre-breakdown. *IEEE transactions on dielectrics and electrical insulation* **2005,** *12* (3), 406-415.
100. Chen, G.; Zhao, J., Observation of negative differential mobility and charge packet in polyethylene. *Journal of Physics D: Applied Physics* **2011,** *44* (21), 212001.
101. Chen, G.; Zhao, J.; Li, S.; Zhong, L., Origin of thickness dependent dc electrical breakdown in dielectrics. *Applied Physics Letters* **2012,** *100* (22), 222904.
102. Dissado, L. A.; Fothergill, J. C., *Electrical degradation and breakdown in polymers*. Iet: 1992; Vol. 9.
103. Nelson, J. K., *Dielectric polymer nanocomposites*. Springer: 2010.
104. Li, S.; Yang, L.; Liu, W.; Wang, W.; Tanaka, T.; Vaughan, A., Dielectric breakdown in polymer nanocomposites. *Tailoring of nanocomposite dielectrics* **2017**, 243-279.
105. Huang, X.; Jiang, P., Core–shell structured high-k polymer nanocomposites for energy storage and dielectric applications. *Advanced Materials* **2015,** *27* (3), 546-554.
106. Shen, Z. H.; Wang, J. J.; Lin, Y.; Nan, C. W.; Chen, L. Q.; Shen, Y., High-throughput phase-field design of high-energy-density polymer nanocomposites. *Advanced Materials* **2018,** *30* (2), 1704380.
107. Jonathan N. Coleman, M. L., 1 Arlene O'Neill,1 Shane D. Bergin,1,6 Paul J. King,1 Umar Khan,1 Karen Young,1 Alexandre Gaucher,1 Sukanta De,1 Ronan J. Smith,1 Igor V. Shvets,1 Sunil K. Arora,1 George Stanton,1 Hye-Young Kim,2,3 Kangho Lee,2,3 Gyu Tae Kim,3 Georg S. Duesberg,2 Toby Hallam,2 John J. Boland,2 Jing Jing Wang,1 John F. Donegan,1 Jaime C. Grunlan,4 Gregory Moriarty,4 Aleksey Shmeliov,5 Rebecca J. Nicholls,5 James M. Perkins,6 Eleanor M. Grieveson,5 Koenraad Theuwissen,5 David W. McComb,6 Peter D. Nellist,5 Valeria Nicolosi, Two-Dimensional Nanosheets Produced by Liquid Exfoliation of Layered Materials. *Science* **2011**.
108. Li, Q.; Han, K.; Gadinski, M. R.; Zhang, G.; Wang, Q., High energy and power density capacitors from solution-processed ternary ferroelectric polymer nanocomposites. *Advanced Materials* **2014,** *26* (36), 6244-6249.
109. Jiang, J.; Zhang, X.; Dan, Z.; Ma, J.; Lin, Y.; Li, M.; Nan, C.-W.; Shen, Y., Tuning Phase Composition of Polymer Nanocomposites toward High Energy Density and High Discharge Efficiency by Nonequilibrium Processing. *ACS Applied Materials & Interfaces* **2017,** *9* (35), 29717-29731.
110. Wang, Y.; Cui, J.; Yuan, Q.; Niu, Y.; Bai, Y.; Wang, H., Significantly enhanced

breakdown strength and energy density in sandwich-structured barium titanate/poly (vinylidene fluoride) nanocomposites. *Advanced Materials* **2015,** *27* (42), 6658-6663.

111. Wang, L.; Dang, Z.-M., Carbon nanotube composites with high dielectric constant at low percolation threshold. *Applied physics letters* **2005,** *87* (4), 042903.
112. Dang, Z.-M.; Wu, J.-P.; Xu, H.-P.; Yao, S.-H.; Jiang, M.-J.; Bai, J., Dielectric properties of upright carbon fiber filled poly (vinylidene fluoride) composite with low percolation threshold and weak temperature dependence. *Applied Physics Letters* **2007,** *91* (7), 072912.
113. Dang, Z. M.; Lin, Y. H.; Nan, C. W., Novel ferroelectric polymer composites with high dielectric constants. *Advanced Materials* **2003,** *15* (19), 1625-1629.
114. Dang, Z. M.; Wang, H. Y.; Zhang, Y. H.; Qi, J. Q., Morphology and dielectric property of homogenous BaTiO3/PVDF nanocomposites prepared via the natural adsorption action of nanosized BaTiO3. *Macromolecular rapid communications* **2005,** *26* (14), 1185-1189.
115. Dang, Z.-M.; Shen, Y.; Nan, C.-W., Dielectric behavior of three-phase percolative Ni–BaTiO 3/polyvinylidene fluoride composites. *Applied Physics Letters* **2002,** *81* (25), 4814-4816.
116. Dang, Z.-M.; Nan, C.-W., Dielectric properties of LTNO ceramics and LTNO/PVDF composites. *Ceramics international* **2005,** *31* (2), 349-351.
117. Yuan, J.-K.; Yao, S.-H.; Dang, Z.-M.; Sylvestre, A.; Genestoux, M.; Bai1, J., Giant dielectric permittivity nanocomposites: realizing true potential of pristine carbon nanotubes in polyvinylidene fluoride matrix through an enhanced interfacial interaction. *The Journal of Physical Chemistry C* **2011,** *115* (13), 5515-5521.
118. Feng, R.; Li, L.; Ou, W.; Song, S.; Zhang, Y.; Xiong, C.; Dong, L., High-energy-density flexible dielectric film via one-step extrusion processing. *ACS Applied Polymer Materials* **2019,** *1* (4), 664-671.
119. Worsley, R.; Pimpolari, L.; McManus, D.; Ge, N.; Ionescu, R.; Wittkopf, J. A.; Alieva, A.; Basso, G.; Macucci, M.; Iannaccone, G., All-2D material inkjet-printed capacitors: toward fully printed integrated circuits. *Acs Nano* **2018,** *13* (1), 54-60.
120. Reinheimer, T.; Azmi, R.; Binder, J. R., Polymerizable ceramic ink system for thin inkjet-printed dielectric layers. *ACS Applied Materials & Interfaces* **2019,** *12* (2), 2974-2982.
121. Chen, H.; Pan, Z.; Wang, W.; Chen, Y.; Xing, S.; Cheng, Y.; Ding, X.; Liu, J.; Zhai, J.; Yu, J., Ultrahigh discharge efficiency and improved energy density in polymer-based nanocomposite for high-temperature capacitors application. *Composites Part A: Applied Science and Manufacturing* **2021,** *142*, 106266.
122. Yializis, A.; Taylor, R. S., High Temperature DC-Bus Capacitor Cost Reduction and Performance Improvements. Sigma Technologies International Group, Inc. Tucson, AZ (United States): 2017.
123. Zhang, X.; Liu, T.; Sreekumar, T.; Kumar, S.; Moore, V. C.; Hauge, R. H.; Smalley, R. E., Poly (vinyl alcohol)/SWNT composite film. *Nano letters* **2003,** *3* (9), 1285-1288.
124. Dufresne, A.; Paillet, M.; Putaux, J.; Canet, R.; Carmona, F.; Delhaes, P.; Cui, S., Processing and characterization of carbon nanotube/poly (styrene-co-butyl acrylate)

nanocomposites. *Journal of materials science* **2002,** *37* (18), 3915-3923.

125. Mitchell, C. A.; Bahr, J. L.; Arepalli, S.; Tour, J. M.; Krishnamoorti, R., Dispersion of functionalized carbon nanotubes in polystyrene. *Macromolecules* **2002,** *35* (23), 8825-8830.
126. Cosgrove, T., *Colloid science: principles, methods and applications*. John Wiley & Sons: 2010.
127. Li, J.; Zheng, Y., Optothermally Assembled Nanostructures. *Accounts of Materials Research* **2021,** *2* (5), 352-363.
128. Kopeliovich, D., SubsTech (Substances & Technologies), Meitar, Israel. *Advances in Ceramic Matrix Composites* **2018**, 93.
129. Matijevic, E., Preparation and properties of uniform size colloids. *Chemistry of materials* **1993,** *5* (4), 412-426.
130. Belloni, L., Colloidal interactions. *Journal of Physics: Condensed Matter* **2000,** *12* (46), R549.
131. van Anders, G.; Klotsa, D.; Ahmed, N. K.; Engel, M.; Glotzer, S. C., Understanding shape entropy through local dense packing. *Proceedings of the National Academy of Sciences* **2014,** *111* (45), E4812-E4821.
132. Elimelech, M.; Gregory, J.; Jia, X., *Particle deposition and aggregation: measurement, modelling and simulation*. Butterworth-Heinemann: 2013.
133. Matusiak, J.; Grządka, E., Stability of colloidal systems-a review of the stability measurements methods. *Annales Universitatis Mariae Curie-Sklodowska, sectio AA–Chemia* **2017,** *72* (1), 33.
134. Iheaturu, N. C., Synthesis, Preparation and Characterization of Nanoporous Core-Shell-Clay Epoxy Composites. Federal University of Technology, Owerri, Nigeria: 2013.
135. Keddie, J. L., Film formation of latex. *Materials Science and Engineering: R: Reports* **1997,** *21* (3), 101-170.
136. Odian, G., *Principles of polymerization*. John Wiley & Sons: 2004.
137. Durant, Y. G.; Sundberg, D. C., An advanced computer algorithm for determining morphology development in latex particles. *Journal of applied polymer science* **1995,** *58* (9), 1607-1618.
138. Charleux, B.; Nicolas, J., Water-soluble SG1-based alkoxyamines: A breakthrough in controlled/living free-radical polymerization in aqueous dispersed media. *Polymer* **2007,** *48* (20), 5813-5833.
139. Nollenberger, K.; Albers, J., Poly (meth) acrylate-based coatings. *International journal of pharmaceutics* **2013,** *457* (2), 461-469.
140. Vanderhoff, J.; Bradford, E.; Carrington, W. In *The transport of water through latex films*, Journal of Polymer Science: Polymer Symposia, Wiley Online Library: 1973; pp 155-174.
141. Sheetz, D., Formation of films by drying of latex. *Journal of Applied Polymer Science* **1965,** *9* (11), 3759-3773.
142. Croll, S., Drying of latex paint. *Journal of coatings technology* **1986,** *58* (734), 41-49.
143. Crawford, K. S., Microstructure Formation of Complex Latex Coatings. **2011**.

144. Hill, A.; Tant, M.; McGill, R.; Shang, R.; Stockl, D.; Murray, D.; Cloyd, J., Free volume distribution during consolidation and coalescence of latex films. *J Coat Technol* **2001,** *73*, 115-124.
145. Dragnevski, K. I.; Routh, A. F.; Murray, M. W.; Donald, A. M., Cracking of drying latex films: an ESEM experiment. *Langmuir : the ACS journal of surfaces and colloids* **2010,** *26* (11), 7747-7751.
146. Tirumkudulu, M. S.; Russel, W. B., Cracking in drying latex films. *Langmuir : the ACS journal of surfaces and colloids* **2005,** *21* (11), 4938-4948.
147. Yunker, P. J.; Still, T.; Lohr, M. A.; Yodh, A., Suppression of the coffee-ring effect by shape-dependent capillary interactions. *nature* **2011,** *476* (7360), 308-311.
148. Deegan, R. D.; Bakajin, O.; Dupont, T. F.; Huber, G.; Nagel, S. R.; Witten, T. A., Capillary flow as the cause of ring stains from dried liquid drops. *Nature* **1997,** *389* (6653), 827-829.
149. Deegan, R. D.; Bakajin, O.; Dupont, T. F.; Huber, G.; Nagel, S. R.; Witten, T. A., Contact line deposits in an evaporating drop. *Physical review E* **2000,** *62* (1), 756.
150. Still, T.; Yunker, P. J.; Yodh, A. G., Surfactant-induced Marangoni eddies alter the coffee-rings of evaporating colloidal drops. *Langmuir : the ACS journal of surfaces and colloids* **2012,** *28* (11), 4984-4988.
151. Sempels, W.; De Dier, R.; Mizuno, H.; Hofkens, J.; Vermant, J., Auto-production of biosurfactants reverses the coffee ring effect in a bacterial system. *Nature communications* **2013,** *4* (1), 1-8.
152. Wu, L.; Dong, Z.; Kuang, M.; Li, Y.; Li, F.; Jiang, L.; Song, Y., Printing patterned fine 3D structures by manipulating the three phase contact line. *Advanced Functional Materials* **2015,** *25* (15), 2237-2242.
153. Zhang, Z.; Zhang, X.; Xin, Z.; Deng, M.; Wen, Y.; Song, Y., Controlled inkjetting of a conductive pattern of silver nanoparticles based on the coffee-ring effect. *Advanced Materials* **2013,** *25* (46), 6714-6718.
154. Crivoi, A.; Duan, F., Elimination of the coffee-ring effect by promoting particle adsorption and long-range interaction. *Langmuir : the ACS journal of surfaces and colloids* **2013,** *29* (39), 12067-12074.
155. Cui, L.; Zhang, J.; Zhang, X.; Huang, L.; Wang, Z.; Li, Y.; Gao, H.; Zhu, S.; Wang, T.; Yang, B., Suppression of the coffee ring effect by hydrosoluble polymer additives. *ACS applied materials & interfaces* **2012,** *4* (5), 2775-2780.
156. Tian, D.; Song, Y.; Jiang, L., Patterning of controllable surface wettability for printing techniques. *Chemical Society Reviews* **2013,** *42* (12), 5184-5209.
157. Chen, L.; Evans, J. R., Drying of colloidal droplets on superhydrophobic surfaces. *Journal of colloid and interface science* **2010,** *351* (1), 283-287.
158. Mampallil, D.; Eral, H.; Van Den Ende, D.; Mugele, F., Control of evaporating complex fluids through electrowetting. *Soft Matter* **2012,** *8* (41), 10614-10617.
159. Mampallil, D.; Reboud, J.; Wilson, R.; Wylie, D.; Klug, D. R.; Cooper, J. M., Acoustic suppression of the coffee-ring effect. *Soft matter* **2015,** *11* (36), 7207-7213.
160. Uskoković, V., Dynamic light scattering based microelectrophoresis: main prospects and limitations. *Journal of dispersion science and technology* **2012,** *33* (12), 1762-1786.

Chapter 2

PVDF Latex/PVA Nanocomposite Films

2.1 Introduction

Energy storage technologies have been pursued to improve the grid-scale load level for instantaneous and periodic fluctuations, particularly with the ever-increasing production of renewable energy that heavily relies on meteorological conditions[1-2]. Current technologies, such as lithium-ion batteries and supercapacitors, have high gravimetric energy density but are unable to provide an extremely rapid response to the peaks in energy production or demand. Stabilizing the load on the grid-scale requires energy storage devices with very fast energy uptake and delivery. Dielectric capacitors store energy electrostatically in the form of electric displacement induced by the applied electric field. This energy storage mechanism offers intrinsically high power density, high operating voltage, and long work lifetime[3-6]. However, such a mechanism also causes limited energy densities that are approximately 3 orders of magnitude less than fuel cells or Li-ion batteries[7-8]. Such limitation requires a larger amount of dielectric materials to be used to reach the same level of stored energy as their counterparts.

Developing dielectric materials with improved energy density is imperative to enabling the continuous miniaturization and increased functionality of cutting-edge electrical power systems. Generally, the energy density U_e of dielectrics is determined by the applied electric field E and the associated electric displacement D[1]. As demonstrated in Chapter 1 and expressed in Equation (1.18), the key to improving the energy density of dielectric materials is to achieve a high breakdown strength E_b and a large electric displacement D_{max}.

Compared with inorganic dielectrics, polymers are attractive because of their high breakdown strengths, low losses, flexibility, and ease of processing[7, 9-12]. Until today, many polymers, such as biaxial oriented polypropylene (BOPP), polyethylene terephthalate (PET), polycarbonate (PC), and poly(vinyl alcohol) (PVA), have been deployed to make film capacitors[1, 7, 13]. However, the low dipole moments of the chemical bonds in these polymers result in a low dielectric constant ($k < 4$), leading to a low energy density (U_e <5 J/cm^3) even under the electric field near breakdown strengths. Conversely, polar polymers, such as poly(vinylidene fluoride) (PVDF)-based ferroelectric polymers, are particularly promising for energy storage because of the high polarization of the C−F bonds and the spontaneous

orientation of dipoles in the crystalline domains[14-15]. However, the strongly coupled dipoles and large ferroelectric domains in these polymers cause high energy barriers for ferroelectric switching, leading to pronounced hysteresis loops and in turn to low charge/discharge efficiency (Equation 1.20). Chemical methods (i.e., copolymerization) or high energy radiation have been developed to increase the efficiency by limiting ferroelectric losses of PVDF-based polymers through changing the ferroelectric polymers into relaxor−ferroelectric ones[16-17].

In spite of the intrinsic improvements in energy density by modifying macromolecular structures, most efforts have been devoted, in the past decades, to the composite approach, a more versatile extrinsic strategy[1, 9, 12, 18-19]. This approach capitalizes upon the combination of different components/phases with high dielectric strength and high dielectric constant, respectively, via engineering their interfaces or interphases[20-25]. Indeed, a large number of ceramic nanoparticles with different dimensionalities, such as highly polarizable $BaTiO_3$ nanoparticles or nanofibers[26], or high-E_b boron nitride nanosheets[7, 27], have been added to PVDF-based polymers to achieve concomitant enhancement of dielectric constant and breakdown strength. Nevertheless, the high density of ceramics and the inorganic/organic discrepancy in physicochemical properties usually lead to sedimentation and unexpected inhomogeneous distribution of nanofillers[28]. This actually poses a great challenge on the mass production of high-quality dielectric nanocomposite films.

In parallel with the inorganic/organic approach, blending lightweight polymers with different polar groups on the side chains has also been explored[29-37]. The similar solubility and chemical structure of polymers allow for easier processability and good adaptability to the roll-to-roll stretching fabrication. For instance, high-E_b and low-loss linear dielectric polymers, such as PET[37] and PC[35], have been multi-layered with PVDF-based polymers to serve as a barrier for treeing propagation through the film thickness. This method largely suppresses the conduction losses, improves the breakdown strength, and eventually enhances the energy density. In addition to the layered 2-2 composite configuration, rubber nanoparticles[32] and thermoplastic polyurethane (TPU)[34] that bear high breakdown strength have also been

introduced into the PVDF matrix to formulate 0−3 nanocomposites with elevated energy density.

In this chapter, we propose another 0−3 nanocomposite that is waterborne and made by mixing high-*k* PVDF latex and high-E_b water-soluble PVA. Different from the continuous phase of PVDF in previously reported composites, the low-cost PVDF latex nanoparticles are adopted as discrete polarizable domains in the PVA matrix. The moderate permittivity and conductivity contrast between PVDF and PVA are expected to achieve a less distorted local electric field. We found that the presence of a small amount (3 wt%) of PVDF nanoparticles within the PVA matrix can concurrently increase the permittivity and breakdown strength from 6.9 to 8.0 and from 438 to 515 MV/m respectively, giving rise to an energy density of 8.1 J/cm^3. Moreover, the nanocomposite can release the stored energy on a load resistor of 10 kΩ at a rate of microseconds, leading to a power density of 1.13 MW/cm^3. Both the energy and power density is nearly 400% greater than those of benchmark BOPP. The use of water-based techniques can provide an environmentally friendly aspect to both processes and consumption of current high-energy dielectric films.

2.2 Experimental Section

2.2.1 Materials

PVA was obtained from Sigma-Aldrich under the trade name of Mowiol 18-88 (CAS number: 9002-89-5) with a molecular weight M_w=195,000 g/mol and a degree of hydrolysis of 99%. PVDF latex was supplied by Arkema (Kynar Aquatec ARC Latex) with an initial concentration of solid content of 44 wt%, in which the ratio between the fluoropolymer and acrylic resin is 70:30. The PVDF nanoparticles are stabilized by negative charges in aqueous solutions with a pH value of 8. Milli-Q water (Q-Gard 00D2) was used for all experiments with a resistivity above 18.2 MΩ·cm at 25°C. Typical PVDF-HFP pellets were purchased from Sigma-Aldrich with an average molecular weight $M_w \approx$ 400,000 g/mol and number-average molecular weight M_n=130,000, whose CAS number is 9011-17-0. The solvent N,N-Dimethylacetamide with a Molar Mass=87.12 g/mol was provided by Sigma-Aldrich and its CAS number is 127-19-5.

2.2.2 Fabrication of PVDF/PVA Nanocomposites

Figure 2-1 shows the process used to fabricate PVDF/PVA nanocomposites. First PVA was dissolved in deionized water at 95°C in an oven overnight, and then magnetically stirred at 300 rpm for 2h at room temperature. The solution was afterward filtrated under a vacuum to obtain a fully dissolved aqueous solution. The PVA concentration was measured at 10.3 wt%. As schematically illustrated in **Figure 2-1** (b), various amounts of PVDF latex were mixed with the PVA solution by magnetic stirring at room temperature for 4 h. The final solute concentration of different aqueous mixtures is kept at 1.1 wt% by adding different amounts of deionized water. The final solid PVA nanocomposites possessed different PVDF contents. The nanocomposite films were prepared by a solution casting method. In detail, a 5ml well-mixed solution was cast onto a petri dish of poly(methyl methacrylate). Water was then evaporated at 56.5°C for 90 min under infrared light. The dry film was peeled off and put into a vacuum oven for drying at 110°C for 20h. The PVDF/PVA nanocomposite films are transparent, as shown in **Figure 2-1** (c). Their thickness ranges from 10 μm to 25 μm.

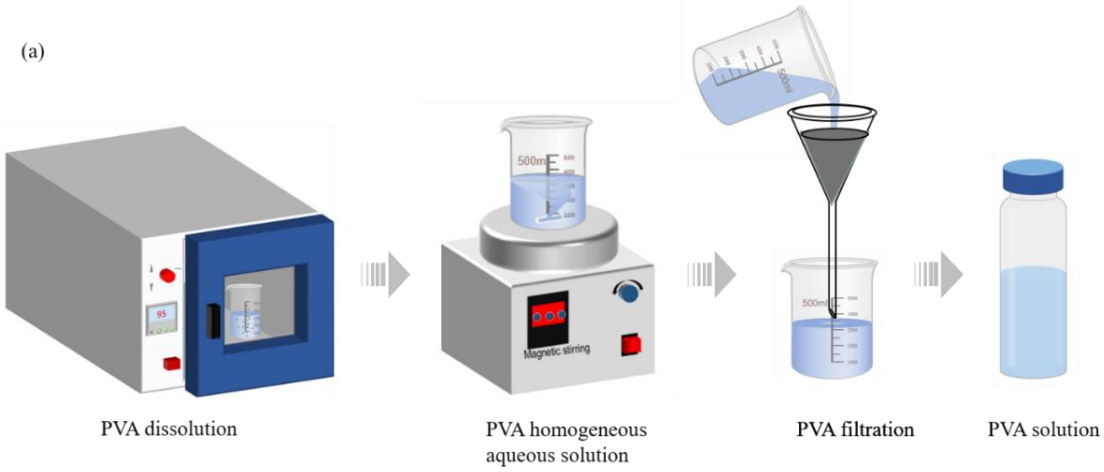

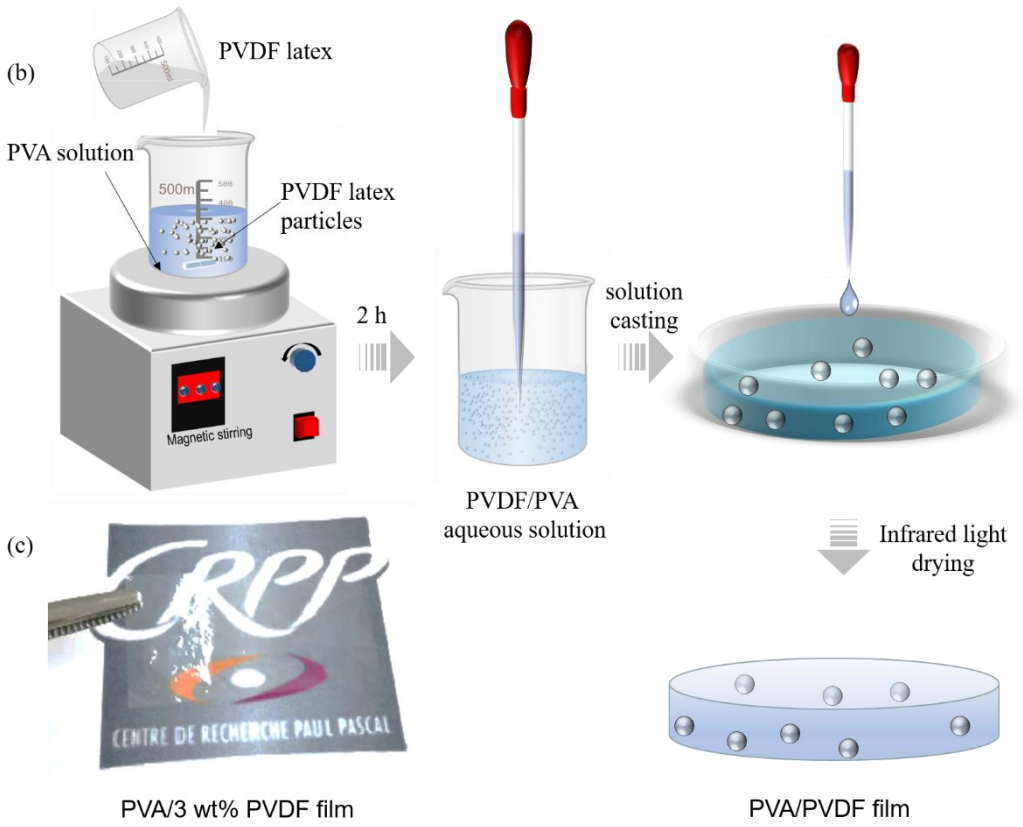

Figure 2-1. (a) Preparation pf PVA aqueous solution. (b) Water-based processes to incorporate PVDF nanoparticles into PVA matrix and make dielectric nanocomposite films. (c) Photograph of a transparent PVA composite film filled with 3 wt% PVDF latex nanoparticles.

2.2.3 Characterizations of PVDF/PVA Nanocomposites

The dielectric properties of the films were recorded as a function of frequency (from 10^{-1} Hz to 10^{6} Hz) at room temperature by an impedance analyzer (MaterialsMates 7260, Italia) under a voltage of 50 mV as shown in **Figure 2-2**. Before the characterizations, each sample was coated with gold electrodes to ensure good contact. The gold was deposited via a Cressington Sputter Coater 108 device with Au as the target. The sputtering is under vacuum conditions and the thickness of the coated electrode can be controlled by changing the sputtering time. A mask with an a-holes radius of 2.5 mm is fabricated with aluminum alloy and used to precisely control the size of the electrode for dielectric characterizations. After metallization, the film with a gold electrode was placed in the sample holder for the impedance measurement.

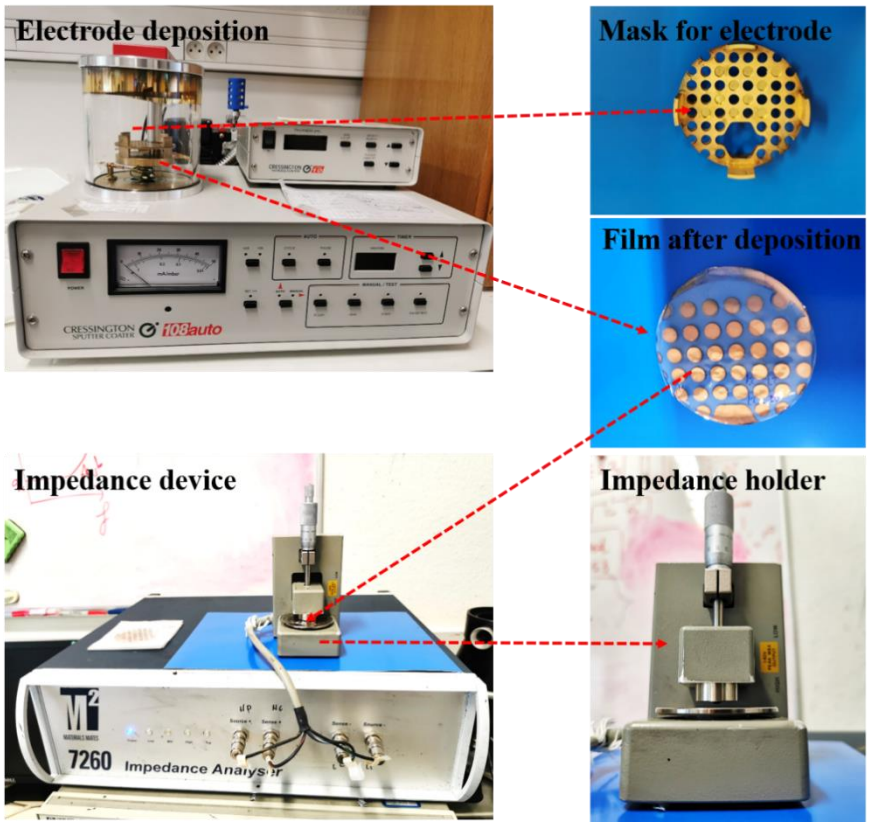

Figure 2-2. The instruments used for the deposition of the gold electrode on sample surfaces and the impedance measurement.

In addition to the good contact, the largest possible bulk capacitance is essential to reliably determine the dielectric constant of the bulk. Our samples have micrometer thicknesses and millimeter transverse dimensions, which are sufficient for the relevant tests. To obtain accurate dielectric properties of the test films, correction of the data to eliminate the contribution of cables and sample holders from the measured impedance is also necessary. Our correction method includes correcting the measured impedance values to remove the resistive and capacitive contributions of the coaxial cable and sample holder. This approach involves measuring three impedance values: the resistive contribution obtained by shorting the system, the capacitive contribution obtained by open-circuit measurements, and the impedance measurement of the sample. **Figure 2-3** shows the RC equivalent circuit of the sample and the contribution of the coaxial cable[38]. The mathematical calculation is discussed below. For the impedance measured in short circuit (Z_1^*) and open circuit (Z_2^*):

$$Z_1^* = Z_{RC}^* \tag{2.1}$$

$$Z_2^* = Z_{C_0}^* + Z_{RC}^* \tag{2.2}$$

Since it is a series capacitor, it can be written as:

$$\frac{1}{C_0} = \frac{1}{C_1^+} + \frac{1}{C_2^-} \tag{2.3}$$

Therefore, for the impedance of the tested sample (Z_3^*):

$$Z_3^* = Z_{RC}^* + \frac{1}{\frac{1}{Z_s^*} + \frac{1}{Z_{C_0}^*}} \tag{2.4}$$

and defined Y_s^* the admittance as the reciprocal of the impedance, we obtain:

$$Y_s^* = \frac{1}{Z_s^*} = \frac{1}{\frac{1}{Z_3^*} + \frac{1}{Z_{RC}^*}} - \frac{1}{\frac{1}{Z_2^*} + \frac{1}{Z_{RC}^*}} \tag{2.5}$$

Therefore, the impedance measurement of the studied sample will be a function of both contributions: pure resistive Z_1^* and totally capacitive Z_2^*.

$$Z_s^* = f(Z_1^*, Z_2^*) \tag{2.6}$$

The impedance correction procedure was performed for all measurements made in this thesis.

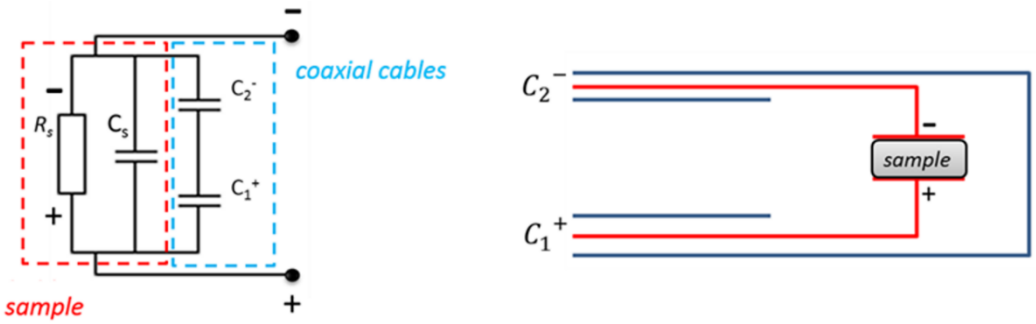

Figure 2-3. Equivalent circuit of the sample and the coaxial cable[38].

The dielectric breakdown strength and electric polarization-electric field (*P*-*E*) loops were measured at room temperature in silicone oil via a PolyK ferroelectric polarization loop and dielectric breakdown test system, as shown in **Figure 2-4.** The applied high voltage was controlled by the PolyK ferroelectric polarization device and can be amplified up to 10 kV with the help of an amplifier. The gold electrodes on the two sample surfaces contacted a copper rod and a conductive stainless steel plate respectively, which were then connected to the terminals of the test instruments. Fast discharge experiments were carried out through a capacitor charge/discharge system (PolyK Technologies) and the sample electrode configuration and cable connection are similar to those of the polarization and breakdown tests.

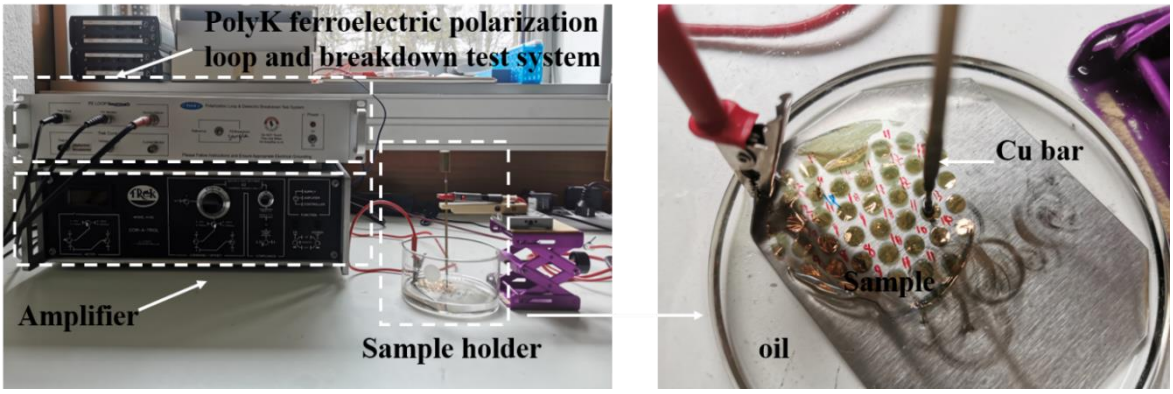

Figure 2-4. The image (left) of the instruments used for dielectric breakdown and polarization loop measurements. The right image shows the connections between the sample electrode and the samples holder.

Scanning electron microscope (SEM) images were obtained on a JEOL 6700F microscope with the sample prepared in liquid nitrogen and coated with gold before characterizations. Transmission electron microscope (TEM) images of PVDF/PVA nanocomposites were taken via a Hitachi H600 microscope operating at 75 kV. To make samples for TEM characterizations, the pure PVDF latex or the mixed solutions with different mass ratios between PVDF latex and PVA solution were directly dropped on carbon-coated copper films (200 mesh), which was followed by room-temperature evaporation of water to formulate an ultrathin layer. X-ray diffraction (XRD) was tested on a Rigaku Nanoviewer (MicroMax 007HF) with a rotating anode coupled to a confocal Max-Flux® Osmic mirror operating at a wavelength of 1.5418 Å. The recorded spectra were corrected by subtraction of the reference noise. Differential scanning calorimetry (DSC) measurements were performed using TA Instrument Q2000 under a dry nitrogen atmosphere. About 3 mg specimens were heated from 30 to 250°C at a rate of 10°C /min with three cycles, and the second curve was selected to record and analyze.

2.3 Results and Discussion

2.3.1 Morphologies of PVDF Latex and Their Nanocomposites

PVDF latex particles are nanoscale spheres. Their mixture solutions with PVA tend to form a coffee-ring effect with the evaporation of water during drying. To ensure the film quality

and the high dielectric properties, the coffee-ring effect should be suppressed in order to achieve a homogeneous PVA/PVDF film without any additives. Here, a temperature gradient was considered to balance the different evaporation rates from the center to the edge of the mixture solution. This temperature gradient can be realized by a specially designed infrared lamp. as shown in **Figure 2-5** (a). The infrared lamp can generate five differentiated areas on a table with different temperatures. **Figure 2-5** (b) illustrates the distribution of the different heating areas. The gaps between highly heated areas receive few infrared lights and are the areas with lower temperatures. When the mixture solution is placed at the center of the middle area of high temperature, the different evaporation rates induced by the temperature gradient will compensate for those induced by capillary outflow, which eventually ensures balanced evaporation all over the whole solution surfaces. Therefore, the particle transportation from the center to the edge would be largely suppressed[39]. As presented in **Figure 2-5** (c), an obvious coffee ring was observed at the edge of the film as it is dried in the air. The film thickness on the edge is over 50 μm yet no more than 5 μm at the center. However, the film prepared under an infrared lamp showed a much more homogeneous morphology, as shown in **Figure 2-5** (d). Moreover, the pure PVA film fabricated under an infrared lamp is still transparent with a high quality (**Figure 2-5** (e)). It can be concluded that a homogeneous and high-quality freestanding film can be prepared by solution casting in a petri dish under an infrared lamp. This process will be also applied to the preparations of other latex-based films in this thesis.

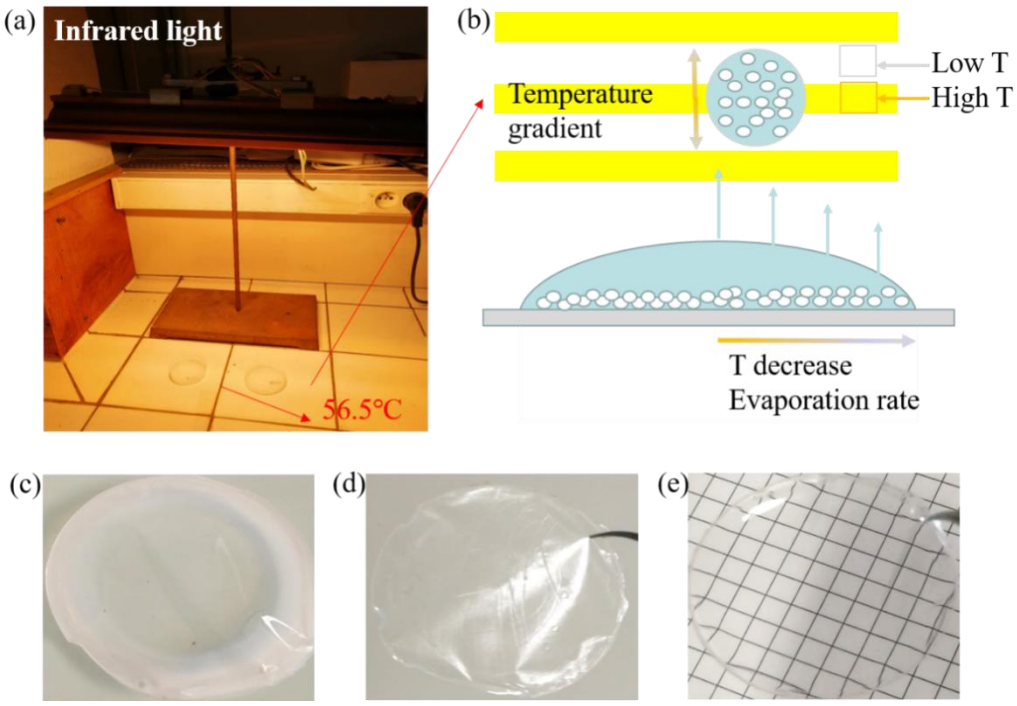

Figure 2-5. (a) Drying processes under an infrared lamp, (b) schematic graph of temperature gradient generated by an infrared lamp, Photograph of the solidified film of (c) PVA/5%PVDF film dried in the air, (d) PVA/5%PVDF film dried under an infrared lamp, (e) PVA film dried under an infrared lamp.

TEM was performed on pristine PVDF latex and their nanocomposites to investigate the dispersion state and morphology of PVDF latex nanoparticles in the PVA matrix. As shown in **Figure 2-6** (a), PVDF latex particles are spherical with a diameter of 149 nm. **Figure 2-6** (b-f) reveals the morphology evolution of nanocomposites with increasing the PVDF content from 1 wt% to 5 wt%. At concentrations below 3 wt%, the natural good dispersibility of PVDF particles can ensure the formation of isolated PVDF nanodomains in the PVA matrix as shown in **Figure 2-6** (b-d). By contrast, as the concentration is beyond 4 wt%, the particles start to coalesce and form clustering due to the attractive interactions during the current water-based processing, as presented in **Figure 2-6** (e-f).

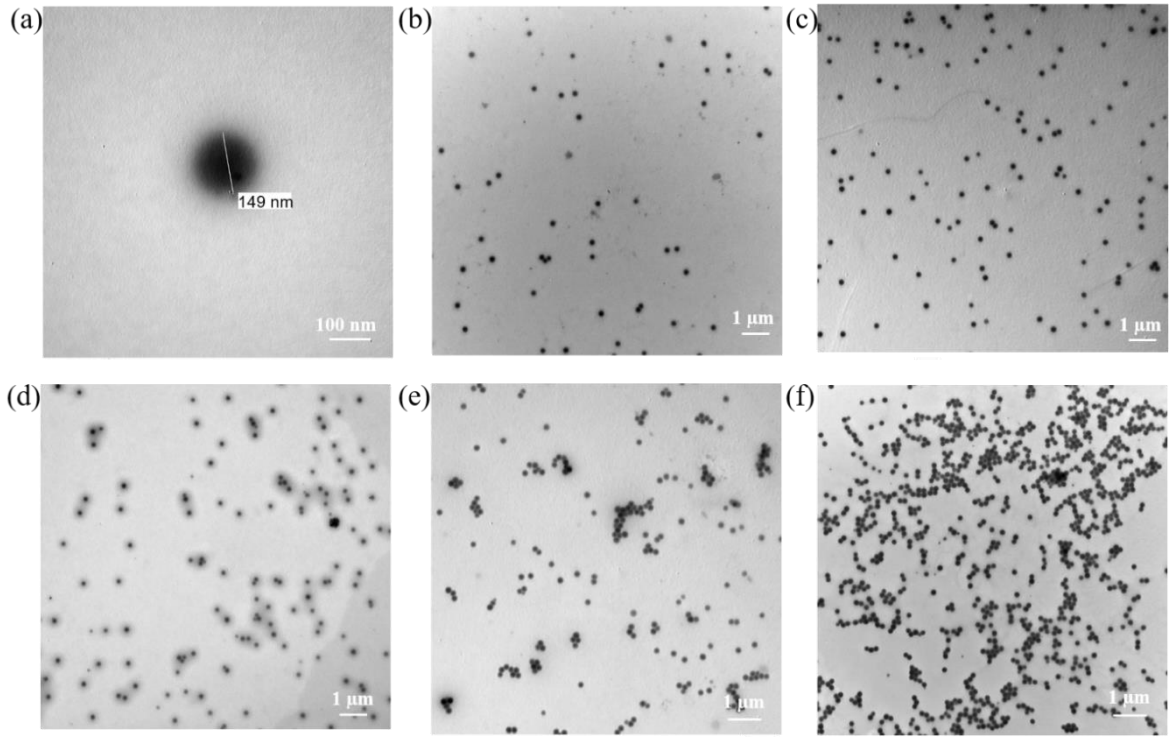

Figure 2-6. (a) TEM image of PVDF latex particle, showing a diameter of 149 nm. TEM morphologies of PVDF/PVA nanocomposite films with various loadings of PVDF nanoparticles: (b) 1 wt%, (c) 2 wt%, (d) 3 wt%, (e) 4 wt%, and (f) 5 wt%.

SEM with different magnifications was also performed on the section of PVA/3 wt% PVDF film. In **Figure 2-7** (a), it is noted that the thin film is flat with a thickness of about 10 μm. PVDF is randomly dispersed in the whole PVA matrix. No large aggregates of latex particles are observed. With increasing the magnification, isolated particles are clearly identified without coalescence in the matrix. Furthermore, no apparent cracks or gaps exist between PVDF latex particles and the PVA matrix, revealing good interfacial compatibility. These results agree well with the optical observations aforementioned and confirm again that a high-quality thin film with randomly dispersed PVDF latex particles can be obtained via simple solution casting under infrared lamp drying.

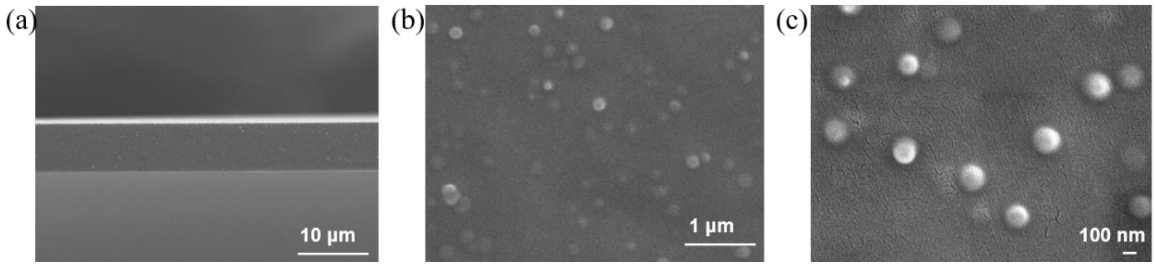

Figure 2-7. SEM images of the cross section of PVA/3wt% PVDF film with different magnifications: (a) x2500, (b) x15000, (c) x50000.

2.3.2 Dielectric Performances of PVDF/PVA Nanocomposite Films

The dependences of the dielectric constant on the frequency are shown in **Figure 2-8** (a). Dielectric constants of all the polymer composites tend to decrease with increasing frequency. At each frequency, the dielectric constant increases monotonously with the PVDF content. Nevertheless, all the dielectric constants of composites fall into the interval of the two single polymer components. The conductivity and loss tangent are weakly affected by the presence of PVDF at frequencies beyond 100 Hz as shown in **Figure 2-8** (b-c). By contrast, fluctuations of conductivity and losses take place as the frequency decreases down to 100 Hz. The lowest conductivity and loss tangent are obtained at 3 wt% of PVDF nanoparticles. The variation of dielectric constant and losses with the concentration of PVDF nanoparticles is presented in **Figure 2-8** (d). At 100 Hz, the dielectric constant increases from 6.9 to 8.1. In spite of the enhancement in dielectric constant, the losses at 100 Hz keep stable with increasing PVDF content and remain at a level below 0.05. The permittivity variation shown here does not follow the models of the mixture rules aforementioned in Chapter 1. We are going to clarify the specific mechanism accounting for the enhancement of permittivity in PVDF/PVA composites.

Generally speaking, in a heterogeneous system, when a current flow across the two-material interfaces, charges will accumulate at the interface between two materials with different relaxation time ($\tau = \varepsilon/\sigma$, where ε is the dielectric constant and σ is the conductivity)[40]. In the present case, the relaxation time of PVDF and PVA is on the same order of magnitude. The induced interfacial polarization is actually very weak and has limited contribution to the improvement of the dielectric constant of PVA/PVDF composites.

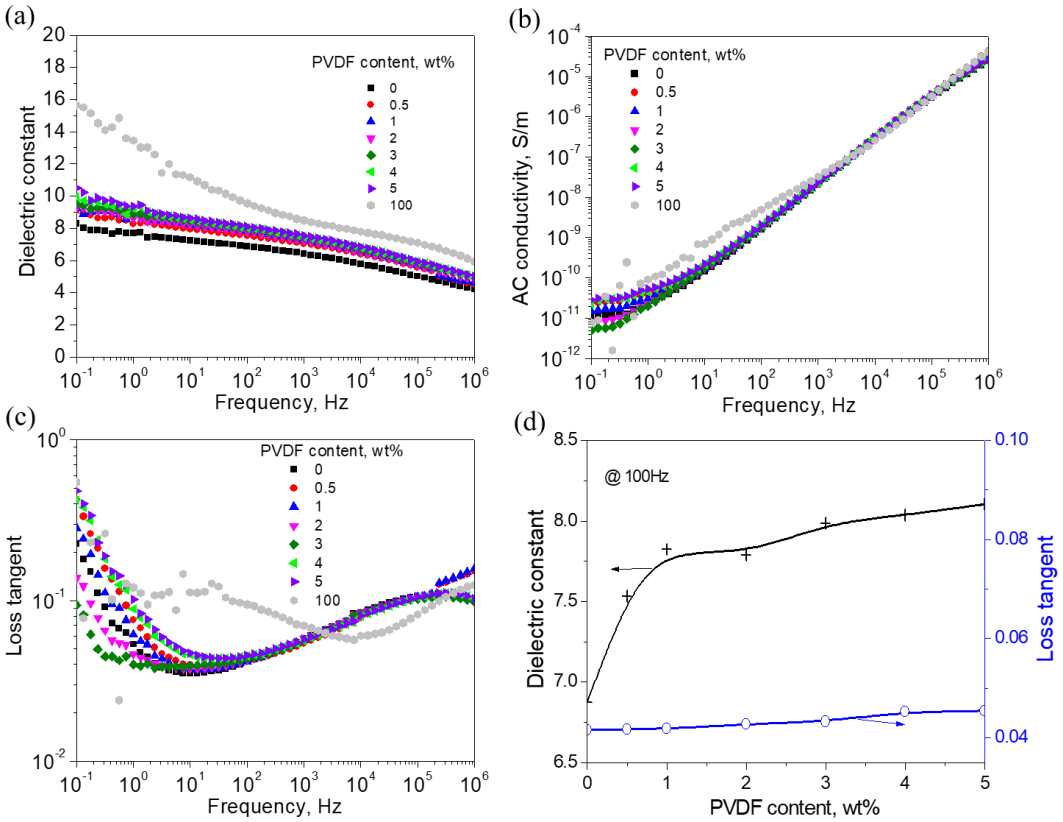

Figure 2-8. (a) The dielectric constant, (b) AC conductivity, and (c) loss tangent of PVDF/PVA films as a function of frequency at room temperature, (d) dielectric constant and loss tangent at 100 Hz vary with PVDF nanoparticle loading.

By contrast, large interface areas can be generated upon the addition of even a small amount of nanofillers, and induce substantial effects in polymer matrices. We characterized the crystalline structure changes of PVA by XRD and DSC (**Figure 2-9**). The degree of crystallinity is determined by evaluating the enthalpy of fusion and comparing it to the enthalpy of fusion of 100% crystalline PVA. The calorimetric crystalline is defined as:

$$X_c(\%)=\Delta H_c/((1-\Phi)\cdot\Delta H_m)\times 100 \qquad (2\text{-}7)$$

where X_c is the weight fraction of crystallinity, Φ is the weight fraction of PVDF in composites, ΔH_c is the enthalpy of fusion at the melting point for each sample, ΔH_m is the enthalpy of fusion of the totally crystalline polymer measured at the equilibrium melting point and equal to 138.6 J/g for PVA. PVDF nanoparticle exhibits strong nucleation ability, substantially increasing the crystallinity of PVA (**Figure 2-9**b). In addition, DSC curves of pure PVDF latex film were also recorded and shown in **Figure 2-9**(c). It is found that the PVDF latex is in an amorphous

phase. Typical PVDF-HFP film was also cast from its DMF solution for comparison purposes. Typical peaks corresponding to the melting and crystallization are observed, giving a melt temperature of 134.9℃ and crystallinity of about 8.95%. Therefore, it is concluded that the improved crystallinity in the PVA/PVDF composites is only associated with the PVA matrix, which is a result of the nucleation effect of PVDF nanoparticles. No crystalline structure formed in the PVDF phase.

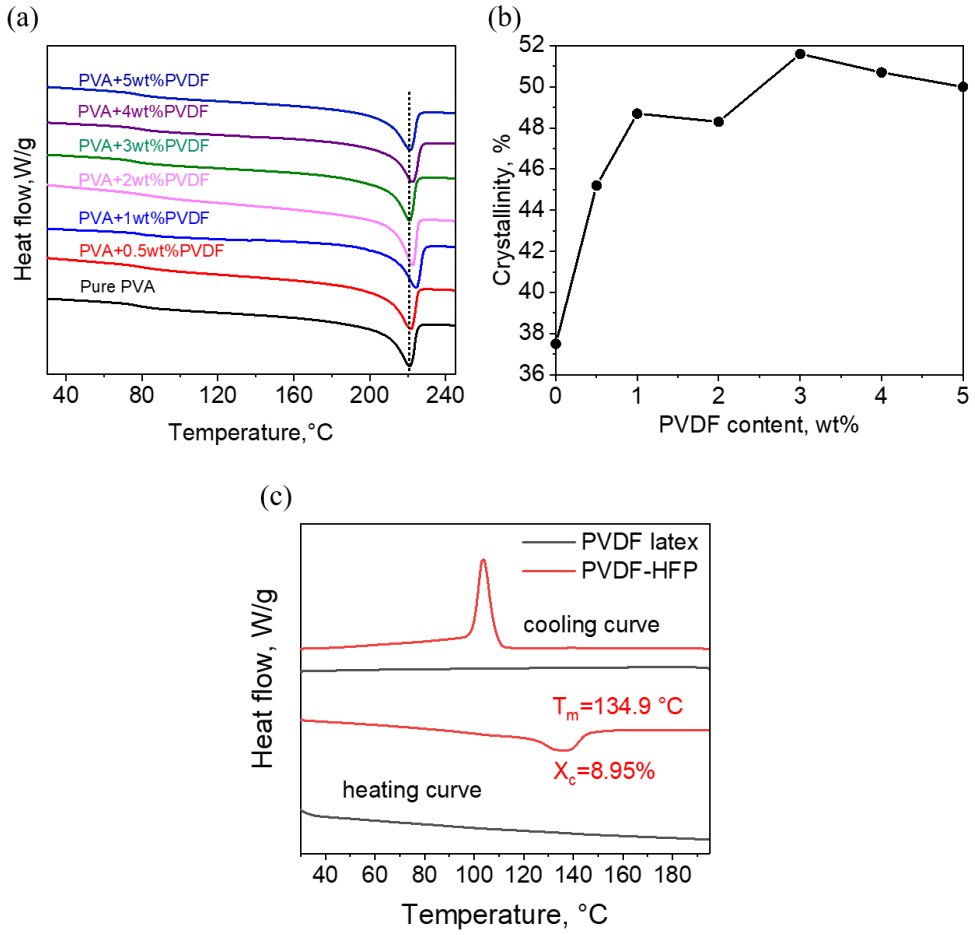

Figure 2-9. (a) DSC curves and (b) the degree of crystallinity of pure PVA and its composites with various PVDF loadings. (c) DSC curves of PVDF latex film and typical PVDF-HFP film prepared via solution casting.

Moreover, the size of crystalline domains has been shown to be also correlated to the dielectric properties of ferroelectric materials[41]. XRD was performed on PVA/PVDF composites to reveal the variation in the size of the crystalline domains in the PVA matrix (**Figure 2-10**). The average size of crystallites is estimated from the Scherrer equation:

$$D=K\lambda/B\cos\theta \quad (2.8)$$

where *D* is the mean size of the crystalline domains. *K* is the shape factor, which has a typical value of about 0.9. λ is the X-ray wavelength. In our case, it is 0.15418 nm. *B* is line broadening at half the maximum intensity (FWHM, in radians). θ is the Bragg angle. The addition of PVDF nanoparticles enhances the crystallinity but does not change the size of the crystallites. The dielectric constant curve presented in **Figure 2-8** (d) resembles the crystallinity curve shown in **Figure 2-9** (b), revealing the correlation between the crystalline structures and the dielectric constant in PVA films. The increased crystallinity makes the dipoles more strongly coupled, resulting in higher dielectric permittivity.

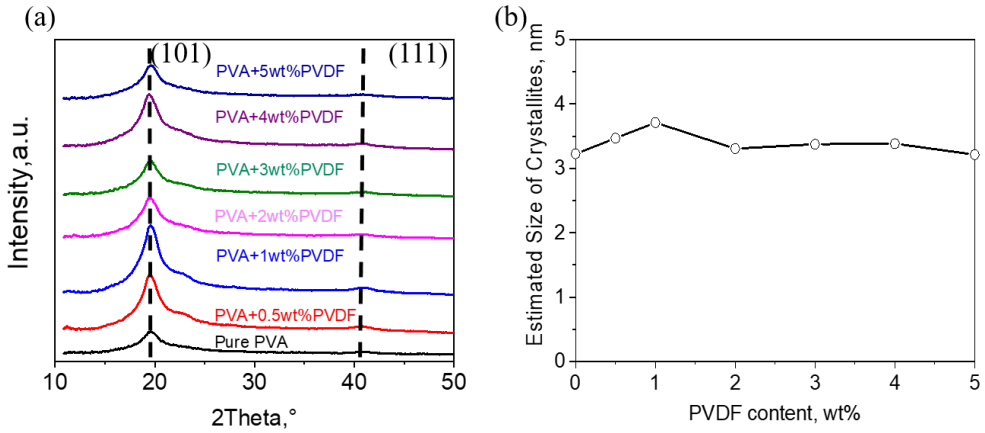

Figure 2-10. (a) XRD patterns of pure PVA and its composites with various PVDF loadings. (b) Estimated size of crystallites of PVA as a function of PVDF loading.

This mechanism can be also supported by the experimental results observed by Zhang et al[42]. in poly(arylene ether urea)/alumina nanocomposites. The introduction of a trace amount (0.21 vol%) of 20-nm-sized alumina nanoparticles can lead to a more than 50% increase in the dielectric constant, as shown in **Figure 2-11** (a). At this optimum concentration, the breakdown strength increases by 46% as compared to the polymer matrix (**Figure 2-11**b). As evidenced by the results of the XRD and DSC characterizations, these desirable dielectric properties are ascribed to the highest degree of crystallinity and the lowest size of crystallites (**Figure 2-11**c, d). It is intriguing that the principle validated in the ceramic nanofiller/polymer composites can be extended to the all-organic polymer composites with a relatively larger nanoparticle size (150 nm).

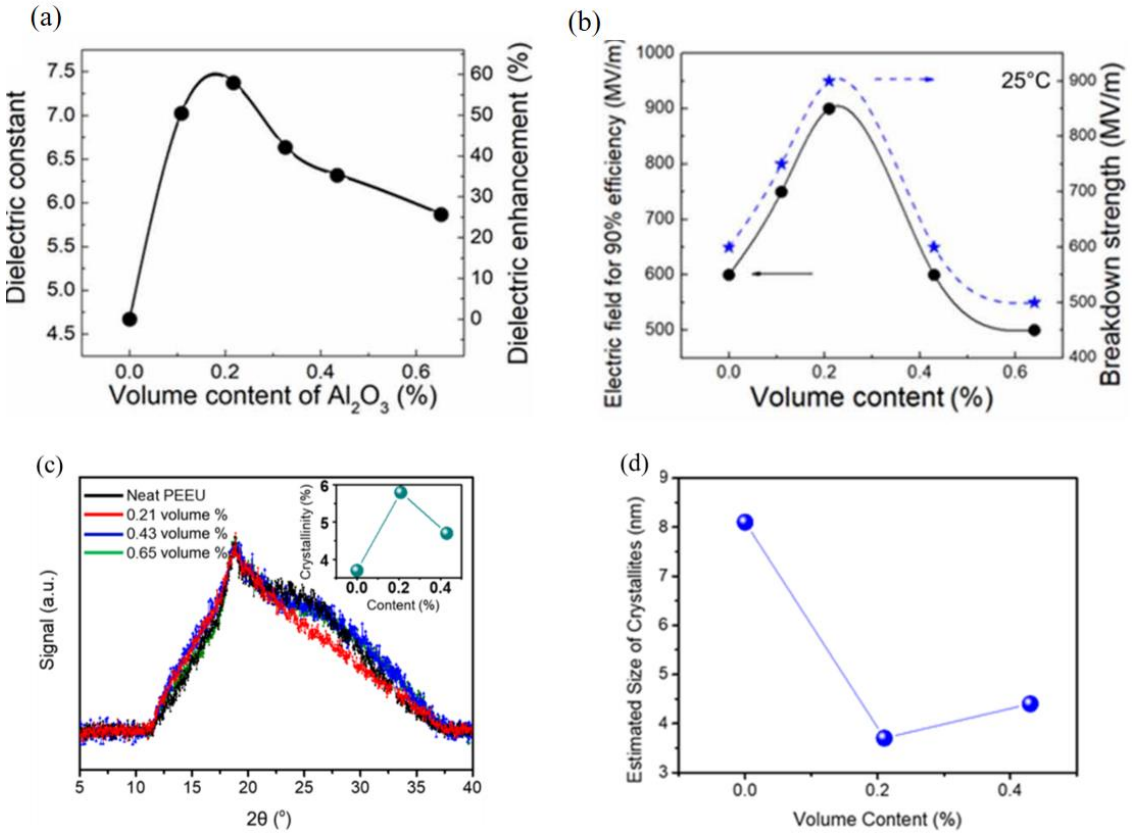

Figure 2-11. (a) The dielectric constant and (b) breakdown strength of PEEU composites with a trace amount of alumina nanoparticles. (c) Wide-angle XRD for PEEU with different alumina nanofiller loadings. The inset presents the crystallinity versus the filler content. (d) Estimated size of crystallites of PEEU with various content of 20-nm alumina[42].

Similar phenomenons were also observed in PEI composites based on different ceramic nanofiller with sizes below 100 nm, such as Al_2O_3, BN, MgO, SiO_2, and $BaTiO_3$ nanoparticles[43]. For example, a small amount of Al_2O_3 with a diameter of 20 nm improved the dielectric constant of the composites and the highest value was achieved at 0.32 vol%, as shown in **Figure 2-12** (a). The achieved dielectric constants of PEI/Al_2O_3 composites are much higher than those predicted by the widely accepted dielectric composites models. Generally, the rigid structure of the pure PEI polymer (T_g ~217°C) glass imposes constraints on the responses of the dipoles to the applied electric fields and leads to the permittivity of only 3. However, the introduction of a trace amount of ceramic nanofillers can significantly reduce such constraints on the dipoles in the glassy state because of the changes in the dynamics of PEI segments near particle interfaces. The extremely small size of the fillers enables the generation of large interfacial areas at a very low filler content because of the huge surface-area-to-volume ratio.

Eventually, a higher dielectric response can be achieved without the penalty of high dielectric loss[43]. Moreover, this principle has been validated in different nanosized Al_2O_3 as presented in **Figure 2-12** (b). However, the dielectric constant decreased with further increasing ceramic particles because of the overlapping of interfacial regions due to the decreased distance between the adjacent particles. But such a trend is not found in our PVDF latex particles filled composites, which is probably compensated by the polarization induced by the counter ions in composites with filler content beyond 3%.

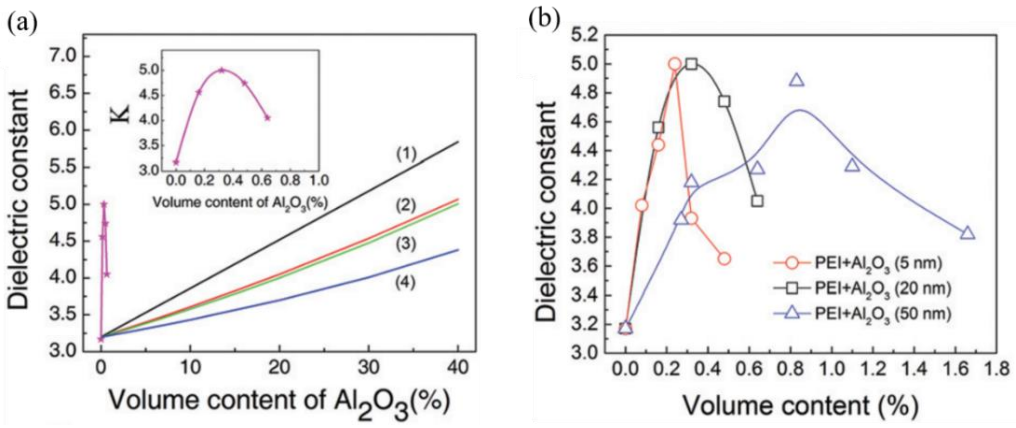

Figure 2-12. (a) Dielectric constant (@1 kHz) of nanocomposite of PEI/alumina (20 nm particle size) composites as a function of the nanofiller volume content. The variation of dielectric constant is compared with several widely applied dielectric composite models (lines with no data points): curves: (1) parallel model, (2) Maxwell model, (3) Lichtenecker model, and (4) series model. Inset shows an expanded view of the dielectric constants of the composite films vs. alumina loading. (b) Effect of nanofiller size on the dielectric response (@ 1 kHz) of PEI/alumina composite films vs. filler volume content[43].

2.3.3 Dielectric Breakdown Strength of PVDF/PVA Films

For a linear dielectric, the dielectric constant is independent of the applied electric field. Consequently, the energy density U_e is linearly proportional to the production of permittivity and the square of the electric field. Several reports show that the addition of high-permittivity nanoparticles can largely enhance the dielectric constant yet at the expense of the breakdown strength[13, 44]. Due to the quadratic dependence on E_b, the energy density of the composites is however found to be inferior to neat polymers in spite of improved permittivity. It is highly desirable to achieve an E_b that is superior to the neat polymers. The characteristic electric breakdown strengths are generally analyzed with a two-parameter Weibull distribution

function[45] described as equation (1.14). Herein, the E_b and β are calculated from a linear fitting using Weibull failure statistics (**Figure 2-13**), and the values are listed in **Table 2-1**. The high β values indicate the structural uniformity and integrity of the investigated composite films. The E_b of pure PVDF and PVA films are 222.6 MV/m and 437.9 MV/m, respectively. It is noted that the breakdown strength of PVDF latex film is lower than that (350-400 MV/m) of typical PVDF films that are solution-casted or melt-extruded[32-34, 46]. The discrepancy arises from the film processing. In the present case, the wet thin film containing suspended colloidal PVDF nanoparticles is dried on a substrate, and the evaporation of water concentrates the nanoparticles into a closed-packed array. The capillary pressures created by liquid menisci between colloidal particles lead to the cracking of the dried film[6]. Without any additive, it is difficult, if not possible, to obtain a uniform large-area PVDF film without microcracks. It is such morphological defects coupled with the effect of counter ions that weaken the capability of the obtained dry films to sustain a high electric field.

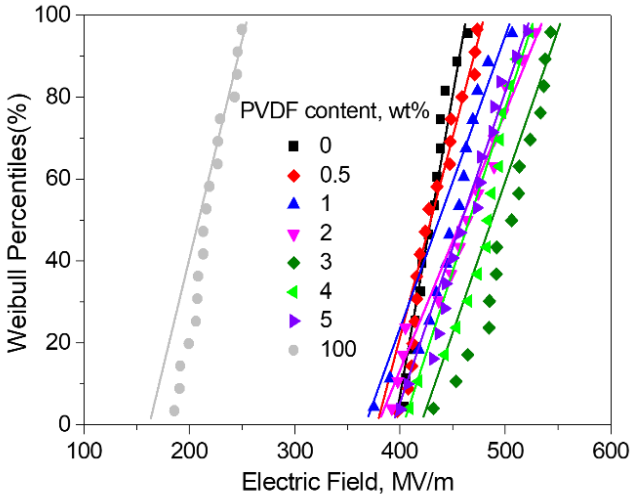

Figure 2-13. Failure probability of dielectric breakdown deduced from Weibull distribution for neat PVA, PVDF and their composites with various PVDF particle loadings.

By contrast, the introduction of a small amount of PVDF nanoparticles into PVA does not deteriorate but greatly promotes the breakdown strength of the PVA matrix. The breakdown strengths of all the polymer composites are superior to that of PVA. At an optimum PVDF content (3 wt%), a maximum breakdown strength reaches 514.7 MV/m, showing an

improvement of 18%. Similar enhancements have been also observed in polymer composites filled with high-permittivity yet low-E_b ceramic nanofillers at low filler loadings[42, 47-50]. The addition of even a small amount of nanofiller can chemically or physically form large-area interfaces between nanoparticles and their surrounding polymers in a nanocomposite[1, 12, 21, 48, 51-52]. The dielectric properties of the interfacial regions can slightly differ from either the nanoparticle or the bulk polymer matrix.[2, 50] They have been proven capable of suppressing space charges as deep trapping sites at high electric fields, and limit thereby the probability for breakdown[47-48, 50]. Actually, the breakdown strength enhances with increasing the interfacial area as a result of adding nanoparticles. Nevertheless, beyond a certain filler content (in our case, 3 wt%), the interfacial regions surrounding nanoparticles would percolate and thus carriers can transport instead of being restrained in the interfacial regions. The density and mobility of carrier increases in the composites, leading to a decrement in breakdown strength[47-48, 50] (**Figure 2-13**, **Table 2-1**). Here, such effect of generated interfaces is also validated in a composite even composed of two polymeric phases with moderate permittivity and conductivity contrast.

Table 2-1. The E_b and β of pure PVA, PVDF, and their composites at various mass ratios

PVDF content (wt%)	E_b (MV/m)	β
0	437.9	25.2
0.5	444.5	19.1
1.0	461.5	15.3
2.0	479.4	12.5
3.0	514.7	19.5
4.0	499.9	18.8
5.0	477.8	15.6
100	222.6	12.4

In addition, previous theoretic simulations[53] and experiment work[42, 54] show that elevated crystallinity in semicrystalline polymers can substantially limit the high-field conduction losses by reducing the mean free path for the mobile charge. As compared to virgin PVA, the improved crystallinity of PVA composites shown in **Figure 2-9** (b) should be also responsible

for the augmentation of the breakdown strength. It should be noted that the enhancements in both the dielectric constant and breakdown field in composites with inorganic nanoparticles occur in an extremely narrow nanofiller composition range[42, 47-50]. By contrast, our composites with PVDF loading ranging from 0 to 5 wt% can exhibit improved breakdown strength as compared to the virgin PVA. This feature allows for a much wider operation window for the preparation of high-E_b PVA composites.

2.3.4 Energy Density of Nanocomposite Films

We first compare the *P-E* loops of different films up to a given electric field which approaches the breakdown strength of pure PVDF film. As shown in **Figure 2-14** (a)**,** being similar to the trend observed for the dielectric constant in **Figure 2-8** (a), all the P_{max} of the composites fall into the interval of the two single polymer components. Nevertheless, the *P-E* loops of all the composites are much slimmer than those of pure PVDF and PVA, indicating that the introduction of PVDF nanoparticles could effectively constrain the movement of free charge carriers, resulting in reduced conduction losses at high fields.

It is particularly interesting to investigate the polarization of composite with 3 wt% PVDF at a much higher electrical field as it shows the highest breakdown strength. With increasing the electric field, the P_{max} increases yet the composites show higher losses at higher fields in **Figure 2-14** (b), which is a result of the ferroelectric losses of PVDF nanodomains and the bulk conduction losses of PVA matrix[28]. Based on the *P-E* loops of pure PVDF, PVA, and their composites at different fields until their breakdown strength, the discharged energy density is calculated and shown in **Figure 2-14** (c). Apparently, below ~250 MV/m, pure PVDF film shows the maximum energy density U_e=3.4 J/cm^3, while all the energy densities of PVDF/PVA composites are inferior to this value but still higher than that of pure PVA films. Intriguingly, the energy density of the composite with 3 wt% of PVDF reaches 8.1 J/cm^3 at 510 MV/m, which is three folds higher than that (U_e=2.4 J/cm^3) of neat PVA, demonstrating a synergistic effect by coupling PVDF and PVA.

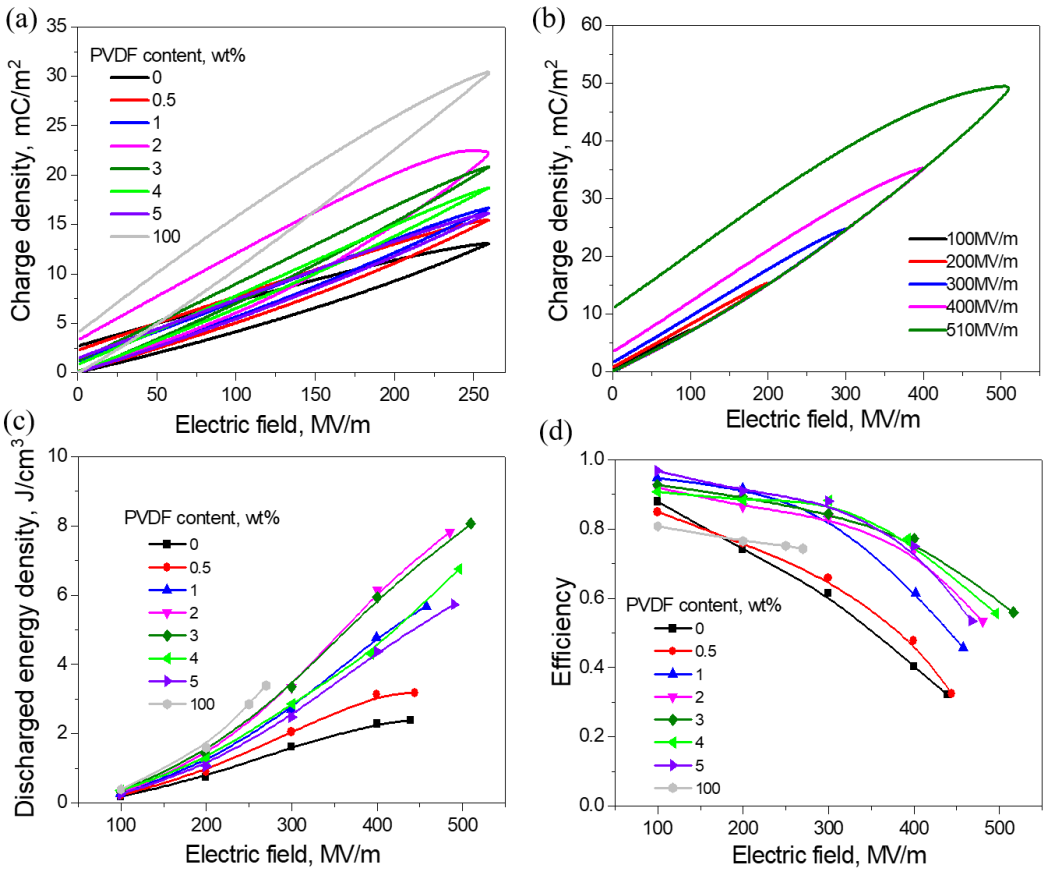

Figure 2-14. (a) *P-E* loops of pure PVA, PVDF and PVDF/PVA nanocomposite films with various PVDF contents. (b) *P-E* loops of PVA nanocomposite films with 3 wt% PVDF at different electric fields. (c) The discharged energy density and (d) charge/discharge efficiency as a function of electric field for pure PVA, PVDF, and PVDF/PVA nanocomposite films.

For practical applications, it is also important to evaluate the charge/discharge efficiency (η), which is defined as equation (1.20). U_1 is calculated by the numerical integration of the closed area of the hysteresis *P-E* loops. As shown in **Figure 2-14** (d), the efficiency of all the films decreases with the applied electric field, because of the more pronounced ferroelectric and conduction losses at higher fields. It is clearly shown that the efficiency is enhanced with the introduction of PVDF nanoparticles as compared to neat PVA films. This is another evidence of the charge carrier constraint via the incorporation of a small amount of PVDF nanoparticles. Consequently, at the maximum electric field, the efficiency of 3 wt% nanocomposites is about 0.6, higher than that (~0.3) of neat PVA. The energy storage performances of pure PVA and its composites have been summarized and shown in **Figure 2-15** as a function of PVDF content.

The overall desirable high-field properties demonstrate the great potential of PVDF/PVA composites for dielectric energy storage applications. The maximum breakdown strength of PVDF/PVA composites can compare with most previously reported all-polymeric dielectric materials, as listed in **Table 2-2**.

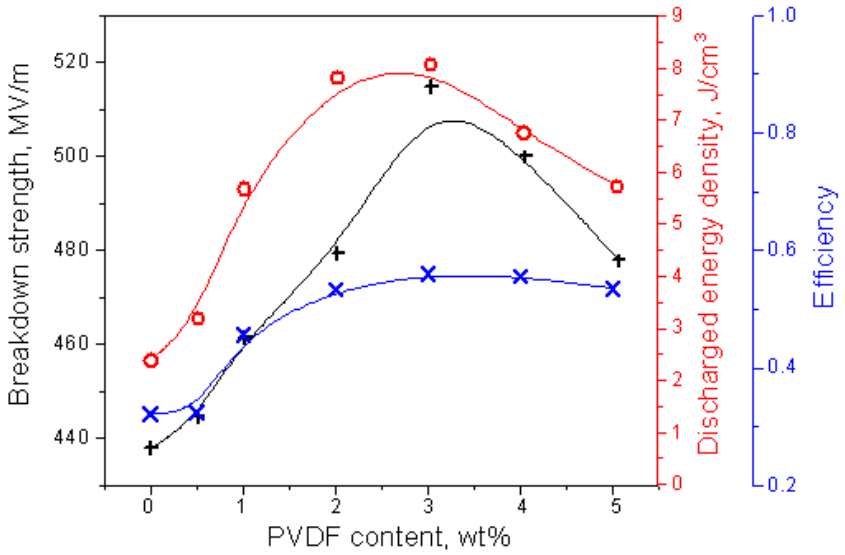

Figure 2-15. The breakdown strength, discharged energy density, and charge/discharge efficiency as a function of PVDF content for the PVDF/PVA composite films. The discharged energy density and the charge/discharge efficiency were measured at the maximum electric field that they can sustain before electrical breakdown.

The improvement of energy density (defined as U_e/U_m, where U_m is the discharged energy density of base materials) is much higher than those of the reported polymeric dielectrics. The charge/discharge efficiency (60%) is relatively lower than its counterparts. However, it should be noted that most polymeric dielectrics are either melt-extruded at high temperatures or solution-processed in harmful organic solvents. Our strategy relies on an environmental-benign process, and has great promise for the "green" manufacturing of next-generation polymeric dielectrics.

Table 2-2. Comparison of the energy storage performances of polymeric materials.

Materials	Processing methods	E_b MV/m	U_e J/cm^3	U_e/U_m	η
MBS/PVDF[32] *a*	solution casting in DMF*j*	535	9.8	2.2	62%
TPU/PVDF[34] *b*	solution casting in DMF	538	10.4	2.3	n/a
PET/PVDF[33]	melt-mixing and hot-pressing	453	7	1.6	n/a
P(VDF-TrFE-CFE)/PVDF[55] *c*	solution casting in DMF	665	19.6	1.6	n/a
PET/PMMA/P(VDF-HFP) multilayer film[37] *d*	melt coextruding	1000	17.4	1.5	n/a
PC/PVDF layered film[36]	melt coextruding	650	11	1.8	60%
P(VDF-HFP)/PMMA[30] *e*	Solution casting in DMAC*k*	475	11.2	2.6	86%
P(VDF-CTFE)-*g*-PS copolymer[56] *f*	grafting copolymerization and solution casting in THF*l*	520	12	1.2	70%
P(VDF-TrFE-CTFE)-*g*-PMMA copolymer[57] *g*	grafting copolymerization and solution casting in DMF	500	10.5	2.6	70%
Bis(double-stranded) Block Copolymer[58]	tandem metathesis polymerization and solution casting in organic solvents	370	9.9	n/a	84%
PMGS-ArTU[59] *h*	polymerization and solution casting in DMF	419	3.2	n/a	87%
c-BCB/BNNS8 [i]	Drop casting from DMM*m* solution and thermally crosslinking	447	2.5	n/a	95%
$BaTiO_3$@TiO_2/P(VDF-HFP)[60]	Solution casting in DMF	500	9.95	1.3	65%
PVDF latex/PVA	Water-based process	514	8.1	3.4	60%

2.3.5 Power Density of Nanocomposite Films

In addition to the high energy density, power energy storage requires a fast discharge rate[14-15, 61]. We used a high-speed capacitor discharge circuit as shown in **Figure 1-8** (a) with a high-voltage MOSFET (metal oxide semiconductor field effect transistor) switch to measure the discharge speed of the nanocomposites with 3 wt% PVDF and commercial BOPP films. Both samples were first charged at 200 MV/m, followed by discharging across a 10 kΩ load resistor in series with the polymer capacitor. The voltage $U(t)$ across the load resistor (R_L) decreases exponentially with time. The discharging curves are shown in **Figure 2-16**(a).

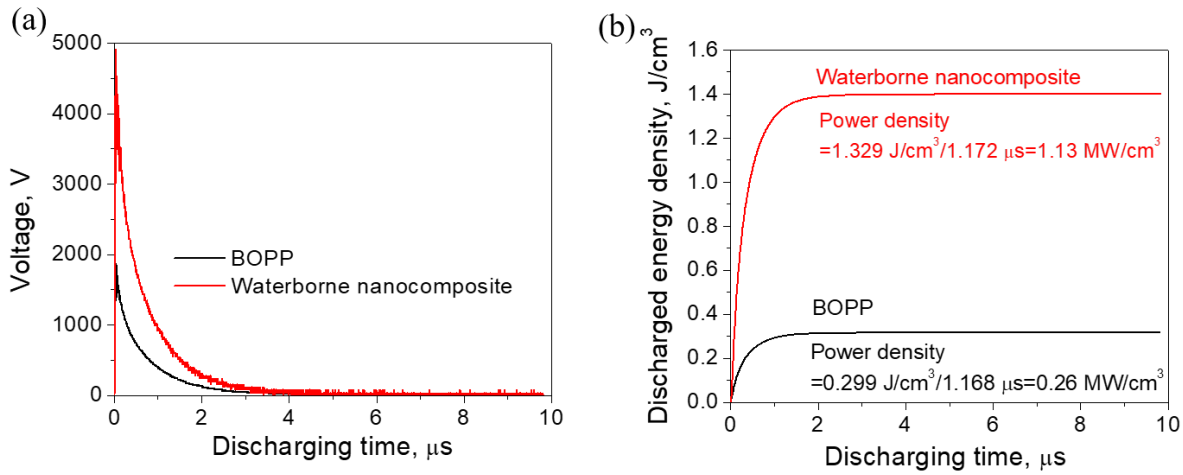

Figure 2-16. The voltage (a) and discharged energy density (b) as a function of time. The BOPP and waterborne nanocomposite films (3 wt% of PVDF) have respectively a thickness of 9.8 μm and 24 μm, which show capacitance of 45 pF and 59 pF respectively. The deduced $R_L C$ values, therefore, are 0.59 μs and 0.45 μs for waterborne nanocomposite and BOPP films respectively.

The fitting to the discharging curves by the equation $U(t) = U_0 e^{-(\frac{t}{\tau})}$ yields the time constant τ. For the waterborne nanocomposite shown in **Figure 2-17** (a-c), obtained τ varies from 0.40 μs to 0.63 μs broadening the fitting time range. Likewise, the τ of the BOPP film capacitor varies from 0.38 μs to 0.65 μs, as shown in **Figure 2-17** (d-f). The change of τ obtained from the fitting to different time ranges can be associated with the increased effect of Equivalent Series Resistor (ESR) of samples at later discharge process[14]. Both sample capacitors have a nearly identical time constant for a given fitting time range, which actually allows for fairly comparing their power densities.

Based on the discharging curves, the instant power P_e can be calculated by equation (1.21) and the discharged energy density U_e of the dielectric material is further calculated by equation (1.22). The calculated energy density is plotted in **Figure 2-16** (b) as a function of time**.** The discharge time is defined here as the time that is needed to reach 95% of the final discharge energy in a load resistor[62]. In this regard, the nanocomposite releases stored energy of 1.329 J/cm^3 at a rate of 1.172 μs, while the rate for BOPP is 1.168 μs for releasing stored energy of 0.299 J/cm^3. Accordingly, the waterborne nanocomposite shows a superior power density of 1.13 MW/cm^3 to that of BOPP (0.26 MW/cm^3).

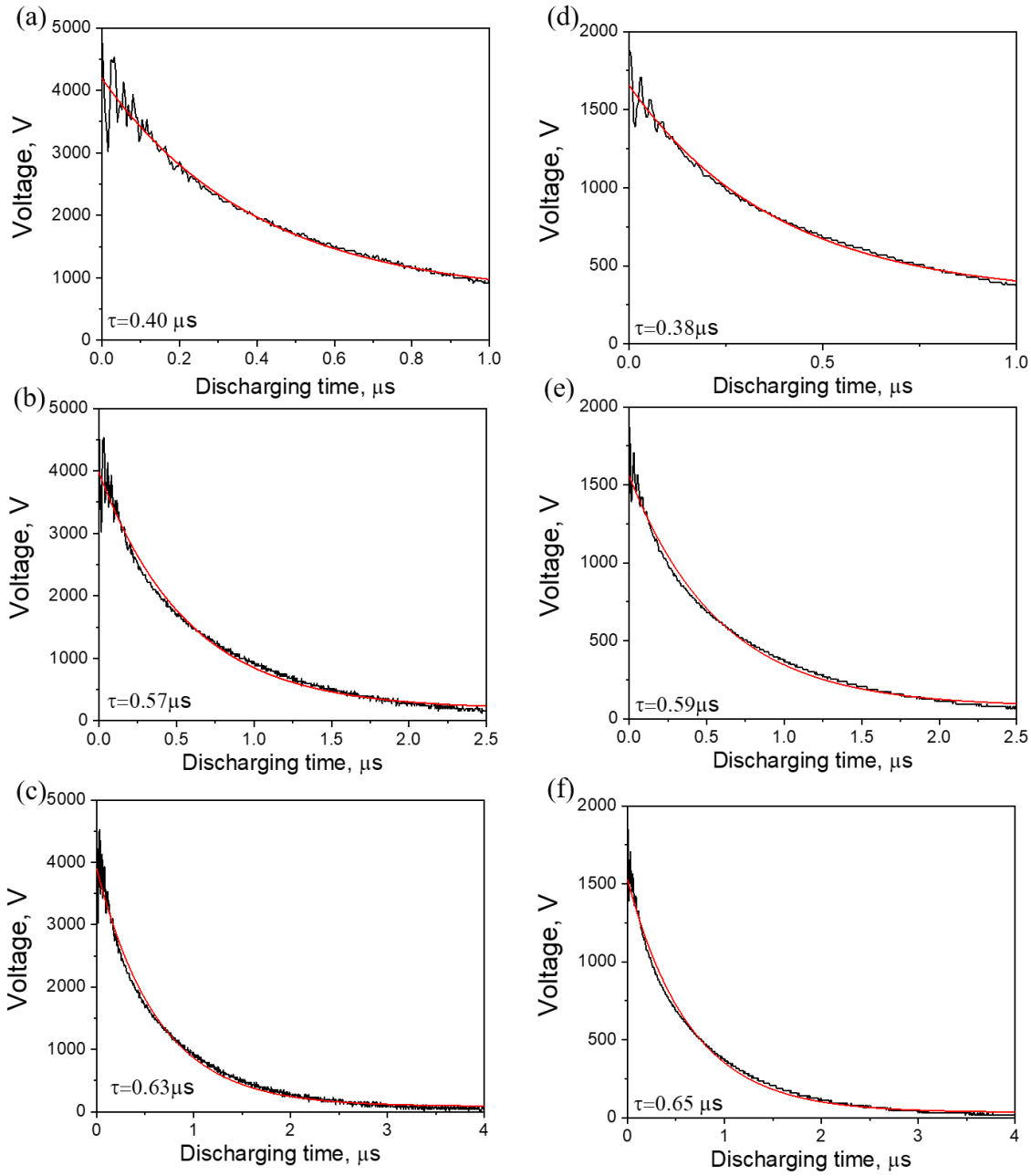

Figure 2-17. Fitting of the discharging voltage as a function of time for (a-c) waterborne nanocomposite as well as (d-f) commercial BOPP film. The τ yielded from the fitting is indicated in the figure. Red curves are the fitting and black curves are the experimental data.

In addition, the stability of the material is also a very important indicator for further application. The cyclic charge/discharge was performed on both samples under an applied field of 200 MV/m to evaluate the stability of the materials. As shown in **Figure 2-18**, like BOPP, the energy storage density of the material remains almost constant and there is no degradation over 1000 cycles of charge/discharge of the waterborne nanocomposites with 3 wt% PVDF.

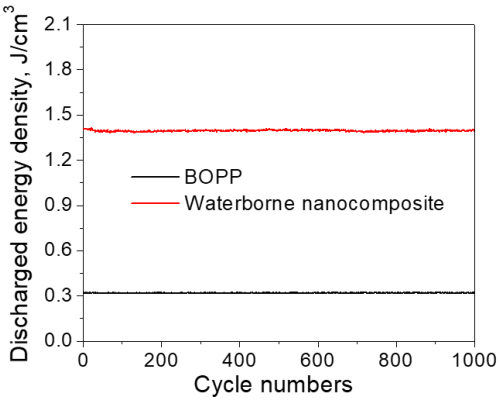

Figure 2-18. Cyclic charge/discharge performances of both samples at 200 MV/m.

2.4 Conclusion

In this chapter, waterborne polymer nanocomposites are prepared by mixing low-cost PVDF latex and water-soluble polymer PVA, followed by a solution-casting method under infrared light evaporation. Compared with pure PVA films, the electric displacement at high electric fields is enhanced in composites due to the introduction of the highly polarizable PVDF nanodomains. Moreover, due to the boosted crystallinity of PVA induced by the incorporated PVDF latex particles and charge carrier constraint in the PVA matrix, the nanocomposite with optimum PVDF content (3 wt%) shows a breakdown strength as high as 515 MV/m and an energy density of 8.1 J/cm^3, which respectively show improvements by 18% and 238% as compared with pure PVA films. The waterborne nanocomposites with a microsecond discharge rate generate a power density on the level of 1.1 MW/cm^3. In this chapter, the introduction of PVDF latex indeed improved the dielectric properties and energy storage performance at a low filler loading. It is anticipated that this work opens an environmentally begin route to boost the energy storage performances of polymer nanocomposites.

References

1. Dang, Z. M.; Yuan, J. K.; Yao, S. H.; Liao, R. J., Flexible nanodielectric materials with high permittivity for power energy storage. *Advanced Materials* **2013,** *25* (44), 6334-6365.
2. Gür, T. M., Review of electrical energy storage technologies, materials and systems: challenges and prospects for large-scale grid storage. *Energy & Environmental Science* **2018,** *11* (10), 2696-2767.
3. Pan, H.; Ma, J.; Ma, J.; Zhang, Q.; Liu, X.; Guan, B.; Gu, L.; Zhang, X.; Zhang, Y.-J.; Li, L., Giant energy density and high efficiency achieved in bismuth ferrite-based film capacitors via domain engineering. *Nature communications* **2018,** *9* (1), 1-8.

4. Riggs, B. C.; Elupula, R.; Grayson, S. M.; Chrisey, D. B., Photonic curing of aromatic thiol–ene click dielectric capacitors via inkjet printing. *Journal of Materials Chemistry A* **2014,** *2* (41), 17380-17386.
5. Riggs, B. C.; Elupula, R.; Rehm, C.; Adireddy, S.; Grayson, S. M.; Chrisey, D. B., Click-in ferroelectric nanoparticles for dielectric energy storage. *ACS Applied Materials & Interfaces* **2015,** *7* (32), 17819-17825.
6. Torres-Canas, F.; Yuan, J.; Ly, I.; Neri, W.; Colin, A.; Poulin, P., Inkjet printing of latex-based high-energy microcapacitors. *Advanced Functional Materials* **2019,** *29* (31), 1901884.
7. Li, Q.; Chen, L.; Gadinski, M. R.; Zhang, S.; Zhang, G.; Li, H. U.; Iagodkine, E.; Haque, A.; Chen, L.-Q.; Jackson, T. N., Flexible high-temperature dielectric materials from polymer nanocomposites. *Nature* **2015,** *523* (7562), 576-579.
8. Zhang, X.; Shen, Y.; Xu, B.; Zhang, Q.; Gu, L.; Jiang, J.; Ma, J.; Lin, Y.; Nan, C. W., Giant energy density and improved discharge efficiency of solution-processed polymer nanocomposites for dielectric energy storage. *Advanced Materials* **2016,** *28* (10), 2055-2061.
9. Huan, T. D.; Boggs, S.; Teyssedre, G.; Laurent, C.; Cakmak, M.; Kumar, S.; Ramprasad, R., Advanced polymeric dielectrics for high energy density applications. *Progress in Materials Science* **2016,** *83*, 236-269.
10. Luna, A.; Yuan, J.; Neri, W.; Zakri, C.; Poulin, P.; Colin, A., Giant permittivity polymer nanocomposites obtained by curing a direct emulsion. *Langmuir : the ACS journal of surfaces and colloids* **2015,** *31* (44), 12231-12239.
11. Yuan, J.; Yao, S.; Li, W.; Sylvestre, A.; Bai, J., Anisotropic percolation of SiC–carbon nanotube hybrids: a new route toward thermally conductive high-k polymer composites. *The Journal of Physical Chemistry C* **2017,** *121* (22), 12063-12070.
12. Chen, Q.; Shen, Y.; Zhang, S.; Zhang, Q., Polymer-based dielectrics with high energy storage density. *Annual review of materials research* **2015,** *45*, 433-458.
13. Fan, B.; Zhou, M.; Zhang, C.; He, D.; Bai, J., Polymer-based materials for achieving high energy density film capacitors. *Progress in Polymer Science* **2019,** *97*, 101143.
14. Chu, B.; Zhou, X.; Ren, K.; Neese, B.; Lin, M.; Wang, Q.; Bauer, F.; Zhang, Q., A dielectric polymer with high electric energy density and fast discharge speed. *Science* **2006,** *313* (5785), 334-336.
15. Wang, Y.; Zhou, X.; Chen, Q.; Chu, B.; Zhang, Q., Recent development of high energy density polymers for dielectric capacitors. *IEEE Transactions on Dielectrics and Electrical Insulation* **2010,** *17* (4), 1036-1042.
16. Zhang, Q.; Bharti, V.; Zhao, X., Giant electrostriction and relaxor ferroelectric behavior in electron-irradiated poly (vinylidene fluoride-trifluoroethylene) copolymer. *Science* **1998,** *280* (5372), 2101-2104.
17. Xia, F.; Cheng, Z. Y.; Xu, H.; Li, H.; Zhang, Q.; Kavarnos, G. J.; Ting, R. Y.; Abdul-Sadek, G.; Belfield, K. D., High electromechanical responses in a poly (vinylidene fluoride–trifluoroethylene–chlorofluoroethylene) terpolymer. *Advanced Materials* **2002,** *14* (21), 1574-1577.
18. Yuan, J.; Luna, A.; Neri, W.; Zakri, C.; Schilling, T.; Colin, A.; Poulin, P., Graphene liquid

crystal retarded percolation for new high-k materials. *Nature communications* **2015,** *6* (1), 1-8.

19. Yuan, J.; Luna, A.; Neri, W.; Zakri, C.; Colin, A.; Poulin, P., Giant electrostriction of soft nanocomposites based on liquid crystalline graphene. *ACS nano* **2018,** *12* (2), 1688-1695.
20. Huang, X.; Jiang, P., Core–shell structured high-k polymer nanocomposites for energy storage and dielectric applications. *Advanced Materials* **2015,** *27* (3), 546-554.
21. Luo, H.; Zhou, X.; Ellingford, C.; Zhang, Y.; Chen, S.; Zhou, K.; Zhang, D.; Bowen, C. R.; Wan, C., Interface design for high energy density polymer nanocomposites. *Chemical Society Reviews* **2019,** *48* (16), 4424-4465.
22. Zhang, X.; Li, B. W.; Dong, L.; Liu, H.; Chen, W.; Shen, Y.; Nan, C. W., Superior energy storage performances of polymer nanocomposites via modification of filler/polymer interfaces. *Advanced Materials Interfaces* **2018,** *5* (11), 1800096.
23. Niu, Y.; Wang, H., Dielectric nanomaterials for power energy storage: surface modification and characterization. *ACS Applied Nano Materials* **2019,** *2* (2), 627-642.
24. Seiler, J.; Kindersberger, J., Insight into the interphase in polymer nanocomposites. *IEEE Transactions on Dielectrics and Electrical Insulation* **2014,** *21* (2), 537-547.
25. Pan, Z.; Yao, L.; Zhai, J.; Yao, X.; Chen, H., Interfacial coupling effect in organic/inorganic nanocomposites with high energy density. *Advanced materials* **2018,** *30* (17), 1705662.
26. Tang, H.; Lin, Y.; Sodano, H. A., Synthesis of high aspect ratio BaTiO3 nanowires for high energy density nanocomposite capacitors. *Advanced Energy Materials* **2013,** *3* (4), 451-456.
27. Zhu, Y.; Zhu, Y.; Huang, X.; Chen, J.; Li, Q.; He, J.; Jiang, P., High energy density polymer dielectrics interlayered by assembled boron nitride nanosheets. *Advanced Energy Materials* **2019,** *9* (36), 1901826.
28. Guo, M.; Jiang, J.; Shen, Z.; Lin, Y.; Nan, C.-W.; Shen, Y., High-energy-density ferroelectric polymer nanocomposites for capacitive energy storage: enhanced breakdown strength and improved discharge efficiency. *Materials Today* **2019,** *29*, 49-67.
29. Baer, E.; Zhu, L., 50th anniversary perspective: dielectric phenomena in polymers and multilayered dielectric films. *Macromolecules* **2017,** *50* (6), 2239-2256.
30. Luo, B.; Wang, X.; Wang, H.; Cai, Z.; Li, L., P (VDF-HFP)/PMMA flexible composite films with enhanced energy storage density and efficiency. *Composites Science and Technology* **2017,** *151*, 94-103.
31. Jiang, J.; Shen, Z.; Qian, J.; Dan, Z.; Guo, M.; Lin, Y.; Nan, C.-W.; Chen, L.; Shen, Y., Ultrahigh discharge efficiency in multilayered polymer nanocomposites of high energy density. *Energy Storage Materials* **2019,** *18*, 213-221.
32. Zheng, M.-S.; Zha, J.-W.; Yang, Y.; Han, P.; Hu, C.-H.; Dang, Z.-M., Enhanced breakdown strength of poly (vinylidene fluoride) utilizing rubber nanoparticles for energy storage application. *Applied Physics Letters* **2016,** *109* (7), 072902.
33. Yao, L.; Wang, D.; Hu, P.; Han, B. Z.; Dang, Z. M., Synergetic Enhancement of Permittivity and Breakdown Strength in All-Polymeric Dielectrics toward Flexible Energy Storage Devices. *Advanced Materials Interfaces* **2016,** *3* (13), 1600016.
34. Zheng, M.-S.; Zha, J.-W.; Yang, Y.; Han, P.; Hu, C.-H.; Wen, Y.-Q.; Dang, Z.-M.,

Polyurethane induced high breakdown strength and high energy storage density in polyurethane/poly (vinylidene fluoride) composite films. *Applied Physics Letters* **2017,** *110* (25), 252902.

35. Wolak, M. A.; Pan, M.-J.; Wan, A.; Shirk, J. S.; Mackey, M.; Hiltner, A.; Baer, E.; Flandin, L., Dielectric response of structured multilayered polymer films fabricated by forced assembly. *Applied Physics Letters* **2008,** *92* (11), 97.
36. Mackey, M.; Schuele, D. E.; Zhu, L.; Flandin, L.; Wolak, M. A.; Shirk, J. S.; Hiltner, A.; Baer, E., Reduction of dielectric hysteresis in multilayered films via nanoconfinement. *Macromolecules* **2012,** *45* (4), 1954-1962.
37. Yin, K.; Zhou, Z.; Schuele, D. E.; Wolak, M.; Zhu, L.; Baer, E., Effects of interphase modification and biaxial orientation on dielectric properties of poly (ethylene terephthalate)/poly (vinylidene fluoride-co-hexafluoropropylene) multilayer films. *ACS applied materials & interfaces* **2016,** *8* (21), 13555-13566.
38. Alfonso, M. S. Liquid carbon dispersions for energy applications. Bordeaux, 2018.
39. Larson, R. G., Re-Shaping the Coffee Ring. *Angewandte Chemie International Edition* **2012,** *51* (11), 2546-2548.
40. Yuan, J.-K.; Yao, S.-H.; Dang, Z.-M.; Sylvestre, A.; Genestoux, M.; Bai1, J., Giant dielectric permittivity nanocomposites: realizing true potential of pristine carbon nanotubes in polyvinylidene fluoride matrix through an enhanced interfacial interaction. *The Journal of Physical Chemistry C* **2011,** *115* (13), 5515-5521.
41. Zhu, L., Exploring strategies for high dielectric constant and low loss polymer dielectrics. *The journal of physical chemistry letters* **2014,** *5* (21), 3677-3687.
42. Zhang, T.; Chen, X.; Thakur, Y.; Lu, B.; Zhang, Q.; Runt, J.; Zhang, Q., A highly scalable dielectric metamaterial with superior capacitor performance over a broad temperature. *Science advances* **2020,** *6* (4), eaax6622.
43. Thakur, Y.; Zhang, T.; Iacob, C.; Yang, T.; Bernholc, J.; Chen, L.; Runt, J.; Zhang, Q., Enhancement of the dielectric response in polymer nanocomposites with low dielectric constant fillers. *Nanoscale* **2017,** *9* (31), 10992-10997.
44. Roscow, J.; Bowen, C.; Almond, D., Breakdown in the case for materials with giant permittivity? *ACS Energy Letters* **2017,** *2* (10), 2264-2269.
45. Claude, J.; Lu, Y.; Wang, Q., Effect of molecular weight on the dielectric breakdown strength of ferroelectric poly (vinylidene fluoride-chlorotrifluoroethylene) s. *Applied Physics Letters* **2007,** *91* (21), 212904.
46. Fan, B.; Xing, Z.; Bedoui, F.; Yuan, J.; Lu, X.; He, D.; Zhou, M.; Zhang, C.; Dang, Z.; Weigand, S., Improving dielectric strength of polyvinylidene fluoride by blending chains with different molecular weights. *Polymer* **2020,** *190*, 122235.
47. Ding, S.; Yu, S.; Zhu, X.; Xie, S.; Sun, R.; Liao, W.-H.; Wong, C.-P., Enhanced breakdown strength of polymer composites by low filler loading and its mechanisms. *Applied Physics Letters* **2017,** *111* (15), 153902.
48. Li, S.; Yin, G.; Bai, S.; Li, J., A new potential barrier model in epoxy resin nanodielectrics. *IEEE Transactions on Dielectrics and Electrical Insulation* **2011,** *18* (5), 1535-1543.
49. Shen, Z. H.; Wang, J. J.; Lin, Y.; Nan, C. W.; Chen, L. Q.; Shen, Y., High-throughput phase-field design of high-energy-density polymer nanocomposites. *Advanced Materials*

2018, *30* (2), 1704380.

50. Lu, Y.-C.; Yu, S.; Zeng, X.; Sun, R.; Wong, C.-P., High energy density polymer nanocomposites with Y-doped barium strontium titanate nanoparticles as fillers. *IET Nanodielectrics* **2018,** *1* (4), 137-142.
51. Li, S.; Yin, G.; Chen, G.; Li, J.; Bai, S.; Zhong, L.; Zhang, Y.; Lei, Q., Short-term breakdown and long-term failure in nanodielectrics: A review. *IEEE Transactions on Dielectrics and Electrical Insulation* **2010,** *17* (5), 1523-1535.
52. Shen, Y.; Lin, Y.; Zhang, Q., Polymer nanocomposites with high energy storage densities. *Mrs Bulletin* **2015,** *40* (9), 753-759.
53. Xu, C.; Zheng, Z.; Boggs, S. In *Simulation of high field resistive and absorption currents in semicrystalline polymer films*, Conference Record of the 2006 IEEE International Symposium on Electrical Insulation, IEEE: 2006; pp 358-361.
54. Zhang, L.; Zhang, Y.; Zhou, Y.; Teng, C.; Peng, Z.; Spinella, S., Crystalline modification and its effects on dielectric breakdown strength and space charge behavior in isotactic polypropylene. *Polymers* **2018,** *10* (4), 406.
55. Zhang, X.; Shen, Y.; Shen, Z.; Jiang, J.; Chen, L.; Nan, C.-W., Achieving high energy density in PVDF-based polymer blends: suppression of early polarization saturation and enhancement of breakdown strength. *ACS Applied Materials & Interfaces* **2016,** *8* (40), 27236-27242.
56. Guan, F.; Yang, L.; Wang, J.; Guan, B.; Han, K.; Wang, Q.; Zhu, L., Confined ferroelectric properties in poly (vinylidene fluoride-co-chlorotrifluoroethylene)-graft-polystyrene graft copolymers for electric energy storage applications. *Advanced Functional Materials* **2011,** *21* (16), 3176-3188.
57. Li, J.; Hu, X.; Gao, G.; Ding, S.; Li, H.; Yang, L.; Zhang, Z., Tuning phase transition and ferroelectric properties of poly (vinylidene fluoride-co-trifluoroethylene) via grafting with desired poly (methacrylic ester) s as side chains. *Journal of Materials Chemistry C* **2013,** *1* (6), 1111-1121.
58. Chen, J.; Wang, Y.; Li, H.; Han, H.; Liao, X.; Sun, R.; Huang, X.; Xie, M., Rational design and modification of high-k bis (double-stranded) block copolymer for high electrical energy storage capability. *Chemistry of Materials* **2018,** *30* (3), 1102-1112.
59. Liu, Y.; Chen, J.; Jiang, X.; Jiang, P.; Huang, X., All-organic cross-linked polysiloxane-aromatic thiourea dielectric films for electrical energy storage application. *ACS Applied Energy Materials* **2020,** *3* (6), 5198-5207.
60. Kang, D.; Wang, G.; Huang, Y.; Jiang, P.; Huang, X., Decorating TiO2 nanowires with BaTiO3 nanoparticles: a new approach leading to substantially enhanced energy storage capability of high-k polymer nanocomposites. *ACS applied materials & interfaces* **2018,** *10* (4), 4077-4085.
61. Zhou, X.; Chu, B.; Neese, B.; Lin, M.; Zhang, Q., Electrical energy density and discharge characteristics of a poly (vinylidene fluoride-chlorotrifluoroethylene) copolymer. *IEEE transactions on dielectrics and electrical insulation* **2007,** *14* (5), 1133-1138.
62. Khanchaitit, P.; Han, K.; Gadinski, M. R.; Li, Q.; Wang, Q., Ferroelectric polymer networks with high energy density and improved discharged efficiency for dielectric energy storage. *Nature communications* **2013,** *4* (1), 1-7.

Chapter 3

Chitosan-Driven Assembly of PVDF Latex Nanocomposites

3.1 Introduction

Dielectric materials are capable of storing energy in the form of electric displacement upon application of an electric field. This energy storage mechanism endows them with inherently fast energy uptake and delivery with times ranging from nanoseconds to milliseconds[1]. The electrostatic capacitors based on dielectric materials are increasingly pervasive in modern electronics and pulsed power systems[2-5]. Nevertheless, capacitors generally have low energy densities relative to other electrochemical energy storage systems such as batteries or fuel cells[6]. Today, many advanced electronic and electrical systems require high integration, compactness, and miniaturization, which therefore drives the rapid development of new dielectric materials of high energy density and efficiency[7-10].

As demonstrated in Chapter 1, the energy built up in dielectric materials is determined by the applied electric field E and the consequent dielectric polarization P. The maximum stored energy density $U_{\max}$ is expressed as Equation (1.17)[11]. Practically only a portion of stored energy density can be effectively discharged due to the remnant polarization P_r. The discharged energy density U_d can then be calculated by Equation (1.18)[12]. Such irreversible polarization or leakage decreases the energy storage efficiency, which is defined as Equation (1.20). Therefore, the key to improving the discharged energy density and efficiency is to achieve a large variation of polarization (P_m-P_r) and a high breakdown strength E_b (the maximum electric field a dielectric can sustain).

Conventional dielectric materials are ceramics with high polarizability, coupled with excellent thermal stability[13]. Yet they suffer from challenging processing conditions and low breakdown strength as a result of the sharp rise in local electric field[14]. As alternatives, polymer dielectric materials have relatively higher breakdown strength, lower energy losses, and facile processability[9, 15-16]. However, their intrinsic low permittivity (k<10) poses a critical challenge for the technological implementation into flexible miniaturized devices. Due to the inverse correlation between the polarization and breakdown strength (E_b=$k^{-0.65}$)[14], the achieved U_d to date is limited (<5 J/cm^3) for capacitors based on ceramics or polymers alone. In the past decades, some strategies have emerged to solve this paradox via developing ceramic/polymer

or all-polymer nanocomposites, capitalizing upon the idea that the combination of disparate components/phases with high E_b and high-k respectively may result in a high-energy storage capacity. Indeed, superior energy densities have been achieved by designing novel morphology of hybrid fillers[17-19], modulating macromolecular reorganizations[9, 20-22], creating multilayered structures[11, 23-27], as well as establishing dielectric anisotropy[28-30]. So far, most of the existing nanocomposites are formulated by randomly mixing nanoparticles with polymers. The random percolation of dielectric breakdown paths is rather difficult to control in the 0–3 nanocomposites or in the layers of 2-2 nanocomposites, due to the lack of effective pathways to pattern nanoparticles in polymer matrix over multiple length scales from nano to macroscale.

Colloids are a promising class of solution-processable materials. They are attractive building blocks for constructing functional materials with emergent physical properties, such as photonic materials, plasmonic conductive films and organic photovoltaic devices[31]. The self-assembly of colloids is emerging as a powerful approach toward creating functional materials with control of the self-assembly at multiple length scales. In particular, the water-based polymer latex solutions, which are low-cost and environmentally friendly, have already opened a wide range of industrial applications, from thickeners and rheology modifiers to architectural coatings[32]. However, since there are large amounts of counter ions to balance the surface charges of particles in the most stable and homogeneous latex solution, it is hard to apply them directly for dielectric applications because of the significant leakage currents as a consequence of ionic conductions. Moreover, as described in Chapter 1, the cracks and coffee ring that often occurred during the solidification of latex films also highly deteriorate the mechanical and high-field dielectric properties (E_b and U_e). In this regard, the key to improving the U_e of latex films is to well confine the migration of counter ions when subjected to an electric field and to optimize the formulation process to achieve defect-free and high-quality films.

In Chapter 2, we have developed 0-3 nanocomposite materials consisting of high-E_b PVA and high-k PVDF latex. The U_e of PVA/PVDF composites were largely enhanced at 3 wt% of PVDF latex nanoparticles, which is contributed by the simultaneously enhanced E_b

and ε_r. The results indicated that the counter ions around PVDF latex particles can be well confined when the latex nanoparticles are naturally dispersed and isolated in an insulating matrix. However, it is only achieved at low PVDF latex loading. With further increasing PVDF latex content beyond 3 wt%, the E_b and U_e of PVA/PVDF composites started to decrease because of the disappearance of such barrier layers as a result of the overlapping of the counter ion filled regions. It is still a challenge to further increase PVDF latex content and fully profit from its polarization while maintaining the conduction losses on a limited level.

Herein, we proposed a new route to fabricate water-processable 0-3 PVDF latex composites films with high E_b and U_e. We use protonated chitosan, a bioresource water-soluble polymer, to electrostatically interact with negatively charged PVDF nanoparticles and control the level of charge neutralization of PVDF hybrid particles. Moreover, the existence of chitosan prevents the coalescences of latex particles and drives the self-assembly of PVDF nanoparticles to form closely packed but segregated thin films. Such structure is highly favorable for profiting from the high polarization of PVDF while eliminating leakage currents with barriers between particles. It is interesting to find that, at the so-called isoelectric point (optimized chitosan/PVDF mass ratio=0.8/99.2), the mixture solution shows a zeta potential near 0, and the resulting nanocomposites demonstrate the highest breakdown strength and energy density (10.14 J/cm^3), which is almost 400% higher than pure PVDF latex film. Moreover, a high power density of 0.92 MW/cm^3 and a mechanical breaking elongation of 835% are also achieved. The discovery of this work provides guidance on preparing dielectric latex films using water-based starting materials and processes.

3.2 Experimental Section

3.2.1 Materials

PVDF latex was supplied by Arkema (Kynar Aquatec ARC Latex) with an initial concentration of solid content of 44 wt%, in which the ratio between the fluoropolymer and acrylic resin is 70:30. The PVDF nanoparticles have an anionic surface and are stabilized by negative charges in aqueous solutions with a pH value of 7.8. Chitosan was purchased from

Sigma-Aldrich chemical company in USA with code 14508. Acetic acid was provided by Sigma-Aldrich chemical company in Germany with CAS:64-19-7. Milli-Q water (Q-Gard 00D2) was used for all experiments with a resistivity above 18.2 MΩ·cm at 25°C. Typical poly(vinylidene fluoride)-co-hexafluoropropylene (PVDF-HFP) pellets were purchased from Sigma-Aldrich with an average molecular weight $M_w \approx$ 400,000 g/mol and number-average molecular weight M_n=130,000, whose CAS number is 9011-17-0. Poly(vinylidene fluoride) (PVDF) pellets are purchased from Sigma-Aldrich chemical company in Germany with an average molecular weight of $M_w \approx$530,000 g/mol. Polyvinyl alcohol (PVA) was supplied from Sigma-Aldrich Chemical Company, Germany, under the trade name Mowiol 20-98 (CAS No. 9002-89-5), with a molecular weight of Mw = 125,000 g/mol and hydrolysis of 99%. The solvent N, N-Dimethylacetamide with a Molar Mass=87.12 g/mol was provided by Sigma-Aldrich and its CAS number is 127-19-5. Sodium hydroxide (NaOH) is obtained from Sigma-Aldrich chemical company in Germany with a CAS number 1310-73-2 whose assay is ≥37%.

3.2.2 Fabrication of PVDF@chitosan Nanocomposites

Chitosan was first dissolved in a 1.5 wt% acetic acid-water solution by magnetically stirring at 300 rpm for 4 h at room temperature. Then, the mixture solution was heated at 120℃ for 10 minutes in an oven for sterilization. It was filtrated afterward to obtain a fully dissolved aqueous solution with a final concentration of 0.66 wt%, as shown in **Figure 3-1** (a). The commercial PVDF latex solution was diluted to 0.77 wt% PVDF by deionized water for all the experiments in this chapter. As schematically illustrated in **Figure 3-1** (b), various amounts of protonated chitosan solution were mixed with PVDF latex by magnetic stirring at room temperature for 2 h. To precisely control the ratio between PVDF and chitosan, the protonated chitosan aqueous solution was added drop by drop into the diluted PVDF latex solution using a syringe with a sharp needle. Afterward, the mixture of PVDF latex and chitosan aqueous solution was redispersed by a tip sonication for 30 minutes with a 30% amplitude and delivered pulses of 0.5 s separated by 0.2 s intervals of silence. During the sonication, the mixture was

placed in an ice bath to prevent overheating. Afterward, the redispersed mixture solution was transferred into a glass container immediately for resting over 2 h.

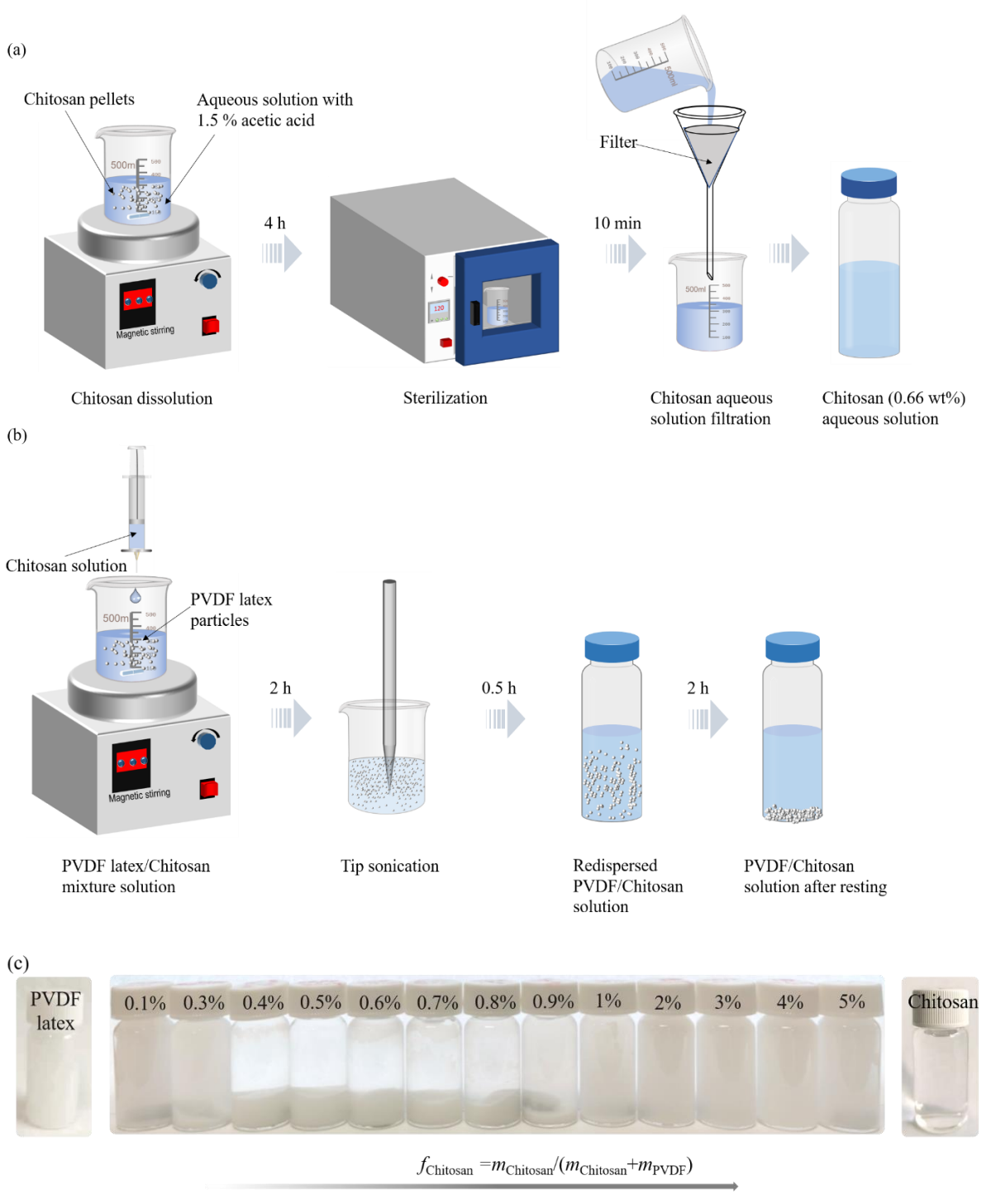

Figure 3-1. (a) The preparation of an aqueous solution of protonated chitosan at a concentration of 0.66 wt%. (b) The mixture of PVDF latex and the protonated chitosan aqueous solution. (c) Photographs of pure PVDF latex, chitosan aqueous solution and their mixtures at different ratios.

Figure 3-1 (c) shows the images of pure PVDF latex solution, pure chitosan solution, and the mixture solutions at different ratios. The chitosan, as a cationic polymer flocculant, can bridge individual colloidal particles by attractive electrostatic interactions, as its content increases up to 1 wt%. The flocculated hybrid particles were sedimented by gravity, leading to jammed, disordered assembly with intimate contact of PVDF nanoparticles. However, further increasing chitosan content, the mixture solutions become macroscopically homogeneous again due to the increased positive charges as a consequence of the full coating of chitosan on the PVDF nanoparticles (**Figure 3-2** (a)). Detailed descriptions of these processes will be given in Section 3.3.4. It should be noted that the final PVDF content in each aqueous mixture is kept at 0.72 wt% by adding different amounts of deionized water. This is to avoid the influence of solute concentration on the subsequent tests of zeta potential and pH values. The concentrations of each constituent component in the solution are listed in **Table 3-1**.

Table 3-1. The content of each constituent component in the mixture solutions

Solutions	Chitosan solution (mg)	PVDF latex solution (g)	PVDF content (wt%)	H_2O (g)
100%PVDF	0.0	7.0	0.72	0.4861
99.9%PVDF/0.1%Chitosan	8.2	7.0	0.72	0.4779
99.7%PVDF/0.3%Chitosan	24.6	7.0	0.72	0.4615
99.6%PVDF/0.4%Chitosan	32.8	7.0	0.72	0.4533
99.5%PVDF/0.5%Chitosan	41.0	7.0	0.72	0.4451
99.4%PVDF/0.6%Chitosan	49.3	7.0	0.72	0.4368
99.3%PVDF/0.7%Chitosan	57.6	7.0	0.72	0.4285
99.2%PVDF/0.8%Chitosan	65.9	7.0	0.72	0.4203
99.1%PVDF/0.9%Chitosan	74.2	7.0	0.72	0.4119
99%PVDF/1%Chitosan	82.5	7.0	0.72	0.4036
98%PVDF/2%Chitosan	166.7	7.0	0.72	0.3194
97%PVDF/3%Chitosan	252.6	7.0	0.72	0.2335
96%PVDF/4%Chitosan	340.3	7.0	0.72	0.1458
95%PVDF/5%Chitosan	429.8	7.0	0.72	0.0563

The process flow illustrated in **Figure 3-2** (a) enables the integration of PVDF latex particles into a nanocomposite film. In detail, 2 mL of well-mixed solution was cast onto a Petri

dish of aluminum. After 2 h of resting, water was then evaporated at 100°C for 60 min in a vacuum oven. Afterward, the sample followed a hot-pressing process at 110°C for 3 min under 40 MPa to make it flat and eliminate the defects. The achieved film was fully dried in a vacuum oven at 110°C for 20 h before the dielectric characterizations. **Figure 3-2** (b) shows the photographs of the PVDF@chitosan nanocomposite films. The patterned PVDF latex films have a thickness ranging from 5 μm to 10 μm and are highly uniform, flexible, and free of cracks. The film with 5 wt% chitosan is even transparent.

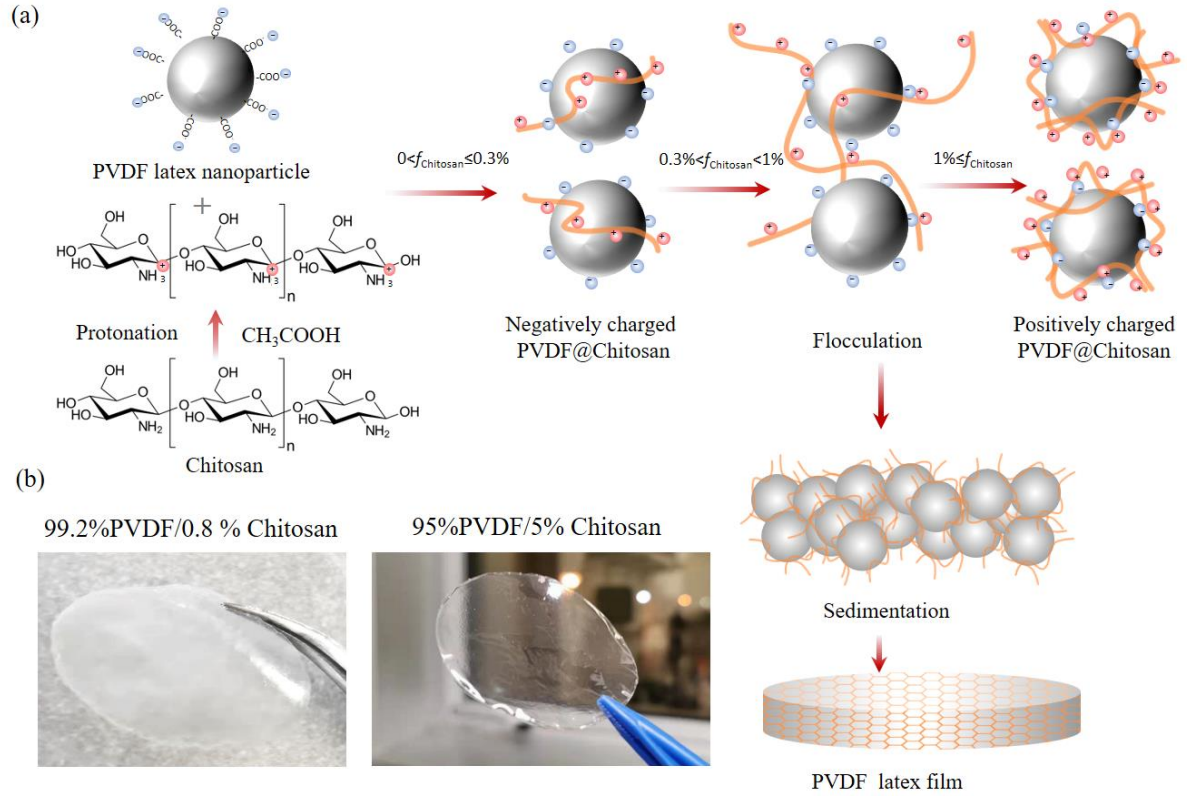

Figure 3-2. (a) The schematic illustrations of the interactions between negatively charged PVDF particles and protonated chitosan at different ratios. (b) The photographs of the PVDF@chitosan composite films at 0.8 wt% and 5 wt% chitosan.

To clarify the impact of the ions on the dielectric performance and energy storage density, PVA aqueous solutions were prepared according to the protocols described in Chapter 2. CH_3COONa aqueous solution is prepared by mixing 1 mol NaOH and 1 mol CH_3COOH in 1L deionized water, followed by magnetic stirring over 4 h. The CH_3COONa solution was then added into the PVA solution to prepare ion-containing PVA precursors at different ion contents.

Afterward, the PVA/CH_3COONa films were cast from their mixture solutions, followed by incubation procedures used for the preparation of PVDF@chitosan composite films.

3.2.3 Characterizations of PVDF@chitosan Nanocomposites

The dielectric properties of the films were characterized at room temperature using an impedance analyzer (MaterialsMates 7260, Italia). The dielectric breakdown strength and electric polarization-electric field ($P-E$) loops were tested at room temperature in silicone oil by a PolyK ferroelectric polarization loop and dielectric breakdown test system. Fast charge and discharge experiments were performed using a capacitor charge/discharge system (PolyK Technologies). Before the characterizations, gold electrodes were sputtered on the two surfaces of each film to ensure good contact. The details of the used equipment and the cable connections can be found in Chapter 2. Transmission electron microscopy (TEM) images of PVDF@chitosan nanocomposites were taken via a Hitachi H600 microscope operating at 75 kV. For TEM analysis, the pure PVDF latex film and the PVDF@chitosan nanocomposite were ultramicrotome to slices of 40–60 nm thickness and placed on copper films for observation. The morphology of the materials was also characterized by scanning electron microscopy (SEM, JEOL 6700F). The zeta potential of PVDF@chitosan solutions was recorded at 20°C using disposable cuvettes with a capillary channel and a Zetasizer Nano ZS apparatus (Malvern Instruments Ltd., Worcestershire, UK). The mechanical properties of the solidified latex films were evaluated via uniaxial tensile tests on a Zwick Z2S apparatus with a load cell of 1000 N.

3.3 Results and Discussion

3.3.1 Dielectric Properties of PVA/CH_3COONa Films

The carboxylic acid groups on PVDF begin to dissociate as there are no excess hydrogen ions in solutions of pH values>7. Herein, the stable PVDF latex solution (pH=7.80) is supposed to consist of counter ions of OH^- and Na^+. On the other hand, chitosan protonates in acetic acid. The resultant aqueous solution (pH=3.47) contains the counter ions of CH_3COO^- and H^+. The introduction of chitosan into PVDF latex results in a mixture that can be considered as polymer solutions consisting of CH_3COONa salts. Therefore, it is important to first examine the

influence of these ions on the dielectric performances and energy storage density of solid polymer composites.

The low-field dielectric properties of PVA/CH_3COONa films were recorded as a function of frequency and shown in **Figure 3-3** to reveal the impact of ions on the low-field dielectric behaviors.

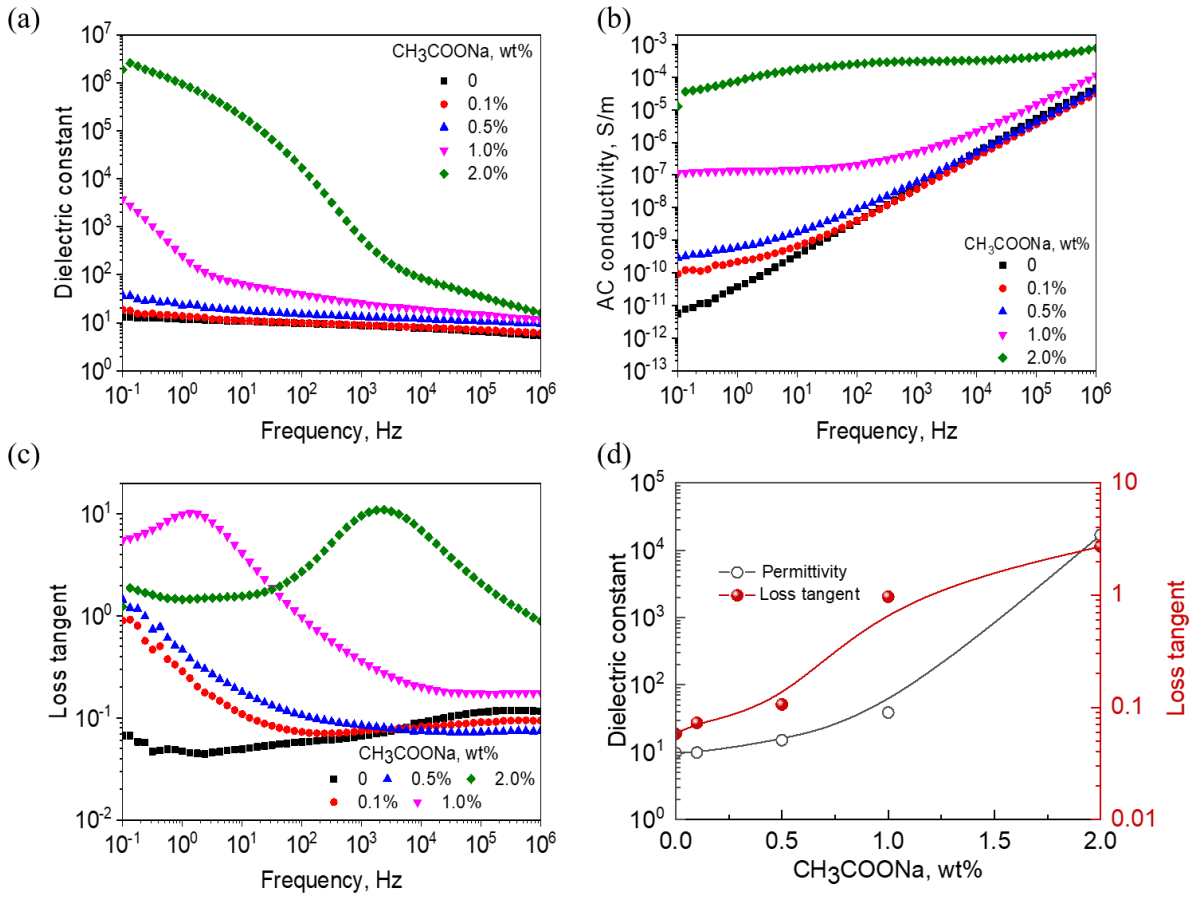

Figure 3-3. (a) The dielectric constant, (b) AC conductivity, and (c) loss tangent of PVA/ CH_3COONa films as a function of frequency at room temperature, (d) Dielectric constant and loss tangent at 100 Hz vary with CH_3COONa loading.

At low CH_3COONa contents (<0.5 wt%), the dielectric constant of the polymer composites increases marginally over the whole frequency range (**Figure 3-3** (a)). However, such a trace amount of ions in the PVA films can lead to a sharp rise in AC conductivity and dielectric losses at a frequency below 10 Hz (**Figure 3-3** (b, c)). Such increase is associated with ion transportation that usually takes time and manifests only at low frequencies. Furthermore, with increasing the salt content from 1 wt% to 2 wt%, a largely boosted dielectric

constant (>10^6, **Figure 3-3** (a)) was observed and accompanied by a significant dielectric relaxation emerging at low frequencies. The relaxation peak shifts to a higher frequency with increasing ion contents. This arises from the so-called electrode polarization as a result of the formation of the electric double layer. In this case, the polymer composites would be considered as a solid electrolyte rather than dielectric anymore[33]. The high loss tangent (~10, **Figure 3-3** (c)) is mainly contributed by the ionic conduction, as evidenced by the high AC conductivity (~10^{-4} S/m) that is almost independent of frequency (**Figure 3-3** (b)). As summarized in **Figure 3-3** (d), the introduction of ions indeed enhances the polarization capability of the system but makes the material very lossy. Only 2 wt% of salts can turn a pure dielectric film into an ionic conductive solid electrolyte.

3.3.2 Dielectric Breakdown Strength of PVA/CH_3COONa Films

It has been argued that high conduction losses lead to a large leakage current at a high electric field, thus limiting the maximum voltage that a material can withstand without undergoing electrical breakdown[8]. It is intriguing to investigate the influence of the ions on the dielectric breakdown behaviors of solid PVA/CH_3COONa nanocomposites. The characteristic electric breakdown strengths are generally analyzed with a two-parameter Weibull distribution function[34], as described by Equation (1.14). The E_b and β are calculated from a linear fitting using Weibull failure statistics (**Figure 3-4**), and the values are listed in **Table 3-2**. The high β values at low salt content (<0.5 wt%) indicate the structural uniformity and integrity of the investigated composite films. However, the sharply decreased β values beyond 1 wt% indicate that the salts are not uniformly distributed in the completely dried films at high CH_3COONa loadings. The E_b of all the PVA/CH_3COONa composite films is inferior to that (~500 MV/m) of the pure PVA film. The breakdown strength decreases rapidly by 21% with the presence of only 0.1 wt% of CH_3COONa in PVA. As the CH_3COONa content increases up to 2.0 wt%, the breakdown continues to drop to 182 MV/m, (**Figure 3-4b**), making PVA lose the capability of sustaining high voltages. The variation in dielectric breakdown strength agrees well with the tendency of loss tangent previously presented in **Figure 3-3** (d).

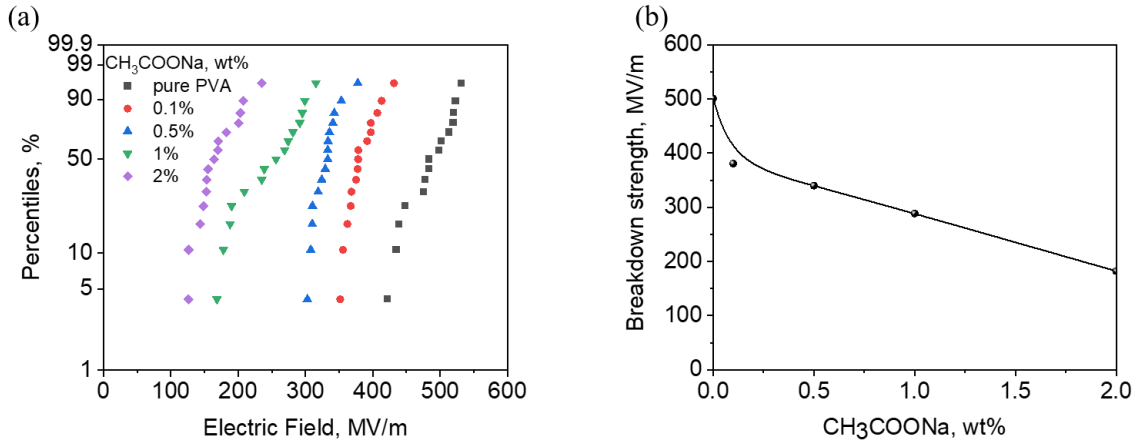

Figure 3-4. (a) Failure probability was determined from Weibull distribution for neat PVA, and their composites at various CH_3COONa loadings. (b) The breakdown strength of PVA/CH_3COONa composite films as a function of CH_3COONa loading.

Table 3-2. The E_b and β of pure PVA, and their composites at various salt contents

CH_3COONa content wt%	E_b MV/m	β
0	500.37	17.66
0.1	394.20	17.28
0.5	339.65	16.12
1.0	265.45	6.29
2.0	182.23	5.84

3.3.3 Energy Density of PVA/CH_3COONa Films

The polarization of pure PVA and PVA/CH_3COONa composites was further characterized at high electric fields to investigate the effect of ions on energy storage performances. We first compared the polarizations of all the samples at an electric field of 200 MV/m. Pure PVA film demonstrates a classical dielectric behavior, displaying a slim hysteresis loop (**Figure 3-5** (a)). The addition of a small amount of salts (<0.5 wt%) favors the polarization and leads to higher electric displacements yet more pronounced loops and higher losses. This is consistent with the variation of the dielectric constant and loss tangent at low fields (**Figure 3-3**). Moreover, further increasing the salt content up to 1 wt% results in a slight increase in polarization but a dramatic augmentation in conduction losses. Because of the high conductivity of the sample at 2 wt% CH_3COONa (**Figure 3-3** (b)), its *P-E* loop test is rather difficult to perform, indicating the material completely loses its capability of energy storage.

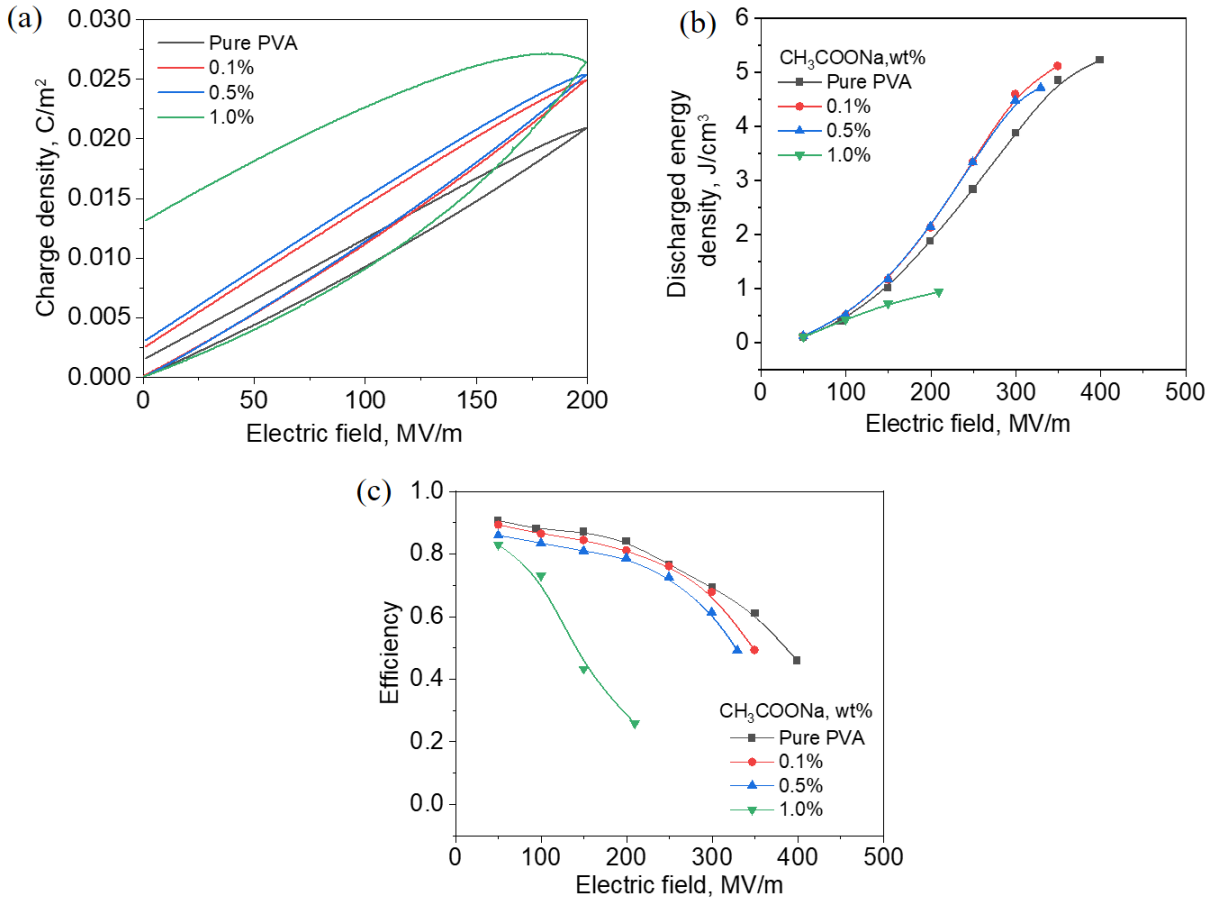

Figure 3-5. (a) *P*−*E* loops of pure PVA and PVA/CH_3COONa nanocomposite films at an electric field of 200 MV/m. (b) The maximum discharged energy density and (c) related charge/discharge efficiency for pure PVA and PVA/CH_3COONa composite films.

We also compared the energy storage density of different samples. Based on the *P*-*E* loops at different fields until their breakdown strength, the discharged energy density is calculated and plotted in **Figure 3-5** (b). Pure PVA film shows a maximum energy density U_e=5.2 J/cm^3. In spite of the enhanced polarization, the discharged energy densities of all the PVA/CH_3COONa composites are still inferior to that of pure PVA, because the improvement in the stored energy cannot fully compensate for the additional dissipated energy derived from the conduction losses during discharging. The more ions added into PVA film, the lower the maximum discharged energy density of the composites. This arises from the decreased maximum field that the composite can sustain (less stored energies) as well as the increased conduction losses (more energy losses). Both trends directly give rise to a declined

charge/discharge efficiency with increasing salt content at each electric field, as shown in **Figure 3-5** (c).

Overall, it can be concluded that the presence of ions makes the materials highly lossy and dramatically deteriorates the breakdown strength. The ion-containing materials are likely to be used as solid electrolytes in supercapacitors but are not suitable to serve as dielectrics in electrostatic capacitors for energy storage, if the ions are not well confined.

3.3.4 Zeta Potential and pH of PVDF@chitosan Solutions

The small counter ions that balance the charges of colloids make them undesirable for dielectric energy storage applications. Actually, the distribution of these counter ions is associated with the electrostatic potential profiles of the charged particles, as depicted by **Figure 1-32** in Chapter 1. In the case of PVDF latex, the positive counter ions are attracted towards the particle by the electric field generated by the negative charges but they are also subject to thermal motion, which tends to distribute them uniformly through the surrounding medium. The end result is usually a compromise in which a few positive ions are bound strongly to the PVDF particle surface and the concentration of the remained ions falls off gradually away from the particle until it approaches the bulk concentration at distances of the order of some tens of nanometers[35]. The protonated chitosan, a bioresource cationic polyelectrolyte, is chosen here to electrostatically interact with anionic PVDF nanoparticles to tailor its level of charge neutralization and passivation so as to affect the distribution of counter ions.

Zeta potential, a measure of the stability of colloidal suspensions, is used to represent the electrostatic charges of the particles. It quantifies the electrical repulsive force exerted between the particles. Normally, the higher the zeta potential, the colloids possess more charges and will be more stable in the dispersing medium. The colloidal solution is considered to be completely stable while the value of the zeta potential is higher than ±30 mV[36]. Zeta potential is sensitive to particle concentration, ionic strength, and pH values. The measured zeta potential, constituent colloid size and pH values of different solutions have been listed in **Table 3-3** and plotted as a

function of the mass ratio between PVDF and chitosan in **Figure 3-6** and **Figure 3-7** respectively.

Table 3-3. The zeta potential, constituent colloid size and pH values of different solutions

Solutions	Zeta potential (mV)	Particle size (nm)	pH
100%PVDF	-45.9	163	7.8
99.9%PVDF/0.1%Chitosan	-44.5	230	7.71
99.7%PVDF/0.3%Chitosan	-43.7	505	7.68
99.6%PVDF/0.4%Chitosan	-37.4	3207	7.66
99.5%PVDF/0.5%Chitosan	-33.7	3674	7.62
99.4%PVDF/0.6%Chitosan	-30.2	3734	7.47
99.3%PVDF/0.7%Chitosan	-19.8	4857	7.3
99.2%PVDF/0.8%Chitosan	-7.9	6486	7.02
99.1%PVDF/0.9%Chitosan	26.6	3759	6.16
99%PVDF/1%Chitosan	29.2	898	5.12
98%PVDF/2%Chitosan	37.4	565	4.71
97%PVDF/3%Chitosan	42.0	444	4.59
96%PVDF/4%Chitosan	48.1	496	4.53
95%PVDF/5%Chitosan	49.9	434	4.51
100% Chitosan	89.0	n/a	3.47

The as-prepared starting materials, 0.77 wt% PVDF latex dispersion and 0.66 wt% chitosan solution, display a zeta potential of -46 mV and +89 mV respectively. Both systems can remain individual particles for an appreciable time, as there are sufficient electric charges on the particles to prevent aggregation during the Brownian collision of particles. Such electrostatic stabilization arises respectively from the dissociation of the carboxylic groups on the PVDF nanoparticles and the protonation of amino groups ($-NH_2$) of chitosan molecules. When mixing chitosan with PVDF latex, the system displays distinct scenarios depending on the mass ratio of PVDF and chitosan.

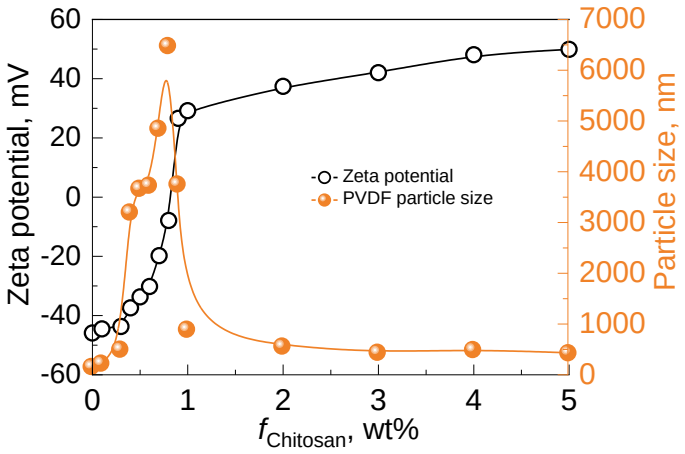

Figure 3-6. Zeta potential of mixture aqueous dispersions and the size of the constituent PVDF@chitosan hybrid particles as a function of the mass ratio of PVDF and chitosan.

As shown in **Figure 3-1**(c), at ratios below 0.3 wt%, the PVDF nanoparticles are partially covered by chitosan, which ensures that there is sufficient surface available on each particle to allow the dispersion stabilized by net negative charges (zeta potential>-43 mV, **Figure 3-2** (a), **Table 3-3, Figure 3-6**).

In contrast, at ratios ranging from 0.3 wt% to 1 wt%, the mixtures are colloidally unstable as the Brownian collisions of colloids result in the formation of loose aggregates, this process is called flocculation. Generally, the flocculation is induced through a bridging mechanism or simple charge neutralization. Here bridging is the dominant mechanism because, even until 0.6 wt%, the zeta potential is still higher (see **Table 3-3**, **Figure 3-6**) than the minimum value (±30 mV) required to maintain the colloidal stability. Bridging is considered to be a consequence of the adsorption of the segments of individual chitosan molecules onto the surfaces of more than one PVDF particle (**Figure 3-2** (a)). Such bridging links the particles together into jammed, disordered assemblies, represented by the detected increase in the size of colloids in the solution (**Figure 3-6**). In addition, the cationic chitosan may also induce flocculation through charge neutralization, in particular at 0.8 wt%. Near this point, bridging flocculation may still be operative, but the mass ratio corresponds quite closely to the dosage of chitosan required to neutralize the surface charge of the PVDF particle. The latter is detected experimentally by the reduction of the measured electrophoretic mobility of the particles to nearly zero (so-called

isoelectric point), the pH down to 7, (**Table 3-3**), and the increase of the colloid size to its peak value (~6.5 µm, **Figure 3-6**).

At higher ratios beyond 1 wt%, the PVDF particles become fully coated by segments of chitosan chains attached solely to one particle. The PVDF@chitosan hybrid particles are overall positively charged and the zeta potential (**Table 3-3**, **Figure 3-6**) is exceeding +30 mV, Steric (or electrosteric) stabilization starts to be in operative.

Based on the foregoing description, it can be inferred that most of the counter ions surround the charged PVDF nanoparticles or chitosan molecules in their respective solutions (**Figure 3-7** (a)). The solid films cast from individual solutions contain small ions that tend to be evenly distributed in the bulk. While the association of PVDF and chitosan, with the mass ratio ranging from 0.3 wt% to 1 wt%, largely screens their Coulombic attraction with respective counter ions as a consequence of the charge neutralization. In particular, at the isoelectric point (0.8 wt%), all charged particles and molecules indeed engage in the formation of loose and jammed assemblies (flocculation), promoting a complete liquid-solid phase separation with the release of all counter ions into the supernatant (**Figure 3-7** (a)). This scenario is highly analogous to the widespread associative process of oppositely charged polyelectrolytes in aqueous solutions. Our colleagues at CRPP have investigated the polyelectrolyte complex suspensions as a function of the molar charge ratio (Z=[-]/[+]) in poly (diallyldimethylammonium chloride)/poly (acrylic acid sodium salt) (PDADMAC/PANa) solution[37]. It was found that as the system approaches charge stoichiometry (Z=1), both polyelectrolytes are neutralized through ion pairing and the hydrophobic and neutralized surface-active species formed. PDADMAC/PANa system undergoes a liquid-liquid phase transition, which can be obviously demonstrated by the clear separation between the dense coacervate phase and the macromolecule-depleted supernatant in **Figure 3-7** (b). The surface tension of the supernatant approaches that of pure water, indicating that the complexes have completely precipitated. The conductivity in the supernatant corresponded to a NaCl concentration, which is in good agreement with the complete release of counter ions from prepared PSS(Na^+) and PDADMAC(Cl^-) solutions[37].

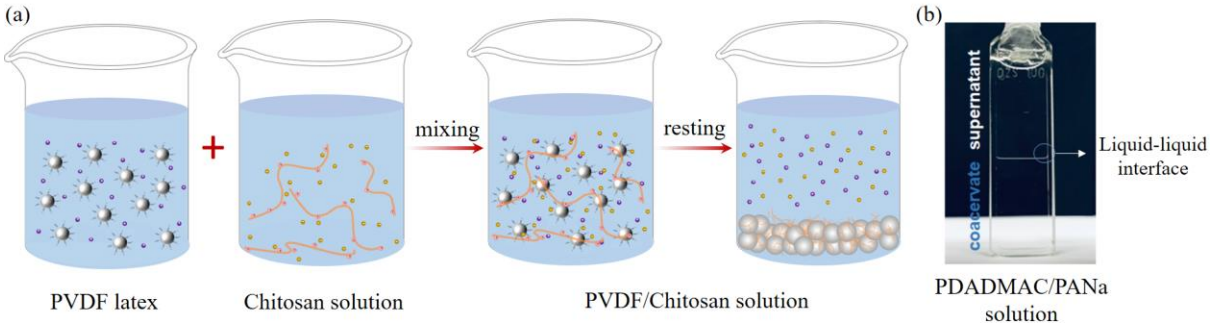

Figure 3-7. (a) The schematic illustration of the distribution of counter ions during the process flow of PVDF@chitosan composites. (b) Macroscopic phase separation was observed after complexation of the PDADMAC/PANa system prepared from polyelectrolyte solutions at charge stoichiometry (Z=1)[37].

The charge neutralization of polymer nanoparticles or polyelectrolytes would result in an out-of-equilibrium system with a complete liquid-solid or liquid-liquid phase separation. In both cases, the counter ions tend to be separated from the original nanoparticles or molecules and relocate in the supernatant phase that is free of charged species. The further processing of the charge-neutral nanoparticle- or polyelectrolyte-containing phase into films can therefore suppress the adverse effect of the ions.

3.3.5 Morphologies of PVDF@chitosan Nanocomposite Film

Figure 3-8 (a, b) illustrate schematically the formation of pure PVDF latex film and PVDF@chitosan nanocomposite film. As the water evaporates, the uniformly and stably dispersed PVDF particles begin to come into contact with each other. When PVDF latex particles have reached maximum packing and the water level falls below the top layer of the particles, the coalescence begins with the initial formation of a continuous film. Due to the diffusion of the polymer chains from one particle to another and filling the voids, the particle interfaces become not clear and the film obtains mechanical strength. Finally, a coalesced PVDF film was formed. Further thermal treatment can remove the defects related to the remained voids or cracks after the solidification of the film (**Figure 3-8** (a, c, e)). On the other hand, the PVDF@chitosan system, due to the bridging and neutralization of charged species, undergoes liquid-solid phase separation. The chitosan-driven assembly of PVDF nanoparticles

will be sedimented by gravity after resting. Such unstable mixture solution was directly dried to form films. Due to the existence of chitosan-coated on the surface of PVDF nanoparticles, they are not able to fully contact each other. The presence of chitosan prevents eventually the coalescence of PVDF nanoparticles and drives the self-assembly of PVDF nanoparticles to form closely packed but the segregated thin film, as shown in **Figure 3-8** (b, d, f).

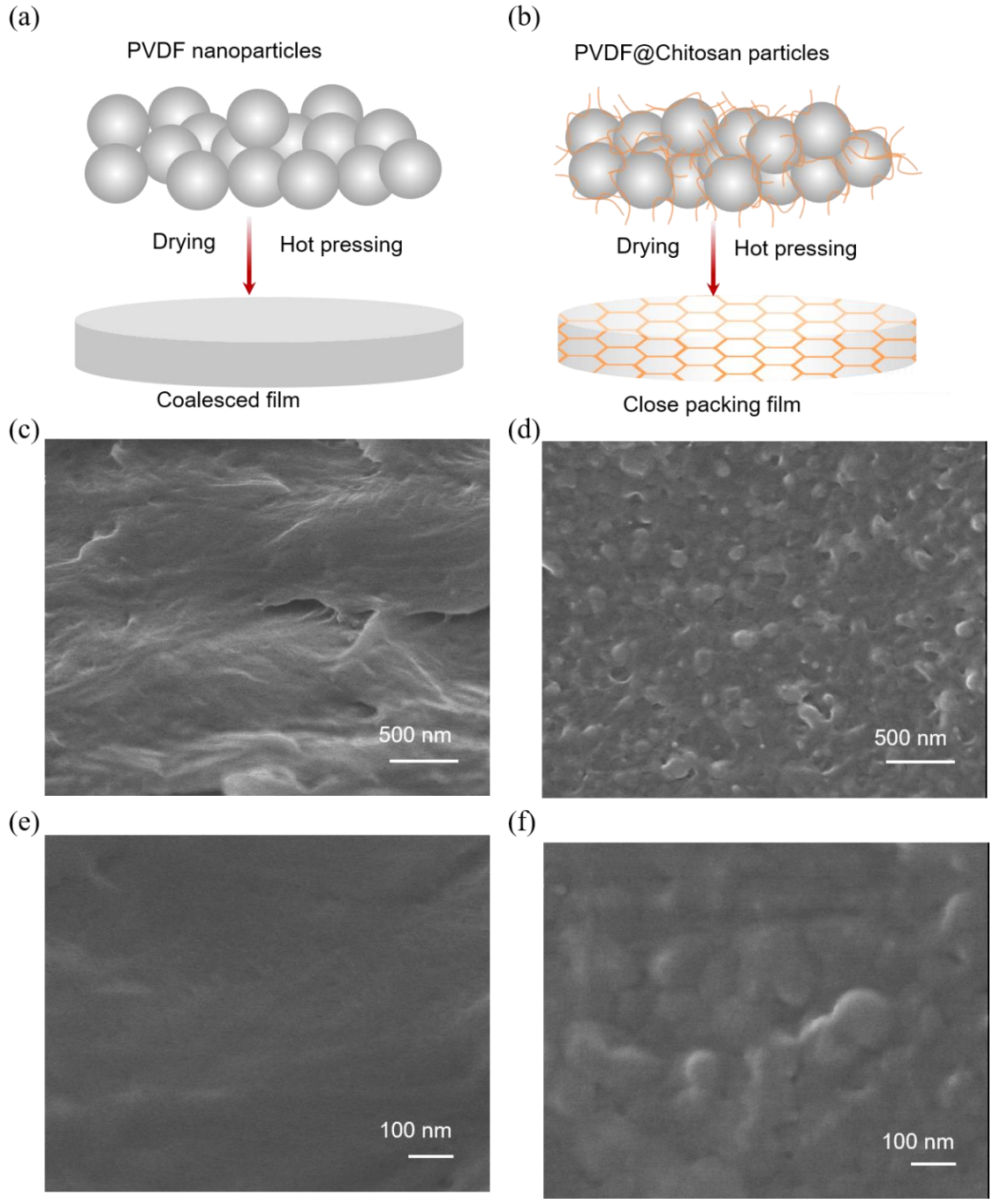

Figure 3-8. Schematic illustrations of (a) pure PVDF latex film and (b) PVDF@1 wt% chitosan films after hot pressing at 110℃. SEM images of (c, e) pure PVDF latex and (d, f) PVDF@1 wt% chitosan films were observed under different magnifications.

SEM and TEM analyses were performed to investigate the nanostructures of coalesced PVDF film and the closely packed PVDF@chitosan film. **Figure 3-8** (c, e) shows the cross-sectional SEM of pure PVDF, which can be easily found that PVDF nanoparticles have undergone coalescence and already formed a continuous single phase. While for PVDF@chitosan nanocomposite film, as shown in **Figure 3-8** (d, f), PVDF still remains in a closely stacked state, being arranged into a segregated nanostructure, even after a hot pressing at an elevated temperature (110℃).

More details on the nanostructures of pure PVDF latex and PVDF@chitosan films can be revealed by TEM analysis, as shown in **Figure 3-9**. The coalescence indeed occurs between adjacent nanoparticles in pure PVDF latex film. Yet, there are still massive cracks and voids of nanometer size (white domains in **Figure 3-9** (a)) in the film. The original shape (sphere) and size (~160 nm) of PVDF nanoparticles in the solution cannot be identified.

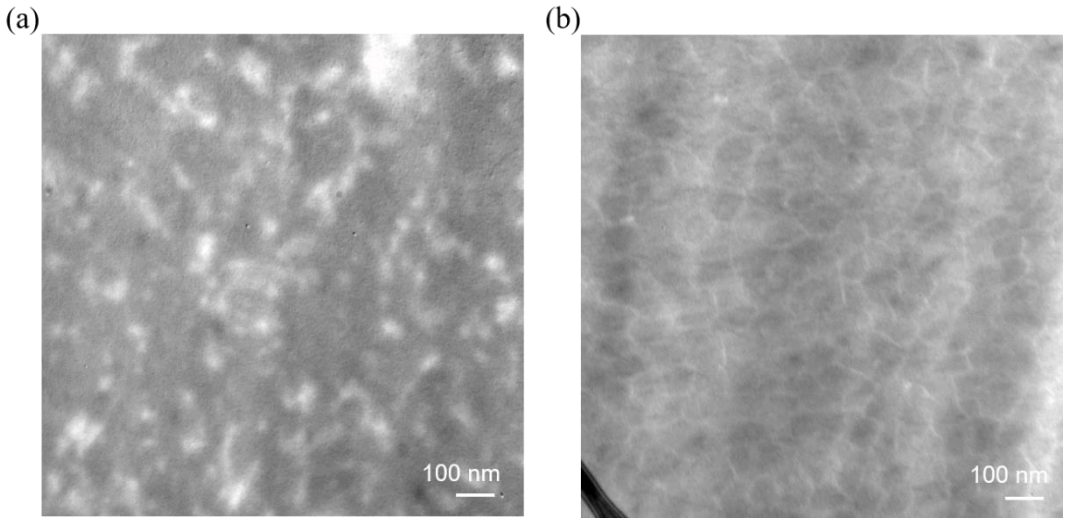

Figure 3-9. TEM images of (a) pure PVDF latex and (b) PVDF@0.8 wt% chitosan films hot-pressed at 110℃.

In **Figure 3-9** (b), the nanostructure of the PVDF@0.8 wt% chitosan composite film is presented, showing a segregated nanostructure with a clear boundary between the PVDF nanoparticles. Indeed, chitosan prevents their coalescence by wrapping the PVDF nanospheres. In addition, such an isolated structure is extremely stable and can be maintained even after hot pressing at 110°C. Actually, chitosan has excellent film-forming properties. It not only drives

the assembly of PVDF latex particles but also fills the voids or cracks usually formed as the water evaporates from the colloid solution. Therefore, no nanometer-sized cracks were found in the PVDF@chitosan composite film (**Figure 3-9** (b)), which demonstrates that the introduced trace amount of chitosan can successfully improve the quality of PVDF latex film.

3.3.6 Mechanical Properties of PVDF@chitosan film

Indeed, the addition of chitosan optimizes the film-forming processes and suppresses the solidification-induced defects. Meanwhile, it largely prevents the diffusion of macromolecules through particle interfaces and thus the overall coalescence of latex particles. Generally, it is the coalescence that affords a sufficient mechanical strength to latex films. Herein, are the non-coalesced PVDF@chitosan composite films still mechanically strong for subsequent applications? To answer this question, we have characterized the tensile properties of waterborne PVDF latex film and PVDF@chitosan composite films, and compared with solvent-processed typical PVDF and PVDF-HFP copolymer films. As shown in **Figure 3-10**, latex-based films display distinct mechanical properties from typical PVDF films.

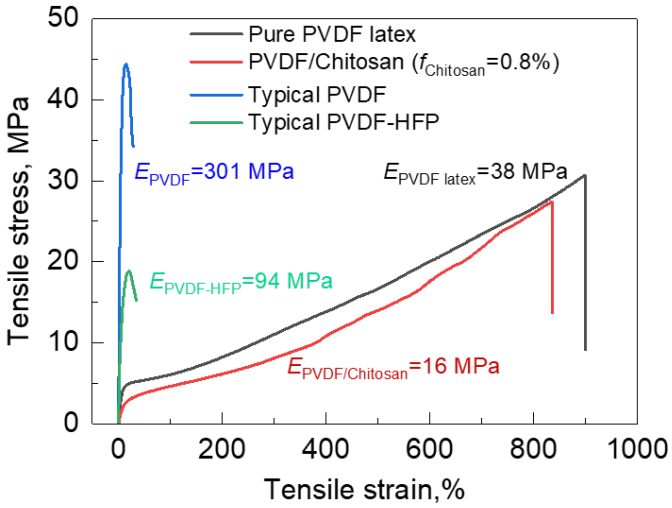

Figure 3-10. The tensile strength versus tensile strain for solvent (DMF)-processed PVDF film, PVDF-HFP film, water-processed pure PVDF latex film and PVDF@chitosan composite film at 0.8 wt% chitosan content.

They are not as rigid as the latter, showing a lower Young's modulus, particularly one order of magnitude lower than PVDF film (E_{PVDF}=301 MPa). However, latex films can sustain

a much larger plastic deformation before the break, being akin to the mechanical behaviors of thermoplastic elastomers[38-39]. Furthermore, as compared to the coalesced PVDF latex film, Young's modulus of PVDF@chitosan composite film decreases by 50%, yet the elongation at break and ultimate tensile strength decline only by 7% and 10% respectively. Basically, the PVDF@chitosan composites maintain the mechanical robustness of PVDF latex.

3.3.7 Dielectric Performances of PVDF@chitosan Films

We have performed also the dielectric characterizations of freestanding samples to explore the potential of PVDF latex composite films for energy storage applications. **Figure 3-11** presented the dielectric behaviors of PVDF latex films as a function of frequency and the dosage of chitosan used to neutralize charges of PVDF nanoparticles. Being similar to the ion-containing PVA films in **Figure 3-3** (**a**), the coalesced PVDF latex film displayed a dielectric relaxation at low frequency because of the electrode polarization of mobile charges in **Figure 3-11** (a). This gives rise to superior dielectric constants over the whole frequency range to typical PVDF films, which is normally showing a frequency-independent permittivity around 10.[40] This is because, in coalesced PVDF latex film, the small counter ions tend to surround the original PVDF nanoparticle and consequently evenly distribute in the bulk materials without any confinement. This can be also evidenced by the ionic conduction and high loss tangent at low frequency, as presented respectively in **Figure 3-11** (b, c). Furthermore, the permittivity of PVDF@chitosan films decreases continuously and becomes less frequently dependent on increasing the level of charge neutralization of latex nanoparticles (as a consequence of the increased dosage of chitosan). The same trends are also found in the evolution of conductivity and loss tangent of PVDF@chitosan films. At the critical isoelectric point (0.8 wt%), the material demonstrates the best insulating properties, i.e., lowest conductivity and losses over the whole frequency range. Although the permittivity approaches its minimum at 5.6 at 100 Hz, this value is still rivaling most polymers, for example, the benchmark BOPP film (k~2.2 at 100 Hz).

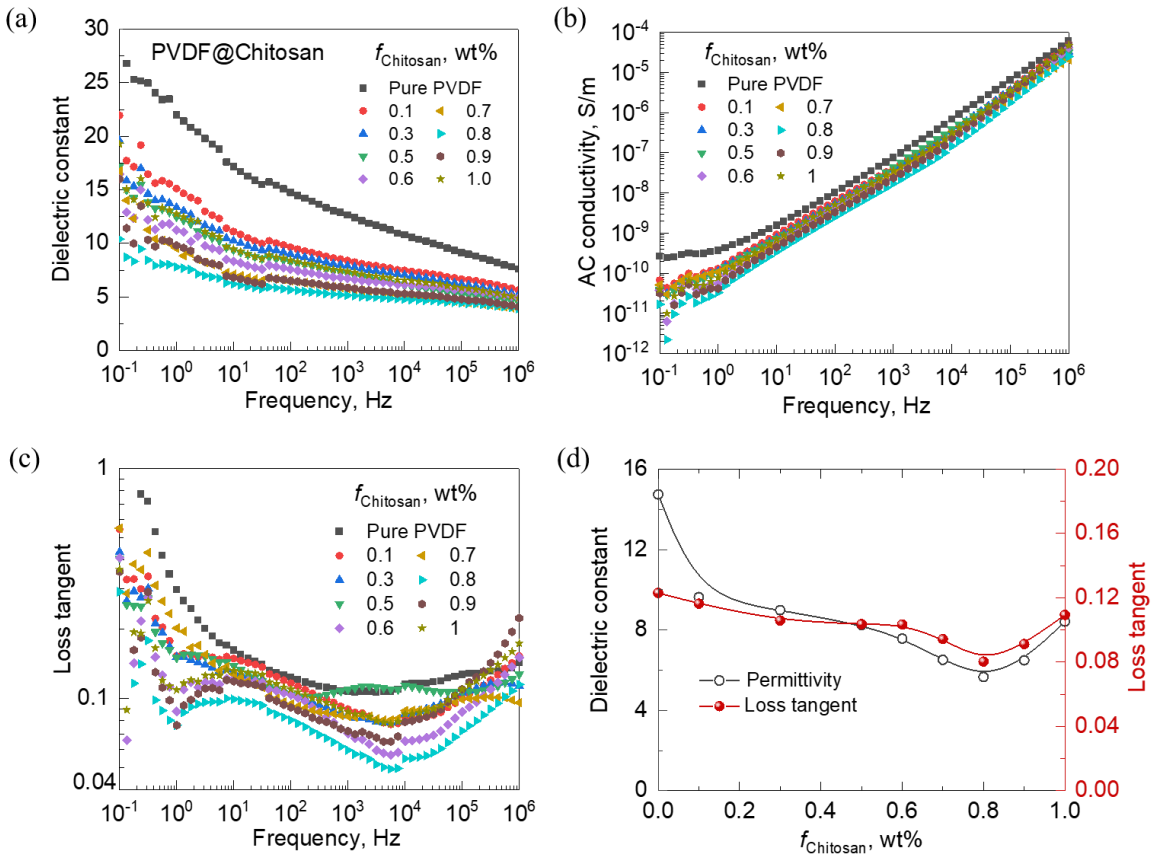

Figure 3-11. (a) Dielectric constant, (b) AC conductivity, and (c) loss tangent of PVDF@chitosan films as a function of frequency at room temperature. (d) Dielectric constant and loss tangent at 100 Hz vary with chitosan content.

To better illustrate the effect of chitosan, we plotted the dielectric constant and loss tangent as a function of its dosage in **Figure 3-11 (**d**)**. At 100 Hz, the dielectric constant decreases from 14.7 to 5.6 and then increase to 8.4, showing a valley at 0.8 wt%. Meanwhile, the loss decreases from 0.12 to 0.08, the minimum value, and then rises again up to 0.11 from 0.8 wt%. Beyond the isoelectric point, both dielectric constant and loss tangent tend to increase again. To verify the trend at more elevated dosages of chitosan, we have characterized the pure chitosan and nanocomposite samples at loadings ranging from 1 wt% to 5 wt% (**Figure 3-12)**. The dielectric constant, AC conductivity, and loss tangent increase monotonically with the chitosan content at each frequency. Indeed, at this stage, the PVDF particles become fully coated by the segments of chitosan chains attached solely to one particle. The surface of PVDF@chitosan hybrid particle is overall positively charged, which will attract counter ions and redistribute them in the

vicinity depending on their electrostatic potential profiles. Beyond the isoelectric point, more chitosan was introduced, more positive charges on the colloids, and more counter ions remained at the boundaries of PVDF particles in the solidified sample. An extreme case is the pure chitosan, it shows an extremely high dielectric constant, i.e., 2053 at 10^{-1} Hz, while relaxes rapidly to 17 at 100 Hz. Also, its conductivity displays a wide plateau below 100 Hz and the loss tangent shows a superior value (1.13 at 100 Hz, **Figure 3-12** (b, c)) to most dielectric polymers[4]. The variation of dielectric constant and loss tangent with chitosan loading is also presented in **Figure 3-12** (d). Clearly, the dielectric behaviors highly resemble those of ions containing PVA/CH_3COONa (**Figure 3-3**), suggesting the presence of counter ions again as excessive chitosan is used.

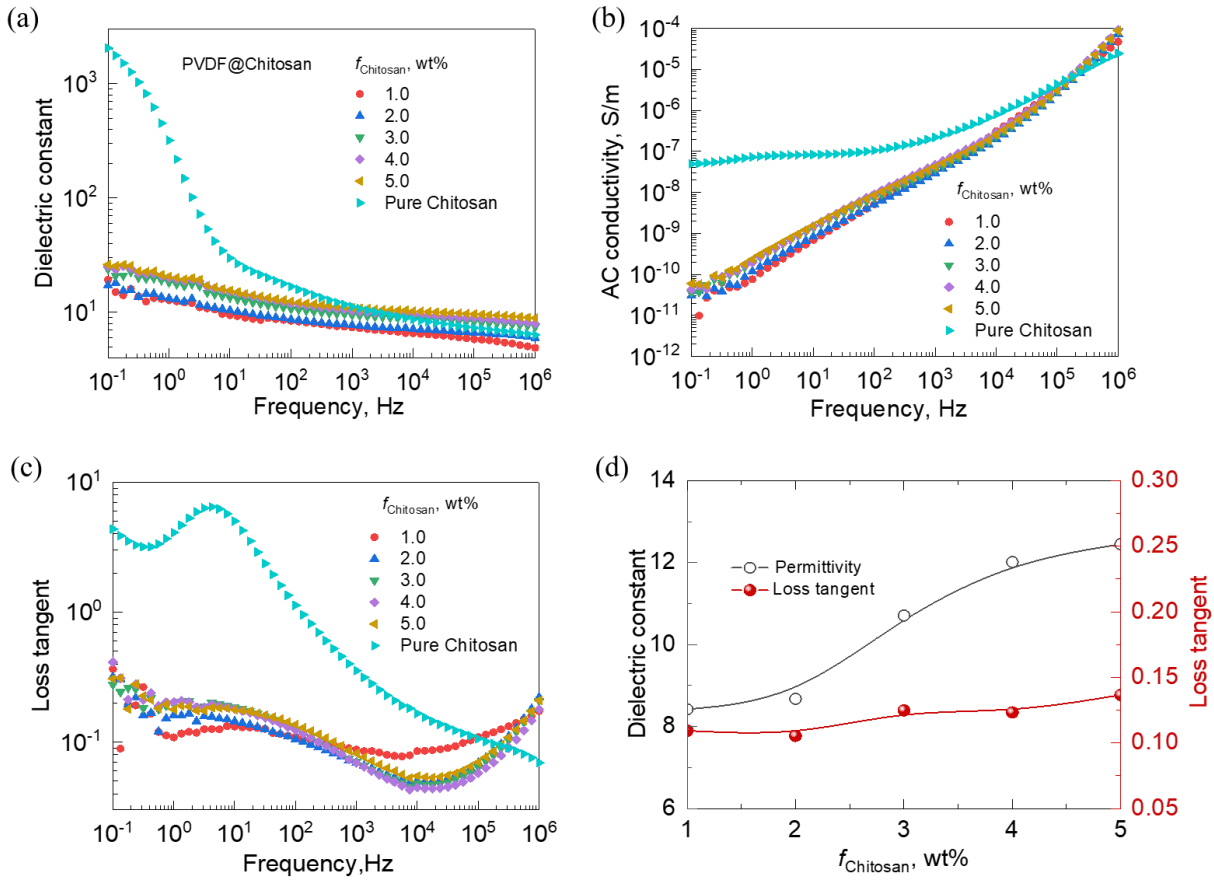

Figure 3-12. (a) Dielectric constant, (b) AC conductivity, and (c) loss tangent of PVDF@chitosan composite films as a function of frequency and chitosan dosage ranging from 1 wt% to 5 wt%. (d) The variation of dielectric constant and loss tangent at 100 Hz as a function of chitosan content.

Overall, the PVDF@chitosan nanocomposite films at the isoelectric point are indeed electrically insulated and pretty interesting for dielectric applications. Although the permittivity at this point was reduced, but the insulating properties (low conductivity, and low dielectric losses) were largely improved. The association between oppositely charged colloids potentially opens a new route toward dielectric materials for energy storage. Actually, the dielectric properties can be tailored in demand by simply changing the ratio of these two oppositely charged species.

3.3.8 Dielectric Breakdown Strength of PVDF@chitosan Films

Generally, as compared to solvent-processed materials, waterborne polymer films tend to have relatively more ions and suffer from lower breakdown strength if the ions are not well confined. Herein, the permittivity of PVDF@chitosan films decreases to ~38% of pure latex film because of the neutralization of charges on latex particles. However, the improved insulating properties are promising to enable the materials potentially sustain a higher voltage. The energy density of linear dielectrics is proportional to the permittivity yet quadratically scales with the electric field (Equation 1.19). So an increased energy density can be eventually expected if the breakdown strength increases by 62%.

We have recorded the maximum voltages that were incrementally applied until the dielectric failure at 15 locations of each sample. The breakdown strength E_b and shape factor β are calculated by a linear fit using the Weibull failure statistics. The experimental data and the fitting results have been listed in **Table 3-4** and plotted in **Figure 3-13**. E_b of pure PVDF latex film was found to be 226 MV/m, which is far inferior to those (from 350 MV/m to 400 MV/m) achieved in typical PVDF films via conventional solution casting or melt-extruding[41-42]. The reasons behind arise from the presence of counter ions in the pure PVDF latex film, on the one hand, and from the large number of nanometer-sized cracks and defects formed during the solidification of latex solutions, on the other hand. In detail, under a high electric field, the mobile charge is excited in the film and can be transported to form a leaky conductive current, making the material susceptible to breakdown. In addition, as a wettable film that contains

suspensions of colloidal PVDF nanoparticles is cast and dried on the substrate, the evaporation of the aqueous solution results in a concentration of nanoparticles into a closely packed array of nanoparticles. The pressure generated by the liquid meniscus between the capillary colloidal particles causes the dried film crack to release the stress. Such physical defects coupled with the existence of counter ions inevitably lead to a reduction in breakdown strength. It is extremely difficult to achieve smooth, uniform, macroscopic pure PVDF latex films that are free of nanosized voids or cracks if no additives are used.

The introduction of a small amount of chitosan greatly improves the breakdown strength of PVDF latex films (**Figure 3-13**). The breakdown strength of PVDF@chitosan nanocomposite continuously increases with chitosan content and reaches the peak value of 578.42 MV/m at the isoelectric point (0.8 wt%), representing an enhancement of 155.6%. Such extremely high voltage tolerance can be associated with the lowest conductivity and dielectric losses at this point (**Figure 3-11**). Beyond the isoelectric point, the breakdown strength declines rapidly with adding more chitosan.

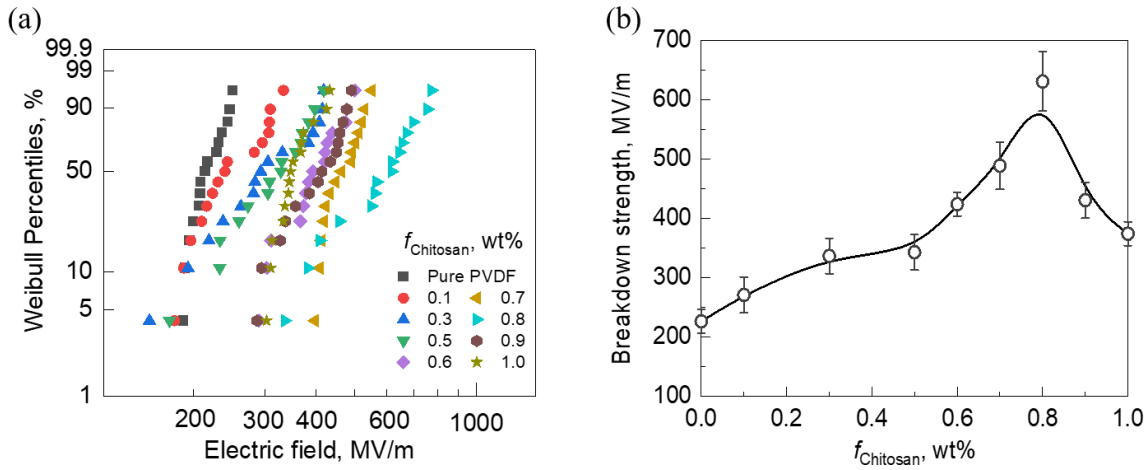

Figure 3-13. (a) Failure probability of dielectric breakdown deduced from Weibull distribution and (b) E_b for neat PVDF latex film, and PVDF@chitosan composite films at various chitosan dosages.

A deep understanding into the dielectric breakdown behavior can be gained by taking account of the flocculation process and the morphology of achieved PVDF@chitosan nanocomposite film. As approaching the isoelectric point, the negatively charged PVDF

nanoparticles are gradually neutralized and linked together via bridging of chitosan segments, which drives the formation of jammed, disordered assemblies and releases the counter ions from the solid phase into the aqueous liquid phase. More approaching the isoelectric point, fewer counter ions remained in the PVDF@chitosan bulk phase and higher breakdown strength of the resultant nanocomposite films. In addition to the counter ion effect, it should be noted that the chitosan tends to wrap the PVDF nanoparticles as a consequence of bridging, which prevents the coalescence between PVDF nanoparticles and drives the self-assembly of PVDF nanoparticles to form closely packed but segregated thin film. Such structure is highly favorable for eliminating leakage currents with barriers between polarizable PVDF particles. The charge-neutral state of the PVDF@chitosan association coupled with the segregated nanostructures contribute to the conspicuous improvement in dielectric breakdown strength.

Table 3-4. E_b and β of pure PVDF, chitosan and their composites at various mass ratios

Chitosan content, wt%	E_b, MV/m	β
Pure PVDF	226.33	12.04
0.1	270.91	5.71
0.3	356.53	4.71
0.5	371.73	5.35
0.6	423.83	7.48
0.7	488.40	10.82
0.8	578.42	4.81
0.9	445.61	5.64
1.0	370.25	8.84
2.0	348.72	8.37
3.0	315.43	10.56
4.0	267.84	7.45
5.0	235.87	10.96
Pure chitosan	126.57	5.45

When the chitosan content increases from 1 wt% to 5 wt%, the breakdown strength of the composites monotonically decreases, as shown in **Figure 3-14**. At this stage, the closely packed PVDF nanostructure can always remain, but the excessive dosage of chitosan would attract negative counter ions to reside at the particle boundaries and make the barrier ionic conductive.

When subjected to a high electric field, the induced ionic conductive current triggers the dielectric breakdown. More chitosan was introduced, and lower dielectric breakdown strength was observed in the composite film in **Figure 3-14** (a). Pure chitosan film displays the lowest E_b of 126 MV/m, which is reconciled with the observation of the high ionic conduction (**Figure 3-12**). Being the same as ion-containing PVA films with 2 wt% of CH_3COONa (**Figure 3-4**), pure chitosan film is not dielectric in nature, being considered a solid electrolyte.

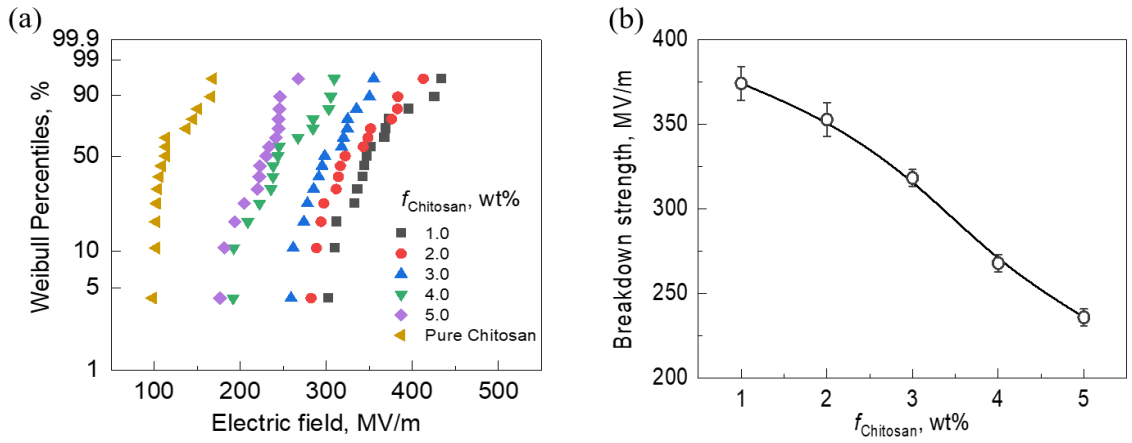

Figure 3-14. (a) Failure probability of dielectric breakdown deduced from Weibull distribution and (b) E_b for neat PVDF, and their composites with various chitosan loadings.

3.3.9 Energy Density of PVDF@chitosan Nanocomposite Films

Thanks to the adequately enhanced breakdown strength, an improved energy density can be envisioned in spite of the reduced permittivity in PVDF@chitosan nanocomposite films. We characterized the polarizations and energy storage densities of PVDF@chitosan films at high electric fields. The *P*-*E* loops of each film were measured first under a fixed electric field (200 MV/m), which is close to the breakdown strength of pure PVDF latex film. As shown in **Figure 3-15** (a), with increasing chitosan content, the maximum electric displacement P_m decreases and the hysteresis loop becomes slimmer, both of which reach the limit at 0.8 wt%. This indicates that the neutralization of PVDF nanoparticles partially loses the polarization capability related to the ion activities in the system but gains a larger portion of the discharged energy. The PVDF@chitosan film at the isoelectric point displays the highest breakdown strength (**Figure 3-13**). It is interesting to evaluate its polarization at high fields until the

breakdown strength. As shown in **Figure 3-15** (b), P_m-P_r increases with the electric field and reaches 40 mC/m^2 at 630 MV/m. Because of the increased P_r, the dielectric losses become more significant at elevated fields but the loops are still slim.

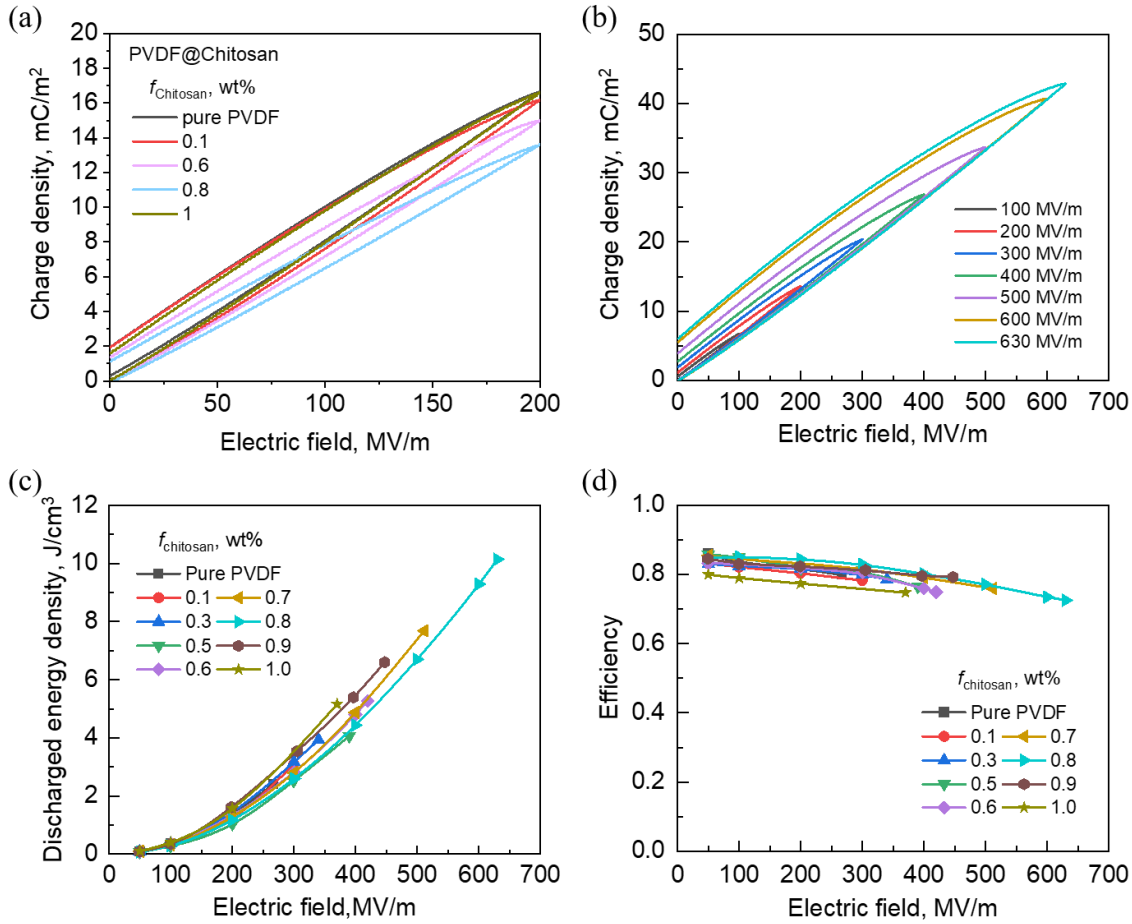

Figure 3-15. (a) *P*−*E* loops of pure PVDF latex film, and PVDF@chitosan nanocomposite films with various chitosan contents. (b) *P*−*E* loops of PVDF@0.8 wt% chitosan composite film at different electric fields. (c) Discharged energy density and (d) charge/discharge efficiency as a function of electric field for pure PVDF, and PVDF@chitosan nanocomposite films.

The discharge energy densities are calculated based on the *P*-*E* loops of each film at different electric fields until their breakdown strengths and are shown in **Figure 3-15** (c). The maximum energy storage density of the composite increases first with adding chitosan until reaching the isoelectric point and then starts to decrease with more chitosan incorporated. At the same relatively low operating fields, the PVDF@0.8 wt% chitosan composite displays a lower energy density than its counterparts. However, near its breakdown strength, the

maximum discharged energy density reaches 10.14 J/cm^3 at 630 MV/m, which is more than four times higher than the energy density of pure PVDF (U_e=2.4 J/cm^3) and more than twice larger than typical PVDF materials. Such conspicuously improved discharged energy density is attributed to the highest breakdown strength and lowest energy losses of the PVDF@0.8 wt% chitosan composite. **Figure 3-15** (d) shows the charge/discharge efficiency η of each sample as a function of the applied electric field. Each film displays a more significant energy loss at higher electric fields. However, the η of PVDF@0.8 wt% chitosan composite film is higher than its counterparts at each field. The efficiency is more than 72%, even near its breakdown strength.

In addition, we have clarified the effect of excessive chitosan content on energy storage performances. **Figure 3-16** shows the maximum energy storage density and efficiency of PVDF@chitosan composite film with chitosan content ranging from 1 wt% to 5 wt%. In spite of the enhanced polarization (**Figure 3-12**), the maximum discharged energy densities decrease with chitosan content increasing, because the improvement in the stored energy cannot fully compensate for the additional dissipated energy derived from the conduction losses during discharging. The more chitosan added into PVDF, the lower the maximum discharged energy density of the composites. This is derived from the decreased breakdown strength as well as the increased conduction losses, both of which lead to a strikingly declined charge/discharge efficiency with increasing chitosan content at each electric field, as shown in **Figure 3-16** (b). It is difficult to perform *P-E* loop tests on pure chitosan films, a negative efficiency was observed from 50 MV/m, indicating that they are not capable of storing charges at a high field because of their ionic conduction feature. Again, strong polarization in ion-containing materials can give rise to a remarkable dielectric constant, but not a superior energy storage density because of the accompanying high losses. This conclusion is also validated in most of the percolative polymer nanocomposites based on electronic conductive inclusions[43].

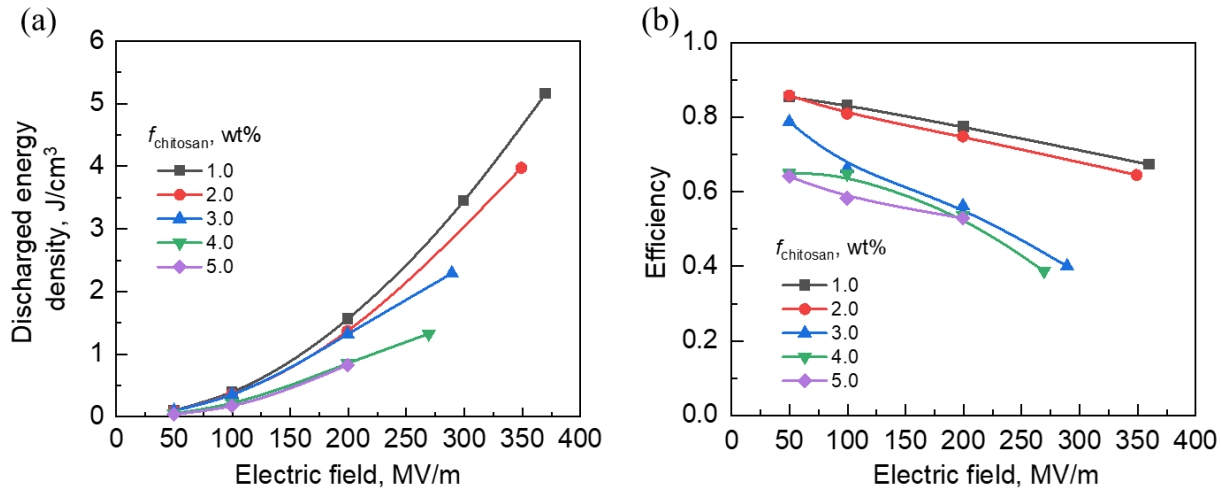

Figure 3-16. (a) Discharged energy density and (b) charge/discharge efficiency as a function of electric field for PVDF@chitosan nanocomposite films with chitosan content ranging from 1 wt% to 5 wt%.

It is highly desirable to achieve concurrently a high energy density and a high charge/discharge efficiency for the energy storage application of dielectric materials. We compared the energy storage properties of PVDF@0.8 wt% chitosan composite with most of the previously reported polymeric dielectric materials, in particular with PVDF-based composite films. As shown in **Figure 3-17**, the benchmark BOPP dielectric films have an efficiency as high as 95 %, which competes with most polymers. However, their energy density is rather low (2-3 J/cm^3). On the other hand, PVDF- or PVDF terpolymer-based composites enjoy elevated energy densities, but the strongly coupled dipoles and large ferroelectric domains in these polymers cause high energy barriers for ferroelectric switching, leading to pronounced hysteresis loops and limited charge/discharge efficiency (η~50% -60%)[44,45]. Indeed, the charge-neutral PVDF@0.8 wt% chitosan film shows a combination of high energy density (~10.1 J/cm^3) and high efficiency (~72%). In addition, it should be noted that most polymer dielectrics are either melt-extruded at high temperatures or processed in hazardous organic solvents. Their manufacturing process is unsustainable. Our strategy relies on environmentally benign processes and holds great promise for "green" manufacturing of next generation high-energy dielectric materials.

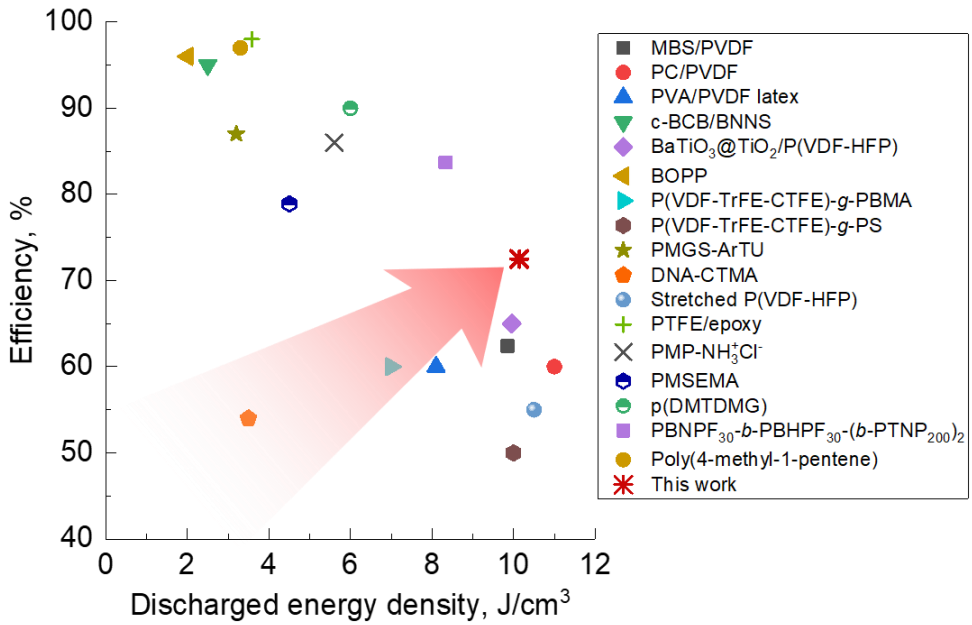

Figure 3-17. The comparison of energy storage density and charge/discharge efficiency between PVDF@0.8 wt% chitosan composite and most of the previously reported polymeric dielectric materials, including MBS/PVDF[41], PC/PVDF[44], PVA/PVDF latex[46], c-BCB/BNNS[3], $BaTiO_3$@TiO2/P(VDF-HFP)[47], BOPP[48], P(VDF-TrFE-CTFE)-g-PBMA[49], P(VDF-TrFE-CTFE)-g-PS[45], PMGS-ArTU[50], DANN-CTMA[51], Stretched P(VDF-HFP)[20], PVDF/Epoxy[52], PMP-$NH_3^+Cl^-$[53], PMSEMA[51], p(DMTDMG)[54], $PBNPF_{30}$-b-$PBHPF_{30}$-(b-$PTNP_{200}$)$_2$[48], Poly(4-methyl-1-pentene)[53].

3.3.10 Power Density of PVDF@chitosan Films

In combination with high energy density, power density also plays an important role in energy storage devices. It determines the charging and discharging rates. A high-speed capacitor discharge circuit (**Figure 1-8** (a)) with a high-voltage MOSFET switch was used to evaluate the discharge rate of PVDF@0.8 wt% chitosan composite and the typical BOPP film. The two samples are initially charged at 200 MV/m and then discharged across a 10 kΩ load resistor in series with the sample capacitor. The discharging curves of the PVDF@0.8 wt% chitosan composite and typical BOPP film are shown in **Figure 3-18** (a). The voltage *U*(t) over the load resistor, drops exponentially with time. The discharged energy density can be then calculated by Equation (1-21, 1-22), and plotted as a function of time in **Figure 3-18** (b). As described in Chapter 2, the discharge time is defined as the time required to achieve 95% of the final discharge energy. The PVDF@0.8 wt% chitosan composite releases a stored energy of 1.148 J/cm^3 at a rate of 1.248 μs, while the BOPP releases a stored energy of 0.299 J/cm^3 at a

rate of 1.168 µs. Thus, the PVDF@0.8 wt% chitosan composite exhibits a higher power density (0.92 MW/cm^3) as compared to 0.26 MW/cm^3 of BOPP.

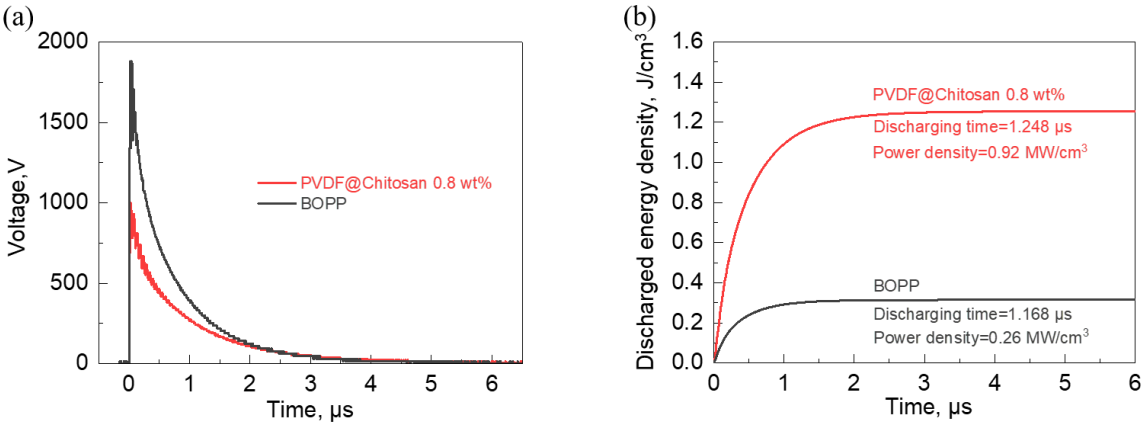

Figure 3-18. (a) The voltage (b) and discharged energy density as a function of time. The BOPP and PVDF@0.8 wt% chitosan composites film have respectively a thickness of 9.8 µm and 5 µm.

Moreover, the stability of the material is a predominant criterion for practical applications. The cyclic charging/discharging of the PVDF@0.8 wt% chitosan composite and the BOPP film was performed under a fixed electric field of 200 MV/m to assess the stability of both two samples. As shown in **Figure 3-19**, the energy storage density of the composite containing 0.8 wt% chitosan maintains constant, without degradation over 7000 cycles of charge/discharge. Overall, the PVDF@0.8 wt% chitosan composite material has an excellent combination of properties, i.e., high energy and power density, excellent charge/discharge efficiency and cycle stability, rivaling the benchmark BOPP dielectrics.

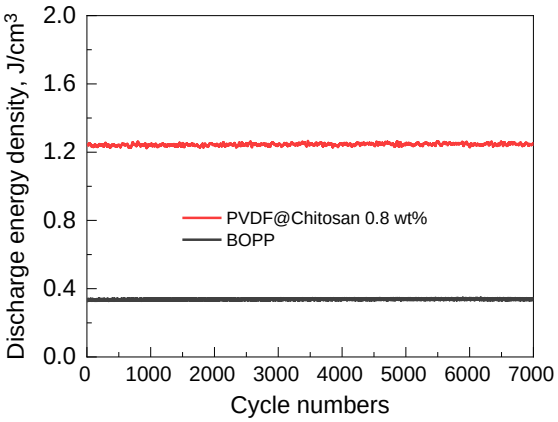

Figure 3-19. Cyclic charge/discharge performances of PVDF@0.8 wt% chitosan composite and the BOPP film under an electric field of 200 MV/m.

In addition to the energy and power density, the leakage current is another essential characteristic for the selection of dielectric capacitors for the end-users. We performed the *P-E* loop test at a constant electric field of 100 MV/m during 1ms and recorded the leakage current through samples. The closer to the isoelectric point (0.8 wt%), the lower the leakage current. The PVDF@0.8 wt% chitosan composite shows the lowest leakage current (10^{-6} A/cm^2) among all the composites. This is again an evidence of the charge neutralization of the association of PVDF and chitosan at the critical mass ratio (0.8 wt%).

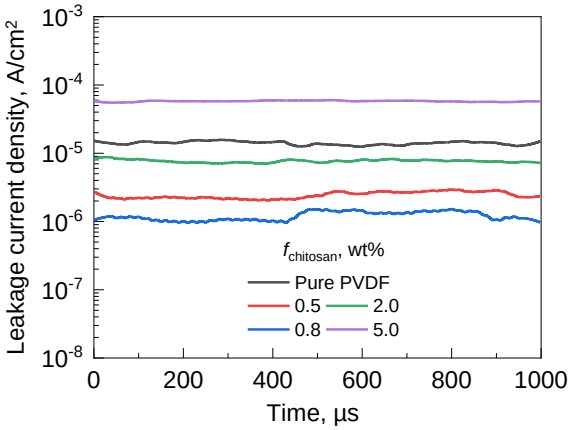

Figure 3-20. The leakage currents at a constant electric field of 100 MV/m for PVDF@chitosan nanocomposite films at different chitosan dosages.

3.4 Conclusion

In summary, we have successfully achieved a flexible, robust, and high-energy dielectric material using charge-stabilized PVDF latex as starting material. By controlling the level of charge neutralization and passivation of PVDF particles via establishing associations of PVDF and cationic chitosan, we can tailor the distribution of the counter ions and in turn suppress their adverse effect on the energy storage at elevated electric fields. Moreover, chitosan macromolecules bridge the PVDF latex particles together yet prevent their coalescence. It drives the assembly of PVDF nanoparticles to form a closely packed but segregated nanostructure. At the neutral charge point (chitosan/PVDF mass ratio=0.8/99.2), such a structure can highly profit from the high polarization of PVDF while eliminating leakage currents with chitosan barriers between particles. With all of these optimized features, the PVDF@0.8 wt% chitosan composite demonstrates superior breakdown strength (578 MV/m),

energy density (10 J/cm^3) and energy storage efficiency (72%) to most of the state-of-the-art polymeric dielectrics. Moreover, a high power density of 0.92 MW/cm^3 and mechanical breaking elongation of 835% are also achieved. This work provides a new route toward high-energy dielectric materials using water-based colloid suspensions and processes.

References

1. Li, H.; Yang, T.; Zhou, Y.; Ai, D.; Yao, B.; Liu, Y.; Li, L.; Chen, L. Q.; Wang, Q., Enabling high-energy-density high-efficiency ferroelectric polymer nanocomposites with rationally designed nanofillers. *Advanced Functional Materials* **2021,** *31* (1), 2006739.
2. Pan, H.; Li, F.; Liu, Y.; Zhang, Q.; Wang, M.; Lan, S.; Zheng, Y.; Ma, J.; Gu, L.; Shen, Y., Ultrahigh–energy density lead-free dielectric films via polymorphic nanodomain design. *Science* **2019,** *365* (6453), 578-582.
3. Li, Q.; Chen, L.; Gadinski, M. R.; Zhang, S.; Zhang, G.; Li, H. U.; Iagodkine, E.; Haque, A.; Chen, L.-Q.; Jackson, T. N., Flexible high-temperature dielectric materials from polymer nanocomposites. *Nature* **2015,** *523* (7562), 576-579.
4. Dang, Z.-M.; Yuan, J.-K.; Zha, J.-W.; Zhou, T.; Li, S.-T.; Hu, G.-H., Fundamentals, processes and applications of high-permittivity polymer–matrix composites. *Progress in materials science* **2012,** *57* (4), 660-723.
5. Chu, B.; Zhou, X.; Ren, K.; Neese, B.; Lin, M.; Wang, Q.; Bauer, F.; Zhang, Q., A dielectric polymer with high electric energy density and fast discharge speed. *Science* **2006,** *313* (5785), 334-336.
6. Simon, P.; Gogotsi, Y., Materials for electrochemical capacitors. In *Nanoscience and technology: a collection of reviews from Nature journals*, World Scientific: 2010; pp 320-329.
7. Palneedi, H.; Peddigari, M.; Hwang, G. T.; Jeong, D. Y.; Ryu, J., High-performance dielectric ceramic films for energy storage capacitors: progress and outlook. *Advanced Functional Materials* **2018,** *28* (42), 1803665.
8. Dang, Z. M.; Yuan, J. K.; Yao, S. H.; Liao, R. J., Flexible nanodielectric materials with high permittivity for power energy storage. *Advanced Materials* **2013,** *25* (44), 6334-6365.
9. Zhang, Q.; Chen, X.; Zhang, B.; Zhang, T.; Lu, W.; Chen, Z.; Liu, Z.; Kim, S. H.; Donovan, B.; Warzoha, R. J., High-temperature polymers with record-high breakdown strength enabled by rationally designed chain-packing behavior in blends. *Matter* **2021,** *4* (7), 2448-2459.
10. Xu, B.; Íñiguez, J.; Bellaiche, L., Designing lead-free antiferroelectrics for energy storage. *Nature communications* **2017,** *8* (1), 1-8.
11. Bai, H.; Zhu, K.; Wang, Z.; Shen, B.; Zhai, J., 2D Fillers Highly Boost the Discharge Energy Density of Polymer-Based Nanocomposites with Trilayered Architecture. *Advanced Functional Materials* **2021,** *31* (41), 2102646.

12. Kim, J.; Saremi, S.; Acharya, M.; Velarde, G.; Parsonnet, E.; Donahue, P.; Qualls, A.; Garcia, D.; Martin, L. W., Ultrahigh capacitive energy density in ion-bombarded relaxor ferroelectric films. *Science* **2020,** *369* (6499), 81-84.
13. Yao, Z. H.; Song, Z.; Hao, H.; Yu, Z. Y.; Cao, M. H.; Zhang, S. J.; Lanagan, M. T.; Liu, H. X., Homogeneous/Inhomogeneous-Structured Dielectrics and their Energy-Storage Performances. *Advanced Materials* **2017,** *29* (20).
14. McPherson, J. W.; Kim, J.; Shanware, A.; Mogul, H.; Rodriguez, J., Trends in the ultimate breakdown strength of high dielectric-constant materials. *IEEE transactions on electron devices* **2003,** *50* (8), 1771-1778.
15. Tan, D. Q., Review of polymer-based nanodielectric exploration and film scale-up for advanced capacitors. *Advanced Functional Materials* **2020,** *30* (18), 1808567.
16. Wu, X.; Chen, X.; Zhang, Q.; Tan, D. Q., Advanced dielectric polymers for energy storage. *Energy Storage Materials* **2022,** *44*, 29-47.
17. Zhang, X.; Shen, Y.; Zhang, Q.; Gu, L.; Hu, Y.; Du, J.; Lin, Y.; Nan, C. W., Ultrahigh energy density of polymer nanocomposites containing BaTiO3@ TiO2 nanofibers by atomic-scale interface engineering. *Advanced materials* **2015,** *27* (5), 819-824.
18. Huang, X.; Jiang, P., Core–shell structured high-k polymer nanocomposites for energy storage and dielectric applications. *Advanced Materials* **2015,** *27* (3), 546-554.
19. Ren, L.; Li, H.; Xie, Z.; Ai, D.; Zhou, Y.; Liu, Y.; Zhang, S.; Yang, L.; Zhao, X.; Peng, Z., High-Temperature High-Energy-Density Dielectric Polymer Nanocomposites Utilizing Inorganic Core–Shell Nanostructured Nanofillers. *Advanced Energy Materials* **2021,** *11* (28), 2101297.
20. Guan, F.; Pan, J.; Wang, J.; Wang, Q.; Zhu, L., Crystal orientation effect on electric energy storage in poly (vinylidene fluoride-co-hexafluoropropylene) copolymers. *Macromolecules* **2010,** *43* (1), 384-392.
21. Meng, N.; Ren, X.; Santagiuliana, G.; Ventura, L.; Zhang, H.; Wu, J.; Yan, H.; Reece, M. J.; Bilotti, E., Ultrahigh β-phase content poly (vinylidene fluoride) with relaxor-like ferroelectricity for high energy density capacitors. *Nature communications* **2019,** *10* (1), 1-9.
22. Zhang, T.; Chen, X.; Thakur, Y.; Lu, B.; Zhang, Q.; Runt, J.; Zhang, Q., A highly scalable dielectric metamaterial with superior capacitor performance over a broad temperature. *Science advances* **2020,** *6* (4), eaax6622.
23. Jiang, J.; Shen, Z.; Qian, J.; Dan, Z.; Guo, M.; He, Y.; Lin, Y.; Nan, C.-W.; Chen, L.; Shen, Y., Synergy of micro-/mesoscopic interfaces in multilayered polymer nanocomposites induces ultrahigh energy density for capacitive energy storage. *Nano Energy* **2019,** *62*, 220-229.
24. Baer, E.; Zhu, L., 50th anniversary perspective: dielectric phenomena in polymers and multilayered dielectric films. *Macromolecules* **2017,** *50* (6), 2239-2256.
25. Jiang, Y.; Zhang, X.; Shen, Z.; Li, X.; Yan, J.; Li, B. W.; Nan, C. W., Ultrahigh breakdown strength and improved energy density of polymer nanocomposites with gradient distribution of ceramic nanoparticles. *Advanced Functional Materials* **2020,** *30* (4), 1906112.
26. Sun, L.; Shi, Z.; He, B.; Wang, H.; Liu, S.; Huang, M.; Shi, J.; Dastan, D.; Wang, H.,

Asymmetric Trilayer All-Polymer Dielectric Composites with Simultaneous High Efficiency and High Energy Density: A Novel Design Targeting Advanced Energy Storage Capacitors. *Advanced Functional Materials* **2021,** *31* (35), 2100280.

27. Wang, T.; Peng, R. C.; Peng, W.; Dong, G.; Zhou, C.; Yang, S.; Zhou, Z.; Liu, M., 2–2 Type PVDF-Based Composites Interlayered by Epitaxial (111)-Oriented BTO Films for High Energy Storage Density. *Advanced Functional Materials* **2022,** *32* (10), 2108496.
28. Shen, Z. H.; Wang, J. J.; Lin, Y.; Nan, C. W.; Chen, L. Q.; Shen, Y., High-throughput phase-field design of high-energy-density polymer nanocomposites. *Advanced Materials* **2018,** *30* (2), 1704380.
29. Tomer, V.; Randall, C.; Polizos, G.; Kostelnick, J.; Manias, E., High-and low-field dielectric characteristics of dielectrophoretically aligned ceramic/polymer nanocomposites. *Journal of Applied Physics* **2008,** *103* (3), 034115.
30. Tang, H.; Lin, Y.; Sodano, H. A., Enhanced energy storage in nanocomposite capacitors through aligned PZT nanowires by uniaxial strain assembly. *Advanced Energy Materials* **2012,** *2* (4), 469-476.
31. Renna, L. A.; Boyle, C. J.; Gehan, T. S.; Venkataraman, D., Polymer nanoparticle assemblies: a versatile route to functional mesostructures. *Macromolecules* **2015,** *48* (18), 6353-6368.
32. DeFusco, A.; Sehgal, K. C.; Bassett, D. R., Overview of uses of polymer latexes. In *Polymeric Dispersions: Principles and Applications*, Springer: 1997; pp 379-396.
33. Alfonso, M.; Yuan, J.; Tardani, F.; Neri, W.; Colin, A.; Poulin, P., Absence of giant dielectric permittivity in graphene oxide materials. *Journal of Physics: Materials* **2019,** *2* (4), 045002.
34. Claude, J.; Lu, Y.; Wang, Q., Effect of molecular weight on the dielectric breakdown strength of ferroelectric poly (vinylidene fluoride-chlorotrifluoroethylene) s. *Applied Physics Letters* **2007,** *91* (21), 212904.
35. Hunter, R. J., *Foundations of colloid science*. Oxford university press: 2001.
36. Uskoković, V., Dynamic light scattering based microelectrophoresis: main prospects and limitations. *Journal of dispersion science and technology* **2012,** *33* (12), 1762-1786.
37. Li, H.; Fauquignon, M.; Haddou, M.; Schatz, C.; Chapel, J.-P., Interfacial Behavior of Solid-and Liquid-like Polyelectrolyte Complexes as a Function of Charge Stoichiometry. *Polymers* **2021,** *13* (21), 3848.
38. Rao, V.; Johns, J., Mechanical properties of thermoplastic elastomeric blends of chitosan and natural rubber latex. *Journal of applied polymer science* **2008,** *107* (4), 2217-2223.
39. Gaina, C.; Gaina, V.; Cristea, M., Poly (Urethane–Urea) Varnishes Containing Tributyltin Groups. *Journal of Inorganic and Organometallic Polymers and Materials* **2009,** *19* (2), 157-165.
40. Yuan, J.-K.; Yao, S.-H.; Dang, Z.-M.; Sylvestre, A.; Genestoux, M.; Bai1, J., Giant dielectric permittivity nanocomposites: realizing true potential of pristine carbon nanotubes in polyvinylidene fluoride matrix through an enhanced interfacial interaction. *The Journal of Physical Chemistry C* **2011,** *115* (13), 5515-5521.
41. Zheng, M.-S.; Zha, J.-W.; Yang, Y.; Han, P.; Hu, C.-H.; Dang, Z.-M., Enhanced breakdown strength of poly (vinylidene fluoride) utilizing rubber nanoparticles for energy

storage application. *Applied Physics Letters* **2016,** *109* (7), 072902.

42. Yao, L.; Wang, D.; Hu, P.; Han, B. Z.; Dang, Z. M., Synergetic Enhancement of Permittivity and Breakdown Strength in All-Polymeric Dielectrics toward Flexible Energy Storage Devices. *Advanced Materials Interfaces* **2016,** *3* (13), 1600016.
43. Zhang, L.; Yuan, S.; Chen, S.; Wang, D.; Han, B.-Z.; Dang, Z.-M., Preparation and dielectric properties of core–shell structured Ag@ polydopamine/poly (vinylidene fluoride) composites. *Composites science and Technology* **2015,** *110*, 126-131.
44. Mackey, M.; Schuele, D. E.; Zhu, L.; Flandin, L.; Wolak, M. A.; Shirk, J. S.; Hiltner, A.; Baer, E., Reduction of dielectric hysteresis in multilayered films via nanoconfinement. *Macromolecules* **2012,** *45* (4), 1954-1962.
45. Guan, F.; Wang, J.; Yang, L.; Tseng, J.-K.; Han, K.; Wang, Q.; Zhu, L., Confinement-induced high-field antiferroelectric-like behavior in a poly (vinylidene fluoride-co-trifluoroethylene-co-chlorotrifluoroethylene)-graft-polystyrene graft copolymer. *Macromolecules* **2011,** *44* (7), 2190-2199.
46. Che, J.; Neri, W.; Ly, I.; Poulin, P.; Zakri, C.; Yuan, J., Waterborne Nanocomposites with Enhanced Breakdown Strength for High Energy Storage. *ACS Applied Energy Materials* **2020,** *3* (9), 9107-9116.
47. Kang, D.; Wang, G.; Huang, Y.; Jiang, P.; Huang, X., Decorating TiO2 nanowires with BaTiO3 nanoparticles: a new approach leading to substantially enhanced energy storage capability of high-k polymer nanocomposites. *ACS applied materials & interfaces* **2018,** *10* (4), 4077-4085.
48. Chen, J.; Wang, Y.; Li, H.; Han, H.; Liao, X.; Sun, R.; Huang, X.; Xie, M., Rational design and modification of high-k bis (double-stranded) block copolymer for high electrical energy storage capability. *Chemistry of Materials* **2018,** *30* (3), 1102-1112.
49. Li, J.; Hu, X.; Gao, G.; Ding, S.; Li, H.; Yang, L.; Zhang, Z., Tuning phase transition and ferroelectric properties of poly (vinylidene fluoride-co-trifluoroethylene) via grafting with desired poly (methacrylic ester) s as side chains. *Journal of Materials Chemistry C* **2013,** *1* (6), 1111-1121.
50. Hougham, G. G.; Jean, Y., Relative contributions of polarizability and free volume in reduction of refractive index and dielectric constant with fluorine substitution in polyimides by positron annihilation spectroscopy. *Macromolecular Chemistry and Physics* **2014,** *215* (1), 103-110.
51. Joyce, D. M.; Venkat, N.; Ouchen, F.; Singh, K. M.; Smith, S. R.; Grabowski, C. A.; Terry Murray, P.; Grote, J. G., Deoxyribonucleic acid-based hybrid thin films for potential application as high energy density capacitors. *Journal of Applied Physics* **2014,** *115* (11), 114108.
52. Gao, Y.; Chen, S.; Kong, B.; Wang, W.; Cheng, Y. In *Epoxy/PVDF/Epoxy Composite Film with Concurrent Enhancement in Energy Density and Charge-discharge Efficiency*, 2020 5th Asia Conference on Power and Electrical Engineering (ACPEE), IEEE: 2020; pp 866-870.
53. Zhang, M.; Zhang, L.; Zhu, M.; Wang, Y.; Li, N.; Zhang, Z.; Chen, Q.; An, L.; Lin, Y.; Nan, C., Controlled functionalization of poly (4-methyl-1-pentene) films for high energy storage applications. *Journal of Materials Chemistry A* **2016,** *4* (13), 4797-4807.

54. Treich, G. M.; Nasreen, S.; Mannodi Kanakkithodi, A.; Ma, R.; Tefferi, M.; Flynn, J.; Cao, Y.; Ramprasad, R.; Sotzing, G. A., Optimization of organotin polymers for dielectric applications. *ACS Applied Materials & Interfaces* **2016,** *8* (33), 21270-21277.

Chapter 4

Colloidal Nanocomposites Based on PS Latex and Bentonite Nanosheets

4.1 Introduction

Waterborne dielectric materials with high polarization coupled with high breakdown strength are highly needed today to manufacture in a more sustainable manner the dielectric capacitors for high-energy storage applications. Colloidal is a promising class of water-processable materials. They are attractive building blocks for the water-based assembly of solids with emergent physical properties that arise from the size, shape, and composition-dependent characteristics of the constituent colloidal[1-2].

In the preceding chapter, we have constructed a flexible, robust and high-energy dielectric material using PVDF latex nanoparticles as building blocks. Being similar to most of the colloidal, PVDF latex nanoparticles are charge stabilized in water. The existence of counter ions that are used to balance the particle charges is troublesome for exploring the energy storage capability of PVDF latex film. We have successfully increased the level of charge neutralization of PVDF particles and suppressed the adverse effect of counter ions by establishing associative complexation of anionic PVDF and cationic polyelectrolyte chitosan. The protonated chitosan macromolecules are found to be highly efficient to drive the assembly of PVDF nanoparticles to form a closely packed yet segregated nanostructure. Such charge-neutral nanostructure endows the PVDF@chitosan films with sufficient mechanical strength, excellent dielectric insulation and high-energy storage capability.

The objective of this chapter is to verify the versatility of the concept and to extend the validated principles to other colloidal systems, such as polystyrene (PS) latex and bentonite nanosheet suspensions, both of which are negative charge stabilized and represent the organic and inorganic colloidal respectively. Bioresource chitosan is again protonated to serve as cationic polyelectrolyte. The charge neutralization of PS@chitosan and bentonite@chitosan associations will be experimentally detected by the measurement of the zeta potential of the solutions at different dosages of chitosan. The effect of the level of charge neutralization on the overall dielectric properties, in particular, the high-field energy storage performances will be addressed. The similarity and differences between the current systems and the preceding PVDF@chitosan materials will be also highlighted in this chapter.

4.2 Experiment Section

4.2.1 Materials

PS latex solution with a solid content of 2.6 wt% and a diameter of 0.202 μm was supplied by Polyscience Inc in Germany under the trade name of Polybead@Polystyrene 0.2 Micron Microspheres (CAS number: 9003-53-6). These non-functionalized particles contain a slight anionic charge from sulfate ester. PS latex was used as received. Bentonite was made in EEC, Prolabo, whose code article is 21792.292. Chitosan pellets were obtained from Sigma-Aldrich Chemical Company, USA, under code 14508. Acetic acid used for the protonation of chitosan is supplied by Sigma-Aldrich Chemical Company, Germany, and the CAS: 64-19-7. Polyvinyl alcohol was received from Sigma-Aldrich chemical company in Germany under the trade name of Mowiol 20-98 (CAS number: 9002-89-5) with a molecular weight M_w = 125 000 g/mol and a degree of hydrolysis of 99%. Hydrochloric acid (HCl) was provided by Sigma-Aldrich chemical company in Germany with a CAS number 7647-01-0 whose assay is 37%. Deionized water (Q-Gard 00D2) with a resistivity above 18.2 MΩ cm at 25°C. Ethanol was supplied by Atlantic labo with a CAS number 64-17-5, which is 96% in purity.

4.2.2 Exfoliation of Bentonite Nanosheets

The process of the exfoliation of bentonite nanosheets and the preparation of their aqueous solution is schematically illustrated in **Figure 4-1**. Following the established protocol in literature[3], the bentonite powder was first washed extensively with ethanol and 1 M HCl to remove excessive surfactant and ionic impurities resulting from the cation exchange process. In detail, the bentonite powders were first dispersed in ethanol by magnetic stirring over 1 day. The washed powders were then collected by gentle centrifugation at 3000 g for 30 min. Such a process was repeated three times before an end washing by 1 M HCl. Subsequently, the fully washed bentonite was exfoliated by liquid phase stripping as follows: 10 g bentonite was dissolved in 200 mL water, and the mixture solution was stirred over 2 h at room temperature. Then the mixture was tip sonicated at 30% amplitude for 1 h to exfoliate bentonite powers into nanosheets. The nanosheet solution was then centrifuged at 7000 g for 0.5 h in order to

precipitate the large-sized unexfoliated aggregates. The supernatant was withdrawn for a further centrifugation process at 30000 g for 0.5 h. Afterward, the bottom bentonite gel was collected after removing the supernatant. Finally, the gel was diluted in an aqueous solution to formulate a well-dispersed nanosheet solution with a concentration of 0.3 wt% for all the subsequent experiments.

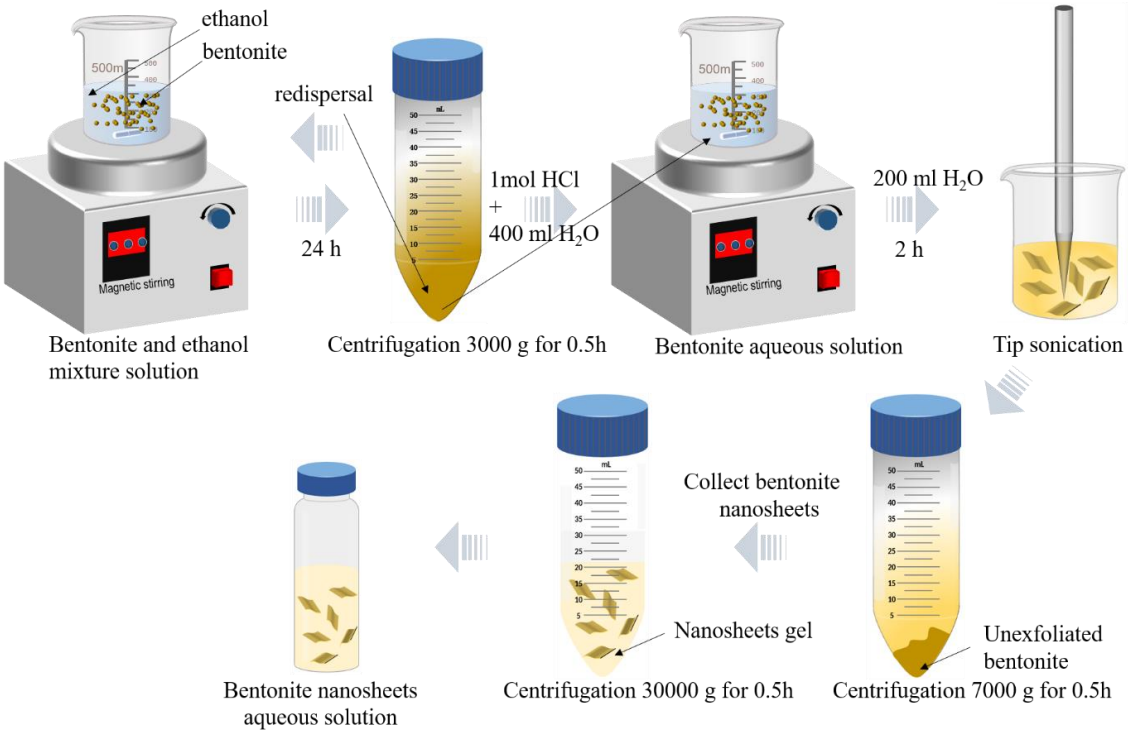

Figure 4-1. Scheme of the protocol for the exfoliation and the preparation of bentonite nanosheet aqueous solutions.

4.2.3 Fabrication of Colloidal Nanocomposite Films

Chitosan pellets were first dissolved in 1.5 wt% acetic acids at room temperature and then magnetically stirred at 300 rpm for 2 h at room temperature. The solution was then heated at 120℃ over 10 min for sterilization purposes and filtrated afterward to obtain a fully dissolved aqueous solution with a measured concentration of 0.66 wt%. The PVA raw materials were dissolved in deionized water in an oven at 90℃ for 4 h. Thermal heating accelerates the dissolution process. After filtration of undissolved pieces, PVA aqueous solution has a solute concentration of 6.5 wt%. The process flow to make chitosan and PVA aqueous solutions have been schematically illustrated in the preceding chapters.

Various amounts of protonated chitosan were mixed with PS latex and bentonite nanosheet suspensions respectively by magnetic stirring at room temperature for 4 h and followed by a tip sonication for 2 h. After several hours of resting, both colloidal particles precipitated at low chitosan dosages, while dispersed homogeneously again as dosing more chitosan (**Figure 4-2**). The PS and chitosan mixture solution was cast directly on an aluminum plate and dried in an oven at 70°C to obtain solidified PS@chitosan nanocomposite with a thickness of 5 μm ~8 μm. To improve the film-forming properties of bentonite nanosheets, 20 wt% PVA was added to the mixture to serve as binders. The final solute concentration of different aqueous mixtures is kept at 0.64 wt% by adding different amounts of deionized water. The bentonite@chitosan/PVA film was finally cast from a 3 mL well-mixed solution in an aluminum petri dish. The water was firstly evaporated at room temperature overnight and then followed by incubation at 100°C for 20 h in a vacuum oven. Before the dielectric test, all the dried films were hot-pressed at 110°C for 3 min under 40 MPa to eliminate the structural defects, as did for the preparation of PVDF@chitosan films in Chapter 3.

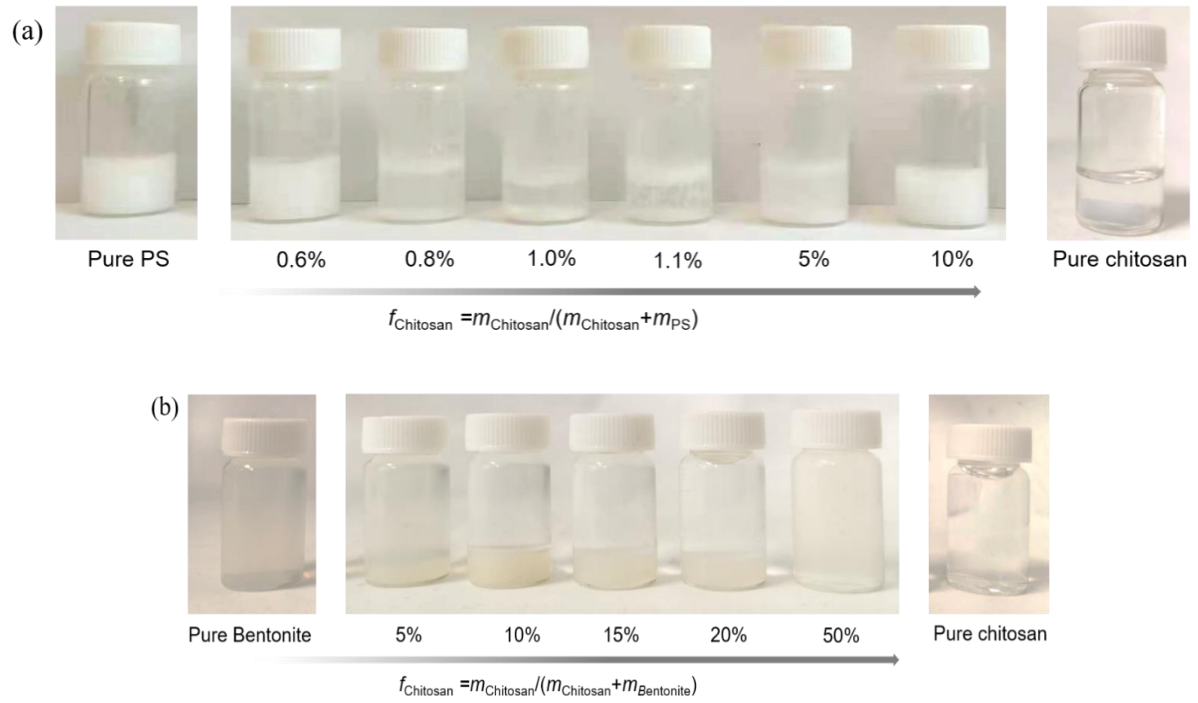

Figure 4-2. (a) Photographs of pure PS latex, pure chitosan aqueous solution and the mixture solution of PS latex and chitosan at different dosages of chitosan. (b) Images of pure bentonite nanosheet aqueous solution, pure chitosan aqueous solution and their mixture solution at different mixing ratios.

4.2.4 Characterizations of Colloidal Nanocomposite Films

Atomic force microscopy (AFM) images of the exfoliated bentonite nanosheets were recorded in the dry state by using Tapping Mode with a scan rate of 1 Hz with a Dimension ICON (Veeco, Bruker). The samples are prepared by spinning coating diluted bentonite solutions on a silicon plate. The data were analyzed with Nanoscope Analysis software. The zeta potential of prepared mixture solutions was measured at 20°C by disposable cuvettes with a capillary channel and a Zetasizer Nano ZS apparatus (Malvern Instruments Ltd., Worcestershire, UK).

The sectional morphology of cast nanocomposite films was observed by scanning electron microscopy (SEM, JEOL 6700F). Each sample was fractured in liquid nitrogen and sputtered with gold prior to observation. Transmission electron microscopy (TEM) images were taken via a Hitachi H600 microscope operating at 75 kV. The samples were ultramicrotome to slices and placed on copper films for observation. The dielectric properties of the films were measured at room temperature with an impedance analyzer (MaterialsMates 7260, Italy) at different frequencies between 10^{-1} and 10^{6} Hz (**Figure 2-2**). At room temperature, the tests of dielectric breakdown strength and electric polarization-electric field ($P-E$) loops were performed on the samples immersed in the silicone oil by a PolyK ferroelectric polarization loop and dielectric breakdown test system. Before measurement, two surfaces of each sample were coated with gold electrodes of 2.5 mm in diameter (**Figure 2-4**).

4.3 Results and Discussions

4.3.1 Zeta Potential of PS/chitosan Solution

As reported in Chapter 2 and 3, counter ions around the charged PVDF nanoparticles will weaken the dielectric energy storage properties of the materials. The distribution of these counter ions in the system is effectively determined by the charge density on the particle surface, as illustrated in **Figure 1-32** in Chapter 1. The zeta potential corresponds to the electrostatic charge level of the particles and it can be used to quantitatively analyze the electrical repulsive forces which are exerted between the particles[4]. Normally, the more charges exist, the particles

in the solution will be more stable and homogeneous. While particles are neutralized, especially close to the isoelectric point, the suspension becomes unstable and flocculation occurs[5]. Normally, the colloidal solution is considerably stable when its zeta potential is exceeding ±30 mV. We first characterized the zeta potential of each solution to analyze the net charge and corresponding counter ions around particles in the colloidal system.

The zeta potential and the mean apparent particle size of the mixture suspension composed of PS latex and chitosan were characterized and shown in **Figure 4-3**. With displaying good dispersion and stability, pure PS latex (0.1 wt%) and chitosan solution (0.66 wt%) showed zeta potentials of -46 mV and +89 mV, respectively. This indicates that there are adequate charges on the particles to inhibit aggregation of the particles and to achieve good stability. The anionic charge on PS nanoparticles arises from the dissociation of the sulfate ether group as the solution pH exceeds 7 (**Table 4-1**). However, the mixed system of chitosan aqueous solution and PS latex is not stable. The flocculation occurs with adding a small amount of chitosan (<1 wt%), while the particles are redispersed and stabilized at high chitosan content (>5 wt%), as shown in **Figure 4-2** (a). Such macroscopic transition is accompanied by the variation of zeta potential from negative to positive as a function of the dosage of chitosan solution (**Figure 4-3**). The neutralization can be considered as a consequence of the charge compensation of cationic chitosan as well as the reduction of pH values (**Table 4-1**). The isoelectric point is located at 1.1 wt%. In the vicinity of this point, the particles form loose aggregates, the size of which reaches a peak value of 15 μm. This value is serval orders of magnitude higher than that of the origin PS latex (180 nm). In comparison with PVDF (1.78 g/cm^3), PS has a lower density (1.02 g/cm^3), closely approaching to water. Therefore, most of the flocculated PS particles accumulate on the surface of the solution instead of settling. In any case, the liquid-solid phase separation allows for the release of counter ions from the solid particle assemblies into the liquid phase.

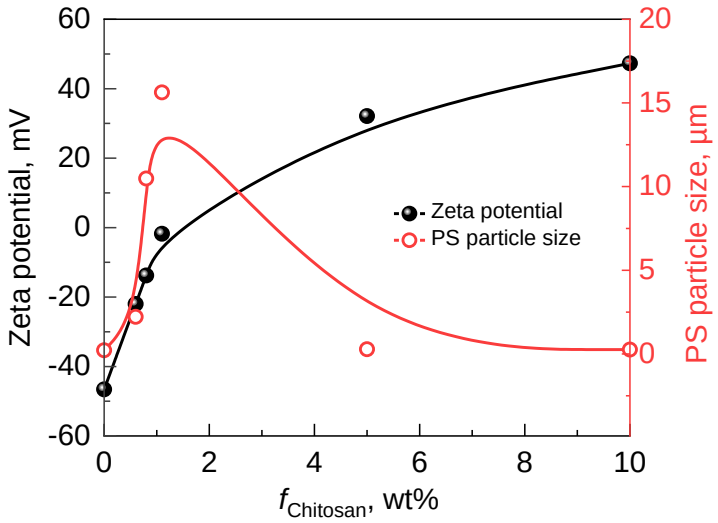

Figure 4-3. Zeta potential and particle size of the PS latex solution with various chitosan dosages.

Table 4-1. The zeta potential, constituent colloid size and pH values of different solutions

Solutions	Zeta potential (mV)	Particle size (um)	pH
100%PS	-46.6	0.219	8.16
99.4%PS@0.6%chitosan	-22	2.214	7.7
99.2%PS@0.8%chitosan	-13.8	10.48	7.57
98.9%PS@1.1%chitosan	-1.79	15.63	7.25
95%PS@5%chitosan	32.1	0.281	6.27
90%PS@10%chitosan	47.3	0.263	4.71
100%chitosan	89.0	n/a	3.47

4.3.2 Morphology of PS Latex and Their Nanocomposites

Figure 4-4 (a) shows the cross-sectional SEM image of pure PS film. PS nanoparticles do not coalesce and are still isolated in the film. This feature induces plenty of nanovoids or porous between particles in the film. It is not the same as what we have observed in pure PVDF latex film, which shows a continuous polymer phase after complete coalescence. While for PS@chitosan nanocomposite film as shown in **Figure 4-4** (b), chitosan fills well the gaps between PS nanoparticles and leads to a defect-free film.

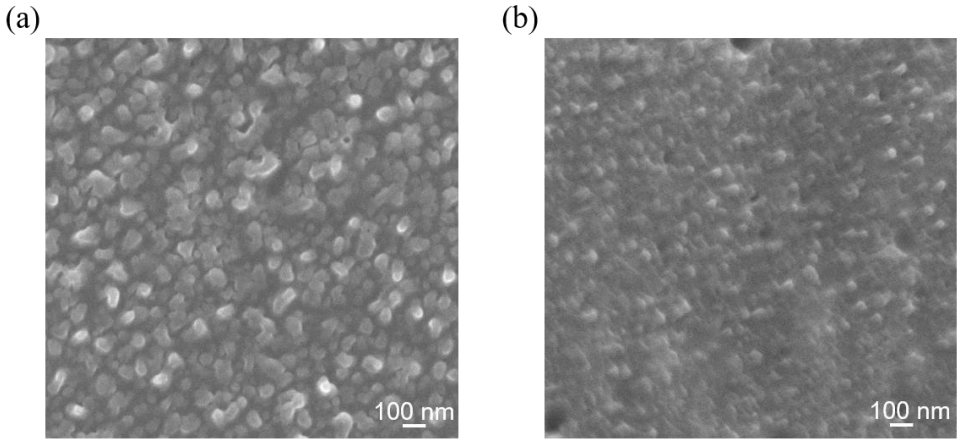

Figure 4-4. The cross-sectional SEM images of (a) pure PS film and (b) PS@1.1 wt% chitosan composites film.

4.3.3 Dielectric Performances of PS@chitosan Films

Figure 4-5 shows the frequency dependency of low-field dielectric properties for each film. Pure PS and PS@chitosan composites at low dosages (<5 wt%) present a frequency-independent permittivity. At the same frequency, the dielectric constant of the composites first decreases and then increases with increasing the chitosan dosage. Being similar to PVDF@chitosan systems, at the isoelectric point (1.1 wt%), the permittivity was reduced from 6.5 to its valley value (2.3 at 100 Hz). These results indicate that the polarization capability of PVDF@chitosan films is perhaps less correlated to the ion activity as compared to PVDF latex systems because of the absence of dielectric relaxation at low frequencies. Still, it is slightly weakened as a consequence of the neutralization of PS nanoparticles. However, the PVDF@chitosan film is more insulating, demonstrating the lowest conductivity and loss tangent, which are 10^{-10} S/m and 0.0161 respectively.

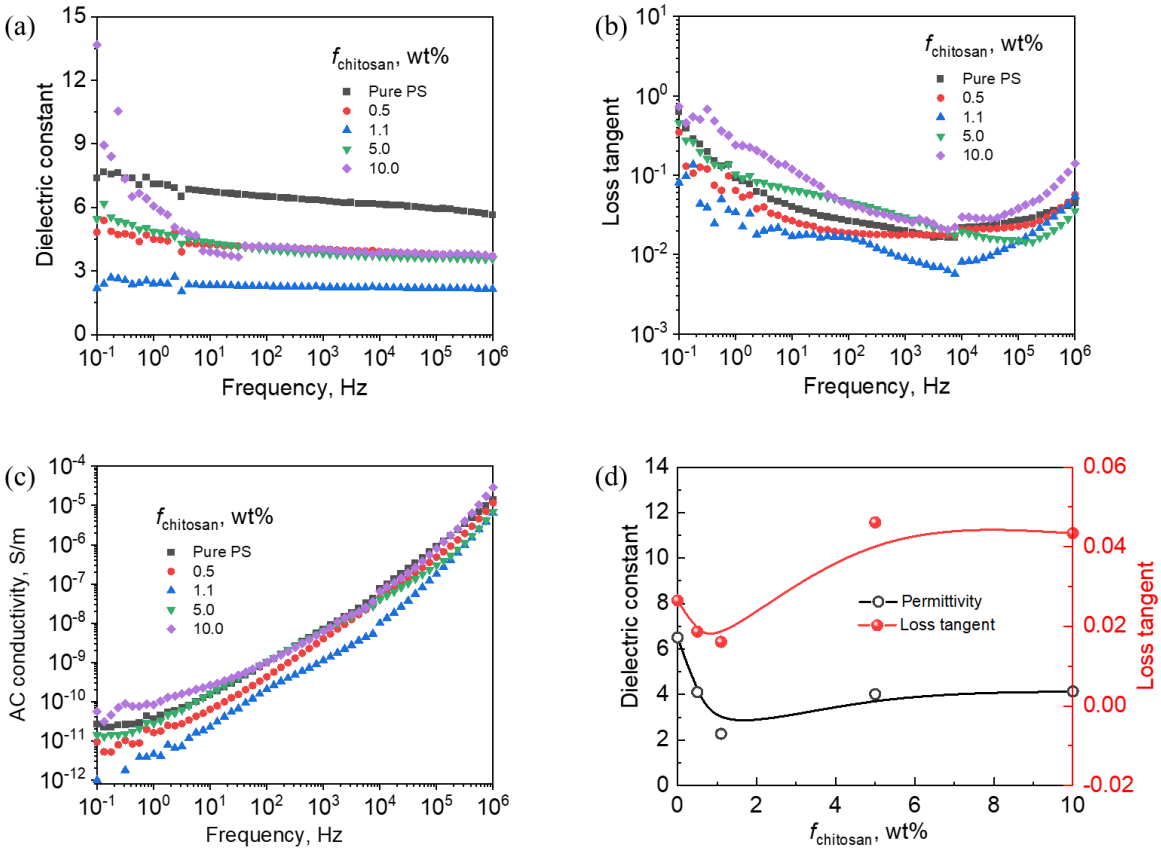

Figure 4-5. (a) Dielectric constant, (b) loss tangent, and (c) AC conductivity of PS@chitosan films as a function of frequency at room temperature. (d) The plot of dielectric constant and loss tangent at 100 Hz as a function of dosage of protonated chitosan.

4.3.4 Dielectric Breakdown Strength of PS@chitosan Films

The two-parameter Weibull distribution, as depicted by Equation (1.14), is commonly used to characterize and analyze the electrical breakdown strength of samples. Here, the two important parameters, E_b and β, were computed based on a linear fitting of the Weibull failure statistics (**Figure 4-6**) and listed in **Table 4-2**. It was found extremely hard to fabricate large-area PS films without cracks for the tests. In this case, we have tried to eliminate the voids between PS nanoparticles by hot pressing at 110°C. (For comparison purposes, the same thermal treatment process was applied to all PS@chitosan composite films.) Unfortunately, E_b of pure PS film is 250 MV/m, which is far inferior to that of typical PS films (398 MV/m) cast from conventional solvent-based solutions[6]. This is mainly due to the presence of counter ions and structural defects (**Figure 4-4**a) in the PS latex film.

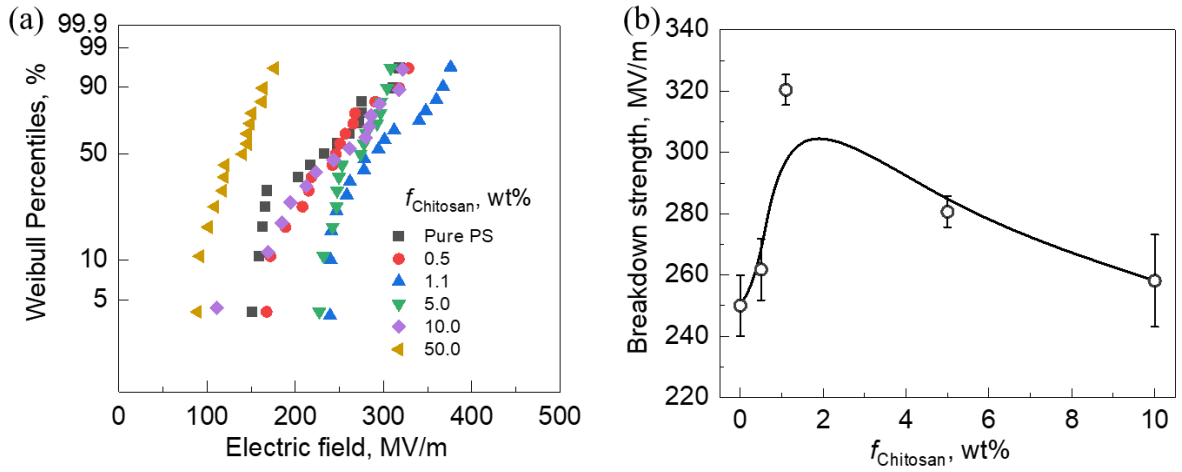

Figure 4-6. (a) Failure probability of dielectric breakdown deduced from Weibull distribution for neat PS and PS@chitosan composites at various chitosan loadings. (b) The breakdown strength as a function of chitosan dosage.

Table 4-2. E_b and β of PS@chitosan films.

Sample	E_b (MV/m)	β
Pure PS	250.20	4.7
PS@ 0.5 wt% chitosan	261.75	5.7
PS@ 1.1 wt% chitosan	320.41	6.8
PS@ 5 wt% chitosan	280.61	11.64
PS@ 10 wt% chitosan	264.19	4.95
PS@ 50 wt% chitosan	142.98	5.87

In contrast, the neutralization of PS nanoparticles by chitosan greatly improves the film quality and suppresses the adverse effect of counter ions, leading to a superior E_b. At the optimum chitosan content (1.1 wt%), the maximum E_b reaches up to 320 MV/m, which shows an enhancement of 128.2% as compared to pure PS latex film, and is rivaling typical PS films[6].

When the content of chitosan is further increased, the PS@chitosan film still displays high quality with nanoparticles assembled in a tightly packed arrangement, but at this stage, the PS particles have a net positive charge due to the adoption of excessive chitosan, which would be easily activated to induce a leakage current at high electric fields. Therefore, the E_b of the composite starts to decrease as the chitosan content exceeds 1.1 wt%.

4.3.5 Energy Density of PS@chitosan Films

To further elaborate on the effect of the introduced chitosan on the polarization, the *P-E* loops of films with different chitosan contents were compared. As shown in **Figure 4-7** (a), the P_{max} of the composite film containing 1.1 wt% chitosan is the smallest among all the composites. Moreover, the hysteresis loop of the PS composite with chitosan content near the isoelectric point is much smaller than its counterparts. The introduction of small amounts of positively charged chitosan could effectively reduce the net charges and associated counter ions distribution in the system, which allows for limiting the motion of charge carriers that would be activated at high fields. The polarization of the composites containing 1.1 wt% chitosan was investigated at different electric fields as shown in **Figure 4-7** (b). Higher electric field, higher P_{max}. The discharged energy density U_d is calculated by integration of the area between the discharge curve and the corresponding displacement ordinate. The values are plotted in **Figure 4-7** (c). Interestingly, the energy density of the composite containing 1.1 wt% chitosan reaches 1.408 J/cm^3 at 319 MV/m, which is almost three times higher than that of pure PS, demonstrating that the coupling of PS and chitosan has a strong effect on the high voltage tolerance of the films.

In practical applications, it is also important to evaluate the charge/discharge efficiency (η), which is defined as $\eta = U_d / (U_d + U_l)$, where U_l is the integral area of the hysteresis *P-E* loop by numerically calculating the closed area of the hysteresis *P-E* loop. As shown in **Figure 4-7** (d), the efficiency of all films decreases with the applied electric field, as there is a more significant conduction loss at higher electric fields. The efficiency is improved with the introduction of chitosan as compared to the pure PS films. At 200 MV/m, the efficiency of 1.1wt% chitosan composite is about 85.8%, which is higher than that of pure PS (54.7%). It still maintains at 80.8% at the maximum electric field of 319 MV/m. Water-processable PS@1.1 wt% chitosan film shows a combination of high energy density and high energy storage efficiency.

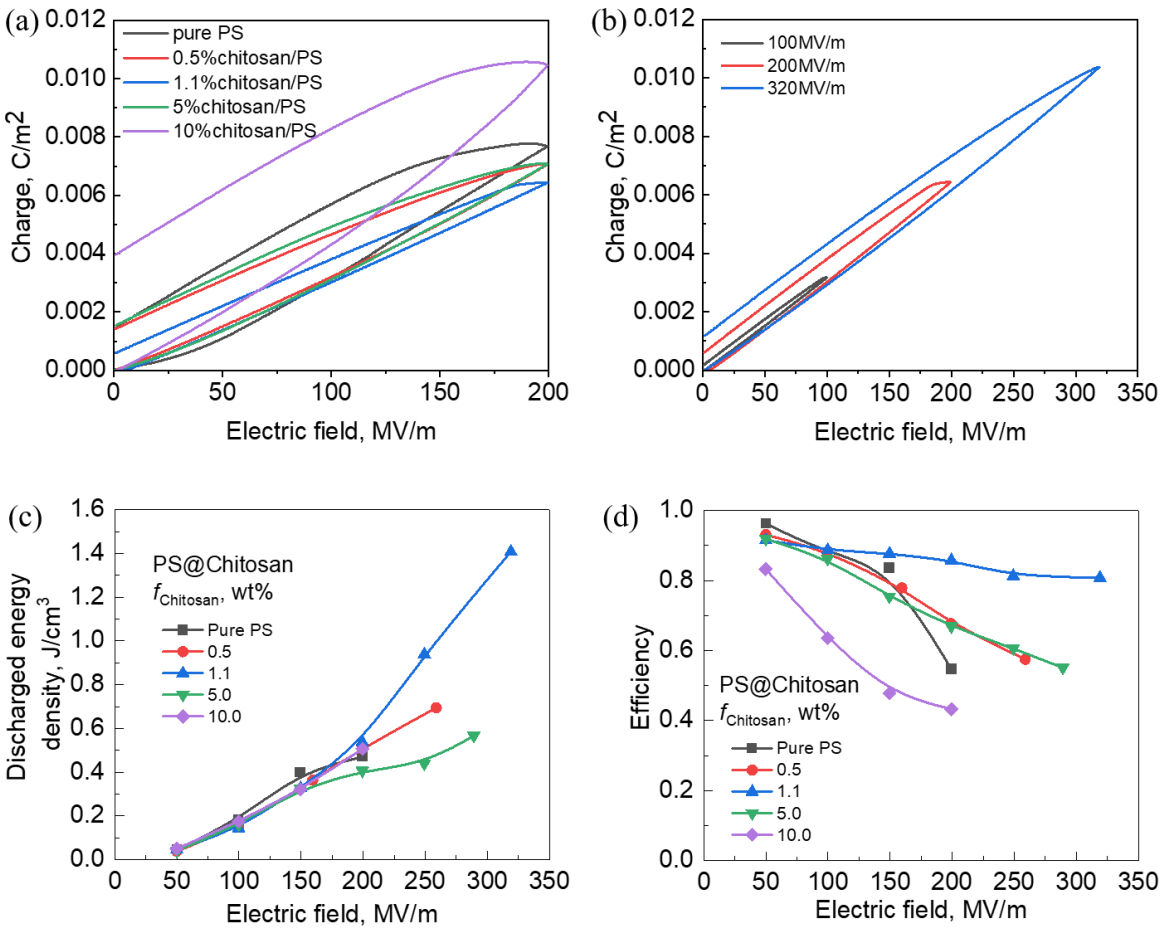

Figure 4-7. (a) *P-E* loops of pure PS and PS@chitosan nanocomposite films with various chitosan contents. (b) *P-E* loops of PS@1.1 wt% chitosan nanocomposite films at different electric fields. (c) The discharged energy density and (d) charge/discharge efficiency as a function of electric field for pure PS and PS@chitosan nanocomposite films.

4.3.6 Morphology and Property of Bentonite Nanosheets

Clay materials are abundant, environmentally benign, and have unique structural and physical properties. In recent years, they have been considered as potential low-cost candidates for clean energy storage either in their raw form or as a support material[7]. The montmorillonite has already demonstrated the capability to improve the breakdown strength of its polymer composites[8]. Bentonite, one of the clay materials, largely exists in the natural world and is able to be well dispersed in aqueous solutions. Furthermore, it is chemically inert and resistant to degradation. Structurally, bentonite clay is made up of two basic building blocks, i.e. the aluminum octahedral sheets and silica tetrahedral sheets (**Figure 4-8**). Each aluminum

octahedral layer is linked together by oxygen and was sandwiched between silicon tetrahedral layers. In such minerals, the anionic charge of the alumina-silicate layer is neutralized by the intercalation of compensating exchangeable cations (e.g. Al^{3+}, Ca^{2+} and/or Mg^{2+}) and their coordinated water molecules. As the bentonite is dispersed in an aqueous solution, it will absorb water to expand its size and release ions to process the negative charges on both surfaces and edges. The application of mechanical energy in the aqueous phase can efficiently exfoliate bentonite into flakes of nanometer size in thickness.

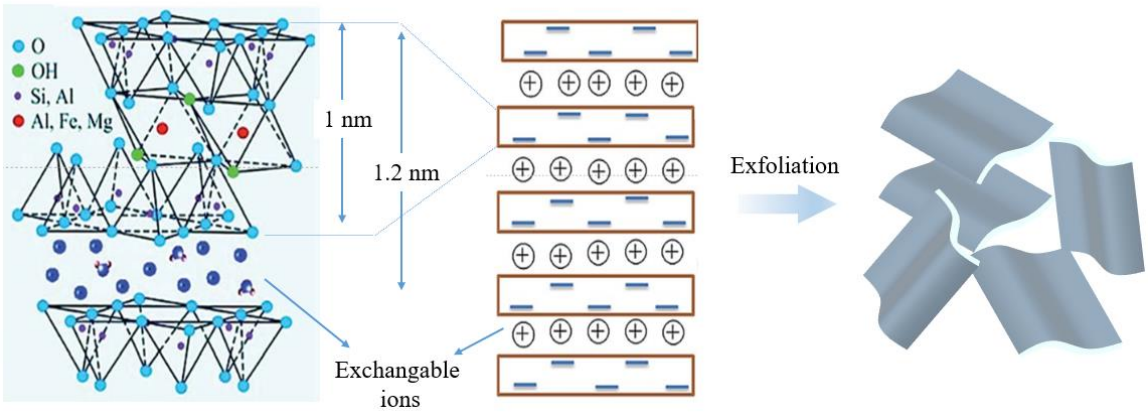

Figure 4-8. A diagrammatic sketch of the structure of bentonite, adapted from ref[9].

The bentonite nanosheets were successfully obtained by exfoliating bentonite powders in deionized water with a tip sonication. Their morphology was characterized by TEM and AFM. As shown in **Figure 4-9** (a), the large bentonite nanosheet is electron transparent, and very flexible with wrinkles being formed. An AFM image in **Figure 4-9** (b) shows more details on the dimensions of achieved bentonite flakes. They have a lateral size of hundred to thousand nanometers and a thickness of tens of nanometers. The thickness profile of the nanosheet along the line was shown in **Figure 4-9** (c), which demonstrates a 1000 nm in sheet dimension and 10 nm in average thickness. **Figure 4-9** (d) shows the size distribution detected by zetameter with laser diffusion method. There is a strong peak, giving the mean apparent particle size at 475 nm.

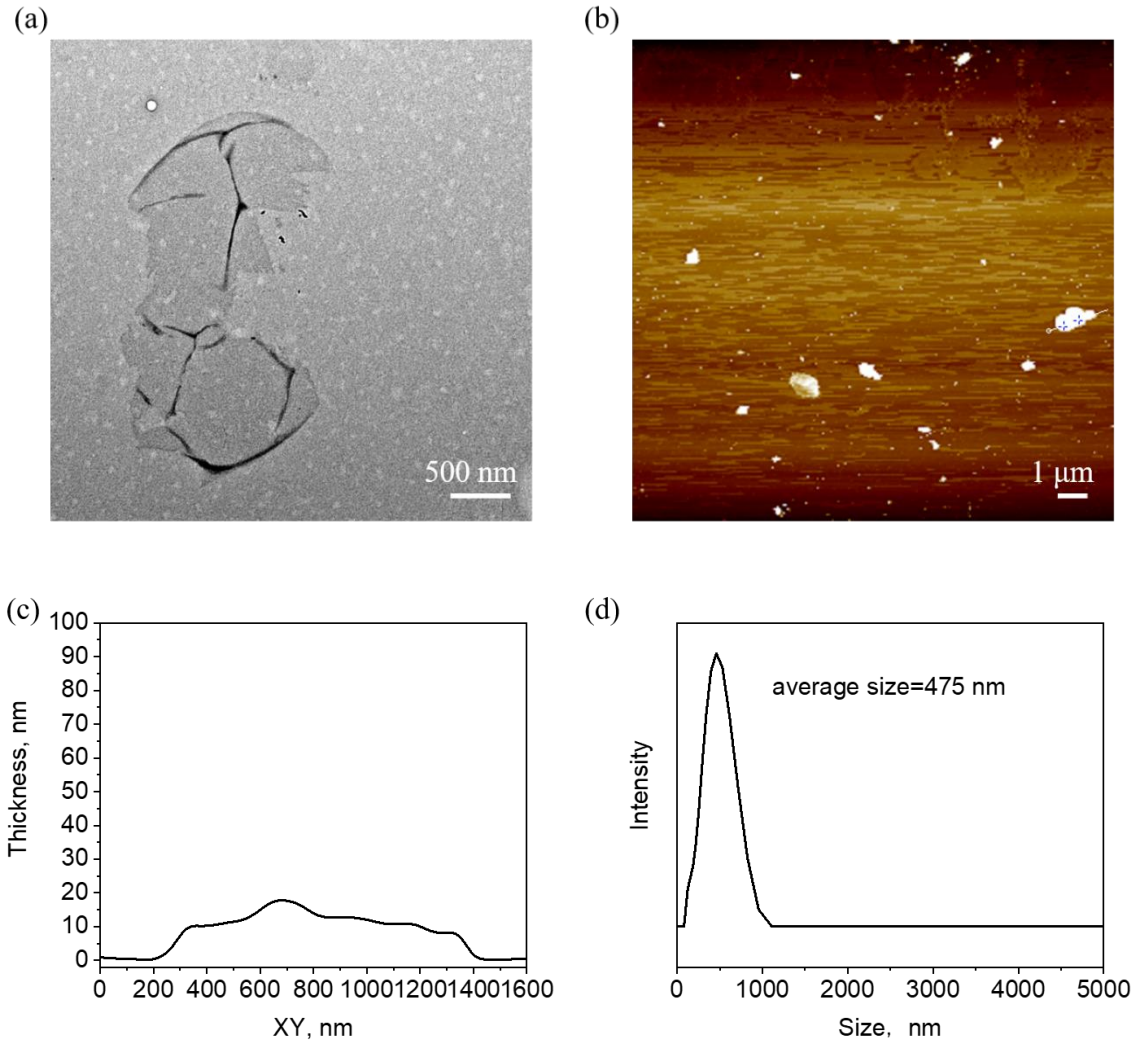

Figure 4-9. (a) The TEM image of bentonite nanosheet. (b) AFM image of several bentonite nanosheets. (c) The thickness profile of along the line in (b). (d) The size distribution of exfoliated bentonite nanosheets detected by zetameter.

4.3.7 Zeta potential and pH of Bentonite@chitosan solutions

The level of charge of bentonite nanosheets was examined at different degrees of dosage of chitosan by measuring the zeta potential and colloid size of the mixture solutions. As shown **Figure 4-10**, pure bentonite nanosheet aqueous solution (pH=6.6, **Table 4-3**) presents a zeta potential of -31 mV, demonstrating negative charges on nanosheets. As adding protonated chitosan into bentonite nanosheets aqueous solution, the zeta potential increases, indicating that negative charges were compensated and the isoelectric point is reached at 10 wt%. Further increasing chitosan content, the zeta potential turns to be positive and increases gradually. As

for the particle size, it increases first and then decreases with increasing the protonated chitosan content, showing a peak (~3 μm) near the isoelectric point.

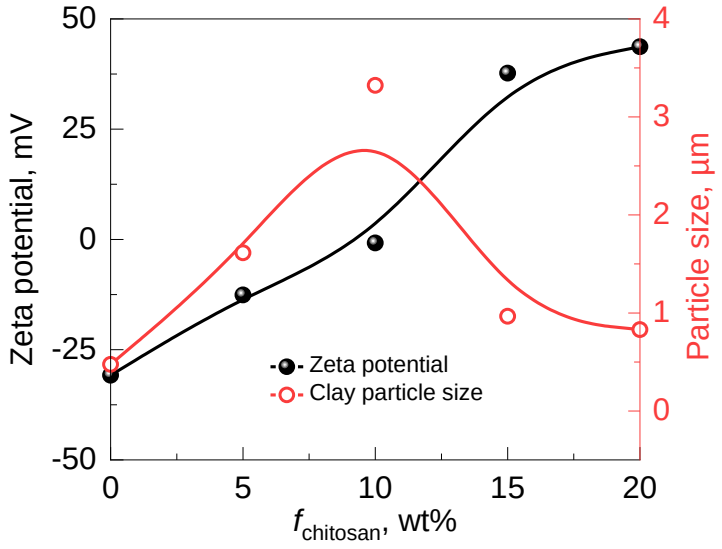

Figure 4-10. Zeta potential and size of constitute particles of the bentonite nanosheet aqueous solution at various chitosan dosages.

Table 4-3. The zeta potential, constituent colloid size and pH of different suspensions

Solutions	Zeta potential (mV)	Particle size (μm)	pH
100%bentonite	-30.8	0.475	6.6
95%bentonite@5%chitosan	-12.6	1.614	5.59
90%bentonite@10%chitosan	-0.815	3.322	5.24
85%bentonite@15%chitosan	37.7	0.9658	4.49
80%bentonite@20%chitosan	43.7	0.8304	4.35
100%chitosan	89.0	n/a	3.47

It is interesting to note that the isoelectric point is achieved in acid solution (10 wt%, pH=5.24, **Table 4-3**), not in the pH neutral one as in the case of PVDF and PS, and the corresponding chitosan dosage is one order of magnitude higher than those needed for PVDF and PS latex. Actually, being different from latex particles, negative charges of which are induced by the dissociation of acid groups and therefore are dependent on pH, the faces of bentonite nanosheet are also negatively charged yet as a consequence of the release of the exchangeable ions. This mechanism allows for the formation of stable bentonite suspensions

within a wide range of pH values. Indeed, the tested zeta potential of bentonite nanosheet suspensions is almost independent of pH varying from 5 to 9.5 (**Figure 4-10**). In this case, the change of pH does not neutralize bentonite particles as does as the case of PVDF and PS latex. The increased level of neutralization of bentonite is promoted alone by the bridging effect and needs a higher chitosan dosage.

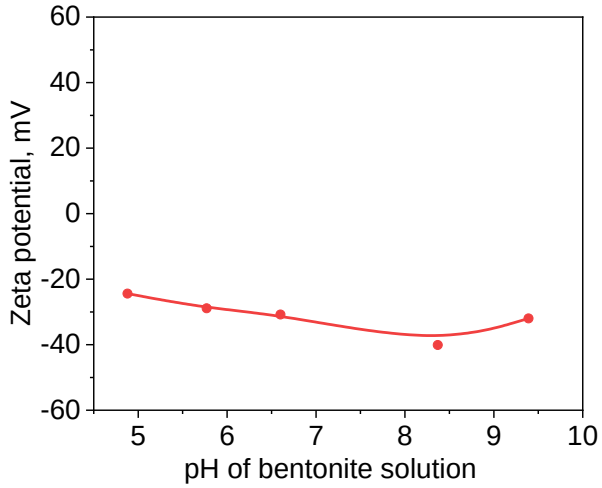

Figure 4-10. Zeta potential as a function of pH of bentonite solution. The pH is tuned by adding CH_3COOH or NaOH solution to reach lower or higher values respectively.

4.3.8 Morphology of Bentonite@chitosan Films

The association of bentonite@10 wt% chitosan is nearly charge neutral. It is interesting to process them into macroscopical film for dielectric applications. To achieve this objective, we added 20 wt% PVA as a binder to make uniform and defect-free composite films and studied the effect of the dosage of chitosan on the energy storage performances of bentonite@chitosan/PVA composites. **Figure 4-11** compares the morphologies of bentonite/PVA composites before and after the coating of chitosan. Intriguingly, bentonite nanosheets tend to be stacked layer by layer and to be separated by PVA matrix in between at a loading as high as 80 wt% (**Figure 4-11**a). Such arrangement is promoted by the significant confinement effect of the film thickness on the orientation of anisotropic nanoparticles with large aspect ratios, particularly at high filling degrees. Before coating with chitosan segments, the bentonite-PVA interfaces can be clearly identified under high magnification (**Figure**

4-11b). The addition of chitosan does not change the layered stacking patterns but the interfaces with PVA become blurry, indicating chitosan is capable of improving the film uniformity together with PVA (**Figure 4-11** c-d).

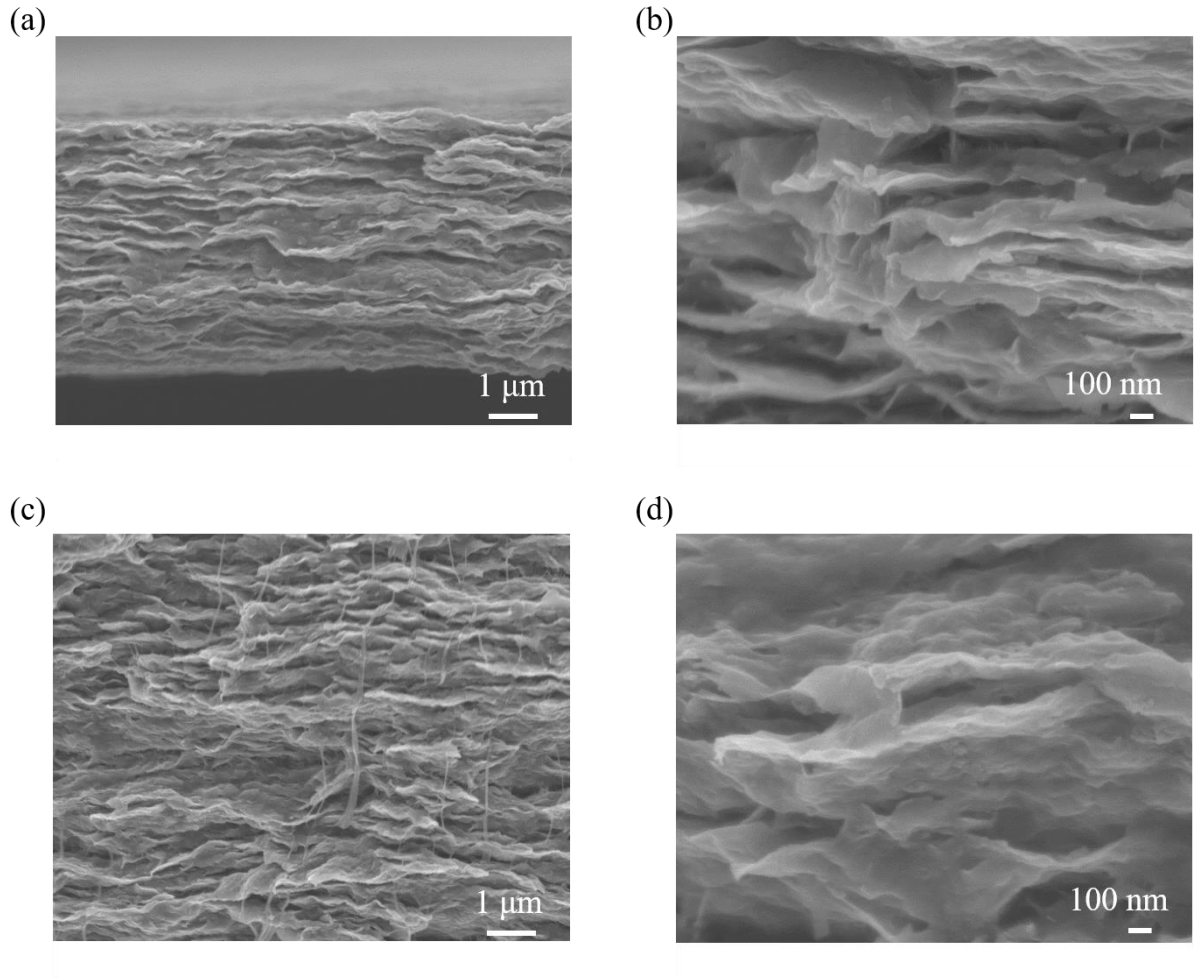

Figure 4-11. SEM images of the cross-sectional SEM image of (a, b) bentonite/PVA composites and (c, d) bentonite@10 wt% chitosan/PVA composites. In each case, PVA accounts for 20 wt% of the composites.

4.3.9 Dielectric Performances of Bentonite@chitosan Films

Figure 4-12 shows the frequency dependence of dielectric properties of bentonite@chitosan/PVA films. The permittivity of bentonite/PVA is strongly dependent on the frequency below 10 Hz, showing a significant interfacial polarization-related relaxation due to the presence of mobile charges. This can be evidenced by the plateau of the conductivity (**Figure 4-12b**) and high losses (**Figure 4-12** c) at low frequency. With coating chitosan, the

permittivity is decreased and the reduction is more significant at low frequency as compared to the one at high frequency. At the isoelectric point (10 wt%), the dielectric constant decreases from 14.31 to 11.69 and the losses decrease from 0.43 to 0.18 at 100 Hz (**Figure 4-12**d). While further increasing the chitosan content to 20 wt%, the dielectric constant and loss increase to 31.76 and 0.65 respectively. Chitosan has been also proved efficient to suppress the adverse effect of counter ions on the insulation of inorganic colloidal systems. It was observed that the level of conductivity and losses of bentonite@chitosan films is not as low as those of PS@chitosan and PVDF@chitosan films due to the addition of water-processed PVA.

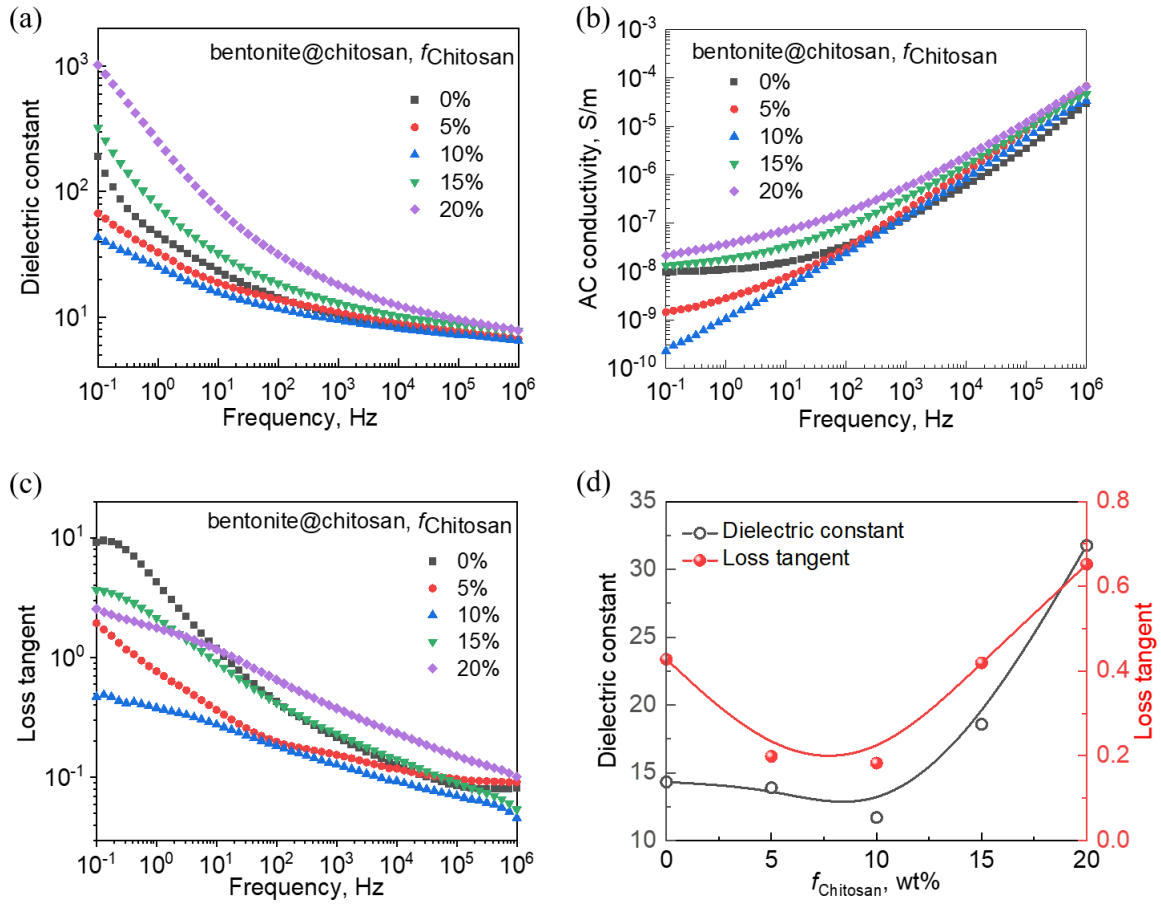

Figure 4-12. (a) Dielectric constant, (b) AC conductivity, and (c) loss tangent of bentonite@chitosan/PVA films as a function of frequency at room temperature, (d) dielectric constant and loss tangent at 100 Hz varies with the protonated chitosan loading. Each sample contains 20 wt% PVA

4.3.10 Dielectric Strength of Bentonite@chitosan Films

As shown in **Figure 4-13**, E_b was 313.95 MV/m for the bentonite/PVA films. As expected, the introduction of chitosan improves the breakdown strength as compared to the bentonite/PVA films. At the optimum chitosan content (10 wt%), the maximum breakdown strength reaches 361.75 MV/m, showing an enhancement of 15.2%. Beyond the isoelectric point, with more chitosan added, the E_b of the composites starts to decrease. Though the improvement is not as pronounced as in the case of PVDF and PS because of the addition of PVA in the system of bentonite, the behind principle that dominates the variation of breakdown strength is the same.

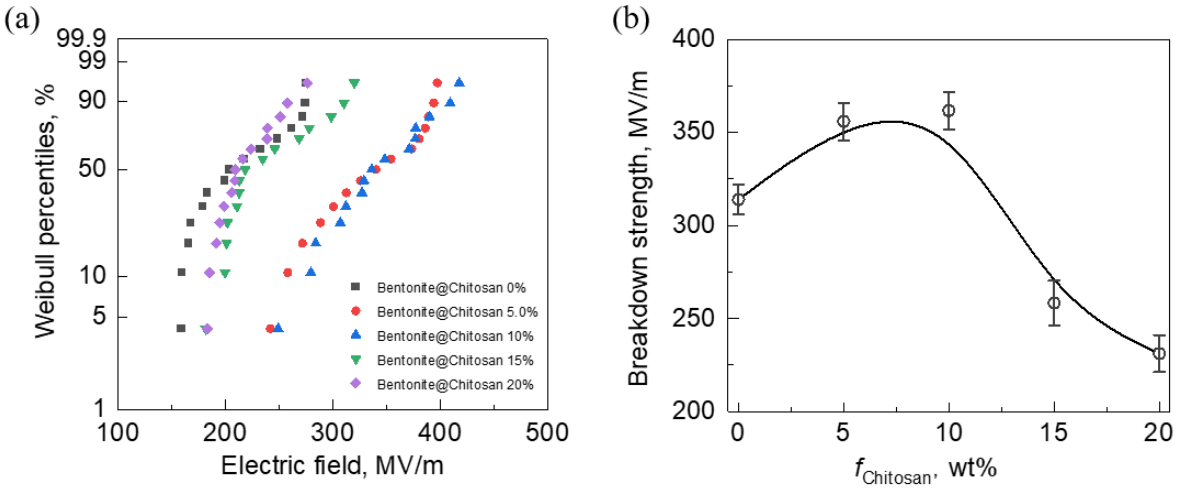

Figure 4-13. (a) Failure probability of dielectric breakdown deduced from Weibull distribution for bentonite@chitosan/PVA films with various chitosan dosages. (b) The breakdown strength of bentonite@chitosan/PVA films as a function of chitosan dosage. For each sample, the PVA content was kept at 20 wt%.

Table 4-2. E_b and β of bentonite@chitosan/PVA films, each of which contains 20 wt% PVA.

Sample	E_b (MV/m)	β
bentonite/PVA	313.96	10.44
bentonite@5 wt% chitosan/PVA	355.98	8.05
bentonite@10 wt% chitosan/PVA	361.75	8.25
bentonite@15 wt% chitosan/PVA	258.39	5.83
bentonite@20 wt% chitosan/PVA	231.23	8.19

4.3.11 Energy Density of Bentonite@chitosan Films

The *P-E* loops of the bentonite@chitoan/PVA films with different chitosan dosages at a given electric field of 150 MV/m were first compared. As shown in **Figure 4-14** (a), the P_{max} value of the composite film with a chitosan dosage of 10 wt% is smaller than its counterparts. In addition, the hysteresis loops of the composites close to the isoelectric point were much slimmer than those of the other samples. This suggests that the neutralized bentonite@chitosan loses some polarization capability related to the motion of free-charge carriers activated at high fields, but it leads to low conduction losses at high fields. **Figure 4-14** (b) shows the polarization of the most insulating bentonite@chitosan/PVA film at the isoelectric point at a varying electric field. The discharged energy densities are calculated based on the *P-E* loop at different electric fields until the E_b (**Figure 4-14**c). Though bentonite/PVA owns a high E_b which is more than 300 MV/m, it loses the capability of energy storage under an electric field above 160 MV/m due to the massive counter ions in the bulk film. At 100 MV/m, the bentonite/PVA film shows the maximum energy density U_e = 0.226 J/cm^3. Interestingly, the energy density of the composite was largely improved with coating bentonite by chitosan. An optimum value achieved at 10 wt% chitosan dosage reaches 5.7 J/cm^3 at 388 MV/m, which is 21 times higher than that of the bentonite/PVA film.

As shown in **Figure 4-14** (d), the η of all films decreases with the applied electric field, as there is a more significant leakage current at higher electric fields. However, the efficiency is greatly improved with adding chitosan compared to the bentonite/PVA films. At electric fields of 100 MV/m, the efficiency of 10 wt% chitosan composite is about 85.4%, which is much higher than that of bentonite/PVA film (23.2%). Its efficiency still maintains 49.3% at the maximum electric field strength of 388 MV/m.

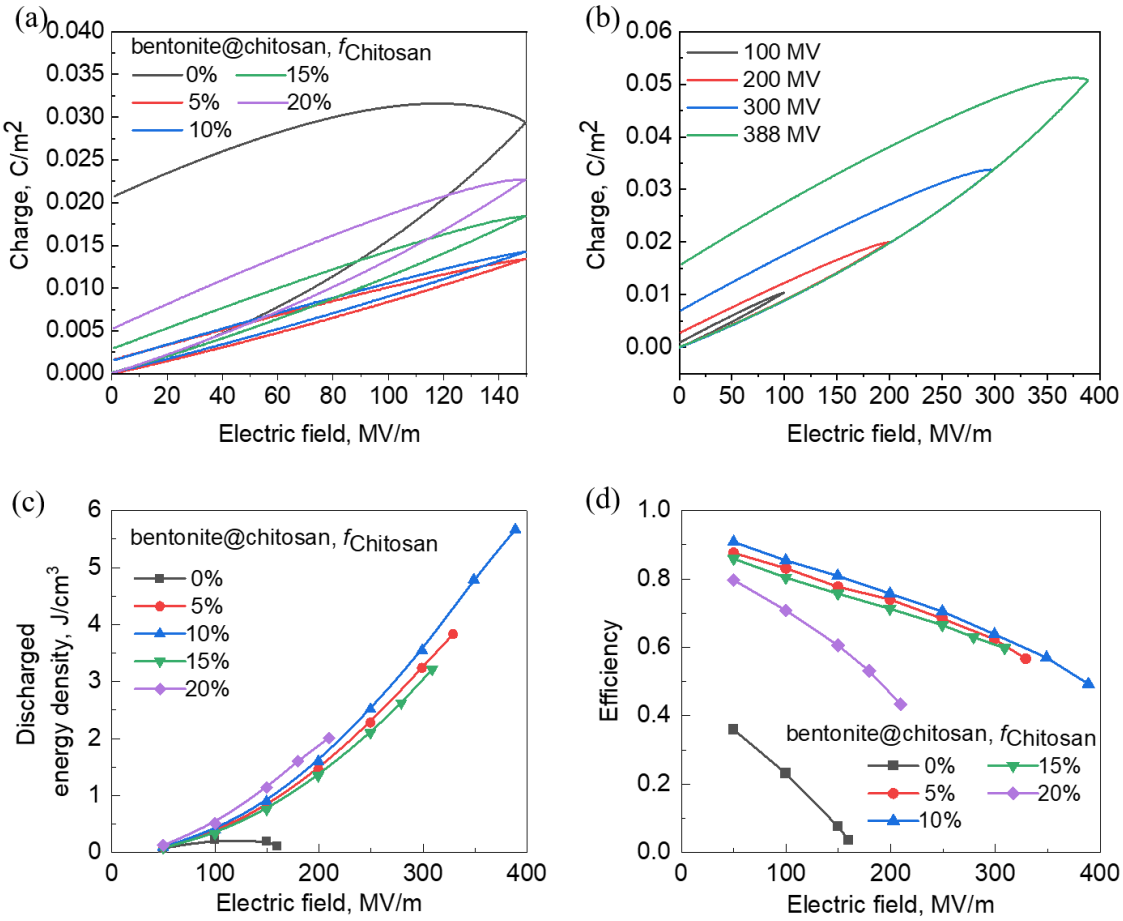

Figure 4-14. (a) *P-E* loops of bentonite@chitosan/PVA nanocomposite films with various chitosan dosages. (b) *P-E* loops of bentonite@10%chitosan/PVA nanocomposite films at different electric fields. (c) The discharged energy density and (d) charge/discharge efficiency as a function of electric field for bentonite@chitosan/PVA nanocomposite films. Each film contains 20wt% PVA.

4.4 Conclusion

We have extended experimentally the concept validated in the preceding chapter into PS latex and bentonite suspensions. Two waterborne colloidal nanocomposites, PS@chitosan and bentonite@chitosan/PVA, are prepared by charge neutralization in water solution, followed by a solution casting method. Compared with pure PS latex film, both the dielectric constant and losses are decreased in PS@chitosan films due to the neutralization of PS particles at 1.1 wt% dosage of chitosan. However, the E_b can be largely enhanced up to 320 MV/m and gives rise to an improved energy density of 1.4 J/cm^3, which respectively show improvements by 128% and 198% in comparison with pure PS films. Furthermore, it was found that a higher amount of

chitosan (10 wt%) was needed to neutralize bentonite nanosheets. The resultant bentonite@chitosan/PVA demonstrates the best insulating properties and shows a maximum energy density of 5.6 J/cm^3, 28 times higher than that of charged bentonite/PVA composites. The versatility of the concept that has been applied to the PVDF latex has been verified in PS and bentonite colloidal systems. It is anticipated that this work opens a new route of building high-energy dielectric materials by using colloidal.

References

1. Murray, C. B.; Kagan, C. R.; Bawendi, M. G., Synthesis and characterization of monodisperse nanocrystals and close-packed nanocrystal assemblies. *Annual review of materials science* **2000,** *30* (1), 545-610.
2. Talapin, D. V.; Lee, J.-S.; Kovalenko, M. V.; Shevchenko, E. V., Prospects of colloidal nanocrystals for electronic and optoelectronic applications. *Chemical reviews* **2010,** *110* (1), 389-458.
3. Jacobs, J. D.; Koerner, H.; Heinz, H.; Farmer, B. L.; Mirau, P.; Garrett, P. H.; Vaia, R. A., Dynamics of alkyl ammonium intercalants within organically modified montmorillonite: dielectric relaxation and ionic conductivity. *The Journal of Physical Chemistry B* **2006,** *110* (41), 20143-20157.
4. Matusiak, J.; Grządka, E., Stability of colloidal systems-a review of the stability measurements methods. *Annales Universitatis Mariae Curie-Sklodowska, sectio AA–Chemia* **2017,** *72* (1), 33.
5. Uskoković, V., Dynamic light scattering based microelectrophoresis: main prospects and limitations. *Journal of dispersion science and technology* **2012,** *33* (12), 1762-1786.
6. Grabowski, C. A.; Fillery, S. P.; Westing, N. M.; Chi, C.; Meth, J. S.; Durstock, M. F.; Vaia, R. A., Dielectric breakdown in silica–amorphous polymer nanocomposite films: The role of the polymer matrix. *ACS applied materials & interfaces* **2013,** *5* (12), 5486-5492.
7. Musyoka, N. M.; Langmi, H. W., Clay and clay-supported materials for clean energy storage applications. *Bentonite: Characteristics, Uses and Implications for the Environment. Nova publishers: New York, USA* **2015**.
8. Li, B.; Xidas, P. I.; Manias, E., High Breakdown Strength Polymer Nanocomposites Based on the Synergy of Nanofiller Orientation and Crystal Orientation for Insulation and Dielectric Applications. *ACS Applied Nano Materials* **2018,** *1* (7), 3520-3530.
9. Hebbar, R. S.; Isloor, A. M.; Ismail, A., Preparation and evaluation of heavy metal rejection properties of polyetherimide/porous activated bentonite clay nanocomposite membrane. *RSC Advances* **2014,** *4* (88), 47240-47248.

Chapter 5

Inkjet-Printing Colloidal-Based Microcapacitors

5.1 Introduction

The demand for miniaturized energy storage devices is rising due to the rapid development of advanced electronics and on-chip applications such as microelectromechanical systems, microrobotics, microsensors, biomedical implants and portable electronics[1-2]. In comparison with batteries, electrostatic capacitors display higher power densities and they are key components for the fabrication of high-power electrical microdevices.[1] Concerning polymer-based dielectric film capacitors, they are appealing due to the flexibility of polymers and the low cost of processing methods, yet they suffer from low energy densities because of the low permittivity of pure polymers[3]. In general, the energy density of a linear dielectric is proportional to the permittivity and scales quadratically with the breakdown strength, as expressed by Equation (1.19)[4]. It is, therefore, crucial to develop materials with enhanced polarizations at the elevated electric field in order to achieve high-energy storage performances. Ceramics and polymers are commonly used dielectric materials owing to the high dielectric constant and thermal stability of the former and the high breakdown strength of the latter[5-7]. An effective way to enhance the energy density is to combine these two components to formulate 0-3 nanocomposites or 2-2 multi-layered structures[3].

When it comes to the fabrication of multi-layered structures, inkjet printing can be considered as a highly attractive method[8], which is a simple, non-contact technique. Compared to traditional manufacturing methods, it does not require costly and time-consuming processes[9]. Additionally, it is compatible with almost any surface of interest (including planar surfaces or 3D objects). The provided design flexibility opens the opportunities for the fabrication of a plethora of complex heterostructures[9-10]. The big challenge in the field is to develop highly efficient dielectric inks, in particular in water.

In general, PVDF latex nanoparticles can be dispersed well in the water thanks to the electrostatic repulsion between the negative charges on their surfaces. The suspension can be stabilized even for years. This feature is highly desirable for the formulation of stable and homogeneous dielectric inks. Unfortunately, the existence of counter ions in the film leads to high conduction losses. Moreover, the inkjet printing of pure PVDF latex is not straightforward

and usually results in poor-quality films full of cracks or voids. The presence of counter ions coupled with the structural defects results in a low breakdown strength, as demonstrated in the preceding chapters. The proposed approach here to overcome these two issues is to formulate PVDF@chitosan hybrid suspensions by introducing excessive chitosan (5-20 wt%). Such dosage is much higher than the one (0.8 wt%, isoelectric point) required to neutralize the surface charge of the PVDF@chitosan association. So the PVDF@chitosan hybrid particles are overall positively charged. Their dispersion in water will be stabilized by the steric (or electrosteric) effect of chitosan. Chitosan will serve as a binder to largely improve the film quality, but it will attract again negative counter ions into the system. To confine these ions, sandwich-structured composite films are printed by intercalating layers of boron nitride nanosheet (BNNS, wide bandgap 2D material with a breakdown strength of over 800 MV/m) between layers of PVDF@chitosan. The BNNS nanolayers that are perpendicular to the electric field serve as an efficient barrier to block the transportation and the avalanche of charges and finally lead to improved breakdown strength and energy density[11].

To demonstrate a proof of concept, we printed microcapacitor configurations on polyimide (PI) substrates. Water-based carbon nanotube (CNT) ink is used to print the two electrodes (top and bottom), whereas the multi-layered dielectric film stacked between the electrodes is deposited by inkjet printing layer by layer the PVDF@chitosan hybrid ink, BNNS ink and again PVDF@chitosan ink. Given the environmental friendliness and the process ease, the used water-based inks are advantageous over most of the commonly used inks that are based on toxic solvents[10].

5.2 Experimental Section

5.2.1 Materials

Carbon nanotubes (CNTs) were supplied by Nanocyl under the series name of NANOCYL NC3100, prepared via the Catalytic Chemical Vapour Deposition (CCVD) process and purified up to 95 wt%. The CNTs have a length of 0.2 μm-5 μm and an average diameter of 9.5 nm. PVDF latex was provided by Arkema (Kynar Aquatec ARC Latex) with an initial concentration

of solid content of 44 wt%. In the PVDF nanoparticles, the ratio between the fluoropolymer and acrylic resin is 70:30. Chitosan was supplied by Sigma-Aldrich (from crab shells, 85% deacetylated). Hexagonal BN (boron nitride) powder was purchased from Merck KGaA, Germany, which has a platelet thickness of ~ 1 μm. IPA (Isopropyl alcohol) was supplied by Sigma-Aldrich (2-Propanol, suitable for HPLC, 99.9%). Sodium hydroxide (NaOH) was supplied by Sigma-Aldrich. Deionized water (with a resistivity above 18.2 MΩ·cm at 25 °C) was used for all the preparation of inks in this chapter.

5.2.2 Ink Preparation

The PVDF latex aqueous solution was prepared by diluting the original PVDF latex with deionized water to a concentration of 0.77 wt%. The mixture was magnetically stirred for 2 h at room temperature to achieve homogeneity. Similarly, protonated chitosan solution was dissolved in deionized water at a concentration of 0.75 wt%. As presented in Chapter 3, chitosan solution was prepared by firstly dissolving chitosan pellets in an aqueous solution with 1.5 wt% acetic acids for 4 h. Afterward, the mixture solution was sterilized in an oven at 120℃ for 10 min[12]. Finally, a paper filter was used to remove the undissolved chitosan and other impurities to obtain homogeneous and transparent chitosan aqueous solution for further use.

For the CNT ink, firstly CNT powder was mixed with deionized water at 2 wt% as schematically illustrated in **Figure 5-1**. The solution was magnetically stirred at room temperature for 2 h. Then it was mixed with the 0.75 wt% pure chitosan solution and deionized water to reach a CNT/Chitosan of 1:1 mass ratio at 0.25 wt% of each. Protonated chitosan serves as a bioresource ionic surfactant to stabilize the dispersion of CNT in water. The mixture solution was magnetically stirred and then was tip sonicated for 30 min at 20% power and delivered pulses of 0.5 s separated by 0.2 s intervals of silence. Afterward, it was centrifuged at 2486 g for 30 min and filtered with a 5 μm filter to obtain a well-dispersed ink without aggregates. During the sonication, the mixture was placed in an ice bath to prevent overheating. This practice was followed for each solution that underwent sonication. The final solute

concentration was remeasured at 0.4794 wt%, and at 0.2397 wt% for CNT and chitosan respectively. This ink is referred to CNT@50 wt% chitosan.

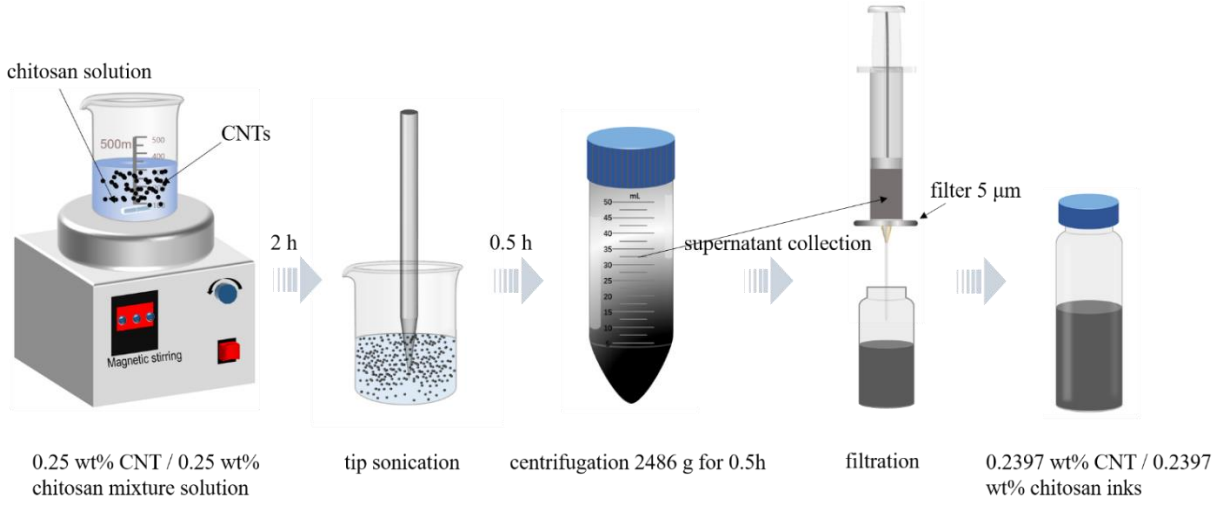

Figure 5-1. The preparation of CNT@chitosan aqueous inks.

Similarly, the PVDF@chitosan aqueous inks were prepared by mixing different quantities of 0.77 wt% PVDF latex, 0.75 wt% chitosan and deionized water to achieve four different inks, namely 0.38 wt% PVDF/0.02 wt% Chitosan, 0.36 wt%/0.04 wt%, 0.34 wt%/0.06 wt% and 0.32 wt%/0.08 wt%. **Figure 5-2** shows a typical process flow for the preparation of the PVDF@5 wt% chitosan ink.

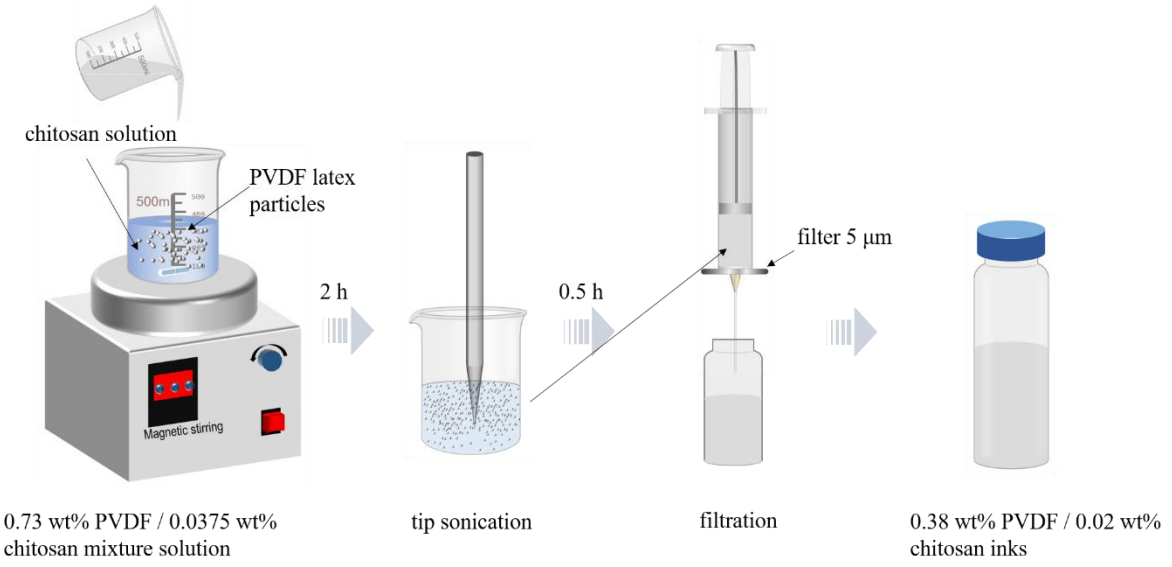

Figure 5-2. The preparation of PVDF/chitosan aqueous solution ink.

The four solutions were magnetically stirred for 2 h at room temperature and afterward 90 min of tip sonication at 20% power with 0.5 s/0.2 s on/off pulses. The stability and homogeneity of the inks were achieved. The final inks were diluted to a concentration of 0.4 wt% solutes by adding deionized water. The four PVDF@chitosan inks are referred to, according to the constituent mass ratio, PVDF@5 wt% chitosan, PVDF@10 wt% chitosan, PVDF@15 wt% chitosan, and PVDF@20 wt% chitosan respectively.

Following the well-established protocols of the liquid phase exfoliation process[13-14], the BN powder was dispersed and exfoliated in a 1:1 co-solution of IPA and deionized water. The schematic process flow to achieve BNNS inks is demonstrated in **Figure 5-3**.

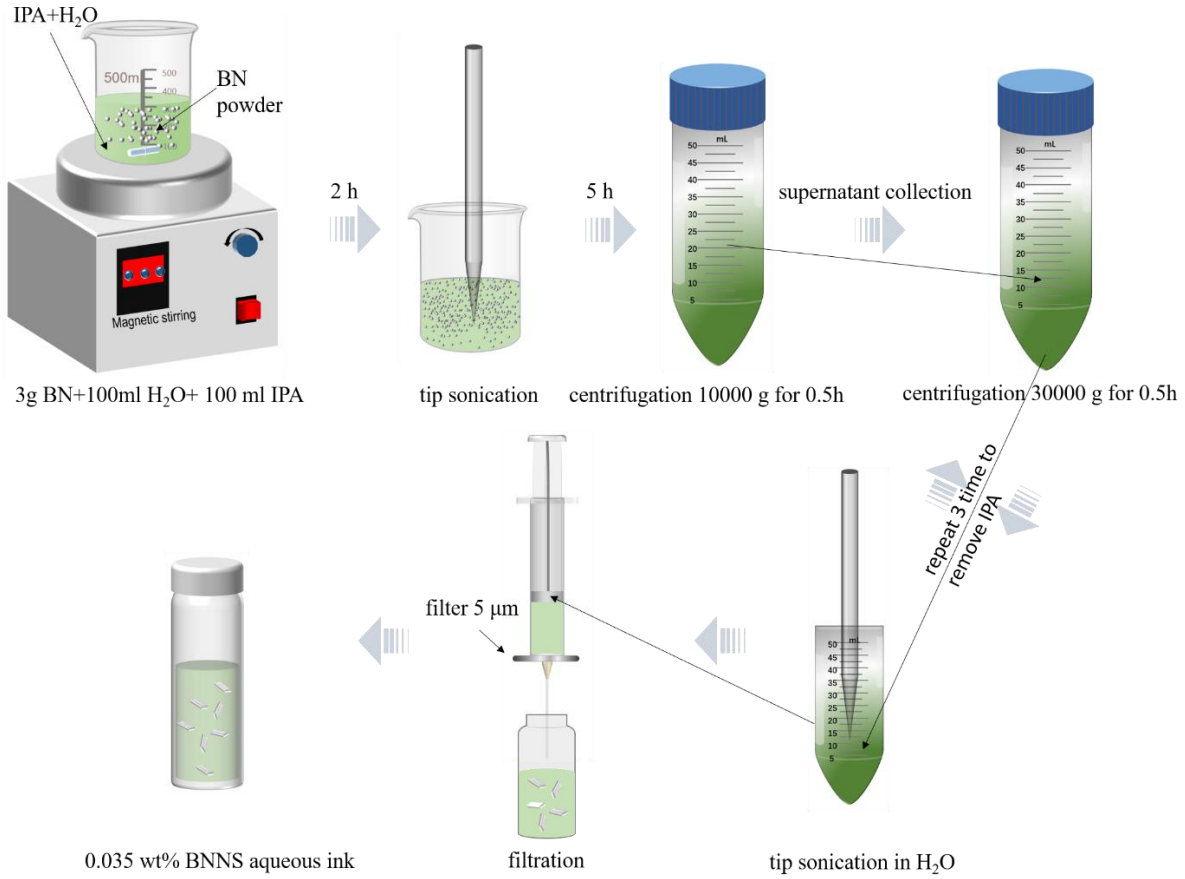

Figure 5-3. The preparation of aqueous BNNS ink.

The solution was magnetically stirred for 2 h at room temperature and then tip-sonicated for 5 h at 30% power with 0.5 s/0.2 s on/off pulses. Then it was centrifuged at 10000 g for 30 min to

remove the thick unexfoliated platelets. Afterward, the supernatant was centrifuged at 30000 g for 30 min to collect the exfoliated flakes. The collected BN flakes were redispersed in water by tip sonication. Such solvent exchange was repeated three times. Finally, the obtained solution was filtered with a 5 μm filter. The final concentration of prepared ink was remeasured at 0.035 wt%.

5.2.3 Characterizations of Inks

The dispersions of colloidal were examined under an optical microscope (Leica DM 2500P). The transmission electron microscope (TEM) image of the BNNS was obtained with a Hitachi H7650 transmission electron microscope operating at 80 kV. For TEM sample preparation, 200 mesh size copper TEM specimen grids (Electron Microscopy Sciences) having a lacey carbon support film were used for picking up sheets from the surface of the BNNS aqueous ink. Atomic force microscopy (AFM) images of BNNS were taken in the dry condition and captured with a Dimension ICON (Veeco, Bruker) at a scan rate of 1 Hz in tapping mode. Samples were obtained by a spin coating of diluted BNNS ink on silicon substrates. All results of AFM were performed with Nanoscope analysis software. The size and the surface charges of the nanoparticles in the prepared inks were measured using Malvern Zetasizer Nano at 20 ℃. The surface tension was measured at 20 ℃ with an optical tensiometer using the pendant drop technique, and as for the rheological properties, steady flow measurements were performed using a rheometer (TA instruments AR 2000 Rheometer) with parallel plate geometry (aluminum plate of diameter d_{plate}=60 mm) at 20℃. For all measurements, the density of the inks was considered as the one of pure water (997 kg/m^3) since all inks are aqueous solutions of very low concentration.

5.2.4 Inkjet Printing

A piezoelectric drop-on-demand inkjet printer (Autodrop compact microdispensing system MD-P-82x) with a nozzle of 100 μm diameter was used for printing microcapacitor. As shown in **Figure 5-4**, the core components (the ink reservoir, nozzle and substrate) are in an enclosed

unit to ensure that the printing process is protected from outside airflow influences. In the nozzle unit, a piezoelectric actuator controls the pressure variation and generates ink droplets on demand. The applied pulse signal can be adjusted to control the droplet properties by tuning the applied voltage, pulse length and frequency. The substrate with several holes connects to a pump, which provides a suction pressure to tightly fix the printing substrate in order to perform precise printing. Moreover, the resistance wire heating under the substrate can allow a temperature control in a range between 30℃ and 130℃.

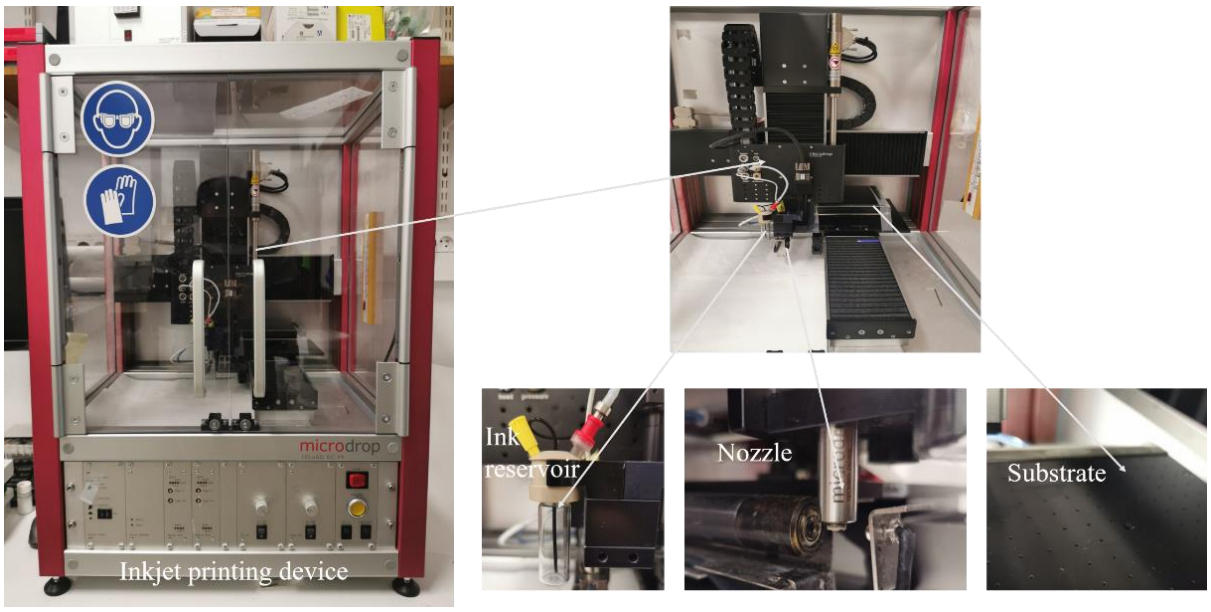

Figure 5-4. The inkjet printing instrument and its key component units.

5.2.5 Printing Dielectric Capacitors

A rectangular-shaped wave signal is used to eject the droplets and deposit them on the substrate. Then a continuous line consisting of suitably spaced droplets is printed on the substrate. Finally, several lines with an approximate distance are printed to form a thin film. All the inks are printed on PI film (~100 μm) on the substrate table preheated up to 130℃. The PI films are previously immersed into a 4 mol/L NaOH aqueous solution, followed by magnetical stirring for 5 h to improve the surface wetting properties.

The all inkjet-printed capacitor was fabricated by sequentially printing well-designed patterns of the bottom electrode layer, the dielectric layer and the top electrode layer (**Figure**

5-5). First, two layers of CNT@50 wt% chitosan were printed on the PI substrate to serve as the bottom electrode. Afterward, 9 layers of pure PVDF (0.77 wt%) or PVDF@5 wt% chitosan ink (0.38 wt% PVDF/0.02 wt% chitosan) were deposited to cover the bottom electrode to serve as a middle dielectric layer. Finally, three layers of CNT@50 wt% chitosan were printed to form a sandwiched capacitor structure. To formulate a 2-2 composite structure (polymer/BNNS/polymer) in the dielectric layer, 6 layers of BNNS ink were printed by interfering with the printing of PVDF dielectric inks. Finally, the printed capacitor devices were fully dried in a vacuum oven at 100℃ overnight before the dielectric characterization process.

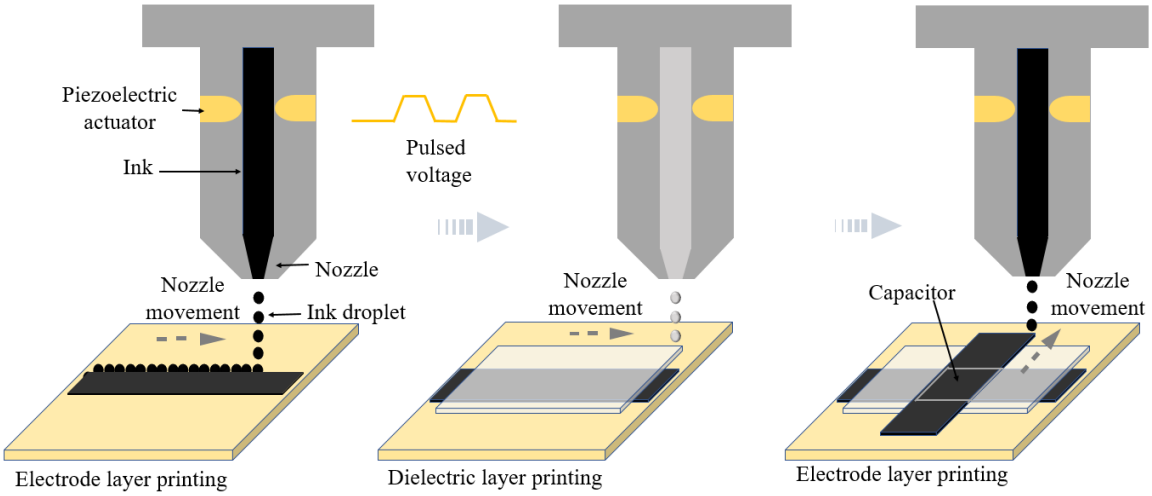

Figure 5-5. The fabrication of a dielectric capacitor via inkjet printing water-based functional inks.

5.2.6 Characterizations of Printed Films

The surface morphology of the printed films was studied by microscopic observation under an optical microscope (Leica DM 2500P) with ×10 and ×40 objectives. The cross-sectional morphology of the printed films was studied by scanning electron microscopy (SEM) (JEOL 6700F), and the cross-sections were achieved by fracturing the samples in liquid nitrogen. Transmission electron microscopy (TEM) images of printed 2-2 nanocomposites were taken via a Hitachi H7650, and the samples were ultramicrotome to slices of 40–60nm thickness and placed on copper films for observation. The dielectric properties of the printed samples were

measured as a function of frequency from 10^{-1} to 10^{6} Hz at room temperature using an impedance analyzer (MaterialsMates 7260, Italia). A PolyK ferroelectric polarization loop and dielectric breakdown system were used for the dielectric breakdown strength and electric polarization-electric field (*P*-*E*) loop measurements. The measurements were conducted at room temperature. Before the characterizations, the terminals of CNT electrodes were coated with silver paint to ensure good contact with the sample holder. The used instruments and cable connections have been detailed in the Experimental Section of Chapter 2.

5.3 Results and Discussion

5.3.1 Properties of Inks

A capacitor consists of a dielectric layer sandwiched between two electrode layers. In this work, the CNT@50 wt% chitosan ink is explored for printing the conductive electrode layer. CNTs are one-dimensional carbon materials with excellent electrical conduction properties. However, it is not easy to form stable suspensions because they tend to aggregate in the medium as a consequence of the van der Waals attraction if there is no repulsive force built between them. Chitosan, a bioresource polymer, is the most abundant natural amino polysaccharide and produced almost as much as cellulose each year. It is of great interest not only as an underutilized resource but also as a new functional material with great potential in various fields[15]. The properties of chitosan depend largely on the degree of deacetylation, where the amino group in the polymer chain makes it possible to be protonated to possess positive charges[12]. Therefore, it owns the great potential to be a bio-additives to modify the nanoparticles. In this chapter, chitosan was selected to modify the CNT surface properties to form a homogeneous ink for further printing conductive components.

On the other hand, low-cost PVDF latex has been proven to be processed into high-energy dielectric materials. It is noted that with the addition of a small amount of chitosan, PVDF nanoparticles can form complexation with chitosan molecules at the isoelectric point. The resultant materials show the highest breakdown strength and energy storage density. Unfortunately, in the vicinity of this critical point, the PVDF@chitosan hybrid particles were

precipitated because of flocculation. These mixture solutions cannot be used as inks for printing anymore. However, the PVDF@chitosan hybrid particles can be redissolved by further increasing chitosan content far beyond the isoelectric point (**Figure 5-6)**, and the formed aqueous solutions can be potentially interesting to serve as dielectric inks.

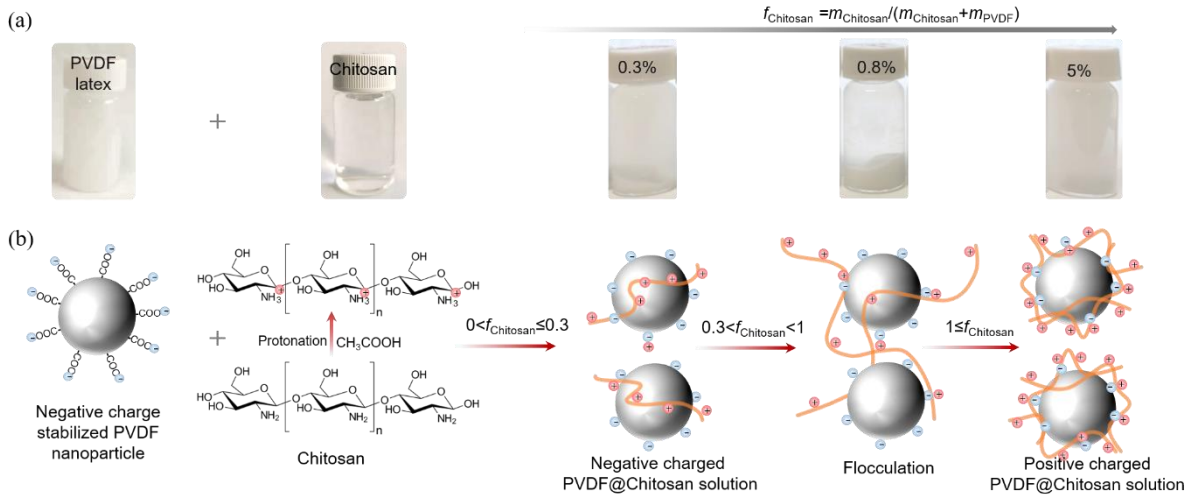

Figure 5-6. (a) Photographs of pure PVDF latex, chitosan aqueous solution and their mixture solutions at different chitosan dosages. (b) The schemes of PVDF latex particle, chitosan molecule structure and their interactions at different mass ratios.

With the excessive chitosan dosage, a flexible, robust and defect-free film can be always cast from stable PVDF@chitosan inks. However, the positively charged PVDF@chitosan hybrid particles would attract again small counter ions, which results in printed films with high-loss and low-E_b. To confine the counter ions and suppress their adverse effects, the dielectric PVDF@chitosan nanocomposite is interlayered by BNNS, which is considered to be able to act as a barrier to improving the E_b and energy density**.**

Given all the inks are suspensions of nanomaterials, uniform dispersion is the prerequisite for ink materials to be ejected by the printer without clogging the microsized nozzle. The stability of inks is also critical as the printing process would take several hours or even days for industrial production. All the ink solutions were first characterized using an optical microscope. As shown in **Figure 5-7**, all the aqueous inks were homogeneous dispersions without showing any sedimentation or formation of aggregates. Such stability can keep for up to several weeks.

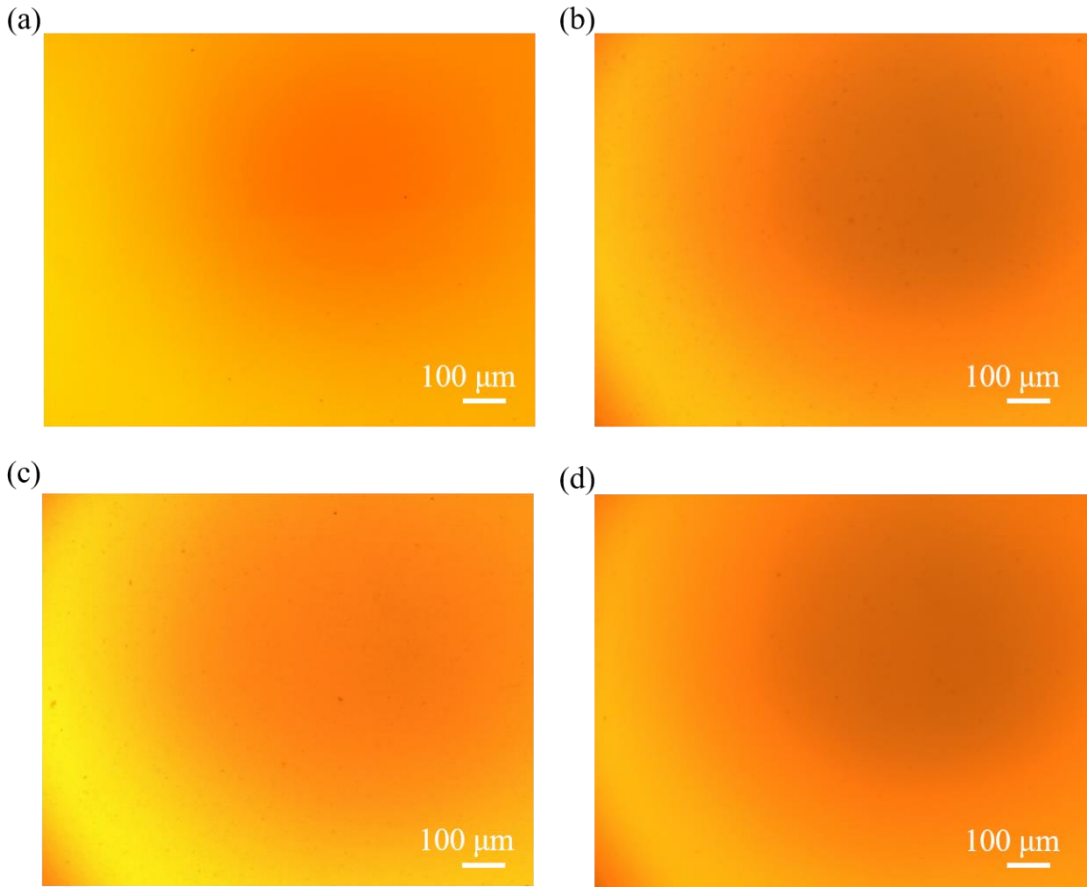

Figure 5-7. Optical microscopic images of prepared ink materials: (a) CNT@50 wt% chitosan ink, (b) 0.77 wt% PVDF latex, (c) PVDF@5 wt% chitosan ink, and (d) 0.035 wt% BNNS aqueous ink.

In order to ensure that the inks are printable and to eliminate the risk of nozzle clogging, the inks were characterized in terms of viscosity, surface tension, size, and surface charges of containing nanoparticles. The size of latex particles and their surface charges and counter ions are essential to the dielectric properties of the final printed film. The zeta potential test is performed to illustrate these influences. As shown in **Figure 5-8** and **Table 5-1**, PVDF latex nanoparticles have negative charges while chitosan positive ones, showing zeta potential values ζ = -30.8 mV and ζ = 81.5 mV respectively. The zeta potential and average particle size (169 nm) of PVDF nanoparticles are independent of the sonication time, indicating the individual dispersion nature in latex raw materials.

Indeed, the addition of chitosan screens the electrostatic potentials of PVDF. The adsorption of segments of chitosan endows the PVDF@chitosan hybrid particles positively

charged, showing positive zeta potentials. With increasing chitosan content, the zeta potential first increases and then nearly saturates at ζ =70 mV before sonication. It is found that the sonication indeed favors the redispersion of PVDF@chitosan nanoparticles. The measured size of PVDF@chitosan hybrid particles rapidly decreases with the sonication time and finally reaches a plateau (**Figure 5-8**b). The powerful waves of vibration during sonication disrupts the loose aggregations of hybrid particle. The augmentation of the number of individual colloids leads to a reduction of net charges on them and thus a reduced zeta potential (**Figure 5-8**a). The PVDF@5 wt% chitosan ink sonicated for 90 mins shows the smallest particle size. Though its zeta potential (ζ = 31.9 mV) is lower than its counterparts, it still meets the requirement of minimum value (ζ = ±30 mV[16]) to maintain the stable dispersion. The PVDF@5 wt% chitosan ink was therefore preferentially used as dielectric ink for the printing of dielectric microcapacitors. Intriguingly, BNNS is negatively charged in water, which will have an electrostatic affinity with PVDF@chitosan layers and ensure the uniformity of the interlayer.

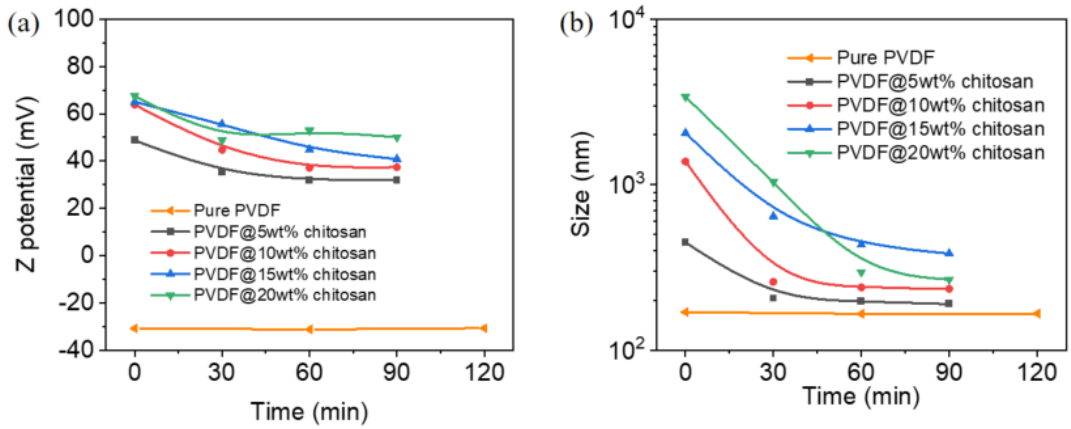

Figure 5-8. (a) Zeta potential and (b) colloidal size as a function of tip-sonication time.

Table 5-1. Average particle size and zeta potential (ζ) were measured at 20°C for the developed aqueous inks used for printing

Samples	Average size (nm)	zeta potential (mV)
Pure chitosan, 0.75 wt%	n/a	81.5
PVDF latex, 0.77 wt%	169.7	-30.8
BNNS, 0.035 wt%	382.1	-21.3
PVDF@5 wt% chitosan, 0.40 wt%	190.0	31.9
PVDF@10 wt% chitosan, 0.40 wt%	234.5	37.4
PVDF@15 wt% chitosan, 0.40 wt%	383.1	40.8
PVDF@20 wt% chitosan, 0.40 wt%	267.1	50.1

As compared to BN powder, BNNS can effectively improve the breakdown performance and energy storage density of composite materials as the intrinsic breakdown strength scales reversely with the thickness of exfoliated BNNS. Therefore, the successful preparation of BNNS is quite critical[17]. BNNS aqueous ink was prepared by exfoliating BN powders in a mixture of IPA and deionized water and followed by solvent exchange and dispersion in deionized water. The nanoscale BNNS were characterized by TEM and AFM. As shown in **Figure 5-9** (a), the TEM image clearly shows the layered structure at the edge of BNNS with a thickness of nanometers. **Figure 5-9** (b) presents a nanosheet of BN with a lateral size of several hundred nanometers and a thickness of tens of nanometers. The thickness profile of the nanosheet along the line was shown in **Figure 5-9** (c), which demonstrates a lateral size of nearly 400 nm and a thickness of 25 nm.

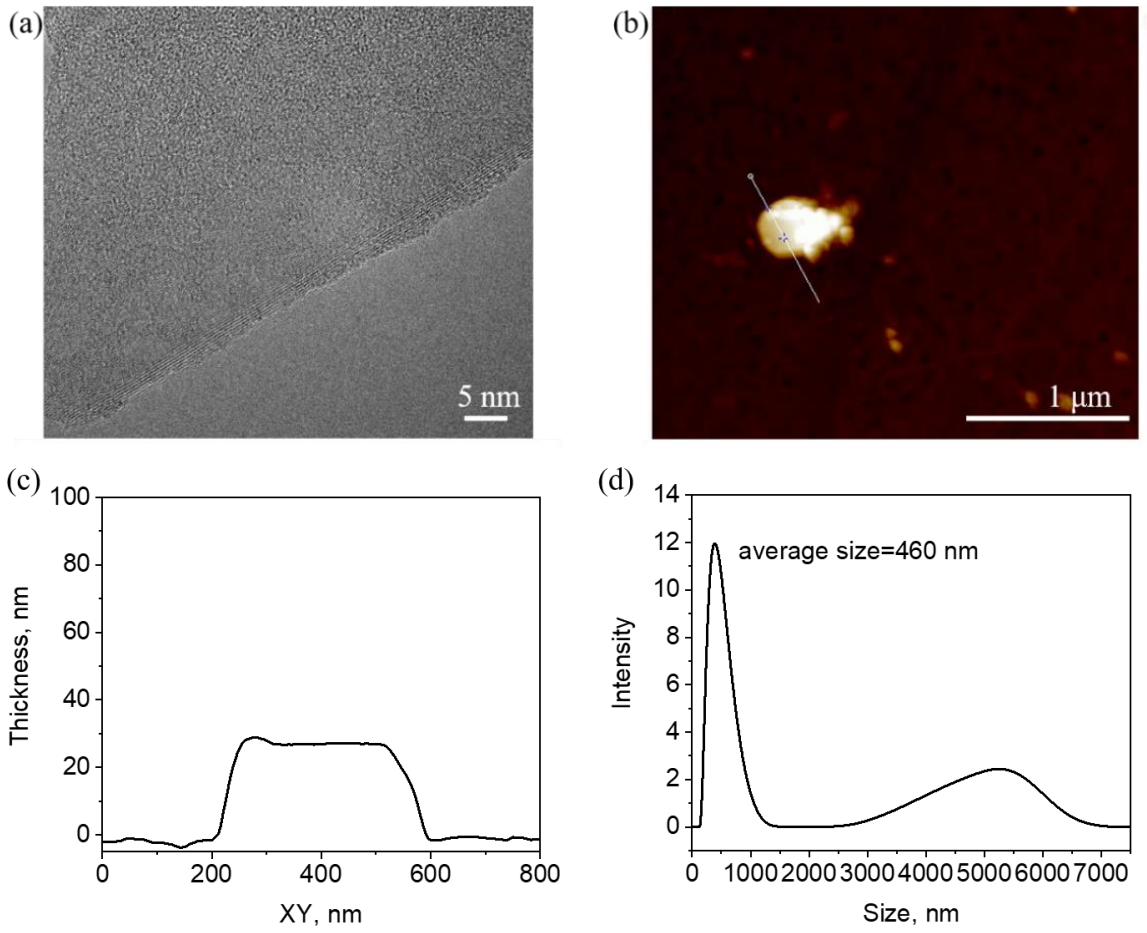

Figure 5-9. (a) TEM and (b) AFM images of BNNS. (c) The thickness profile of exfoliated BNNS along the line in (b). (d) The size distribution of constituent particles of BNNS ink, measured by a Zetasizer system with laser diffusion.

In addition to the characterizations performed on a single nanosheet, **Figure 5-9** (d) shows the particle size distribution detected by a Zetasizer system. There is a sharp peak centered near 450 nm, which represents an average size of the exfoliated nanosheets and agrees well with the scale observed by AFM. Meanwhile, a broad and weak peat near 5300 nm indicates that a small amount of big unexfoliated BN exists in the ink.

The stable printability of inks requires that individual droplets are stably generated without long tails and satellites. Two dimensionless parameters, the Ohnesorge number (*Oh*) and the Reynolds number (*Re*), are used to evaluate the printability of inks, which are described as:[18]

$$Oh = \psi/\sqrt{\gamma\rho l} \tag{5.1}$$

$$Re = \rho v l/\psi \tag{5.2}$$

where v is the ejecting velocity of the droplet, ψ is viscosity, γ surface tension, ρ density, and l nozzle diameter. Here, l = 100 μm, v = 11.5 m/s, and the density of inks is considered the same as water (ρ = 997 kg/cm^3). The surface tension and rheology properties of each ink have been listed in **Table 5-2** and plotted in **Figure 5-10**. Pure PVDF latex ink owns the highest surface tension, which is close to water (72.53 mN/m at 20°C), and the lowest viscosity among all inks. The viscosity of composite inks increases with the increase of chitosan content because of the high viscosity of starting chitosan solution. While the surface tension of nanocomposite inks decreases with the increase of chitosan concentration, even lower than the pure chitosan as approaching 15 wt%[19].

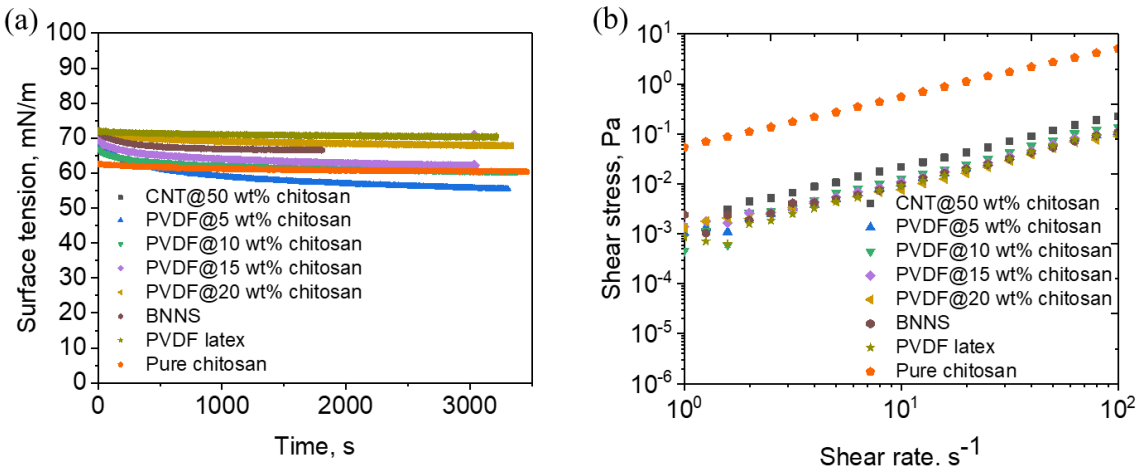

Figure 5-10. (a) Surface tension (γ) as a function of the measurement time. (b) Shear stress versus shear rate for each ink. The viscosity is shear stress divided by shear rate.

Table 5-2. Viscosity (ψ) and surface tension (γ) of each ink were measured at 20℃

Sample	Surface tension γ (mN/m)	Viscosity ψ (mPa·s)
CNT@50 wt% chitosan, 0.47 wt%	70.2	2.317
PVDF latex, 0.77 wt%	71.6	1.090
Pure chitosan, 0.75 wt%	61.3	52.49
PVDF@5 wt% chitosan, 0.4 wt%	67.7	1.222
PVDF@10 wt% chitosan, 0.4 wt%	62.2	1.476
PVDF@15 wt% chitosan, 0.4 wt%	60.3	1.484
PVDF@20 wt% chitosan, 0.4 wt%	55.4	1.499
BNNS, 0.035 wt%	66.7	1.110
H_2O (20 ℃)	72.6	1.002

Theoretical prediction of the printability of each ink was done by identifying their location in a schematic diagram (**Figure 5-11**) showing the operating regime for stable operation of inkjet printing[20]**.** Generally, the inks should fall into the printable fluid window. Surprisingly, except for the pure chitosan ink, the inks fall into the area of "satellite droplets" as shown in **Figure 5-11** (b) due to their significantly low viscosity. Indeed, efforts have been made to prepare more concentrated inks to enhance the viscosity. Unfortunately, the concentrated inks clog the nozzle very frequently. Eventually, we insist on using these diluted inks and try to experimentally control the ejection of droplets by management of the actuation pulse (drive voltage, pulse width, and frequency).

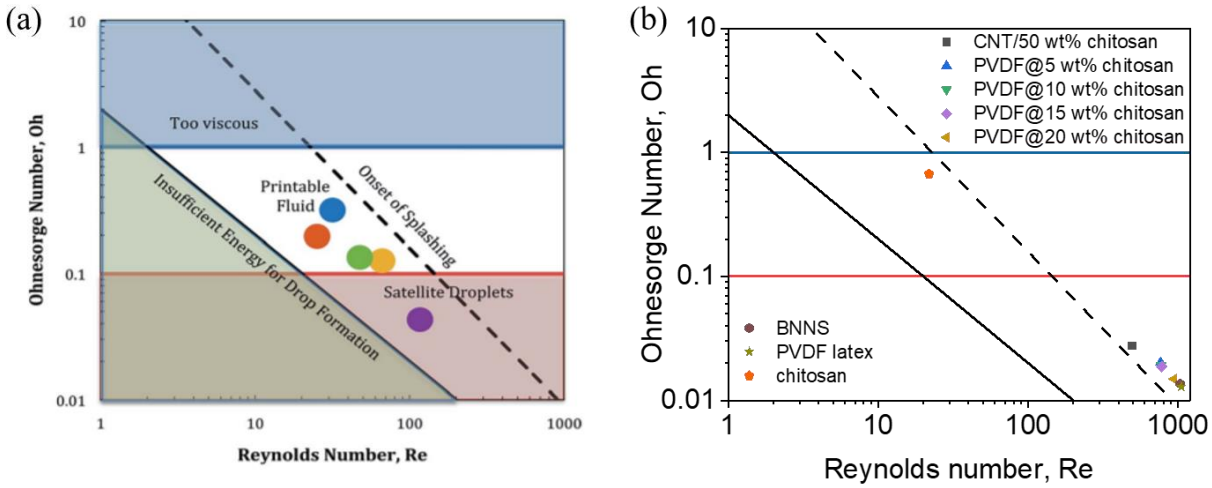

Figure 5-11. (a) Ohnesorge number plotted over Reynolds number, a schematic diagram showing the operating regime for stable operation of inkjet printing[20]. (b) The dots indicate the position of the testing liquids.

Figure 5-12 presents the photographs of each ink, the ejected droplets and the required pulse signal for the droplet generation. 87 V of pulse voltage and 27 μs of pulse length at an ejection frequency of 100 Hz were chosen to produce CNT@50 wt% chitosan ink droplets of typical volume between 300 pL and 400 pL. Drop spacing of 60 μm was utilized for the printing of electrodes. The PVDF latex ink and PVDF@5 wt% chitosan aqueous ink were ejected by using 50 V of pulse voltage and 30 μs of pulse length at an ejection frequency of 100 Hz. A drop spacing of 50 μm is set for the printing of the dielectric layers. Droplets of BNNS aqueous ink were generated with 90 V of pulse voltage and 15 μs of pulse length at an ejection frequency of 100 Hz. Experimentally, we found that all the inks are suitable to generate well-shaped and stable droplets of pL scale in volume, demonstrating the printability of developed inks and the high resolution of inkjet printing.

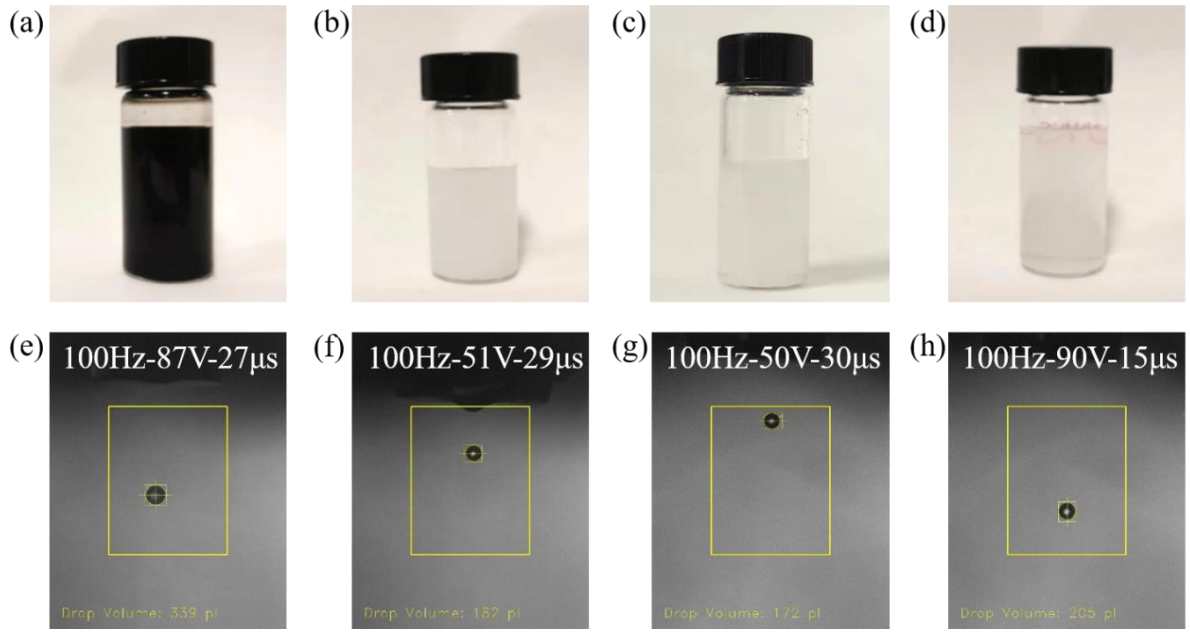

Figure 5-12. Photographs of prepared inks: (a, e) CNT@50 wt% chitosan ink; (b, f) PVDF latex ink; (c, g) PVDF@5 wt% chitosan ink; (d, h) BNNS ink. Photographs below are the images of droplets of each ink generated by the inset pulse signal. The images are captured by the camera installed in the printer, showing the size and volume of ejected droplets.

5.3.2 Morphologies of Printed Samples

The dielectric capacitor is printed layer by layer in the order of the bottom electrode, the dielectric layer and the top electrode, as schematically illustrated in **Figure 5-5**. The

morphologies of inkjet-printed samples were presented in **Figure 5-13**. We first printed a two-layer CNT@50 wt% chitosan electrode film with a width of 1mm and a thickness of ~500 nm (**Figure 5-13a**). As presented in **Figure 5-13** (b), CNTs form a network structure in the printed electrode layer, which contributes to the high conductivity. **Figure 5-13** (c) shows an optical image of a bottom CNT@50 wt% chitosan electrode covered by a PVDF@5 wt% chitosan dielectric layer that is transparent and of high quality. As shown in **Figure 5-13** (d), the CNTs keep the formed network structure and its morphology and integrity were not influenced by the deposition of dielectric ink of PVDF@5 wt% chitosan. **Figure 5-13** (e) shows a fully inkjet-printed capacitor with two electrodes and one dielectric layer in between. The inkjet-printed patterns on PI substrate are fully flexible and robust, as shown in the photographs in **Figure 5-13** (f).

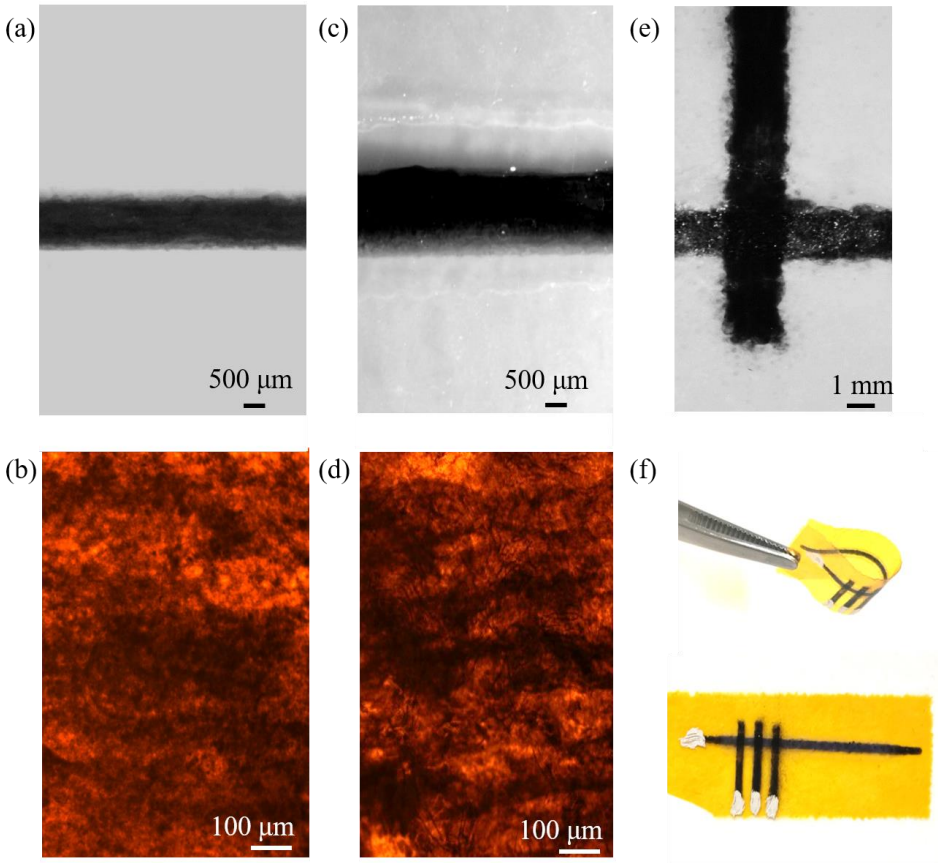

Figure 5-13. Optical microscope images of inkjet-printed two layers of CNT@50 wt% chitosan electrode at 130℃ under (a) low magnification and (b) high magnification. (c, d) The bottom CNT electrode was covered by a wider dielectric layer of PVDF@5 wt% chitosan. (e, f) The inkjet-printed dielectric capacitor was realized by printing a top electrode on the previously formulated layer of PVDF@5 wt% chitosan. Particular attention was paid to avoiding the short cut of the two electrode layers.

The surface morphologies of the dielectric layer deposited directly on PI substrate were also examined by the optical microscope. **Figure 5-14** (a) reveals the poor quality of the dielectric film when pure PVDF latex is used. The formation of cracks and high roughness is evident[18, 21]. On the contrary, when chitosan is introduced to the PVDF latex nanocomposite inks, the quality of the printed film is drastically improved (**Figure 5-14** (b)), showing a smooth surface with no cracks. It should be noted, that for both films, the slight scratch and dark points are the structural defects on the surface of NaOH-treated PI films.

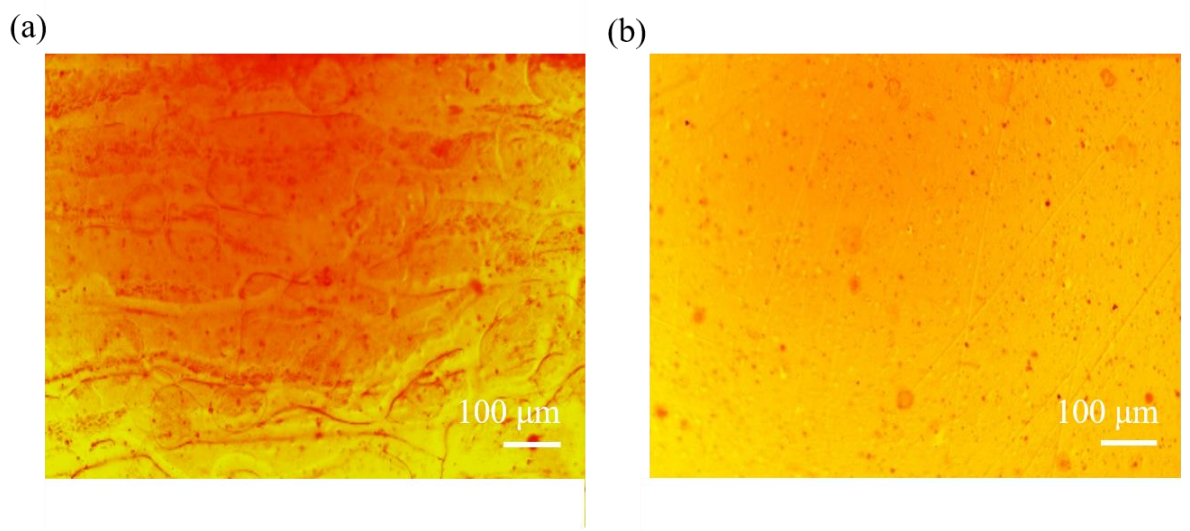

Figure 5-14. Optical microscopic image of (a) inkjet-printed PVDF latex film and (b) inkjet-printed PVDF@5 wt% chitosan film.

The SEM images were used to reveal the structures of the inkjet-printed films. As shown in **Figure 5-15** (a), the SEM image of the pure PVDF latex indicates that the latex particles coalesced. While PVDF particles can be still identified in the PVDF@5 wt% chitosan film under relatively high magnification, as shown in **Figure 5-15** (b). In this case, chitosan wraps the PVDF latex particles and acts as a barrier to prevent the coalescence of the neighboring particles.

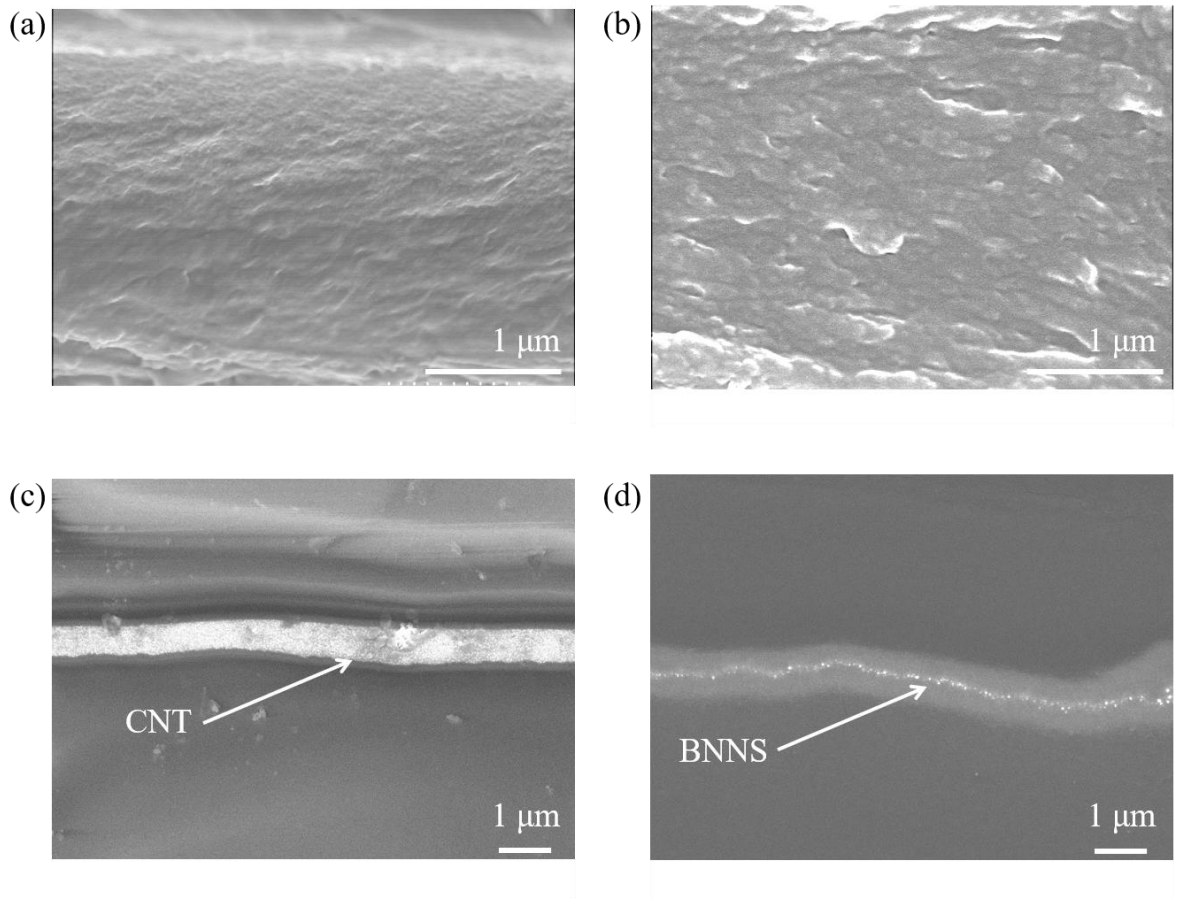

Figure 5-15. Cross-sectional SEM images of (a) inkjet-printed PVDF latex film and (b) inkjet-printed PVDF@5 wt% chitosan film, (c) the interfaces between inkjet-printed CNT@50 wt% chitosan electrode layer and PVDF@5 wt% chitosan layer and PI substrate, (d) the interfaces between inkjet-printed BNNS layer and PVDF@5 wt% chitosan layers.

The affinity between the CNT electrode layer with the dielectric layer and PI substrate were proved in **Figure 5-15** (c). Indeed, the thickness and morphology of the electrode layer are quite uniform, ensuring high quality and high conductivity. **Figure 5-15** (d) shows the PVDF@5 wt% chitosan film interlayered by the BNNS layer. It is noted that a continuous and compact BNNS nanolayer was formed without apparent cracks or defects between BNNS and polymer, indicating excellent compatibility between the ceramic layer and the polymer layer. This is actually driven by the electrostatic attraction between negatively charged BNNS and positively charged PVDF@chitosan hybrid particles.

Particular attention needs to be paid to the layer interfaces as printing heterostructures, which usually suffer greatly from the redispersion of materials as printing subsequent layers. TEM images were shown in **Figure 5-16** to further reveal the details of layer interfaces.

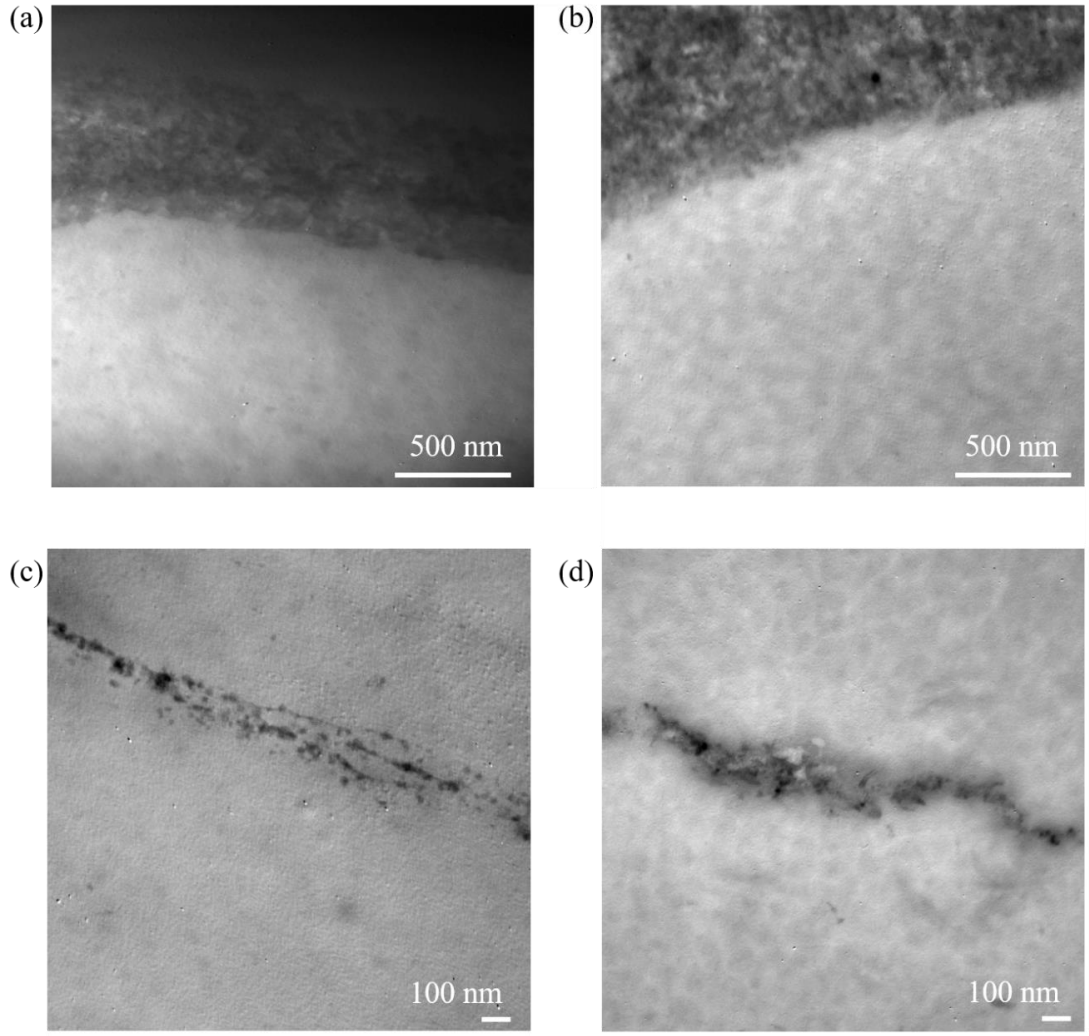

Figure 5-16. TEM images of (a) the inkjet-printed PVDF latex layer deposited on CNT electrode layer, (b) the inkjet-printed PVDF@5 wt% chitosan layer with electrode layer, (c) the inkjet-printed PVDF latex film and (d) inkjet-printed PVDF@5 wt% chitosan layer, both of which are interlayered by a BNNS layer.

Clear and straight interfaces can be found between the CNT@50 wt% chitosan and the PVDF latex (**Figure 5-16**a), and the PVDF@5 wt% chitosan dielectric layer (**Figure 5-16** (b)). BNNS does not form, as shown in **Figure 5-16** (c), a compact layer between the two PVDF latex layers because of the high roughness of the latex film substrate. Given the existence of

chitosan, the coalescence between PVDF can be prevented. While as shown in **Figure 5-16** (d), the BNNS layer is slightly distorted but still compact in the PVDF@5 wt% chitosan dielectric layer, the charge blocking effect of which should be still in operative as subjected to high electric fields.

5.3.3 Dielectric Performances of All-Inkjet-printed Films

The conductivity of the printed CNT@chitosan electrodes was optimized by changing the drop spacing and printed layer numbers, as shown in **Figure 5-17.** A high conductivity needs a sufficient number of CNT to contribute to the electric conduction, while the increased CNT contact interfaces decrease the overall conductivity, the compromise between both can be achieved with optimized printing parameters, i.e., 60 μm drop spacing and two-layer printing. The maximum conductivity is more than 5500 S/m, which is high enough to serve as an electrode in dielectric capacitors.

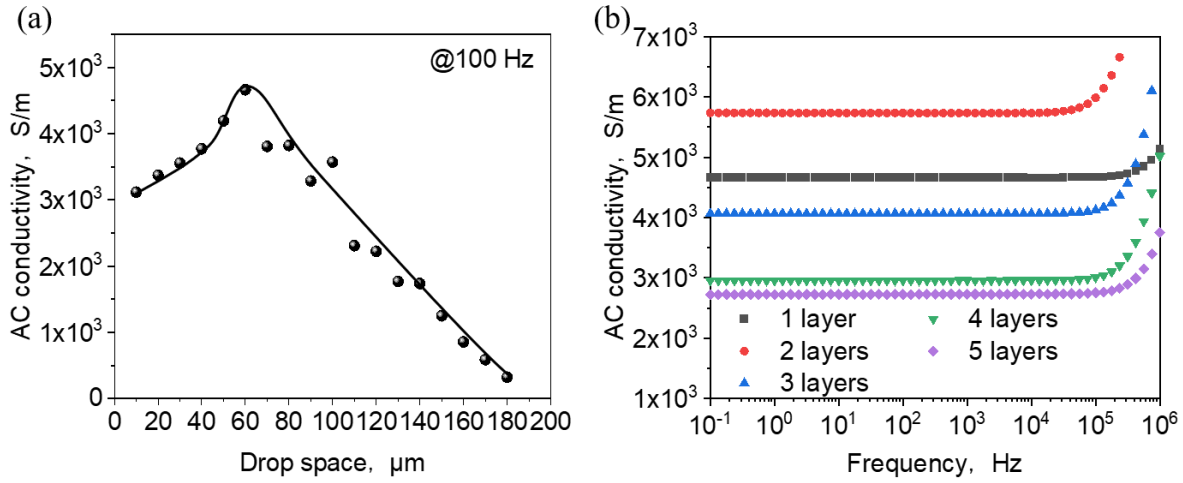

Figure 5-17. (a) The conductivity of CNT@50 wt% chitosan electrodes as a function of drop spacing. (b) The conductivity of CNT@50 wt% chitosan electrodes as a function of frequency for a different number of layers.

The frequency dependence of the dielectric constant is shown in **Figure 5-18** (a). For all samples, the dielectric constants tend to decrease with increasing frequency. The results show that the PVDF@5 wt% chitosan nanocomposite film exhibits a decrease in dielectric constant

compared to pure PVDF latex films (8.7 and 14.7 respectively at 100 Hz). The introduction of BNNS layers to the formation of sandwich structures also leads to lower dielectric constants compared to the pristine films (11.7 and 7.4 at 100 Hz for PVDF/BNNS and PVDF@5 wt% chitosan/BNNS layers). It is also important to note that at low to mid-frequencies the dielectric loss (loss tangent) of sandwich-structured films is also decreased compared to the pure dielectric films in **Figure 5-18** (c). This indicates that the BNNS layers can successfully suppress the mobility of free charges associated with the counter ions in the inks[22]. This is also supported in **Figure 5-18** (b), all conductivity curves follow the same trend and the conductivity is lower for sandwich structures in a considerable range of frequencies.

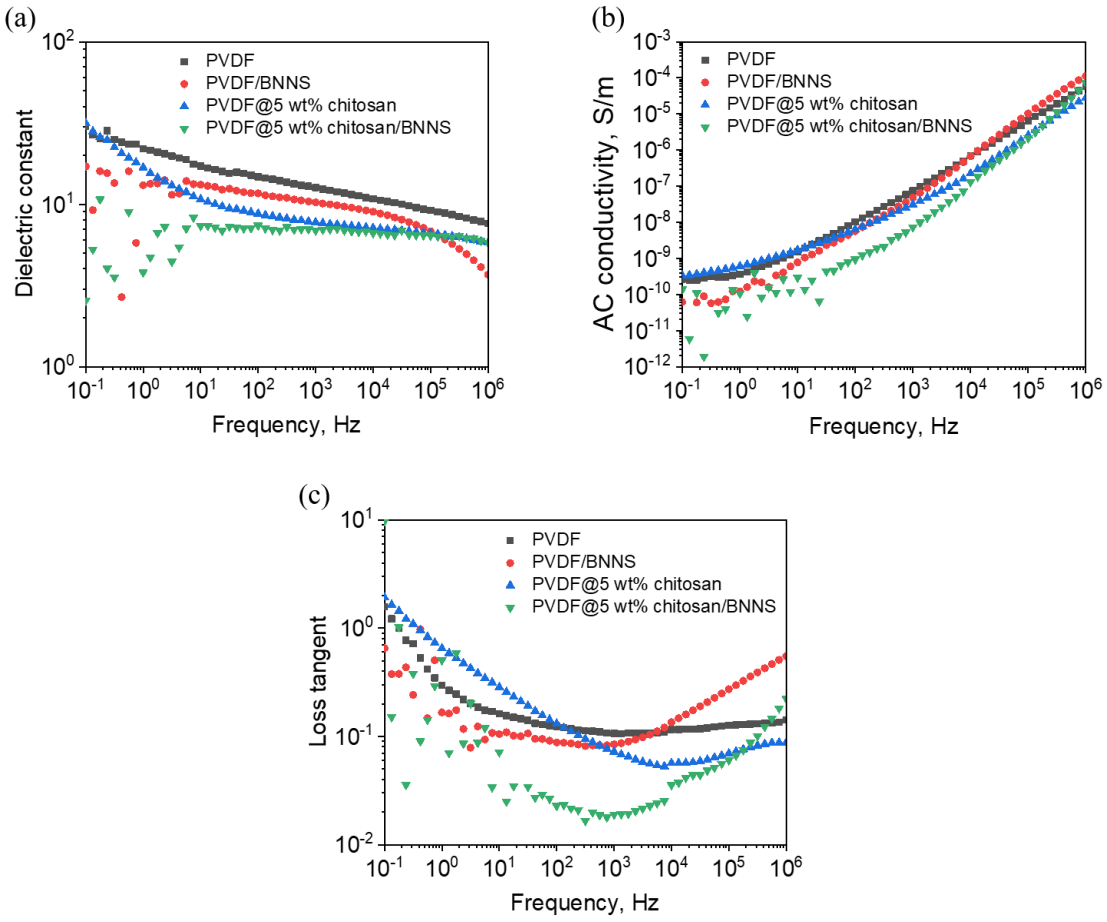

Figure 5-18. (a) Dielectric constant, (b) AC conductivity and (c) loss tangent of printed films as a function of frequency at room temperature.

5.3.4 Dielectric Breakdown Strength of All Inkjet-printed Films

We have used the Weibull distribution function (Equation (1.14)) to evaluate the breakdown strength. **Figure 5-19** shows the failure probability of dielectric breakdown given by Weibull distribution for the printed films. The E_b of pure PVDF and PVDF@5 wt% chitosan films is 203.7 MV/m and 271.3 MV/m respectively (**Table 5-3**). The increased breakdown strength of PVDF@5 wt% chitosan nanocomposites is a result of the improved film quality that has fewer morphological defects (cracks) than the pure PVDF films, as it was previously mentioned. As for the sandwich-structured films, they show significantly higher breakdown strengths compared to the pristine films, namely 386.7 MV/m for the PVDF/BNNS film and 586.7 MV/m for the PVDF@5 wt% chitosan/BNNS film. E_b is ~1.9 and ~2.2 times higher than the pure PVDF and PVDF@chitosan films respectively. This is attributed to the suppressed leakage currents due to the presence of the insulating BNNS layers, which serve as a blocking barrier at the dielectric/dielectric interface[23]. The two parameters, E_b and β, are summarized in Table 5-3.

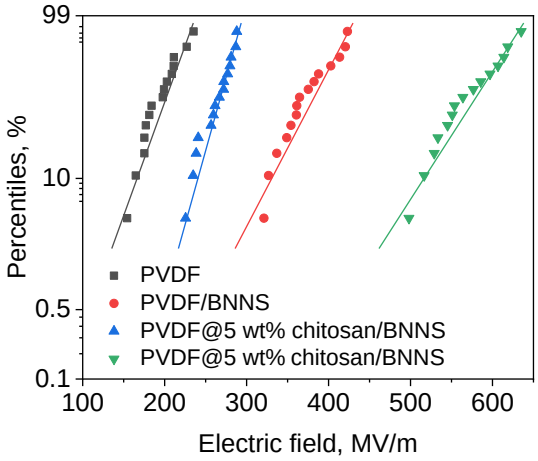

Figure 5-19. Failure probability of dielectric breakdown given by Weibull distribution.

Table 5-3. E_b and β of printed films.

Sample	E_b (MV/m)	β
PVDF	203.7	9.5
PVDF/BNNS	386.7	12.8
PVDF@5 wt% chitosan	271.3	17.3
PVDF@5 wt% chitosan/BNNS	586.7	16.2

5.3.5 Energy Density of All Inkjet-printed Films

We first compared the polarization of all films at 200 MV/m in **Figure 5-20** (a). The P_{max} of the PVDF@5 wt% chitosan/BNNS composites displays the lowest value. However, the *P-E* loop of the PVDF@5 wt% chitosan/BNNS film is much slimmer than others, showing dramatically reduced conduction losses at high fields as a consequence of the strong constrain effect on the movement of free charge carriers.

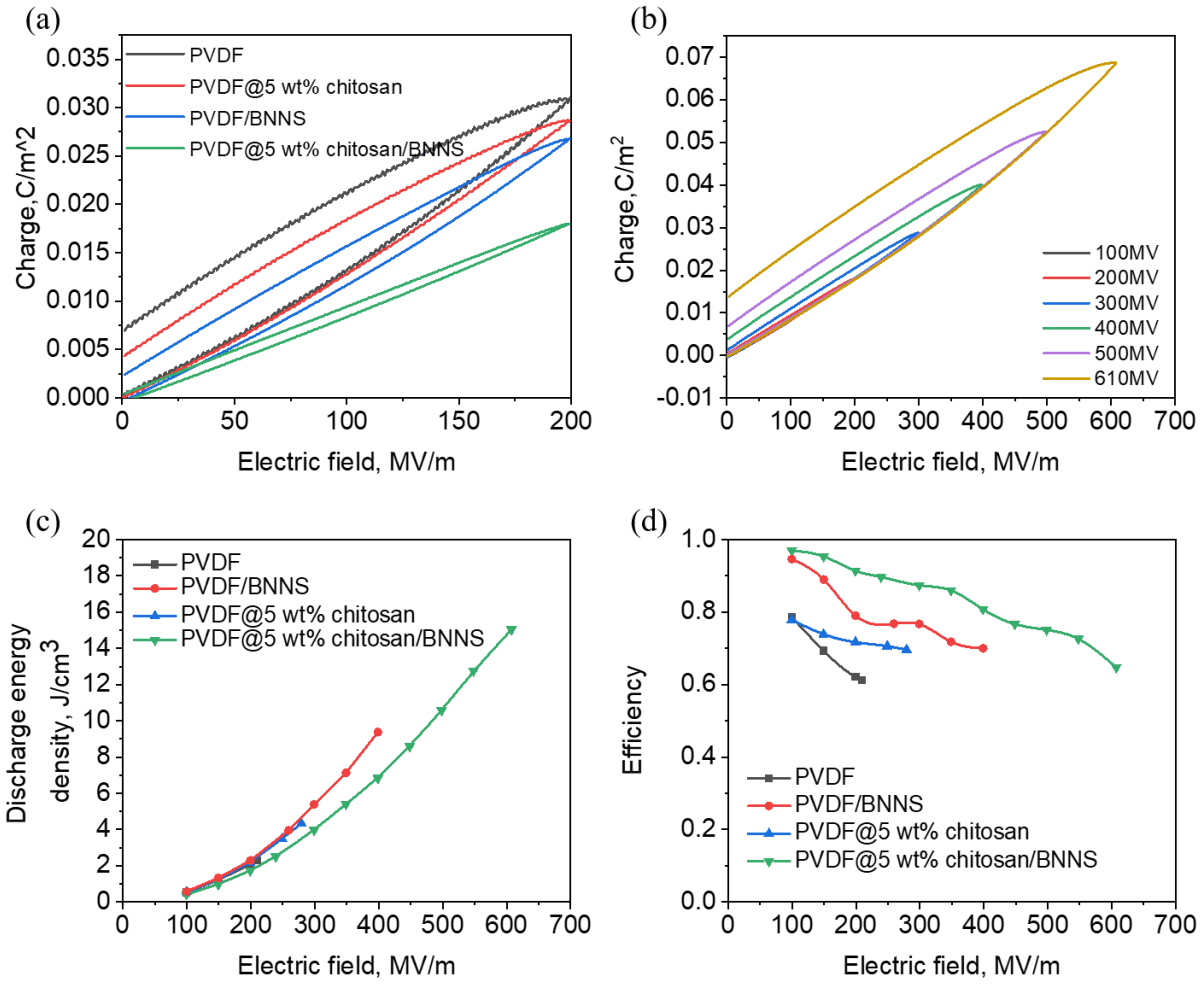

Figure 5-20. (a) *P-E* loops of inkjet-printed pure PVDF, PVDF/BNNS, PVDF@5 wt% chitosan and PVDF@5 wt% chitosan/BNNS nanocomposite films. (b) *P-E* loops of the PVDF@5 wt% chitosan/BNNS nanocomposite films at different electric fields. (c) The discharged energy density and (d) charge/discharge efficiency as a function of electric field for pure PVDF, PVDF/BNNS, PVDF@5 wt% chitosan and PVDF@5 wt% chitosan/BNNS nanocomposite films.

It is particularly interesting to investigate the polarization of the PVDF@5 wt% chitosan/BNNS film at a much higher electrical field as it shows the highest breakdown strength. With increasing the electric field, the P_{max} increases yet the composites show higher losses at higher fields as shown in **Figure 5-20** (b). The discharged energy density is shown in **Figure 5-20** (c). For each sample, the applied electric field was increased until the dielectric failure. Pure PVDF and PVDF@5 wt% chitosan films exhibit discharge energy density of 2.3 J/cm^3 and 4.3 J/cm^3 respectively, both of which are lower than the sandwich-structured films. The PVDF/BNNS film has an energy density of 9.4 J/cm^3 while PVDF@5 wt% chitosan/BNNS film shows the maximum value at 15 J/cm^3.

It is also important to evaluate the charge-discharge efficiency, which is an important parameter to be taken into consideration when it comes to practical applications of dielectric capacitors. The efficiency η is defined as Equation (1.20).[5,7] As shown in **Figure 5-20** (d), the efficiency decreases with the applied field due to the conductive losses at high fields. It is clear that the introduction of chitosan and especially of BNNS layers enhances the efficiency, which is another proof of the film's quality improvement due to the existence of chitosan as well as the ability of BNNS to largely block the leakage currents and decrease the conductivity losses.

Table 5-4 compares the dielectric properties of PVDF@chitosan films with the state of the art inkjet printed materials in the literature. So far, most of the printed capacitors have been realized by inkjet-depositing droplets of ceramic nanopowder suspensions or polymer dielectric inks. The solvent based polymer inks allow for the printing of very thin and homogeneous dielectric layers. But polymers show low dielectric constants. High-*k* ceramics enjoy strong polarizations but they are brittle and it is difficult to print large-area and crack-free films. Printing composite inks can combine the high permittivity of ceramics with the good printability of polymers. The printed composites display an improved dielectric constant, but suffer from a limited breakdwon strength E_b. Our work relies on aqueous functional inks to design and prepare sandwich structured dielectric layers that not only have excellent capacitance and low losses, but also demonstrate extremely high breakdown strength and

energy storage properties, providing therefore a sustainable route towards next-generation high-enegy dilectric materials.

Table 5-4. The formulated dielectric inks and the dielectric properties of inkjet printed materials reported in the literatures.

Ink Materials	Areal capacitance (pF/mm^2)	Dielectric constant (@1kHz)	Loss tangent	E_b (MV/m)	Energy density (J/cm^3)
PVP[24]	43.6				
PMMA/82 wt% CNO[25]		8.5	0.12		
$BaTiO_3$/P(VDF-TrFE)[26]	12	70	0.07		
SiO_2/BoPET[27]		4.1	0.08		
PMMA/BST[28]		28	0.043		
PTD[29]		13	0.1	767.4	32
BN[30]	11	1.63			
HfO_2[31]	9.5	12.6@1MHz	0.0125		
PMMA/BPMA[32]	40	3	0.04	200	
PBPDA[33]	13	0.5@3MHz			
TAS-GP10[34]		16.5	0.07		
$ZrSiO_4$[35]		5.1	0.075		
PVP[36]	50(1GHz)				
PI[37]	28.2 ±6.4	2.90			
SU-8[38]		3@100 Hz	0.04	14	
PVPh[38]		5@100 Hz	0.025	120	
TAS[39]	~2800	~17@100 Hz	~0.1		
PMMA/33 vol%$BaSrO_3$[40]		~23@100 Hz	~0.09		
PMMA/50 vol%$BaSrO_3$[40]		~34@100 Hz	~0.11		
PMMA/66 vol%$BaSrO_3$[40]		~50@100 Hz	~0.14		
$BaTiO_3$/resin[41]	44	75(@1MHz)	0.011		
hBN[42]	20 ± 3	6.1		190±30	
PVDF/PVA[18]	~46	~10	0.06	550	12
PVDF@chitosan	3.28	7.39	0.023	610	15

5.4 Conclusions

We have inkjet-printed capacitors with high energy density and high efficiency by using environmentally friendly water-based functional inks. The formulation of stabilized and homogeneous CNT conductive inks, PVDF-based dielectric inks and BNNS dielectric inks was achieved. These inks are fully printable and the formation of stable droplets of pL in volume was achievable. The introduction of chitosan to the formulation of polymer nanocomposites was a key element as it resulted in the formation of higher quality dielectric films with fewer defects compared to pure PVDF ones. Noticeably, chitosan not only allows a homogeneous film to be obtained but also improves the breakdown strength of the produced films. Moreover, it was successfully proved that the BNNS nanolayer limits the leakage currents as a barrier. The breakdown strength and the energy density of the sandwiched-structured films were significantly improved. This principle is validated for both pure PVDF and PVDF@chitosan-based sandwich structures. The latter showed the greatest enhancement of energy storage properties, exhibiting a breakdown strength of 586.7 MV/m and an energy density of 15 J/cm^3. It is also important to highlight that no fabrication methods employed in this study demanded any extreme temperature, pressure conditions, and harmful solvents.

References

1. Wu, Z.-S.; Feng, X.; Cheng, H.-M., Recent advances in graphene-based planar micro-supercapacitors for on-chip energy storage. *National Science Review* **2014,** *1* (2), 277-292.
2. Dang, Z. M.; Yuan, J. K.; Yao, S. H.; Liao, R. J., Flexible nanodielectric materials with high permittivity for power energy storage. *Advanced Materials* **2013,** *25* (44), 6334-6365.
3. Fan, B.; Zhou, M.; Zhang, C.; He, D.; Bai, J., Polymer-based materials for achieving high energy density film capacitors. *Progress in Polymer Science* **2019,** *97*, 101143.
4. Wang, J.; Shen, Z.-H., Modeling-guided understanding microstructure effects in energy storage dielectrics. *Microstructures* **2021,** *1* (1), 2021006.
5. Shrout, T. R.; Zhang, S. J., Lead-free piezoelectric ceramics: Alternatives for PZT? *Journal of Electroceramics* **2007,** *19* (1), 113-126.
6. Rabuffi, M.; Picci, G., Status quo and future prospects for metallized polypropylene energy storage capacitors. *IEEE transactions on plasma science* **2002,** *30* (5), 1939-1942.
7. Zhang, H.; Marwat, M. A.; Xie, B.; Ashtar, M.; Liu, K.; Zhu, Y.; Zhang, L.; Fan, P.; Samart, C.; Ye, Z.-g., Polymer matrix nanocomposites with 1D ceramic nanofillers for

energy storage capacitor applications. *ACS Applied Materials & Interfaces* **2019,** *12* (1), 1-37.

8. Reinheimer, T.; Azmi, R.; Binder, J. R., Polymerizable ceramic ink system for thin inkjet-printed dielectric layers. *ACS Applied Materials & Interfaces* **2019,** *12* (2), 2974-2982.
9. Worsley, R.; Pimpolari, L.; McManus, D.; Ge, N.; Ionescu, R.; Wittkopf, J. A.; Alieva, A.; Basso, G.; Macucci, M.; Iannaccone, G., All-2D material inkjet-printed capacitors: toward fully printed integrated circuits. *Acs Nano* **2018,** *13* (1), 54-60.
10. McManus, D.; Vranic, S.; Withers, F.; Sanchez-Romaguera, V.; Macucci, M.; Yang, H.; Sorrentino, R.; Parvez, K.; Son, S.-K.; Iannaccone, G., Water-based and biocompatible 2D crystal inks for all-inkjet-printed heterostructures. *Nature nanotechnology* **2017,** *12* (4), 343-350.
11. Zhu, Y.; Zhu, Y.; Huang, X.; Chen, J.; Li, Q.; He, J.; Jiang, P., High energy density polymer dielectrics interlayered by assembled boron nitride nanosheets. *Advanced Energy Materials* **2019,** *9* (36), 1901826.
12. Kumar, M. N. R., A review of chitin and chitosan applications. *Reactive and functional polymers* **2000,** *46* (1), 1-27.
13. Gautam, C.; Chelliah, S., Methods of hexagonal boron nitride exfoliation and its functionalization: covalent and non-covalent approaches. *RSC Advances* **2021,** *11* (50), 31284-31327.
14. Nair, R. M.; Surendran, V. S.; Bindhu, B., Efficient mixed solvent strategy for boron nitride exfoliation. **2019,** *2100*, 020010.
15. Bobritskaya, E.; Castro, R.; Gorokhovatsky, Y. A.; Temnov, D. In *Dielectric relaxation of chitosan films*, Advanced Materials Research, Trans Tech Publ: 2013; pp 336-339.
16. Uskoković, V., Dynamic light scattering based microelectrophoresis: main prospects and limitations. *Journal of dispersion science and technology* **2012,** *33* (12), 1762-1786.
17. Zhu, Y.; Zhu, Y.; Huang, X.; Chen, J.; Li, Q.; He, J.; Jiang, P., High Energy Density Polymer Dielectrics Interlayered by Assembled Boron Nitride Nanosheets. *Advanced Energy Materials* **2019**, 1901826.
18. Torres-Canas, F.; Yuan, J.; Ly, I.; Neri, W.; Colin, A.; Poulin, P., Inkjet printing of latex-based high-energy microcapacitors. *Advanced Functional Materials* **2019,** *29* (31), 1901884.
19. Krainer, S.; Smit, C.; Hirn, U., The effect of viscosity and surface tension on inkjet printed picoliter dots. *RSC advances* **2019,** *9* (54), 31708-31719.
20. McKinley, G., Renardy M. *Wolfgang von Ohnesorge. Phys. Fluids* **1994**.
21. Che, J.; Neri, W.; Ly, I.; Poulin, P.; Zakri, C.; Yuan, J., Waterborne nanocomposites with enhanced breakdown strength for high energy storage. *ACS Applied Energy Materials* **2020,** *3* (9), 9107-9116.
22. Huang, X.; Zhang, X.; Ren, G.; Jiang, J.; Dan, Z.; Zhang, Q.-H.; Zhang, X.; Nan, C.; Shen, Y., Non-Intuitive Concomitant Enhancement of Dielectric Permittivity, Breakdown Strength and Energy Density in Percolative Polymer Nanocomposites by Trace Ag Nanodots. *Journal of Materials Chemistry A* **2019**.

23. Guo, H.; Duan, B.; Wu, H.; Yang, Y., Breakdown mechanisms of power semiconductor devices. *IETE Technical Review* **2018**.
24. Cook, B. S.; Cooper, J. R.; Tentzeris, M. M., Multi-layer RF capacitors on flexible substrates utilizing inkjet printed dielectric polymers. *IEEE Microwave and Wireless Components Letters* **2013,** *23* (7), 353-355.
25. Wu, X.; Fei, F.; Chen, Z.; Su, W.; Cui, Z., A new nanocomposite dielectric ink and its application in printed thin-film transistors. *Composites Science and Technology* **2014,** *94*, 117-122.
26. Siponkoski, T.; Nelo, M.; Peräntie, J.; Juuti, J.; Jantunen, H., BaTiO3–P (VDF-TrFE) composite ink properties for printed decoupling capacitors. *Composites Part B: Engineering* **2015,** *70*, 201-205.
27. Surendran, K.; Varghese, J.; Sebastian, M. T., Room temperature curable silica ink. **2014**.
28. Mikolajek, M.; Friederich, A.; Kohler, C.; Rosen, M.; Rathjen, A.; Krüger, K.; Binder, J. R., Direct inkjet printing of dielectric ceramic/polymer composite thick films. *Advanced Engineering Materials* **2015,** *17* (9), 1294-1301.
29. Riggs, B. C.; Elupula, R.; Grayson, S. M.; Chrisey, D. B., Photonic curing of aromatic thiol–ene click dielectric capacitors via inkjet printing. *Journal of Materials Chemistry A* **2014,** *2* (41), 17380-17386.
30. Kelly, A. G.; Finn, D.; Harvey, A.; Hallam, T.; Coleman, J. N., All-printed capacitors from graphene-BN-graphene nanosheet heterostructures. *Applied Physics Letters* **2016,** *109* (2), 023107.
31. Vescio, G.; López-Vidrier, J.; Leghrib, R.; Cornet, A.; Cirera, A., Flexible inkjet printed high-k HfO 2-based MIM capacitors. *Journal of Materials Chemistry C* **2016,** *4* (9), 1804-1812.
32. Ge, Y.; Plötner, M.; Berndt, A.; Kumar, A.; Voit, B.; Pospiech, D.; Fischer, W.-J., All-printed capacitors with continuous solution dispensing technology. *Semiconductor Science and Technology* **2017,** *32* (9), 095012.
33. Liu, Y.; Cui, T.; Varahramyan, K., All-polymer capacitor fabricated with inkjet printing technique. *Solid-State Electronics* **2003,** *47* (9), 1543-1548.
34. Matavž, A.; Frunză, R.; Drnovšek, A.; Bobnar, V.; Malič, B., Inkjet printing of uniform dielectric oxide structures from sol–gel inks by adjusting the solvent composition. *Journal of Materials Chemistry C* **2016,** *4* (24), 5634-5641.
35. Varghese, J.; Teirikangas, M.; Puustinen, J.; Jantunen, H.; Sebastian, M. T., Room temperature curable zirconium silicate dielectric ink for electronic applications. *Journal of Materials Chemistry C* **2015,** *3* (35), 9240-9246.
36. McKerricher, G.; Perez, J. G.; Shamim, A., Fully inkjet printed RF inductors and capacitors using polymer dielectric and silver conductive ink with through vias. *IEEE Transactions on Electron Devices* **2015,** *62* (3), 1002-1009.
37. Zhang, F.; Tuck, C.; Hague, R.; He, Y.; Saleh, E.; Li, Y.; Sturgess, C.; Wildman, R., Inkjet printing of polyimide insulators for the 3 D printing of dielectric materials for microelectronic applications. *Journal of Applied Polymer Science* **2016,** *133* (18).

38. Tehrani, B. K.; Mariotti, C.; Cook, B. S.; Roselli, L.; Tentzeris, M. M., Development, characterization, and processing of thin and thick inkjet-printed dielectric films. *Organic Electronics* **2016,** *29*, 135-141.
39. Matavž, A.; Malič, B.; Bobnar, V., Inkjet printing of metal-oxide-based transparent thin-film capacitors. *Journal of Applied Physics* **2017,** *122* (21), 214102.
40. Mikolajek, M.; Reinheimer, T.; Bohn, N.; Kohler, C.; Hoffmann, M. J.; Binder, J. R., Fabrication and characterization of fully inkjet printed capacitors based on ceramic/polymer composite dielectrics on flexible substrates. *Scientific reports* **2019,** *9* (1), 1-13.
41. Lim, J.; Kim, J.; Yoon, Y. J.; Kim, H.; Yoon, H. G.; Lee, S.-N.; Kim, J., All-inkjet-printed metal-insulator-metal (MIM) capacitor. *Current Applied Physics* **2012,** *12*, e14-e17.
42. Ke, W.; Li, J.; Mohammed, F.; Wang, Y.; Tou, K.; Liu, X.; Wen, P.; Kinoh, H.; Anraku, Y.; Chen, H., Therapeutic polymersome nanoreactors with tumor-specific activable cascade reactions for cooperative cancer therapy. *ACS nano* **2019,** *13* (2), 2357-2369.

General Conclusions and Perspectives

This thesis first reviews the fundamentals of dielectric materials, especially of the polymer-based dielectric composites. Even though great progress has been realized in developing high-energy polymer-based composites, there are still several challenging issues that not only hinder the further improvement of energy storage performances but also associate concerns of environmental pollution and sustainable development of society. Colloidal, in particular polymer latex, are commonly used materials in our daily life, but are seldom applied for the dielectric applications. In this thesis, we target to design and develop water-processable high-energy storage materials starting from the aqueous colloidal suspensions. The main achievements are summarized here. Some longstanding problems and topics that warrant further investigation are addressed.

General conclusions

Due to the intrinsic good dispersion and the unique polarization capability of PVDF latex particles, they are potentially to be able to serve as novel building blocks to construct waterborne high-energy dielectric materials. In this thesis, we first developed a 0−3 nanocomposite that is waterborne and made by mixing and high-k PVDF latex and high-E_b water-soluble PVA. We found that the presence of a small amount (3 wt%) of PVDF nanoparticles within the PVA matrix can concurrently increase the permittivity and breakdown strength from 6.9 to 8.0 and from 438 to 515 MV/m respectively, giving rise to an energy density of 8.1 J/cm^3. The improved permittivity and breakdown strength are derived respectively from the increased crystallinity of PVA matrix and the confinement of the counter ions around isolated PVDF latex particles.

Higher energy density can be envisioned by improving the PVDF particle loading content in the system. We have successfully constructed a flexible, robust and high-energy dielectric material composed of 99.2% PVDF latex nanoparticles. By controlling the level of charge neutralization and passivation of PVDF particles via establishing associations of PVDF and

cationic chitosan, we can tailor the distribution of the counter ions and in turn suppress their adverse effect on the energy storage at elevated electric fields. It was found that chitosan macromolecules bridge the PVDF latex particles together yet prevent their coalescence. It drives the assembly of PVDF nanoparticles to form a closely packed but segregated nanostructure. At the neutral charge point (chitosan/PVDF mass ratio=0.8/99.2), such a nanostructure can highly profit the high polarization of PVDF while limiting conduction losses with chitosan as barriers between particles, which gives rise to a higher energy density (~10 J/cm^3) and a high energy storage efficiency (72%).

The principle validated in PVDF latex systems can be largely extended to other colloidal systems. We experimentally verify it in polystyrene (PS) latex and bentonite nanosheet suspensions, which are negative charge stabilized and represent the organic and inorganic colloidal respectively. At the point of the charge neutralization, the PS@chitosan and bentonite@chitosan associations demonstrate the highest breakdown strength and energy density.

Colloidal, particularly polymer latex nanoparticles, have naturally excellent dispersibility in water. Most of them can be used straightforwardly as function ink materials to print electronic devices. In this thesis, we go further to combine a microfabrication method, inkjet printing, and polymer latex to control the multiscale structure of composite materials to further improve the energy storage density. The formulated dielectric ink composed of PVDF latex particles coated by chitosan beyond the isoelectric point demonstrates excellent printability and film forming properties. Chitosan serves as a binder to largely improve the film quality, but it attracts negative counter ions into the system. To confine these ions, the printed PVDF@chitosan layer was interlayered by BNNS nanolayers, which are perpendicular to the electric field and serve as efficient barrier to block the transportation and the avalanche of charges and eventually lead to an energy storage density of 15.04 J/cm^3. This value is superior to most of the state of the art printed dielectric materials.

Perspectives

Chitosan, as a bioresouced cationic flocculant, can electrostatically interact with negatively charged colloidal, such as PVDF, PS latex and bentonite suspensions, and then drive their assembly into freestanding flexible dielectric films. Nevertheless, the charge density of chitosan is largely influenced by pH values, making the control of the electrostatic interaction relatively complicated. In contrast, polyelectrolytes with strongly ionized groups, such as sodium polystyrene sulphonate or poly (diallyldimethylammonium chloride), display charge densities that are essentially independent of pH. They are quite promising to be studied in the future to neutralize colloidal and form dielectric materials that can withstand high electric fields and display high energy storage density.

In addition to the electrostatic stabilization, steric stabilization can be also considered to prevent aggregation of colloids. Steric stabilization is usually achieved by encapsulating the particles with polymers that prevent the particles from coming closer together in the attractive range. This mechanism associates with additional steps of polymer coating or the in-situ synthesis of polymers on the surface of particles, but it can avoid the adverse effect of counter ions, as presented in the systems of colloidal that are electrostatically stabilized. The sterically stabilized colloidal inks can be also used directly as dielectric inks to print dielectric layers without the need of intercalating insulating barriers.